
Electronic Thesis and Dissertation Repository

10-4-2018 12:30 PM

Development Of Granulation Tissue Mimetic Scaffolds For Skin Healing

Adam Hopfgartner
The University of Western Ontario

Supervisor
Hamilton, Douglas W.
The University of Western Ontario Co-Supervisor
Pickering, J. Geoffrey.
The University of Western Ontario

Graduate Program in Biomedical Engineering
A thesis submitted in partial fulfillment of the requirements for the degree in Master of Engineering Science
© Adam Hopfgartner 2018

Follow this and additional works at: <https://ir.lib.uwo.ca/etd>

 Part of the [Biomaterials Commons](#), and the [Molecular, Cellular, and Tissue Engineering Commons](#)

Recommended Citation

Hopfgartner, Adam, "Development Of Granulation Tissue Mimetic Scaffolds For Skin Healing" (2018).
Electronic Thesis and Dissertation Repository. 5767.
<https://ir.lib.uwo.ca/etd/5767>

This Dissertation/Thesis is brought to you for free and open access by Scholarship@Western. It has been accepted for inclusion in Electronic Thesis and Dissertation Repository by an authorized administrator of Scholarship@Western. For more information, please contact wlsadmin@uwo.ca.

Abstract

Impaired skin healing is a significant and growing clinical concern, particularly in relation to diabetes, venous insufficiency and immobility. Previously, we developed electrospun scaffolds for the delivery of periostin (POSTN) and connective tissue growth factor 2 (CCN2), matricellular proteins involved in the proliferative phase of healing. This study aimed to design and validate a novel electrospayed coaxial microsphere for the encapsulation of fibroblast growth factor 9 (FGF9), as a component of the POSTN/CCN2 scaffold, to promote angiogenic stability during wound healing. For the first time, we observed a pro-proliferative effect of FGF9 on human dermal fibroblasts (HDF) *in vitro*, indicating a potential cellular mechanism of action during wound healing. POSTN/CCN2 scaffolds containing encapsulated FGF9 decreased wound diameter, with no negative or adverse effects at day 7, in a porcine model of acute cutaneous wound healing. Future work is required to investigate the effect of the POSTN/CCN2/FGF9 scaffold during impaired healing.

Keywords

Skin Healing, Chronic Wound, Granulation Tissue Biomimetic Scaffold, Electrospinning, Electrospaying, Poly(Lactic-co-Glycolic Acid), Gelatin, Fibroblast Growth Factor 9, Periostin, Connective Tissue Growth Factor 2, Dermal Fibroblast.

Co-Authorship Statement

This thesis was written by A.J. Hopfgartner with input, suggestions, and revisions from Dr. D.W. Hamilton and Dr. J.G. Pickering.

Experiments were designed by Dr. D.W. Hamilton and Dr. A. Rizkalla. All studies were conducted by A.J. Hopfgartner with the exception of UWO Animal Care and Veterinary Services performing all surgeries for both porcine studies.

Acknowledgements

Foremost, I would like to express my sincere gratitude to my supervisor Dr. Hamilton for the continuous support of my research, for his patience, motivation, enthusiasm, and immense knowledge. His guidance helped me in all the time of research and writing of this thesis. I would like to thank Dr. Rizkalla for his assistance during my many hours of electrospinning. I am also grateful to Dr. Pickering for providing valuable feedback during committee meetings, for focussing my project when I needed it, and for providing valuable input during the writing of this thesis.

To my fellow lab members: Aref, Georgia, JT, Karrie, Madeleine, and Sarah, all of whom guided and supported me throughout my research, thank you for showing me the ropes and tolerating my inexperience during the first months of my project. Thank you to Hong, an unexpected friend, who showed me the value of persistence. I wish all of you the best in your future endeavors.

Finally, thank you to my parents, sister, and to Jess for providing me with unfailing support and continuous encouragement throughout my years of study and through the process of researching and writing this thesis. This accomplishment would not have been possible without you.

Table of Contents

ABSTRACT	II
KEYWORDS	II
CO-AUTHORSHIP STATEMENT	III
ACKNOWLEDGEMENTS	IV
TABLE OF CONTENTS	V
LIST OF TABLES	IX
LIST OF FIGURES	X
LIST OF APPENDICES	XIII
LIST OF ABBREVIATIONS	XV
CHAPTER 1	1
GENERAL INTRODUCTION	1
1.1 – WOUND HEALING & CHRONIC WOUNDS – THE ROLE OF FIBROPLASIA AND ANGIOGENESIS.....	1
1.1.1– <i>The Skin – Anatomy & Physiology</i>	1
1.1.2 – <i>Cutaneous Wound Healing</i>	5
1.1.3 – <i>Chronic Wounds – Pathophysiology</i>	7
1.1.4 – <i>Chronic Wounds – Classification & Prevalence</i>	9
1.2 – CHRONIC WOUND CARE & STRATEGIES CURRENTLY UNDER INVESTIGATION	11
1.2.1 – <i>Clinical Treatment of Chronic Wounds</i>	11
1.2.2 – <i>Strategies Currently Under Investigation</i>	17
1.3 – ELECTROHYDRODYNAMIC ATOMIZATION AS A FABRICANT OF WOUND-HEALING THERAPIES	18
1.3.1 – <i>Scaffold Design for Tissue Regeneration</i>	18
1.3.2 – <i>Methods of Scaffold Fabrication</i>	18
1.3.3 – <i>Electrospun Nanofibrous Scaffolds</i>	21
1.3.4 – <i>Coaxial Electrospinning</i>	26

1.3.5 – <i>Scaffold Materials</i>	28
1.4 – PERIOSTIN, CONNECTIVE TISSUE GROWTH FACTOR 2 & FIBROBLAST GROWTH FACTOR 9 AS THERAPEUTICS FOR CHRONIC WOUNDS	31
1.4.1 – <i>Periostin & Connective Tissue Growth Factor 2</i>	31
1.4.2 – <i>Fibroblast Growth Factor 9</i>	35
1.5 – RATIONALE, HYPOTHESIS & OBJECTIVES.....	39
1.5.1 – <i>Rationale</i>	39
1.5.2 – <i>Hypothesis</i>	39
1.5.3 – <i>Objectives</i>	40
1.6 – REFERENCES.....	41
CHAPTER 2	57
INFLUENCE OF NANOFIBROUS ELECTROSPUN PERIOSTIN AND CONNECTIVE TISSUE GROWTH FACTOR 2 SCAFFOLDS ON ANGIOGENESIS AND WOUND REPAIR IN A 28-DAY PORCINE MODEL	57
2.1 – INTRODUCTION.....	57
2.2 – MATERIALS AND METHODS.....	59
2.2.1 – <i>28-Day Porcine Study</i>	59
2.2.2 – <i>Scaffold Preparation</i>	62
2.2.3 – <i>Porcine Cutaneous Wound-Healing Outcomes</i>	65
2.3 – RESULTS.....	67
2.3.1 – <i>Wound Closure Kinetics</i>	67
2.3.2 – <i>Angiogenesis</i>	68
2.3.3 – <i>Collagen Deposition</i>	68
2.4 – DISCUSSION.....	86
2.5 – CONCLUSIONS	89
2.6 – REFERENCES.....	90

CHAPTER 3	92
DESIGN AND VALIDATION OF A MATRICELLULAR PROTEIN-LOADED ELECTROSPUN SCAFFOLD CONTAINING ENCAPSULATED FIBROBLAST GROWTH FACTOR 9 IN A PORCINE MODEL OF CUTANEOUS WOUND HEALING.....	92
3.1 – INTRODUCTION.....	92
3.2 – MATERIALS AND METHODS.....	93
3.2.1 - <i>In Vitro Effect of FGF9 on Cell Populations Involved in Wound Healing</i>	93
3.2.2 – <i>Scaffold Fabrication, Design, and Validation</i>	96
3.2.3 – <i>FGF9 Release Kinetics & Assessment of Biological Activity</i>	105
3.2.4 – <i>7-Day Porcine Study</i>	108
3.3 – RESULTS.....	109
3.3.1 – <i>In Vitro Effect of FGF9 on Cell Populations involved in Wound Healing</i> ..	109
3.3.2 – <i>Scaffold Fabrication, Design, and Validation</i>	117
3.3.3 – <i>FGF9 Release Kinetics & Assessment of Biological Activity</i>	133
3.3.4 – <i>7-Day Porcine Study</i>	138
3.4 – DISCUSSION.....	158
3.4.1 – <i>In Vitro Effects of FGF9 on Cell Populations Involved in Wound Healing</i>	158
3.4.2 – <i>Scaffold Fabrication, Design, and Validation</i>	159
3.4.3 – <i>FGF9 Release Kinetics & Assessment of Biological Activity</i>	164
3.4.4 – <i>7-Day Porcine Study</i>	166
3.5 – CONCLUSIONS	167
3.6 – REFERENCES.....	168
CHAPTER 4.....	172
GENERAL DISCUSSION	172
4.1 – SUMMARY & FINAL CONCLUSIONS	172
4.2 – CONTRIBUTIONS TO THE CURRENT STATE OF KNOWLEDGE	173
4.2.1 – <i>General Significance</i>	173
4.2.2 – <i>POSTN/CCN2/FGF9 Scaffolds for Tissue Repair</i>	175
4.2.3 – <i>Therapeutic Efficacy of Fibroblast Growth Factor 9</i>	178

4.2.4 – <i>The Porcine Model for Chronic Wound-Healing Research</i>	179
4.3 – LIMITATIONS	181
4.3.1 – <i>Microsphere Fabrication</i>	181
4.3.2 – <i>Acute Porcine Wound-Healing Model</i>	181
4.4 – FUTURE DIRECTIONS	182
4.4.1 – <i>Animal Wound Models</i>	182
4.4.2 – <i>Co-Structural Scaffold Development</i>	182
4.5 – FINAL SUMMARY	183
4.6 – REFERENCES	184
APPENDICES	188
CURRICULUM VITAE	205

List of Tables

Table 1 – Electrospinning Parameter Combinations. 100

Table 2 – Electrospaying Parameter Combinations. 104

List of Figures

Figure 1. 1 – Anatomy of the skin	3
Figure 1. 2 – Diagrammatic representation of simultaneous fabrication of an electrospun nanofibrous scaffold with electrospayed coaxial microspheres	22
Figure 1. 3 – Structural domains of human POSTN and CCN2.....	33
Figure 1. 4 – Amino Acid Sequence Alignment of FGF9	37
Figure 2. 1 – Division of porcine wounds for post-experimentation.....	60
Figure 2. 2 – Representative scanning electron microscopy image of an electrospun nanofibrous scaffold utilized in the 28-day porcine wound-healing study.....	63
Figure 2. 3 – Representative images of wound closure from day 0 to day 28 in a porcine full-thickness cutaneous wound-healing model.....	70
Figure 2. 4 – 28-day wound closure kinetics after full-thickness cutaneous wounding in a porcine model.....	72
Figure 2. 5 – Individual 28-day wound closure kinetics after full-thickness cutaneous wounding in a porcine model.....	74
Figure 2. 6 – Representative images of vascular growth 28 days post-wounding in a porcine full-thickness cutaneous wound model.....	76
Figure 2. 7 – Effect of biomimetic scaffolds on angiogenesis 28 days post-wounding in a porcine full-thickness cutaneous wound-healing model.....	78
Figure 2. 8 – Angiogenic phenotype in porcine wound tissue 28 days post-wounding	80
Figure 2. 9 – Effect of biomimetic scaffolds on collagen deposition 28 days post-wounding in a porcine full-thickness cutaneous wound model.....	82

Figure 2. 10 – Hydroxyproline content as an indicator of collagen deposition 28 days post-wounding in a porcine full-thickness cutaneous wound model	84
Figure 3. 1 – Electrohydrodynamic Setup.....	97
Figure 3. 2 – Coaxial Needle dimensions	102
Figure 3. 3 – Effect of FGF9 on HDF migration	111
Figure 3. 4 – Effect of FGF9 on HDF chemotaxis.....	113
Figure 3. 5 – Effect of FGF9 on HDF proliferation.....	115
Figure 3. 6 – Effect of flow rate, distance and voltage on electrospun fiber diameter	119
Figure 3. 7 – Effect of varied gelatin solution concentration on fiber diameter	121
Figure 3. 8 – Refined scaffold morphology	123
Figure 3. 9 – Effect of electro spraying parameter variation on microsphere diameter ...	125
Figure 3. 10 – Representative images of microspheres electro sprayed at each parameter combination.....	127
Figure 3. 11 – Potential confounding effect of extraneous variables on microsphere diameter measurements.....	129
Figure 3. 12 – Confocal imaging shows core-shell structure of electro sprayed microspheres	131
Figure 3. 13 – Release kinetics and biological activity of encapsulated rhFGF9.....	134
Figure 3. 14 – Edu incorporation during S-phase DNA replication as an indicator of HDF proliferation and biological activity of released FGF9	136
Figure 3. 15 – Representative images of wound closure from day 0 to day 7 in a porcine full-thickness cutaneous wound model	140

Figure 3. 16 – Representative image of POSTN/CCN2/FGF9 scaffolds used in the 7-day porcine full-thickness cutaneous wound study	142
Figure 3. 17 – 7-day wound closure kinetics after full-thickness porcine cutaneous wounding.....	144
Figure 3. 18 – Individual 7-day wound closure kinetics after full-thickness cutaneous wounding in a porcine model.....	146
Figure 3. 19 – Representative images of vascular growth 7 days post-wounding in a porcine full-thickness cutaneous wound model.....	148
Figure 3. 20 – Effect of biomimetic scaffolds on angiogenesis 7 days post-wounding in a porcine full-thickness cutaneous wound model	150
Figure 3. 21 – Angiogenic phenotype in porcine wound tissue 7 days post-wounding ..	152
Figure 3. 22 – Effect of biomimetic scaffolds on collagen deposition 7 days post-wounding in a porcine full-thickness cutaneous wound model	154
Figure 3. 23 – Hydroxyproline content as an indicator of collagen deposition 7 days post-wounding in a porcine full-thickness cutaneous wound model	156

List of Appendices

Appendix A: GAL3 results included in representative wound images from the day 28 porcine cutaneous wound-healing study.	188
Appendix B: GAL3 results included in wound closure kinetics data from the day 28 porcine cutaneous wound-healing study.	189
Appendix C: GAL3 results included in angiogenic outcomes from the day 28 porcine cutaneous wound-healing study.	190
Appendix D: GAL3 results included in representative CD146 immunofluorescent images of the wound bed vasculature from the day 28 porcine cutaneous wound-healing study.	191
Appendix E: GAL3 results included in representative CD146/CD105 immunofluorescent images of the wound bed vasculature from the day 28 porcine cutaneous wound-healing study.	192
Appendix F: GAL3 results included in Masson's Trichrome images and hydroxyproline content from the day 28 porcine cutaneous wound-healing study.	193
Appendix G: Standard curve for the quantification of hydroxyproline content in 28-day porcine tissues using a Hydroxyproline Assay Kit.	194
Appendix H: Standard curve for the quantification of NIH3T3 cell number using the Cultrex® Cell Migration Assay Kit.	194
Appendix I: Standard curve for the quantification of HDF cell number using the Cultrex® Cell Migration Assay Kit.	195
Appendix J: Standard curve for the quantification of HDF cell number using the CyQUANT® Proliferation Assay Kit.	195
Appendix K: Standard curve for the quantification of HDF cell number using the CyQUANT® Proliferation Assay Kit.	196

Appendix L: Standard curve for the quantification of released FGF9 from electrosprayed PLGA microspheres using the Human FGF9 ELISA Kit.....	196
Appendix M: Standard curve for the quantification of hydroxyproline content in 7-day porcine tissues using a Hydroxyproline Assay Kit.	197
Appendix N: Angiogenic outcomes of the 28-day porcine wound-healing study presented per pig	198
Appendix O: S-phase EdU incorporation at 48 hours in response to elevated levels of FGF9 released from core-shell microspheres presented per cell line.	199
Appendix P: Angiogenic outcomes of the 7-day porcine wound-healing study presented per pig.	200
Appendix Q: No primary antibody negative control images of CD146/CD105 (Endoglin) immunofluorescent staining in the 28-day porcine study	201
Appendix R: No primary antibody negative control images of CD146/CD105 (Endoglin) immunofluorescent staining in the day 7 porcine study	202
Appendix S: Porcine cutaneous wound-healing angiogenic outcomes on day 7 compared to day 28.....	203
Appendix T: List of Antibodies	204

List of Abbreviations

AA – Antimycotic-Antibiotic

AF – Alexa Fluor

α -SMA – α -Smooth Muscle Actin

AU – Arterial Ulcer

BMP – Bone Morphogenetic Protein

BSA – Bovine Serum Albumin

BSS – Bioengineered Skin Substitute

CCN2 – Connective Tissue Growth Factor 2

DFU – Diabetic Foot Ulcer

DMEM – Dulbecco's Modified Eagle Medium

EHDA – Electrohydrodynamic Atomization

ECM – Extracellular Matrix

EdU – 5-ethynyl-2'-deoxyuridine

EGF – Epidermal Growth Factor

ELISA – Enzyme-Linked Immunosorbent Assay

ERK – Extracellular Signal-Regulated Kinase

FAS – Fasciclin-Like Domain

F64H – HDF cell line isolated from the healthy tissue of a 55-year-old, female, chronic wound patient

FBS – Fetal Bovine Serum

FDA – Federal Drug Association

FGF – Fibroblast Growth Factor

FGFR – Fibroblast Growth Factor Receptor

GA – Glycolic Acid

GAL3 – Galectin 3

HDF – Human Dermal Fibroblast

HBOT – Hyperbaric Oxygen Therapy

HSM – High Serum Media (DMEM – 10% FBS; 1% AA)

HSPG – Heparin Sulfate Proteoglycan

IGFBP – Insulin-Like Growth Factor Binding Protein

IL – Interleukin

IF – Interferon

LA – Lactic Acid

LRP – Low Density Lipoprotein Receptor-Related Protein

LSM – Low Serum Media (DMEM – 2% FBS; 1% AA)

M55H – HDF cell line isolated from the healthy tissue of a 55-year-old, male, chronic wound patient

M60H – HDF cell line isolated from the healthy tissue of a 60-year-old, male, chronic wound patient

Micro-CT – Microcomputed Tomography

MMP – Matrix Metalloproteinase

MRWD – Moisture Retentive Wound Dressing

NPWT – Negative Pressure Wound Therapy

PCL – Poly(ϵ -Caprolactone)

PDGF – Platelet-Derived Growth Factor

PLGA – Poly(Lactic-co-Glycolic Acid)

POSTN – Periostin

PRP – Platelet Rich Plasma

PU – Pressure Ulcer

RGD – Arginine-Glycine-Aspartame Cell Adhesive Peptide Sequence

rh – Recombinant Human

SEM – Scanning Electron Microscope/Microscopy

SFM – Serum Free Media (DMEM – 0% FBS; 1% AA)

SHH – Sonic hedgehog

SM – Serum Media

SMC – Smooth Muscle Cell

SP – Signal Peptide

TGF – Transforming Growth Factor

TIMP – Tissue Inhibitor of Matrix Metalloproteinase

TNF – Tumour Necrosis Factor

TSP – Thrombospondin Type 1 Repeat

VEGF – Vascular Endothelial Growth Factor

VLU – Venous Leg Ulcer

VWC – Von-Willebrand Factor

Chapter 1

General Introduction

1.1 – Wound Healing & Chronic Wounds – The Role of Fibroplasia and Angiogenesis

1.1.1– The Skin – Anatomy & Physiology

The skin is a complex, multifunctional organ tasked with protection, regulation and sensation. The barrier function of the skin protects the internal environment from harmful pathogens, inherent physiological mechanisms control thermoregulation, and various types of sensory neurons allow us to safely interact with our environment. These processes are guided by structures in the skin, organized into three major layers: the epidermis, dermis and subcutaneous hypodermis (Figure 1.1) [1].

The epidermis consists of multiple sublayers and cell types. Ninety-five percent of the cells located in the epidermis are keratinocytes; defined by their ability to produce keratin which is composed of intermediate filaments and forms the internal cytoskeleton [2, 3]. The stratum germinativum, or basal cell layer, consists of a single layer of column-shaped, proliferating keratinocytes [4], which migrate through the stratum spinosum and granulosum towards the superficial layers of the epidermis while differentiating into flat, polyhedral, anucleated corneocytes. The thick, superficial layer of corneocytes forms the stratum corneum to provide mechanical protection, reduce water loss and inhibit the invasion of foreign substances [2, 4]. Pigment producing melanocytes, immunocompetent Langerhans cells, and sensory Merkel cells (located in hairless skin) also populate the epidermis [3].

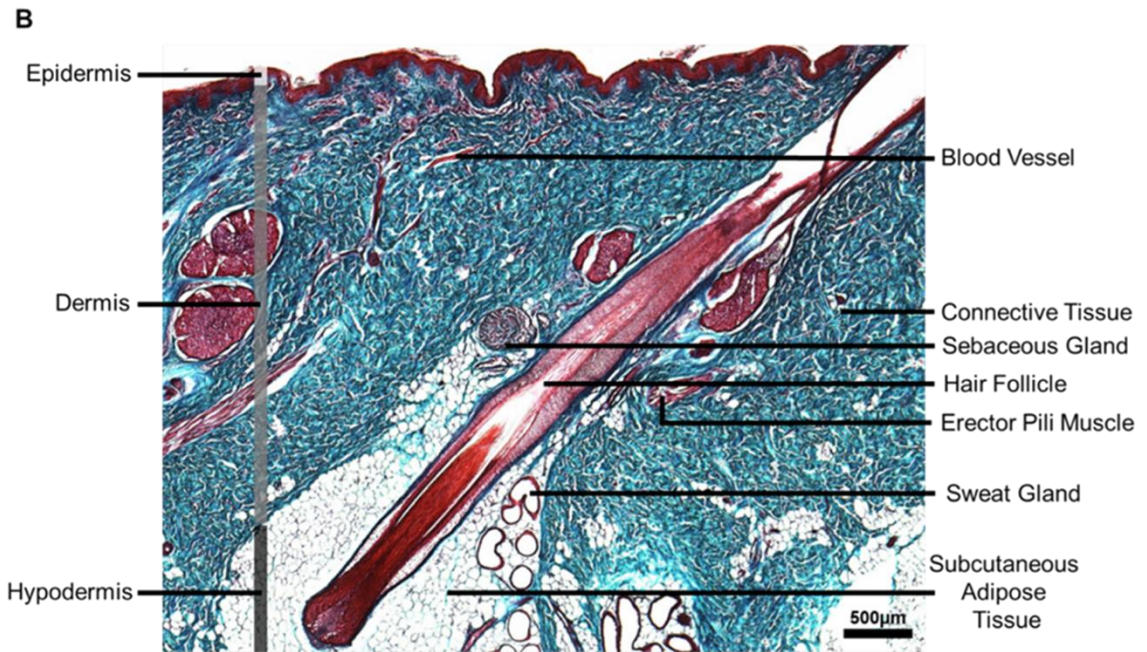
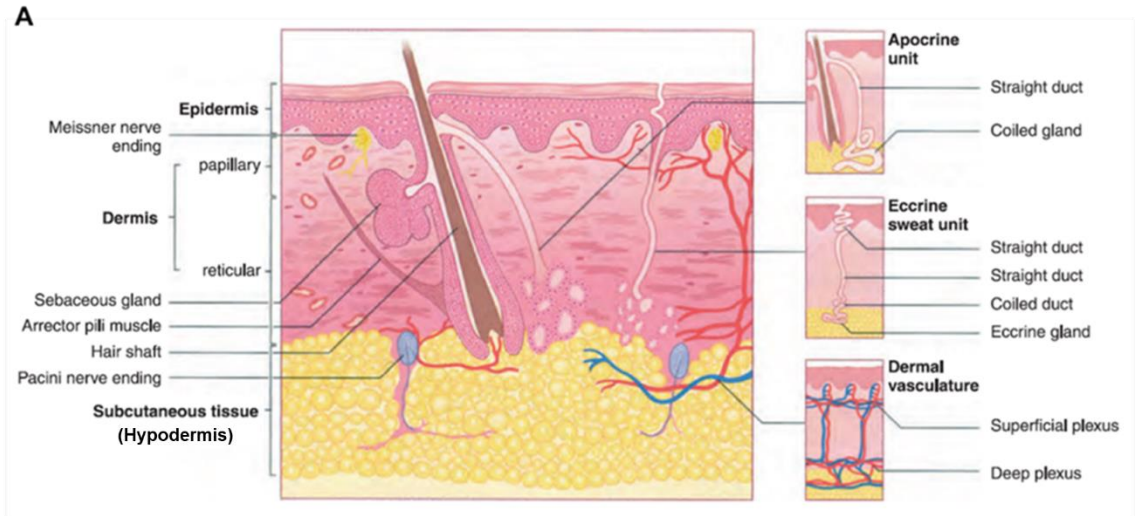
The dermal layer provides the skin its pliability, elasticity, and tensile strength with its diverse set of connective tissues, cell types, and structural components. Stress-resistant fibrillar collagens I and III synthesized by dermal fibroblasts are the major components of the extracellular matrix (ECM) and convey structural integrity to the skin. Other dermal components include: epidermally derived appendages, dermal dendrocytes, mast cells, histiocytes, blood vessels, nerves, lymphatics, sebaceous glands, apocrine glands, and

sweat glands [2]. The dermis is subdivided into upper papillary dermis and lower reticular dermis, defined by the structural and organizational differences of collagen and elastin fibers [4]. The dermal vasculature is organized into parallel superficial and subpapillary plexuses located near the base of papillary and reticular derma, respectively. Blood flow in the dermis provides nutrition to the skin and assists the body in thermoregulation [4]. Heat dissipation or conservation via vasodilation and vasoconstriction is controlled by intercommunication between superficial and subpapillary plexuses in response to external stimuli [4]. Thermoregulation is also controlled by hair follicles/arrector pili muscles and sweat glands. Piloerection traps air close to the skin for an additional layer of insulation when the body is cold and endothermic evaporation of sweat cools the surface of the skin [4, 5].

The hypodermal subcutaneous layer of the skin consists primarily of fatty lipocytes but also contains connective tissue, nerves, and blood vessels [4]. This fatty underbelly insulates and cushions the body, provides buoyancy, and stores energy [4].

The skin's exposure to the external environment makes it vulnerable to damage. Cutaneous injury disrupts the skin's ability to function properly and exposes the internal environment. Therefore, rapid and robust wound healing is essential for the maintenance of internal homeostasis and sterility.

Figure 1. 1 – Anatomy of the skin. A) Cross-sectional schematic illustration of the layers and structures composing human skin [5]. B) Masson’s Trichrome stained cryosection of porcine cutaneous tissue; porcine skin is very similar in structure and function to human skin. Connective tissues (collagen) are stained blue; muscle, erythrocytes and cytoplasm are stained red; and nuclei are stained black. The epidermis is divided into four sublayers (not shown due to scale): Stratum Corneum, Stratum Granulosum, Stratum Spinosum, and Stratum Basale (listed superficial to deep). Scale bar = 500µm.



Hopfgartner et al. 2018

1.1.2 – Cutaneous Wound Healing

After injury, wound healing restores the cutaneous barrier, prevents infection, re-balances internal homeostasis, and minimizes fluid loss. The spatial and temporal sequence of events involved in normal wound healing are organized into four overlapping phases: haemostasis, inflammation, proliferation, and remodelling.

Within one-hour post-injury, thrombin cleaves fibrinogen to create a polymerized fibrin matrix that captures circulating platelets to form a hemostatic plug. Aggregated platelets release cytokines and growth factors to recruit inflammatory cells and guide the initial stages of healing [6]. Inflammation begins one-hour after injury as inflammatory cytokines [interleukin (IL) -1 α , IL-1 β , IL-6, IL-8, tumour necrosis factor (TNF) - α , platelet derived growth factor (PDGF), transforming growth factor (TGF) - β] released by platelets, and leukocytes produce a chemotactic gradient that stimulates the migration of neutrophils, monocytes, smooth muscle cells (SMCs), and fibroblasts [7]. Neutrophils release reactive oxygen species to kill bacteria, secrete serine proteases and matrix metalloproteinases (MMPs) to debride nonviable tissue, and phagocytose dead bacteria and wound debris [7]. Monocytes responding to paracrine signals are converted into macrophages and resident and differentiated macrophages phagocytose debris and exhausted neutrophils and release another wave of signaling molecules [TGF- α , TGF- β , fibroblast growth factor (FGF) 2/basic FGF (bFGF), PDGF, vascular endothelial growth factor (VEGF)] to recruit keratinocytes, fibroblasts and endothelial cells to initiate the next stage of healing [8].

The proliferative stage is initiated three to four days post-injury and extends to four weeks. This period is dominated by fibroblast, endothelial cell, and keratinocyte proliferation, migration, and differentiation. Fibroplasia begins as fibroblasts, interacting with fibronectin, fibrinogen, and thrombin in the haemostatic clot proliferate and migrate into the wound bed [9, 10]. Migrating fibroblasts deposit collagen-rich ECM, gradually replacing the fibrin clot to increase structural integrity and provide a framework for neovascular growth [10]. Fibroplasia is regulated via a paracrine-mediated mechanism involving re-epithelializing keratinocytes. Keratinocytes upregulate anti-fibrotic urokinase-type plasminogen activator, MMP-1 and MMP-3, and downregulate pro-fibrotic connective tissue growth factor 2 (CCN2), collagen I and II, fibronectin, plasminogen

activator inhibitor-1, α -smooth muscle actin (α -SMA), and tissue inhibitor of matrix metalloproteinase (TIMP)-2/3 controlling catabolic fibroblast action on the ECM [11]. Granulation tissue, composed of the newly deposited collagen network and migrating endothelial cells and macrophages, functions as a structural and supportive matrix for angiogenesis and re-epithelialization [12].

Angiogenesis is the process of vascular growth by endothelial cell migration, proliferation and tube formation [13]. In the healing wound, angiogenesis functions to re-establish normoxia and nutrient supply [8]. Tissue hypoxia post-injury promotes the release of inflammatory mediators that act on the wound periphery to increase vascular permeability and dilation. Extravasation occurs, and endothelial cells migrate into the wound bed [14, 15]. Proteolysis reduces ECM density to facilitate endothelial migration, and angiogenic factors in the wound bed milieu (especially VEGF-A and FGF2/bFGF) promote endothelial cell proliferation and the formation of new capillary tubules in the developing granulation tissue [16-20]. Under hypoxic conditions in the early stages of wound healing, myofibroblasts mechanically support microvascular endothelial cells to facilitate neoangiogenesis [21]. Proliferating fibroblasts continue to deposit new ECM into the later stages of wound healing when normoxia has been re-established and as TGF- β levels continue to rise. Several studies have indicated angiogenesis as a key event in the wound-healing process, and suppression of angiogenesis during conditions of delayed wound healing [22, 23].

It is very important that fibroplasia and angiogenesis work synergistically during wound healing. The control of ECM composition throughout the wound-healing process is closely related to specific endothelial cell behaviour and vessel organization. Proteolytic ECM remodelling decreases ECM density, exposes endothelial cell binding sites, and releases matrix-bound angiogenic factors to stimulate endothelial cell migration [24-30]. Sequestration of angiogenic growth factors, cytokines, and ECM fragments by the ECM also promotes angiogenesis [31]. The influence of angiogenesis on fibroplasia is less clear however, proangiogenic factors have been linked to scar formation in adult wounds [32-35].

Re-epithelialization begins within hours of injury. Migrating fibroblasts and macrophages release FGF-2/7, TGF- α/β , TNF- α , and epidermal growth factor (EGF) stimulating keratinocyte migration and proliferation. Dissolution of desmosomal adhesions separates cell-cell and cell-substratum linkages allowing keratinocyte migration over the granulation tissue [36]. Proliferating and maturing keratinocytes behind the leading migratory edge restore the barrier function of the epithelium [37].

Remodeling begins two to three weeks after injury and can last for over a year [8, 37]. Fibroblasts, responding to increased collagen density, mechanical tension, and cytokines (especially TGF- β), transform into myofibroblasts with increased expression of α -SMA. These contractile myofibroblasts work to close the wound via integrin-ECM receptor mediated interaction [7]. Myofibroblast contractile phenotype is dependent on a positive feedback loop initiated by endogenous TGF- β and tensile forces that increase the density of α -SMA containing stress fibers, increase force production and tension development, and consequently upregulate TGF- β [38]. The granulation tissue is gradually replaced as fibroblasts upregulate expression of collagen I, and MMPs breakdown the old collagen III composed matrix [42, 43]. In the final stages of remodelling, apoptosis of most of the remaining endothelial cells, fibroblasts, myofibroblasts, and macrophages reduce the scar tissue to a relatively acellular mass of parallel collagen I fiber bundles [37, 39, 40]. The final scar tissue consists mainly of the few remaining fibroblasts and collagen I ECM that regains only ~80% of the mechanical properties of unwounded skin [37, 41, 42].

1.1.3 – Chronic Wounds – Pathophysiology

A chronic wound is defined as a tissue injury that has failed to proceed through the reparative process in a timely and organized fashion to establish a sustained anatomic and functional result within 3 months [43]. Chronic wounds are characterized by irregular proteolytic activity and chronic inflammation, heightened bacterial load, cellular senescence and inhibited mitogenic activity [42]. Activated keratinocytes, fibroblasts, endothelial cells, neutrophils, and macrophages increase expression of proteases in the wound bed [44]. Additionally, the over-production of reactive oxygen species from neutrophils directly damages the ECM and cell membrane leading to early cell senescence, and interferes with transcriptional pathways controlling pro-inflammatory signalling

molecules, up-regulating various MMPs and down-regulating antagonistic TIMPs [45, 46]. Studies examining biomarkers from the wound exudate of chronic wounds support this claim. In one study, biomarkers obtained from healthy and chronic wounds were compared [47]. Certain protease inhibitors (serine protease inhibitors and cystatins) were solely identified within wound exudate from healthy individuals. Additional evidence suggests that neutrophils and macrophages responsible for synthesizing proteolytic factors such as MMP-9, neutrophil elastase, and proteinase 3 were present at higher levels within the cellular infiltrate of chronic wounds. Further analysis revealed increased expression of these proteolytic products (MMP-9, neutrophil elastase, proteinase 3) [47], and serine proteases [48-51]. These results indicate a disturbed balance between proteases and their inhibitors within chronic wounds, which can lead to the excessive breakdown of matrix (hindering re-epithelialization and angiogenesis) and digestion of growth factors and their receptors.

Activated neutrophils and macrophages release pro-inflammatory cytokines such as IL-1 β and TNF- α that further contribute to imbalanced MMP expression and TIMP inhibition [7]. Regularly, wound-healing macrophages release soluble factors (such as TGF- β , PDGF- β and galectin 3) to counteract the degradation of extracellular matrix by MMPs. These small molecules increase the deposition of matrix and the release of TIMPs by myofibroblasts [52]. However, a pair of studies showed an increase of infiltrating neutrophils and proinflammatory macrophages, and a downregulation of anti-inflammatory factors responsible for the termination of inflammation and initiation of angiogenesis, matrix deposition, and remodelling within a population of chronic venous ulcers [53, 54]. Specifically, the expression of IL-1 β and TNF- α is upregulated during pathological wound healing [36, 55, 56]. These cytokines promote the release of MMPs from macrophages and suppress the synthesis of ECM proteins and TIMPs resulting in inhibition of cellular migration due to the degradation of matrix, prolonging the wound-healing response [6, 36, 55]. This unbalanced proteolytic activity results in the excessive degradation of ECM components, protease inhibitors, growth factors, and other wound repair mediators. These mechanisms produce a hostile environment that distorts the chemical and physical cues necessary for normal cellular action to take place, delaying the final stages of wound healing [57]. Without the resolution of inflammation and formation of the barrier function,

continued bacterial presence contributes to a feedforward mechanism which elevates the proinflammatory response. Additionally, the sustained bacterial load can result in the formation of a biofilm that physically impedes wound closure and blocks antibiotic treatments [47, 58-61].

Angiogenesis and vasculogenesis are critical steps ensuring adequate nutrition and oxygenation during tissue healing. Within the diabetic chronic wound microenvironment, antiangiogenic factors (ex. myeloperoxidase) are upregulated while angiogenic stimulators (ex. extracellular superoxide dismutase, VEGF variants) are decreased [62]. This downregulation of angiogenic factors is due to proteolytic degradation which may account for the inadequate capillary growth witnessed in chronic venous leg ulcers [49, 63, 64]. Pathological angiogenesis may also contribute to the development of chronic wounds from pressure ulcers. Chemotaxis of endothelial cells during the proliferative stage of wound healing relies on chemokine ligand 9. However, expression of this proangiogenic factor is decreased in pressure ulcers resulting in abnormal angiogenesis [65].

1.1.4 – Chronic Wounds – Classification & Prevalence

Four main classes of chronic wounds exist, categorized based on underlying etiology – venous leg ulcers (VLUs), arterial ulcers, diabetic foot ulcers (DFUs) and pressure ulcers (PUs). VLUs caused by chronic venous insufficiency are the most common class of chronic wound affecting 1 to 2% of the adult population [7, 42]. Risk factors associated with chronic venous insufficiency and VLUs include: trauma, advanced age, obesity, pregnancy, phlebitis, deep vein thrombosis, congestive heart failure, and a history of previous ulcers. Arterial ulcers subsequent to arterial disease and inadequate blood supply to the skin account for up to 25% of leg ulcers [66]. Arterial disease is most commonly the manifestation of systemic atherosclerosis [67, 68]. DFUs are one common and serious complication of diabetes, affecting 4-10% of diabetics annually [42]. Risk factors associated with diabetes and DFUs include: neuropathy, hyperglycemia, and lower extremity arterial disease [68]. Peripheral neuropathy due to impaired nerve function caused by hyperglycemia reduces sensation, causes foot deformity, limits joint mobility, and structurally weakens affected areas. DFUs most commonly occur on the plantar region of the foot where a difficult viewing angle paired with an insensate foot increases the risk

of ulceration from repeated mechanical stress [7, 69]. PUs are localized areas of tissue necrosis that form after prolonged soft tissue compression causes localized hypoxia and ischemic-reperfusion injury [42, 70]. One to five percent of hospitalized patients and up to 26% of nursing home patients presenting to the emergency department are affected by PUs [42]. Risk factors associated with PUs include: impaired mobility, decreased level of consciousness, diabetes mellitus, peripheral vascular disease, malnutrition, and fecal/urinary incontinence [71]. Patients with compromised sensation or mobility who are unaware or incapable of responding to the periodic need for repositioning are at greatest risk of developing PUs [7, 45]. PUs most commonly occur over bony prominences, specifically on the heel (lateral malleolus) and sacrum (ischial tuberosity/greater trochanter) [42].

Currently in developed countries, the average person is at a 1-2% risk of developing a chronic wound in their lifetime. It is estimated that approximately 6.5 million people suffer from chronic wounds in the United States alone [72-75]. Amputation rate is increased 20-fold in the diabetic population and 85% of diabetic related amputations are preceded by a foot ulcer [76, 77]. Furthermore, the five-year mortality rate associated with diabetic amputation is 45%, which is 25% greater for patients suffering from DFUs and ischemic ulcers than either pancreatic or breast cancer [78-81]. Chronic wounds treated with conventional therapy that are under 53% closed four weeks post-injury have a 9% chance of healing while 49% of DFUs never heal [81].

Chronic wounds pose a significant burden on the health care system. Three billion dollars is spent per year in the US, \$135 million per year in Canada (the average cost to treat a DFU in Canada is \$39,000), and 2-4% of the total annual global health care expenditure is associated with chronic wounds and their comorbidities [73, 74, 82, 83]. The debilitating nature of these lesions limits function and quality of life, causes pain, incurs high costs of treatment, and causes emotional and physical distress to both patient and family. With an increasing prevalence of obesity, diabetes and atherosclerosis, as well as an aging population, the impact of these injuries on both the patient and system will continue to rise.

1.2 – Chronic Wound Care & Strategies Currently Under Investigation

1.2.1 – Clinical Treatment of Chronic Wounds

General measures – including glycemic control, normalization of blood pressure, management of dyslipidemia, smoking cessation, and an appropriate diet – can reduce the risk of ulcer development [41]. However, once an ulcer has formed, standard clinical wound care involves debridement of necrotic or devitalized tissue, management of infection, dressing to control exudate and moisture, mechanical off-loading to reduce shear forces and ulcer recurrence, and possible revascularization to restore blood flow to the affected tissue [84]. Adequate pressure off-loading, and revascularization provide the necessary support to allow optimal success of tissue engineering approaches [85, 86]. The application of advanced multidisciplinary wound care significantly improves rates of chronic wound healing [87].

1.2.1.1 – Debridement

Surgical, autolytic, enzymatic, and biosurgical debridement techniques involve the removal of hyperkeratotic epidermis (callus), necrotic tissue, foreign debris, and pathogens from the wound site to reduce the risk of infection and facilitate re-epithelialization by exposing underlying healthy tissue at the wound edge [41]. Surgical debridement is the gold-standard debridement technique, involving rapid and accurate removal of tissue with scissors and a scalpel however, it can be painful and may damage viable tissue. Autolytic debridement degrades nonviable tissue via the catabolic action of endogenous enzymes within a moist wound environment; autolytic debridement is slower but less painful than surgical debridement. Mulder et al. showed that DuoDerm, a clinically available hydrocolloid dressing with autolytic properties, successfully lysed fibrin cuffs thought to reduce tissue perfusion and lead to the development of venous disease and chronic venous ulcers [88]. Enzymatic debridement involves exogenous enzymes in topical ointments to degrade and remove necrotic material from the wound bed [89]. Collagenase is the only Federal Drug Association (FDA) approved enzymatic debriding agent and has been shown to increase endothelial cell and keratinocyte migration *in vitro* and *in vivo* via stimulation by degraded bioactive fragments within the wound bed [90]. Enzymatic debridement is faster than autolysis and easy to use. Biosurgical debridement involves the dissolution and ingestion

of necrotic tissue by enzymes in the saliva of medical grade maggots (e.g., *Lucilia sericata*, *Phaenicia sericata*, *Lucilia cuprina*). Biosurgical debridement rapidly and efficiently removes necrotic tissue and has been shown to stimulate fibroblast proliferation [89, 91-93]. However, biosurgical debridement can be painful, may require patient coaching, and is rarely used due to reluctance by patients and care providers [92].

1.2.1.2 – Management of Infection

Impaired healing and infection are secondary consequences of bacterial colonization in chronic wounds. Cleansing agents such as water, saline, or dilute vinegar (0.5% acetic acid), and topical antimicrobials such as low-concentration povidone iodine, cadexomer iodine gel beads, metronidazole gel, silver, and medical grade manuka honey, are effective at reducing bacterial load and wound size [89]. Without intervention, bacterial invasion into adjacent tissues can develop into necrotizing infection, gangrene, or deep abscesses with the need for surgical intervention to avoid amputation [94].

1.2.1.3 – Wound Dressing

Wound dressings function to protect the wound from infection, provide a moist environment, absorb exudate, and promote tissue regeneration [41, 89]. Moisture-retentive wound dressings (MRWDs) maintain adequate moisture balance (moisture vapor transmission rate $<35 \text{ g/m}^2/\text{hr}$) to promote keratinocyte migration and wound healing. Chronic wound treatment with MRWDs have been shown to improve closure (up to 3.83-fold) and reduce costs compared to conventional gauze dressings [95-97]. However, chronic wounds recur in up to 70% of patients [98]. The five basic categories of MRWDs are films, foams, hydrocolloids, alginates, and hydrogels [89]. Bioengineered skin substitutes may be considered a sixth category, as MRWDs with regenerative properties.

1.2.1.3.1 – Films

Films are comprised of thin, elastic layers of polyurethane applied mainly to the site of split-thickness skin grafts and acute surgical wounds. Films are permeable for gas exchange, transparent for visualization of the wound, and provide a barrier against bacteria. Disadvantages of films include poor drainage, and tissue damage upon removal. Commercially available films include Opsite®, Askina Derm®, and Bioclusive® [41, 89].

1.2.1.3.2 – Foams

Foams are comprised of bilaminate hydrophobic polyurethane foam sheets with hydrophilic surfaces and are suitable for mild to moderately exudative wounds. Foams are absorbent, comfortable, and conformable but may require application of a secondary dressing to facilitate absorption, occlusion or drainage. Commercially available foams include Allevyn®, 3 M® Tegaderm®, and Askina® [41, 89, 99].

1.2.1.3.3 – Hydrocolloids

Hydrocolloid dressings combine a foam or polyurethane film backing with adhesive gelatin, pectin and carboxymethylcellulose matrix. Interaction between hydrocolloid matrix and wound exudate produces a gel that promotes autolytic debridement and stimulates granulation tissue formation. Hydrocolloids are conformable, waterproof, easily removed and are appropriate for wounds with mild to moderate levels of exudate. However, hydrocolloids are inappropriate for highly exudative and infected wounds, can be odorous, difficult to remove, and may cause skin maceration with highly exudative wounds. Commercially available hydrocolloids include Comfeel®, Tegisorb®, and DuoDERM® CGF [41, 89, 100]. A substantial body of evidence exists supporting the benefits of hydrocolloid dressings in chronic wound treatment [101, 102].

1.2.1.3.4 – Alginates

Alginate dressings are composed of sodium and calcium salts of alginic acid (a polysaccharide from brown algae). Alginates have haemostatic properties, are highly absorbent, and are ideally suited for highly exudative wounds, but require secondary dressing changes when they become saturated. Alginates are inappropriate for dry wounds, potentially causing pain and tissue damage upon removal. Commercially available alginates include Sorbalgon®, Seasorb®, and Kaltostat® [41, 89, 99].

1.2.1.3.5 – Hydrogels

Hydrogels contain insoluble methyl-acrylate polymers containing hydrophilic components and adhesive/absorbent methylcellulose, propylene glycol, pectins, and alginates. Hydrogels are highly absorbent, forming a gel after interaction with wound exudate which stimulates autolytic debridement. Hydrogels may be applied to a range of wounds from mildly to highly exudative. Skin maceration can occur with highly exudative wounds.

Commercially available hydrogels include Allevyn®, Aquacell®, and Exu-Dry® [41, 89, 100].

1.2.1.3.6 – Bioengineered Skin Substitutes

Like conventional MRWDs, bioengineered skin substitutes (BSSs) are protective dressings that preserve a moist wound environment and limit fluid loss. However, BSSs also actively stimulate healing. The design and structure of BSSs are tailored to the depth and remaining structural integrity of the wound being treated. BSSs for the replacement of the epidermis (e.g., for the donor site of large split-thickness grafts) are primarily autogenic keratinocyte expansions formulated into carrier dressings or suspensions that can be placed or sprayed onto the wound site. Currently, clinical autogenic epidermal BSSs include Epicel®, Epidex®, Myskin®, Bioseed®, and Cellspray® [103].

Dermal BSSs are necessary when the native dermis has been removed. Dermal substitutes are designed as three-dimensional biomaterial matrices, similar in structural, elastic, and mechanical properties to the ECM, with or without a cellular component. Endogenous fibroblasts and endothelial cells repopulate acellular dermal BSSs (e.g., Oasis® and Alloderm®), gradually vascularizing and remodelling the skin substitute [103]. Acellular dermal BSSs are nonimmunogenic, mechanically robust, and can be used off the shelf. Cellular dermal BSSs are seeded with neonatal human foreskin fibroblasts and/or keratinocytes (e.g., Dermagraft® and Orcel®) and have been shown to regenerate skin at 35 days post-wounding and improve wound healing with depressed myofibroblast activity in acute and chronic wounds (by reducing wound contractility to allow re-epithelialization to restore a more natural tissue barrier) [41, 104]. Dermagraft® was observed to stimulate cellular infiltration, angiogenesis, and re-epithelialization in chronic wounds [105]. Furthermore, in separate studies of murine and human models of diabetic and venous ulcers, Dermagraft® increased the rate of vascularization and wound closure compared to acellular dermal skin substitutes [106, 107].

Bilayer skin substitutes are the most advanced class of BSSs consisting of both epidermal and dermal components. Apligraf® is a FDA-approved cellular bilayer skin substitute consisting of an epidermal layer of neonatal human foreskin keratinocytes and a dermal layer composed of type-I bovine-collagen fibrils seeded with neonatal human fetal

fibroblasts, and is intended for use in acute wounds, chronic skin ulcers, and burns [41, 89]. The keratinocyte and fibroblast populations contained in Apligraf® dressings are responsible for the production and delivery of cytokines [interferon (IF) - α , IF- β , IL-1/6/8], growth factors (e.g., PDGF) and ECM components to the wound bed [8]. In two studies of venous leg ulcers, application of Apligraf® with compression therapy was shown to significantly improve wound closure compared to compression therapy alone [106, 108]. However, high cost and limited shelf life are two major limitations of bilayer skin substitutes [106].

1.2.1.4 – Adjunctive Therapies

There are currently several therapies used adjunctively with standard care to improve healing outcomes. Adjunct therapies increase closure rates, improve the quality of repaired tissue, decrease amputation rate and associated mortality, and lead to an overall reduction in the cost of care [41].

1.2.1.4.1 – Negative Pressure Wound Therapy

Negative-pressure wound therapy (NPWT) or vacuum-assisted closure therapy applies sub-atmospheric pressure to a local area of tissue damage through a specialized pump connected to a foam dressing with an adhesive backing while a canister attached to the NPWT system collects wound exudate [109]. NPWT reduces tissue edema, improves circulation, promotes granulation tissue formation, and inhibits bacterial growth [110]. NPWT significantly improved rate of wound closure, time to complete closure and rate of granulation tissue formation after partial foot amputation in diabetic patients [109]. In one case study, NPWT accelerated wound healing of an infected chronic leg ulcer after reducing exudate and bacterial count [111]. After one week of treatment with NPWT, reduced inflammatory damage and improved perfusion was observed in three chronic wounds [112].

The exact molecular mechanism of NPWT is unknown however, cytokine, chemokine, growth factor, and MMP expression is altered in response to NPWT [113]. TNF expression was downregulated [114] and proangiogenic factors IL-8, and VEGF were upregulated in human chronic wounds following NPWT [115]. Inflammatory mediators IL-1 β and TNF- α expression was reduced in skeletal muscle after NPWT [116]. Conflicting evidence has

been presented on MMP expression in response to NPWT. Expression of MMPs-1/2/9/13 were reduced in two studies of human chronic wounds treated with NPWT [117, 118] however, a separate study of eight human chronic wounds found no difference in MMP-2/3 and TIMP-1 expression following NPWT [114].

1.2.1.4.2 – Hyperbaric Oxygen Therapy

Hyperbaric oxygen therapy (HBOT) involves a patient breathing 100% oxygen for a specific period of time in a pressurized chamber (1-3 atmospheres) [119]. A standard treatment regimen involves 90-120-minutes of HBOT for 30 sessions [113]. HBOT is based on Henry's law which states that the dissolution of gas in a liquid or tissue is proportional to the partial pressure of that gas in contact with the liquid or tissue [120]. Oxygen saturation of hemoglobin and dissolved oxygen in plasma both rise during HBOT. Hyperoxia stimulates the generation of ROS which disrupt bacterial metabolism and enhance the bactericidal oxygen-dependent leukocyte peroxidase system [121]. Enhanced blood and tissue oxygenation by HBOT improves oxygen delivery to hypoxic tissues and vasoconstricts surrounding healthy tissue, alleviating edema and allowing natural host responses to infection and ischemia to proceed [122]. The resolution of edema stimulates angiogenesis, fibroblast proliferation and differentiation, and collagen formation and cross linking [123]. The mechanisms that produce the beneficial molecular effects of HBOT are unclear however, HBOT has been established as an effective adjunct to standard chronic wound care. HBOT improves wound closure, reduces rates of lower leg amputation., and reduces rates of amputation in diabetic patients with ischemic foot ulcers [41, 119, 124]. Additionally, HBOT possesses bactericidal capability; reducing cellular viability of biofilms *in vitro*, and bacterial load *in vivo* [125]. Disadvantages of HBOT include ear, sinus or lung damage, oxygen poisoning, and high costs and impracticality of the equipment involved [124]. Alternative techniques of enhanced oxygen delivery (e.g., topical oxygen delivery) can provide the benefits associated with HBOT and improve practicality, improve ease of use, and decrease costs [126].

1.2.1.4.3 – Growth Factors

Growth factors mediate cell division, migration and proliferation, and have a central role in each stage of the wound-healing process [127]. Topical growth factor formulations have

been used in chronic wound healing with beneficial results. Regranex®/Becaplermin is a recombinant human-derived PDGF gel, was the first growth factor to obtain FDA approval for use in DFUs and has also been shown effective in PUs. Application of 100 or 300µg/mL Becaplermin gel once per day significantly decreased wound size compared to placebo and standard care in PUs [128] and in DFUs [129]. However, the FDA has warned of the increased risk of cancer mortality associated with use of three or more tubes of Becaplermin [130]. Positive effects of other growth factors for the treatment of chronic wounds, such as bFGF/FGF2, recombinant human (rh) EGF, rhVEGF, and nerve growth factor, have been demonstrated [131-134]. Topical growth factor treatment is limited by rapid proteolytic degradation of the applied bioactive factor(s) *in vivo* [135].

1.2.2 – Strategies Currently Under Investigation

Many of the current biological therapies focus on provision of a single bioactive factor targeted at a specific stage or mechanism. Many cutting-edge strategies still in the research phase are attempting to avoid this limitation by incorporating various active constituents and cellular components for more comprehensive chronic wound treatments. Three main areas have been focussed on: stem cell therapy, platelet-rich plasma, and gene therapies. Stem cell therapies for the treatment of chronic wounds supply adult stem and progenitor cells to the site of injury to recruit other cell types such as keratinocytes, macrophages and endothelial progenitor cells [136]. Platelet-rich plasma is autologous blood plasma containing a high concentration of platelets that release vital growth factors (PDGF, EGF, TGF-β, bFGF/FGF2, FGF9) to replenish the chronic wound environment upon application, and enhance cell migration, proliferation, angiogenesis, and matrix remodelling [137, 138]. Gene therapies involve the delivery of viral vectors containing genes encoding growth factors, and inflammatory mediators [139, 140].

Bioengineered skin substitutes, topical growth-factor delivery, stem-cell therapies, platelet-rich plasma, gene therapies, and the other adjunct treatment modalities use factors and equipment that are extremely expensive and impractical. Furthermore, scaling research of developing bioactive therapies is difficult due to the exorbitant cost, and a lack of animal models that accurately reflect the human condition [58].

1.3 – Electrohydrodynamic Atomization as a Fabricant of Wound-Healing Therapies

1.3.1 – Scaffold Design for Tissue Regeneration

Standard chronic wound care is limited by the passive nature of conventional dressings and rapid degradation of topical growth factors by proteolytic, acidic and heat sensitive mechanisms *in vivo* [141]. Biomaterial scaffolds act as delivery vehicles to protect and prolong the release of bioactive agents and confer mechanical or biological properties reminiscent of the natural granulation tissue or ECM. Biomaterial scaffolds interact with the wound microenvironment to physically promote cell adhesion, proliferation, differentiation, and migration, and to re-establish the normal cellular signaling gradients that have been disrupted by the pathological chronic wound microenvironment [142]. Biomaterial design involves the choice of appropriate fabrication methods, appropriate materials, and incorporation of the appropriate bioactive factors. The ideal biomaterial scaffold is biocompatible, structurally similar to the natural ECM (fiber diameter 50-500 nm, 90% porosity, and average pore size of 100 μm), optimized to coordinate scaffold degradation with tissue repair, nonimmunogenic, and biodegradable [143-147]. Commonly utilized fabrication methods and materials for the design of biomaterial scaffolds, including three-dimensional porous scaffolds and core-shell spheres, are presented here.

1.3.2 – Methods of Scaffold Fabrication

1.3.2.1 – Three-Dimensional Porous Scaffolds

1.3.2.1.1 – Self-Assembly

Self-assembly involves spontaneous structural organization via covalent bonding of individual components. The most efficient self-assembling polymers are amphiphilic peptides. Amphiphilic peptide molecules, containing a peptide sequence and an alkyl ester lipid region, self assemble into three-dimensional triple-helical structures reminiscent of natural collagen's secondary triple-helical structure by hydrophobic interaction of the lipophilic tail regions [148]. Amphiphilic peptides form triple helical fibers 5-8 nm in diameter in aqueous solution and are composed of 1) an alkyl tail, 2) four consecutive cysteine residues to form disulfide bridges and polymerize the molecules, 3) triple glycine residue hydrophilic head group, 4) a phosphorylated serine residue for interaction with calcium ions to direct mineralization, and 5) an arginine-glycine-aspartame (RGD)

sequence for cellular adhesion. Altering pH, solution concentration, and temperature can change self-assembly into structures such as gels, sheets, spheres, rods, disks, or channels [147]. Self-assembling amphiphilic peptides promote cell adhesion, cell proliferation, and angiogenesis [149], and fiber diameters coincide with the thinnest ECM collagen fibers (5-8 nm). However, self-assembly only creates short fibers ($<1 \mu\text{m}$), has a low diversity of applicable polymers, and the complexity and low yield limits its scalability [148].

1.3.2.1.2 – Phase-Separation

Phase separation utilizes thermodynamic or water-based solvent extraction to separate polymer from the solvent component of a polymer solution to fabricate heterogeneously porous polymer scaffolds with diameters between 50-500 nm, similar to the natural ECM. Variation of temperature and polymer concentration, and addition of various porogens (e.g., sugar, salt) produce tunable microporous scaffold architecture [148]. Phase separation is a simple technique with adjustable mechanical properties, pore size, and pore interconnectivity (based on temperature and polymer concentration), and batch-batch uniformity. However, heterogeneity of the porous structure may negatively impact cellular infiltration, so the suitability of phase-separated scaffolds as wound-healing therapies is controversial [150]. Additionally, low yield, and low applicable polymer diversity are limitations associated with phase separation.

1.3.2.1.3 – Lyophilization

Lyophilization or freeze-drying involves vacuum sublimation of frozen hydrogels saturated with water. Evacuation of ice from within the hydrogels produces porous membranes, tunable by controlling the freezing temperature; decreasing temperature decreases final pore size [151]. Lyophilization is a simplistic method of producing a highly interconnected, three-dimensional, porous matrix, but thermoregulation is necessary to maintain structural integrity and inhibit collapse of the internal porous structure. The process is also limited by small, irregular pore sizing, long processing times, and expensive equipment [152].

1.3.2.2 – Core-Shell Spheres

1.3.2.2.1 – Solvent Evaporation/Emulsification-Evaporation

Solvent evaporation or emulsification-evaporation involves solidification of particles during simultaneous solvent evaporation and polymer emulsification under high shear

stress to produce particles 200 nm to 2 μ m in diameter. Solvent evaporation is a simple drug encapsulation process that is appropriate for scale-up however, toxicity of remaining organic solvents and an inverse relationship between drug content and particle diameter limit its use [153].

1.3.2.2.2 – Emulsification-Diffusion

Emulsification-diffusion involves dissolution of polymer and active constituent into a saturated solution of water and miscible organic solvent before stabilizers, surfactant, and sufficient water are added to induce solvent diffusion into the external aqueous phase, thus aggregating residual polymer and active constituent into solid nanoparticles under 200 nm in diameter [154]. Emulsification-diffusion is reproducible, easy to scale-up, and allows incorporation of thermosensitive drugs. Encapsulation efficiency of lipophilic drugs is high, however, low encapsulation efficiency of hydrophilic drugs and long processing times are substantial drawbacks [155].

1.3.2.2.3 – Spray Drying

Spray drying atomizes a drug or polymer solution through fine pores into a drying chamber heated above the vaporization temperature of the solvent to produce spherical nano-scale droplets of polymer and drug. Spray drying is a single-step, scalable process capable of tunable particle size and drug encapsulation however, thermosensitive bioactive agents are incompatible with the elevated temperatures involved [156].

1.3.2.2.4 – Nanoprecipitation

Nanoprecipitation involves dissolution of active constituents and polymer into a water-miscible organic solvent before addition of a non-polymer solvent aqueous solution. Nanoparticle precipitation occurs under moderate stirring due to rapid diffusion of organic solvent into the aqueous phase, similar to the emulsification-diffusion process [157]. Nanoprecipitation is simple, fast, reproducible, scalable, and capable of producing monodisperse particles. However, low polymer concentration in the organic phase and low loading efficiency of hydrophilic drugs, due to hydrophobicity of the nanoparticle matrix, are significant limitations [158].

1.3.2.2.5 – Electrohydrodynamic Atomization

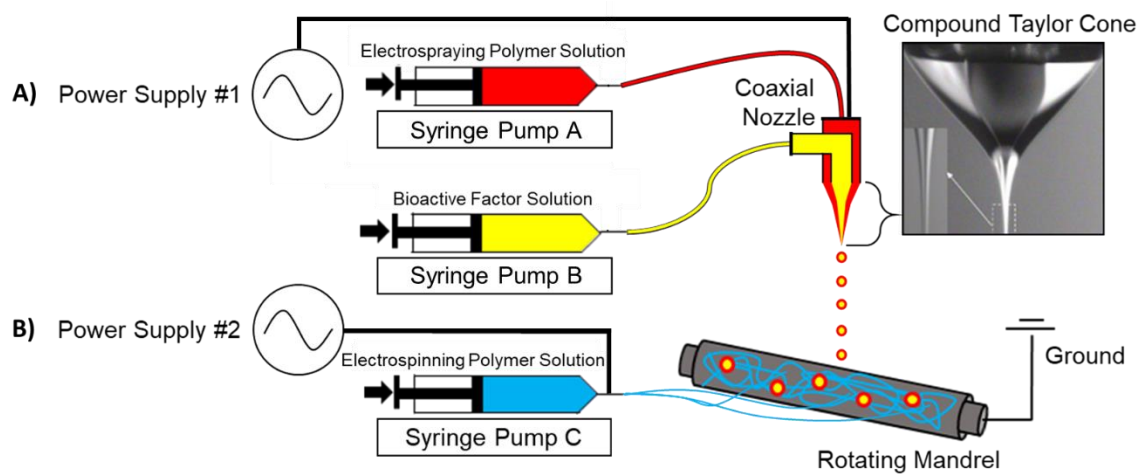
Finally, electrohydrodynamic atomization (EHDA) utilizes electromechanical and hydrodynamic forces to transform a polymer solution into either fibrous or spherical structures. Electrospinning and electrospraying are the two-main operative EHDA techniques, differing mainly in their processing conditions.

1.3.3 – Electrospun Nanofibrous Scaffolds

Studies have successfully utilized nanofibrous scaffolds or meshes for topical wound treatment [159, 160]. Blend electrospinning is an established method for the fabrication of nanofibrous meshes or scaffolds in which a bioactive agent is blended into the polymer solution that will eventually form the scaffold structure. Biomimetic scaffolds fabricated by blend electrospinning incorporate favourable qualities including biocompatibility, biodegradability, sterilizability, and important physical and mechanical properties reminiscent of the native ECM [161].

A sufficiently high voltage (10 - 20 kV) is applied to a polymer solution [after blending with therapeutic agent(s)] that is actively pumped out of a syringe. Repulsive electrostatic forces eventually overcome surface tension of the liquid droplet (Taylor cone) at the spinneret tip, propelling a fine jet of electrically charged polymer solution towards a grounded collecting surface. As the stream travels, solvent evaporates, and the charge migrates to the surface of the polymer fiber. Bending of the travelling polymer due to electrostatic repulsion promotes elongation and thinning of the fiber until it is deposited on the grounded collecting surface. Depending on the polymer and solvent used, this process results in fibers of uniform diameter ranging from 50 nm to 10 μm (Figure 1.2B) [162].

Figure 1. 2 – Diagrammatic representation of simultaneous fabrication of an electrospun nanofibrous scaffold with electro sprayed coaxial microspheres. A) Electro spraying involves the appropriate combination of processing parameters (i.e., solution concentration, solution viscosity, flow rate, applied voltage, and collector distance) and a coaxial needle to form a compound Taylor Cone, elongating the solution meniscus until electrical repulsion overcomes surface tension to separate the solution into core-shell droplets that are deposited on a grounded collecting surface. **B)** Electro spinning utilizes a uniaxial needle and the same set of processing parameters to eject a thin fiber onto the collecting surface under the appropriate combination of processing parameters.



High protein loading (up to 100%), polymer diversity, ability to manipulate protein release, simplicity, cost efficiency, versatility, and the morphological resemblance of electrospun nanofibers to native ECM (including high surface area to volume ratio, interconnected porosity, and fiber diameter) are significant factors contributing to the utilization of electrospun nanofibrous scaffolds in tissue engineering applications [163, 164]. Additionally, the various parameters involved in the electrospinning process provide a means to customize scaffold characteristics [165]. Concentration and resultant viscosity of the polymer solution, solvent properties, distance from needle to collecting surface, applied voltage, flow rate, temperature, and humidity all contribute to the scaffold's final morphology [166, 167].

Perhaps the greatest advantage of blend electrospinning is that incorporation of bioactive factors into the polymer solution disperses bioactive molecules evenly throughout the scaffold, enabling a more controlled release compared to physical adsorption onto the surface of the fibers [168]. Electrospun scaffolds are highly interactive with the *in vivo* environment due to their high surface-area-to-volume ratio, nanoscale diameter, and highly porous structure. An initial burst release followed by sustained release of diffusing bioactive factors occurs during degradation of polymer fibers *in vivo* [169]. Bioactive factors that are present during normal healing, such as antimicrobial peptides, cytokines, and growth factors, are absent in chronic wounds [170]. Incorporation of EGF, bFGF, and antimicrobial peptide LL-37 into silk nanofibers by blend electrospinning re-established biological gradients of these bioactive factors in full-thickness excisional wounds on the dorsal surface of diabetic rabbits, accelerating wound healing, lowering MMP expression, regulating ECM secretion by fibroblasts, and eliminating biofilm or bacterial colonization [171].

However, poor cellular infiltration and ingrowth due to small average pore radiuses [172], potential toxicity of residual solvents or cross-linking agents [173], and inefficient production [174, 175], are challenges involved with electrospinning in cutaneous wound-healing applications. Pore size is proportional to fiber diameter. Decreasing the electrospun fiber diameter increases fiber-to-fiber contacts resulting in decreased average pore radius [176]. Small pore sizes combined with an inherently high degree of packing density

associated with the electrospinning process (due to overlying layers compressing fibers beneath) constrains the ability of cellular migration, limiting vascularization and tissue ingrowth *in vivo* [177]. Potential solutions to this problem include: increasing flow rate or increasing concentration of the polymer solution to produce thicker fibers, or selective and controlled heating of the electrospinning environment to facilitate solvent evaporation [161, 178, 179]. Larger fibers can counteract the limitation of pore size due to packing density however, increasing fiber diameter also inhibits cellular adhesion and migration [180]. The estimated ideal porosity of an electrospun scaffold to allow cellular infiltration is 100-500 μm [181]. Cytotoxicity of residual organic solvents or chemical cross-linking agents is a common concern associated with blend electrospinning due to the limited availability of biocompatible solvents and water-soluble polymers [173]. Alternative cross-linking methods to increase stability while maintaining safety include enzymatic crosslinking, electrostatic crosslinking, or hydrogen bonding with sugars or polyphenols [165]. However, increased procedural difficulty and degradation of bioactive factors loaded into the scaffolds are concerns associated with these alternative cross-linking methods [165]. Inefficient production, due to insufficient insulation of the electrospinning chamber, impurities in the polymer solution, or the difficulty of achieving a stable Taylor cone, reduces encapsulation efficiency and future release of incorporated bioactive factors [182].

Adjunct therapies have successfully enhanced the positive effects of electrospun scaffolds on wound healing. Electrospun poly-L-lactic acid nanofibrous scaffolds coated with aloe vera gel accelerated wound closure and improved inflammatory outcomes, reducing polynuclear immune cell infiltration, increasing fibroblast maturation, re-epithelialization, and collagen deposition, compared to Vaseline-coated gauze [183]. Recent advances have enhanced the complexity and capability of EHDA. Coaxial needles fabricate core-shell structures to encapsulate bioactive factors instead of simple incorporation into fibrous or spherical structures, and the tunability of the electrospinning parameters allows for morphological variation to control release kinetics [184, 185]. For example, Shoba et al. designed a combinatorial multiphasic core-shell nanofiber delivery system with tailored release of bromelain (a debridement enzyme) and salvianolic acid B which consequently enhanced keratinocyte proliferation, endothelial cell migration, neovascularization, vessel density, and *in vitro* inhibition of bacterial colonization [186].

Electrospun nanofibers promote wound healing and skin regeneration [187]. Electrospun scaffolds share morphological similarities with the native ECM and offer the ability to incorporate bioactive molecules into nanofibers for targeted release within the wound microenvironment. However, the soluble nature of most biomolecules can cause a rapid initial burst release from the nanofibrous scaffolds, followed by degradation or aggregation due to the instability of these proteins against proteolysis, acidity, and heat in the wound microenvironment *in vivo* [188, 189]. The initial burst release of bioactive agents from electrospun protein fibers can be as rapid as 70% within 30 minutes of exposure to the biological environment [190]. Therefore, the success of an electrohydrodynamic tissue-engineered treatment for chronic wounds may depend on an approach that combines the structural integrity of an electrospun scaffold with the ability to sustain prolonged and targeted release of functional bioactive factors throughout the wound-healing process [191, 192].

1.3.4 – Coaxial Electrospaying

Polymeric core-shell microspheres are efficient vehicles for the delivery of therapeutic agents. The polymer shell protects the internalized (i.e. core) therapeutic agents, which gradually diffuse through the porous shell structure, thus sustaining release. Emulsion electrospaying is a cost-efficient, versatile technique capable of producing monodisperse core-shell microparticles [193].

Emulsion coaxial electrospaying is one technique capable of fabricating uniformly sized microspheres with an outer polymer shell and inner colloid core [194]. Coaxially electrospun microparticles and nanofibers have been shown to convey stability and sustained release of growth factors that may otherwise undergo rapid degradation *in vivo* [135]. Liao and Leong observed 10-14 day sustained release of VEGF-A and VEGF-C from core-shell polyurethane nanofibers [195]. An additional study showed maintenance of growth factor bioactivity after release from coaxial fibers or microparticles, when compared to fresh growth factor activity [196, 197].

The basic concept of uniaxial electrospinning is preserved during coaxial electrospaying however, by varying parameters such as concentration of the polymer solutions, flow rate, and applied voltage, the charged stream can be divided into droplets [198, 199].

Furthermore, the coaxial nozzle consists of two concentric but separate nozzles which are controlled by two individual syringe pumps. An electric field is introduced between the coaxial nozzle and a grounded collecting surface [200-203] and repulsive electric forces elongate the core and shell liquid menisci until a jet of multilayered liquid droplets is sprayed towards the grounded collecting surface, given the correct electrohydrodynamic forces are applied (Figure 1.2A) [204].

Accurate control of the core-shell architecture, a high encapsulation rate (up to 100%), and protection of the contained therapeutic agents are the main advantages of coaxial electrospinning [200, 202]. Additionally, the utilization of separate solutions reduces the interaction of aqueous-based biological molecules with the organic solvents required to dissolve the shell-forming polymers, which can improve the functionality of the bioactive agent(s) [196].

On the other hand, the thickness of the outer shell and size of the core solution must be tightly controlled since release of the therapeutic agent is highly dependent on diffusion through the polymeric shell [205]. The production of a functional microparticle with sufficient structural integrity, as well as the physical and chemical properties to allow sustained release via diffusion of the inner core material through to the biological environment, can be difficult to accomplish due to the multiple variables at play (e.g., flow rate, solution viscosity, applied voltage) and the different properties of core- and shell-solutions. Imperfections in the shell structure due to mixing of core-shell solvents during electrospinning or defects in the core-shell structure can compromise sustained release and result in burst release of the bioactive agent from within the core [206]. Additionally, the thickness and composition of the shell layer is a major contributing factor to sustained release. Using hydrophobic poly(lactic acid) core and poly(3-hydroxy butyrate) shell, Wang et al. showed that hydrophobicity, as well as shell thickness, significantly effect the release profile of contained factors. Thin shells (~120 nm) exhibited 70% drug release within 11 days, while the same cumulative percent release required more than 30 days when the shell was ~230 nm thick [207].

Hierarchically structured nanofiber and microsphere composite membranes have been fabricated with simultaneous electrospinning and electrospinning. Electrospun nanofibers

provide biomimetic mechanical properties of natural ECM, and electrospun core-shell microspheres re-establish signalling gradients that have been disrupted in the chronic wound microenvironment with protected and sustained release of bioactive factors. EHDA of nanofibers and microspheres from different source solutions onto a common collecting surface has been shown to produce uniform distribution of microspheres while maintaining porosity of the nanofibrous scaffold. Microsphere aggregation produces nonuniform distribution of the electrostatic field near the collecting surface resulting in uniform self-organization of microsphere deposition [208]. Guo et al. electrospayed bFGF encapsulating microspheres within electrospun poly-caprolactone (PCL) nanofibers to establish a chemotactic gradient to successfully enhance murine dermal fibroblast infiltration, and suggested accelerated angiogenic growth into the scaffolds [209].

1.3.5 – Scaffold Materials

Choice of polymer composition is an important consideration in the design of electrospun nanofibrous scaffolds and electrospayed core-shell microspheres. Both natural and synthetic polymers have been utilized [210]. Natural polymers (such as collagen, gelatin, silk, fibrinogen and chitin) are biocompatible, biodegradable and abundant in the natural environment. However, weak mechanical properties, processing difficulties, enzymatic degradation and potential immunogenicity limit their use. Due to the weak mechanical properties and rapid degradation of natural polymers *in vivo*, cross-linking is required to stabilize scaffold integrity. Chemical crosslinkers (e.g., glutaraldehyde, formaldehyde, polyether oxide, hexamethylene diisocyanate and polyurethane, acyl azide and carbodiimides, and glycerol) and physical crosslinkers (e.g., drying, heating, UV/gamma radiation) covalently bond amino acids on adjacent scaffold structures.

Glutaraldehyde is a widely accepted chemical crosslinking agent of natural polymers; it is a five-carbon aliphatic molecule with a single aldehyde group at each terminus, it is easily accessible, inexpensive, and the vapour of a dilute solution effectively crosslinks collagen fibers within 24 hours [211]. Several functional groups (amine, thiol, phenol, and imidazole) and amino acids (lysine, tyrosine, tryptophan, phenylalanine, histidine, cysteine, proline, serine, glycine, glycyglycine, arginine) are reactive with glutaraldehyde [212, 213]. However, crosslinking generally occurs between lysine ϵ -amino groups on adjacent

polypeptides [214]. Residual glutaraldehyde must be removed post-crosslinking due to the cytotoxicity of this chemical. Furthermore, depolymerization of glutaraldehyde crosslinks can release glutaraldehyde *in vivo* which may impair cellular function [211, 215, 216].

Synthetic polymers poly(lactic acid), poly(glycolic acid), poly(lactide-co-glycolide), and PCL provide efficient processing, flexible and tunable physical properties, resistance to enzymatic degradation, and stable mechanical properties. However, questionable biocompatibility and biodegradability, and high production costs are limiting factors [217]. Hydrophobicity of synthetic surfaces and a lack of cellular recognition sites (e.g., RGD sequences) limits cellular interaction with synthetic biomaterials [218].

Alternatively, biomaterial composites aim to reduce the limitations associated with natural and synthetic polymers. Copolymers containing natural and synthetic components combine the physical, mechanical, and chemical properties of synthetic polymers with the biocompatibility, hydrophilicity, biodegradability, and important cellular recognition sequences contained in the polypeptide chains of natural polymers [218]. Incorporation of a synthetic polymer also eliminates the need for cytotoxic crosslinking [219]. The beneficial effects of copolymer materials were demonstrated in two studies investigating PCL/collagen and poly(L-lactic acid)-co-poly(ϵ -caprolactone)/gelatin scaffolds. The copolymer scaffolds significantly increased mechanical stability and cellular proliferation compared to scaffolds fabricated with the synthetic material alone [220, 221].

1.3.5.1 – Gelatin

Collagen I composes approximately 90% of the total collagen content in the skin [222]. Biomaterial scaffolds fabricated with collagen have been used extensively as a major component in dermal skin substitutes due to collagen's high biocompatibility, biodegradability, and similar molecular composition to the natural ECM [223]. However, antigenicity of xenogeneic sources and high costs are two substantial limiting factors to the utilization of collagen in biomaterial scaffolds. Gelatin is a natural polymer alternative to collagen for use in biomaterial scaffolds [224]. Collagen denaturation via alkaline or acid processing produces gelatin with relatively low antigenicity and increased exposure of previously internalized cellular recognition sequences [225]. Type A gelatin is produced by acid pre-treatment of dermal porcine collagen, while type B gelatin is produced by

alkaline pre-treatment of dermal bovine hide [226]. Gelatin maintains the favourable biocompatibility and biodegradability of collagen, at a fraction of the cost [226]. Gelatin scaffolds have been shown to stimulate cellular adhesion, migration and proliferation, and accelerate wound healing [144, 227, 228].

1.3.5.2 – Poly(lactic-co-glycolic acid)

Poly(lactic-co-glycolic acid) (PLGA) is a biocompatible and biodegradable copolymer of lactic and glycolic acid (LA and GA, respectively) capable of encapsulating hydrophilic and hydrophobic factors, is surface modifiable, and has been approved by both the European Medicines Agency and FDA for parenteral application [158]. LA to GA ratio, molecular weight, and acid or ester terminal end groups convey tunability of the physicochemical properties of PLGA, including: inherent viscosity, hydrophilicity, and degradability. Ester end groups improve resistance to hydrolytic degradation [229], and methyl groups on LA increase hydrophobicity (relative to GA), affecting solvent affinity, influencing interactions between polymer chains to affect viscosity of the PLGA solution, and reducing hydrolytic degradation of LA [230]. As the proportion of LA increases, PLGA resorption slows significantly from under 2 months at 50:50 LA:GA, to 12-16 months at 85:15 LA:GA [229]. Bulk hydrolytic degradation reduces PLGA to monomeric lactate and glycolate which are metabolized naturally *in vivo* [231]. Initial hydrolytic ester cleavage is autocatalyzed by exposed carboxylic chain ends. Detached oligomers solubilize and are hydrolyzed further into individual LA/GA monomers before degradation by the body's natural metabolic pathways to produce energy, carbon dioxide, and water [232]. However, acidification of the microenvironment can occur due to exposure of entrapped acidic carboxylic groups, perturbing protein structure and destabilizing encapsulated proteins [229]. The acidic destabilization of bioactive factors has been attenuated by incorporation of poorly water-soluble bases [233]. PLGA has been used extensively in targeted and controlled delivery of functional bioactive agents via electrosprayed core-shell microspheres with over 90% encapsulation efficiency and uniform sphere diameter ranging from 165 nm to 10 μm [202, 234].

1.4 – Periostin, Connective Tissue Growth Factor 2 & Fibroblast Growth Factor 9 as Therapeutics for Chronic Wounds

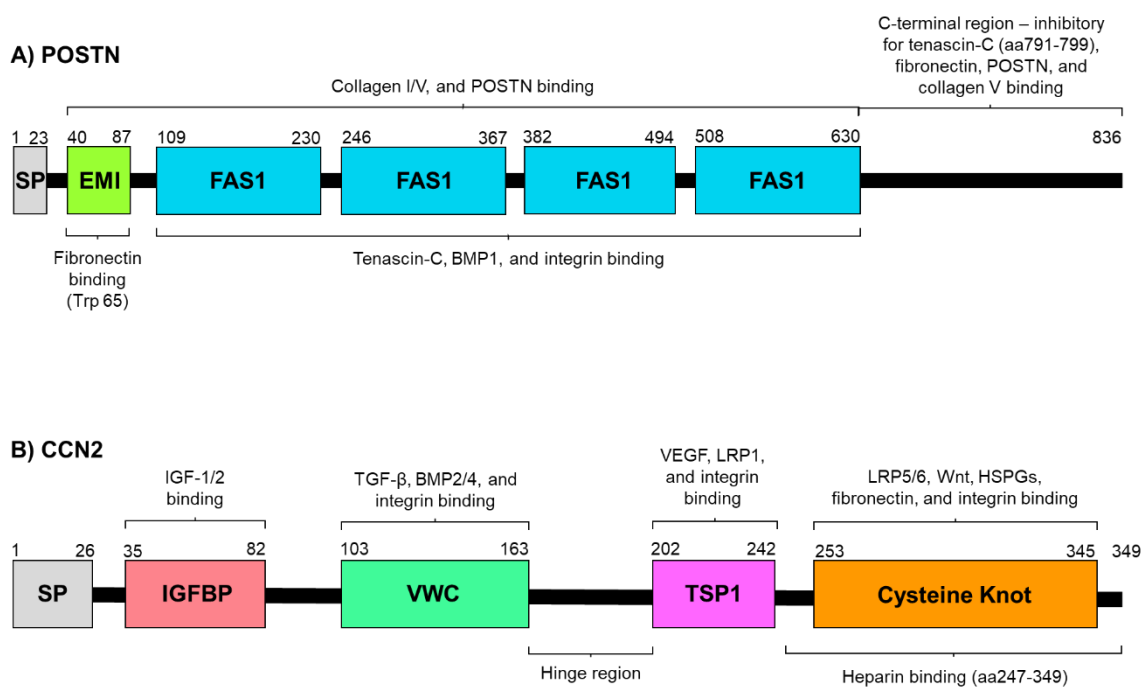
1.4.1 – Periostin & Connective Tissue Growth Factor 2

The extracellular matrix (ECM) is a dynamic structure that displays multifunctional control over cellular behaviour. While its importance for structural integrity has been established [235], its functional role has also been recognized within the last two decades. Components of the ECM are targets for cell surface receptors controlling cell shape, survival, movement, and gene expression [236]. Further influence over cell behaviour is controlled through mechanotransduction, whereby the fluidity of the membrane conveys information to adhered cells [237]. Additionally, the ability of matrix proteins to serve as binding sites for diffusible growth factors and other proteins provides the ECM with control over the location and concentration of these factors to establish gradients and reservoirs for tissue morphogenesis and regeneration.

Matricellular proteins are a class of non-structural proteins found within the ECM that modulate cell-matrix interactions to influence cell function [238]. These nonhomologous proteins are primarily expressed during development however, upregulation has also been described in response to tissue repair, remodelling, and disease [239]. Periostin (POSTN) is a 93.3 kDa N terminus-glycosylated matricellular protein containing four tandem fasciadin cell adhesion domains (Figure 1.3A) [240]. It was first observed as osteoblast specific factor 2, after Takeshita et al. discovered its secretion by murine osteoblasts in 1993 [241]. Since then, POSTN has been witnessed in tissues, including skin [242] and bone [243], as well as pathological conditions, such as vascular injury [244], muscle injury [245], and myocardial infarction [246]. POSTN enhances keratinocyte proliferation and re-epithelialization [247], interacts with α v-integrins to accelerate cutaneous wound repair via the phosphatidylinositol 3-kinase/Akt and MAP kinase pathways [247, 248], and modulates vascular SMC migration via focal adhesion kinase signalling [249]. In normal skin, POSTN is localized to the cells in the basal lamina [250]. However, during the remodelling phase of wound healing, it migrates to the extracellular compartment where it facilitates dermal fibroblast activation, differentiation, and contraction, contributing to dermal regeneration and wound closure [247, 248, 251].

Connective tissue growth factor 2 (CCN2) is one of six members of the CCN family of matricellular proteins involved in the regulation of cell adhesion, migration, proliferation, differentiation, apoptosis, survival, senescence, and gene expression [252]. The acronym (CCN) comes from the first three members of the family to be described: CYR61 (cysteine-rich 61/CCN1), CTGF (connective tissue growth factors/CCN2) and NOV (nephroblastoma overexpressed/CCN3) [253]. The structure of these proteins includes an N-terminal secretory peptide, four conserved modular domains (sequence homologies to insulin-like growth factor binding proteins, von Willebrand factor type C repeat and thrombospondin type I repeat, respectively), and a cysteine-knot motif containing carboxyl-terminal domain (Figure 1.3B). Binding specificity to ECM and cell surface receptors is conferred by a protease-sensitive central hinge that bisects the proteins [252]. Throughout embryonic development, CCNs are widely expressed however, in the adult, these proteins are downregulated except during inflammation and repair [254, 255]. During wound healing, CCN2 is released by platelet α -granules and acts synergistically with TGF- β to promote ECM deposition and fibrogenesis by proliferating myofibroblasts [256]. Furthermore, CCN1-3 bind integrin $\alpha_v\beta_3$ and promote neovascular tubule formation through stimulation of endothelial cell proliferation and chemotaxis [257, 258]. CCN1-3 proteins have also exhibited control of the expression and activities of other angiogenic factors (e.g., VEGF-A and VEGF-C) [259, 260]. Recent evidence suggests a role of these matricellular proteins in inflammation. CCN1 and CCN2, upregulated by extracellular signals released during inflammation (TNF- α , IL-1 β , TGF- β , prostaglandins, nitric oxide, histamine, serotonin, ECM enzymes), serve to regulate the immune response by modulating the activity and expression of inflammatory markers [255]. The functions of POSTN and CCN2 during wound healing have been described previously in greater depth [261, 262].

Figure 1. 3 – Structural domains of human POSTN and CCN2. **A)** The first isoform of human POSTN contains a signal peptide region (SP), an EMI domain and four tandem fasciclin-like domains (FAS1). A Tryptophan (Trp-65) residue located within the EMI domain is responsible for fibronectin binding. The four FAS1 domains bind Tenascin-C, bone morphogenetic protein-1 (BMP1) and integrins. Together, the EMI and FAS1 domains bind collagen I and collagen V, and mediate POSTN ligand binding interactions. Residues within the C-terminal region inhibit tenascin-C, fibronectin, collagen V, and POSTN ligand binding. **B)** Human CCN2 contains a signal peptide region and four domain structures with sequence homology to insulin-like growth factor binding proteins (IGFBP), von Willebrand factor-C (VWC), thrombospondin type 1 repeat (TSP1), and a C-terminal cysteine knot region. The IGFBP homologue is responsible for IGF-1/2 binding, the VWR domain is responsible for TGF- β , and BMP-2/4 binding, the TSP1 domain is responsible for VEGF, and low-density lipoprotein receptor-related protein-1 (LRP1), and the Cysteine Knot region is responsible for LRP-5/6, Wnt, heparin sulfate proteoglycan (HSPG), and fibronectin binding. Integrin binding is mediated by the VWC, TSP1, and Cysteine Knot domains. Amino acids 247-349 bind heparin. Proteolytic cleavage of the hinge region between residues 163 and 202 produces various splice variants. Numbers represent the ascending sequence of amino acid residues from N- to C-terminal regions.



1.4.2 – Fibroblast Growth Factor 9

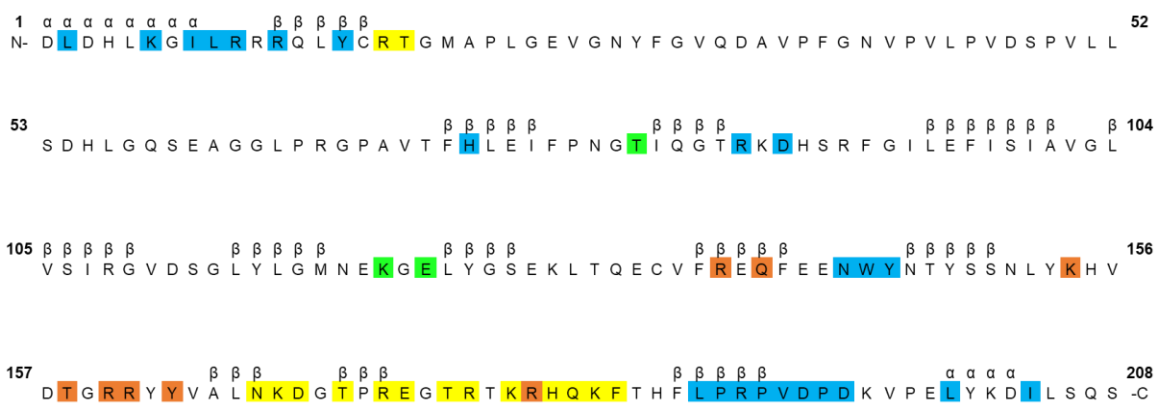
Previously labelled glia-activating factor, FGF9 was identified in 1993 as a 208 amino acid polypeptide after purification from the culture supernatant of a human glioma cell line [263]. FGF9 secretion occurs without a N-terminal signal peptide, indicating a different physiological role than other members of the FGF family [264]. It has been suggested that a co-translational pathway targets nascent FGF9 to the endoplasmic reticulum via N-terminal and core-structure hydrophobic regions, without peptide cleavage, before FGF9 is glycosylated and subsequently secreted [265]. FGF9 maintains 30% sequence homology to prototypic FGF1/2. A β -trefoil fold (three copies of a four-stranded β -sheet) with peripheral N- and C- terminal segments composes FGF9 and drives protein dimerization (Figure 1.4). Unique β 1-2 and β 9-10 loop conformations within the β -trefoil core and ordered α -helical regions in the N- and C- terminal regions separate FGF9 structurally and functionally from other members of the FGF family. External interaction of α N/C-helices and internal interaction between β -trefoil β -1 and -12 strands, and the β 8-9 loop are responsible for FGF9 dimerization and occlusion of important receptor binding sites, suggesting a biologically relevant autoinhibitory mechanism behind FGF9 dimerization [266].

Fibroblast growth factor receptors (FGFRs) are single-pass transmembrane receptor tyrosine kinases with a single extracellular domain composed of three Ig-like domains and an intracellular split tyrosine kinase domain. Alternative splicing of the third Ig loop regulates FGFR ligand binding specificity [267]. FGF, HSPG, and FGFR complex formation results in receptor dimerization and transphosphorylation of intracellular tyrosine residues, activating downstream signal cascades. FGFRs initiate two main intracellular signalling pathways: FRS2 and PLC γ receptor substrate dependent upregulation of Ras-dependent MAPK and PI3K-Akt pathways [268]. High affinity FGF-FGFR binding requires heparin sulfate proteoglycans (HSPGs); cell-surface or ECM glycoproteins known to bind many growth factors and regulate signal transduction pathways including: TGF- β , sonic hedgehog (SHH), Wnt, and FGFs [269]. HSPGs promote 2:2 FGF-FGFR complex formation and tissue-specific FGFR activation *in vivo* [270]. Furthermore, HSPGs stabilize FGFs to inhibit proteolytic degradation and reduce thermal denaturation, and restrict FGF diffusion to enhance local FGF action [270].

FGF9 is involved in the mesenchymal development of the cerebellum, lung, heart and intestine [271-274]. While FGF9 is involved in the formation of neovasculature, it plays a limited role in tube formation [275]. Instead, the evidence suggests that this growth factor acts through upregulation of platelet-derived growth factor receptor- β via SHH signalling to promote mural cell (progenitors of SMCs and pericytes) layering around newly forming vasculature to improve the stability (enhancing flow) and vasoreactivity of the vessels [275]. FGF9 positively regulated murine mesenchymal SHH signalling [276] to promote VEGF-A mediated capillary plexus formation in early murine lung development [277]. Furthermore, FGF9 successfully reconfigured the microvasculature of murine renal tumors, reducing hypoxia and improving vasoreactivity of the tumors [278]. FGF9 has also been indicated as a mitogenic factor, stimulating neointimal SMC proliferation via activation of the extracellular signal-regulated kinase (ERK) 1/2 pathway *in vitro* [275, 279].

The role of FGF9 in cutaneous wound healing has yet to be fully elucidated. FGF9 was found to be upregulated 2- to 33-fold post-wounding, relative to low or moderate expression in healthy dorsal skin of young and aged mice, during full-thickness excisional wound healing [280]. The same study found that, among the four FGFRs, only expression of FGFR1 was upregulated during healing [280]. Alternatively, a recent study showed that $\gamma\delta$ T lymphocytes accumulating in the wound bed before reepithelization release FGF9 which stimulates Wnt2 expression in dermal fibroblasts. Wnt2 expression causes activation of autocrine fibroblast Wnt signalling which induces FGF9 expression in Wnt-activated dermal fibroblasts. The authors found that wound closure occurs normally in mice lacking $\gamma\delta$ T lymphocytes or T cells lacking FGF9 expression however, hair neogenesis was impaired in these animals. This work suggests FGF9 may have a regenerative role through the restoration of adnexal structures (due to activated Wnt2 signalling) which are usually lost in deep cutaneous wound healing [281]. Furthermore, Zheng et al. found FGF9 to be upregulated from days 3 to 21, peaking on day 7 through 10, and FGF9 mediated activation of FGF-Wnt/ β -catenin signalling in mouse and human skin after laser ablation, and when rhFGF9 was cultured with normal human epidermal keratinocytes. These findings suggest an important role of FGF9 in the wound healing process through interaction with the FGF-Wnt/ β -catenin signalling pathway [282].

Figure 1. 4 – Amino Acid Sequence Alignment of FGF9. FGF9 sequence alignment is based on crystal structure analysis performed using CLUSTALW [266]. Residues comprising terminal α -helices and the twelve β -strands are indicated above the sequence alignment. Residues associated with dimerization are colour coded *blue*, low and high affinity heparin binding sites are *yellow*, and peripheral and central heparin binding sites are *green* and *brown*, respectively. Low and high affinity heparin binding sites are well established in the literature [283], while the peripheral and central heparin binding sites presented here, were first reported by Plotnikov et al. [266].



1.5 – Rationale, Hypothesis & Objectives

1.5.1 – Rationale

Chronic wounds present a significant burden on the healthcare system and on patients suffering from these afflictions. The passivity of dressings involved in standard care does little to correct the pathological microenvironment of chronic wounds. Tissue engineered approaches include electrohydrodynamic scaffolds and core-shell microspheres, which act as biomimetic granulation tissue to physically support vascular development, fibroplasia, re-epithelialization, and contraction, and serve as delivery vehicles of bioactive factors to re-establish the disturbed biochemical gradients within chronic wounds.

Elliot et al. showed POSTN/CCN2 scaffolds significantly improve angiogenic growth in full-thickness cutaneous wounds on the dorsal surface of db/db mice when compared to control conditions (Hamilton lab, In Review, J Tissue Eng). However, vascular growth in response to POSTN and CCN2 was insufficient to recover wild-type wound closure (Hamilton lab, In Review, J Tissue Eng). Furthermore, microcomputed tomography (micro-CT) images indicated incomplete tubule formation and an immature vascular bed (Hamilton lab, In Review, J Tissue Eng). Therefore, POSTN/CCN2 scaffolds require a factor capable of supporting the pro-angiogenic effects of POSTN/CCN2 to improve wound-healing outcomes associated with this scaffold.

FGF9 recruits mural cell populations and promotes endothelial tube wrapping to produce durable and vasoresponsive microvessels [275, 278, 284, 285]. The role of FGF9 in mesenchymal development (cerebellum, lung, heart, and intestine) and tissue repair outside of the skin has been well documented [271-274, 286, 287] but there is a lack of basic knowledge on the role of FGF9 within the cutaneous wound-healing environment. Therefore, FGF9 may serve adjunctively with POSTN/CCN2 scaffolds to stabilize angiogenesis and improve wound repair, however there is a need to further investigate the role of FGF9 in cutaneous wound healing.

1.5.2 – Hypothesis

It is hypothesized that the POSTN/CCN2 scaffold will serve as a granulation tissue mimetic to physically and functionally support re-epithelialization, fibroplasia, and angiogenesis.

POSTN/CCN2 released from gelatin electrospun scaffolds will facilitate angiogenesis, matrix deposition, and regulate myofibroblast phenotype during the inflammatory and proliferative stages of wound healing. Sustained FGF9 released from PLGA microspheres will support POSTN/CCN2 induced neoangiogenesis by promoting mural cell recruitment and wrapping around endothelial tubes to stabilize the neovasculature. The production of robust, functional vessels will increase nutrient and oxygen delivery to improve reparative processes and facilitate regeneration.

1.5.3 – Objectives

The specific objectives of this project were:

1. To determine the influence of nanofibrous electrospun POSTN/CCN2 scaffolds on angiogenesis and wound repair 28 days post-wounding in a porcine model of cutaneous wound healing.
2. To design and validate an electrospun POSTN/CCN2 scaffold with coaxially electrospayed core-shell microspheres encapsulating FGF9, comprising the following sub-objectives:
 - a. Assess *in vitro* effect of FGF9 on cellular populations involved in wound healing.
 - b. Design and validate a novel POSTN/CCN2 scaffold with FGF9/PLGA microspheres using a new electrohydrodynamic system.
 - c. Determine release kinetics and biological activity of FGF9 released from core-shell PLGA microspheres.
3. To determine the influence of nanofibrous electrospun POSTN/CCN2 scaffolds with FGF9/PLGA microspheres (POSTN/CCN2/FGF9 scaffold) on angiogenesis and wound repair 7 days post-wounding in a porcine model of cutaneous wound healing.

1.6 – References

1. Kanitakis, J., *Anatomy, histology and immunohistochemistry of normal human skin*. European journal of dermatology : EJD, 2002. **12**(4): p. 390-9; quiz 400-1.
2. Zaidi, Z. and S.W. Lanigan, *Skin: Structure and Function*. 2010: p. 1-15.
3. Wickett, R.R. and M.O. Visscher, *Structure and function of the epidermal barrier*. American Journal of Infection Control, 2006. **34**(10): p. S98-S110.
4. Kolarsick, P.A.J., M.A. Kolarsick, and C. Goodwin, *Anatomy and Physiology of the Skin*. Journal of the Dermatology Nurses' Association, 2011. **3**(4): p. 203-213.
5. Parish, L., *Andrews' diseases of the skin: Clinical dermatology*. JAMA, 2011. **306**(2): p. 213-213.
6. Eming, S.A., P. Martin, and M. Tomic-Canic, *Wound repair and regeneration: mechanisms, signaling, and translation*. Sci Transl Med, 2014. **6**(265): p. 265sr6.
7. Zhao, R., et al., *Inflammation in Chronic Wounds*. Int J Mol Sci, 2016. **17**(12).
8. Greaves, N.S., et al., *Current understanding of molecular and cellular mechanisms in fibroplasia and angiogenesis during acute wound healing*. Journal of Dermatological Science, 2013. **72**(3): p. 206-217.
9. Xu, J. and R.A. Clark, *Extracellular matrix alters PDGF regulation of fibroblast integrins*. J Cell Biol, 1996. **132**(1-2): p. 239-49.
10. Clark, R.A., *Fibrin and wound healing*. Ann N Y Acad Sci, 2001. **936**: p. 355-67.
11. Koskela, A., et al., *Regulation of fibroblast gene expression by keratinocytes in organotypic skin culture provides possible mechanisms for the antifibrotic effect of reepithelialization*. Wound Repair Regen, 2010. **18**(5): p. 452-9.
12. Eming, S.A., et al., *Interrelation of immunity and tissue repair or regeneration*. Semin Cell Dev Biol, 2009. **20**(5): p. 517-27.
13. Patan, S., *Vasculogenesis and angiogenesis*. Cancer Treat Res, 2004. **117**: p. 3-32.
14. Kimura, H. and H. Esumi, *Reciprocal regulation between nitric oxide and vascular endothelial growth factor in angiogenesis*. Acta Biochim Pol, 2003. **50**(1): p. 49-59.
15. Suri, C., et al., *Increased vascularization in mice overexpressing angiopoietin-1*. Science, 1998. **282**(5388): p. 468-71.
16. Kalebic, T., et al., *Basement membrane collagen: degradation by migrating endothelial cells*. Science, 1983. **221**(4607): p. 281-3.
17. Sahni, A., L.A. Sporn, and C.W. Francis, *Potentiation of endothelial cell proliferation by fibrin(ogen)-bound fibroblast growth factor-2*. J Biol Chem, 1999. **274**(21): p. 14936-41.
18. Brooks, P.C., R.A. Clark, and D.A. Cheresh, *Requirement of vascular integrin alpha v beta 3 for angiogenesis*. Science, 1994. **264**(5158): p. 569-71.
19. Koolwijk, P., et al., *Cooperative effect of TNFalpha, bFGF, and VEGF on the formation of tubular structures of human microvascular endothelial cells in a fibrin matrix. Role of urokinase activity*. J Cell Biol, 1996. **132**(6): p. 1177-88.
20. Kroon, M.E., et al., *Urokinase receptor expression on human microvascular endothelial cells is increased by hypoxia: implications for capillary-like tube formation in a fibrin matrix*. Blood, 2000. **96**(8): p. 2775-83.
21. Powell, D.W., et al., *Myofibroblasts. I. Paracrine cells important in health and disease*. Am J Physiol, 1999. **277**(1 Pt 1): p. C1-9.

22. Reed, M.J. and J.M. Edelberg, *Impaired angiogenesis in the aged*. Sci Aging Knowledge Environ, 2004. **2004**(7): p. pe7.
23. Sadoun, E. and M.J. Reed, *Impaired angiogenesis in aging is associated with alterations in vessel density, matrix composition, inflammatory response, and growth factor expression*. J Histochem Cytochem, 2003. **51**(9): p. 1119-30.
24. Hangai, M., et al., *Matrix metalloproteinase-9-dependent exposure of a cryptic migratory control site in collagen is required before retinal angiogenesis*. Am J Pathol, 2002. **161**(4): p. 1429-37.
25. Pepper, M.S., *Extracellular proteolysis and angiogenesis*. Thromb Haemost, 2001. **86**(1): p. 346-55.
26. Xu, J., et al., *Proteolytic exposure of a cryptic site within collagen type IV is required for angiogenesis and tumor growth in vivo*. J Cell Biol, 2001. **154**(5): p. 1069-79.
27. Jonca, F., et al., *Cell release of bioactive fibroblast growth factor 2 by exon 6-encoded sequence of vascular endothelial growth factor*. J Biol Chem, 1997. **272**(39): p. 24203-9.
28. Saksela, O. and D.B. Rifkin, *Release of basic fibroblast growth factor-heparan sulfate complexes from endothelial cells by plasminogen activator-mediated proteolytic activity*. J Cell Biol, 1990. **110**(3): p. 767-75.
29. Ribatti, D., et al., *In vivo angiogenic activity of urokinase: role of endogenous fibroblast growth factor-2*. J Cell Sci, 1999. **112** (Pt 23): p. 4213-21.
30. Wijelath, E.S., et al., *Novel vascular endothelial growth factor binding domains of fibronectin enhance vascular endothelial growth factor biological activity*. Circ Res, 2002. **91**(1): p. 25-31.
31. Sottile, J., *Regulation of angiogenesis by extracellular matrix*. Biochimica et Biophysica Acta (BBA) - Reviews on Cancer, 2004. **1654**(1): p. 13-22.
32. Wilgus, T.A., et al., *Regulation of scar formation by vascular endothelial growth factor*. Lab Invest, 2008. **88**(6): p. 579-90.
33. Wu, W.S., et al., *Dexamethasone induction of keloid regression through effective suppression of VEGF expression and keloid fibroblast proliferation*. J Invest Dermatol, 2006. **126**(6): p. 1264-71.
34. Zhang, N., et al., *Tracking angiogenesis induced by skin wounding and contact hypersensitivity using a Vegfr2-luciferase transgenic mouse*. Blood, 2004. **103**(2): p. 617-26.
35. Haynes, J.H., et al., *Platelet-derived growth factor induces fetal wound fibrosis*. J Pediatr Surg, 1994. **29**(11): p. 1405-8.
36. Barrientos, S., et al., *Growth factors and cytokines in wound healing*. Wound Repair Regen, 2008. **16**(5): p. 585-601.
37. Gurtner, G.C., et al., *Wound repair and regeneration*. Nature, 2008. **453**(7193): p. 314-21.
38. Tomasek, J.J., et al., *Myofibroblasts and mechano-regulation of connective tissue remodelling*. Nat Rev Mol Cell Biol, 2002. **3**(5): p. 349-63.
39. Clark, R.A., et al., *Collagen matrices attenuate the collagen-synthetic response of cultured fibroblasts to TGF-beta*. J Cell Sci, 1995. **108** (Pt 3): p. 1251-61.
40. Varedi, M., et al., *Stress-relaxation and contraction of a collagen matrix induces expression of TGF-beta and triggers apoptosis in dermal fibroblasts*. Biochem Cell Biol, 2000. **78**(4): p. 427-36.

41. Baltzis, D., I. Eleftheriadou, and A. Veves, *Pathogenesis and treatment of impaired wound healing in diabetes mellitus: new insights*. *Adv Ther*, 2014. **31**(8): p. 817-36.
42. Morton, L.M. and T.J. Phillips, *Wound healing and treating wounds: Differential diagnosis and evaluation of chronic wounds*. *J Am Acad Dermatol*, 2016. **74**(4): p. 589-605; quiz 605-6.
43. Panasci, K., *Chapter 12 - Burns and Wounds*, in *Acute Care Handbook for Physical Therapists (Fourth Edition)*, J.C. Paz and M.P. West, Editors. 2014, W.B. Saunders: St. Louis. p. 283-311.
44. Barrick, B., E.J. Campbell, and C.A. Owen, *Leukocyte proteinases in wound healing: roles in physiologic and pathologic processes*. *Wound Repair Regen*, 1999. **7**(6): p. 410-22.
45. Eming, S.A., T. Krieg, and J.M. Davidson, *Inflammation in wound repair: molecular and cellular mechanisms*. *J Invest Dermatol*, 2007. **127**(3): p. 514-25.
46. Wenk, J., et al., *Selective pick-up of increased iron by deferoxamine-coupled cellulose abrogates the iron-driven induction of matrix-degrading metalloproteinase 1 and lipid peroxidation in human dermal fibroblasts in vitro: a new dressing concept*. *J Invest Dermatol*, 2001. **116**(6): p. 833-9.
47. Eming, S.A., et al., *Differential proteomic analysis distinguishes tissue repair biomarker signatures in wound exudates obtained from normal healing and chronic wounds*. *J Proteome Res*, 2010. **9**(9): p. 4758-66.
48. Buchstein, N., et al., *Alternative proteolytic processing of hepatocyte growth factor during wound repair*. *Am J Pathol*, 2009. **174**(6): p. 2116-28.
49. Lauer, G., et al., *Expression and proteolysis of vascular endothelial growth factor is increased in chronic wounds*. *J Invest Dermatol*, 2000. **115**(1): p. 12-8.
50. Wlaschek, M., et al., *Protease inhibitors protect growth factor activity in chronic wounds*. *Br J Dermatol*, 1997. **137**(4): p. 646.
51. Yager, D.R., et al., *Wound fluids from human pressure ulcers contain elevated matrix metalloproteinase levels and activity compared to surgical wound fluids*. *J Invest Dermatol*, 1996. **107**(5): p. 743-8.
52. Forbes, S.J. and N. Rosenthal, *Preparing the ground for tissue regeneration: from mechanism to therapy*. *Nat Med*, 2014. **20**(8): p. 857-69.
53. Sindrilaru, A., et al., *An unrestrained proinflammatory M1 macrophage population induced by iron impairs wound healing in humans and mice*. *J Clin Invest*, 2011. **121**(3): p. 985-97.
54. Loots, M.A., et al., *Differences in cellular infiltrate and extracellular matrix of chronic diabetic and venous ulcers versus acute wounds*. *J Invest Dermatol*, 1998. **111**(5): p. 850-7.
55. Tarnuzzer, R.W. and G.S. Schultz, *Biochemical analysis of acute and chronic wound environments*. *Wound Repair Regen*, 1996. **4**(3): p. 321-5.
56. Beidler, S.K., et al., *Inflammatory cytokine levels in chronic venous insufficiency ulcer tissue before and after compression therapy*. *J Vasc Surg*, 2009. **49**(4): p. 1013-20.
57. Mustoe, T.A., K. O'Shaughnessy, and O. Kloeters, *Chronic wound pathogenesis and current treatment strategies: a unifying hypothesis*. *Plast Reconstr Surg*, 2006. **117**(7 Suppl): p. 35s-41s.

58. Han, G. and R. Ceilley, *Chronic Wound Healing: A Review of Current Management and Treatments*. Adv Ther, 2017.
59. Frank, D.N., et al., *Microbial diversity in chronic open wounds*. Wound Repair Regen, 2009. **17**(2): p. 163-72.
60. Pastar, I., et al., *Interactions of methicillin resistant Staphylococcus aureus USA300 and Pseudomonas aeruginosa in polymicrobial wound infection*. PLoS One, 2013. **8**(2): p. e56846.
61. Roche, E.D., et al., *Increasing the presence of biofilm and healing delay in a porcine model of MRSA-infected wounds*. Wound Repair Regen, 2012. **20**(4): p. 537-43.
62. Krisp, C., et al., *Proteome analysis reveals antiangiogenic environments in chronic wounds of diabetes mellitus type 2 patients*. Proteomics, 2013. **13**(17): p. 2670-81.
63. Pastar, I., et al., *Attenuation of the transforming growth factor β -signaling pathway in chronic venous ulcers*. Molecular Medicine, 2010. **16**(3-4): p. 92.
64. Leu, A.J., et al., *Microvascular changes in chronic venous insufficiency--a review*. Cardiovasc Surg, 1995. **3**(3): p. 237-45.
65. Edsberg, L.E., et al., *Analysis of the proteomic profile of chronic pressure ulcers*. Wound Repair Regen, 2012. **20**(3): p. 378-401.
66. Nelson, E.A. and M.D. Bradley, *Dressings and topical agents for arterial leg ulcers*. Cochrane Database Syst Rev, 2007(1): p. Cd001836.
67. Hirsch, A.T., et al., *Peripheral arterial disease detection, awareness, and treatment in primary care*. Jama, 2001. **286**(11): p. 1317-24.
68. Bonham, P.A., *Assessment and management of patients with venous, arterial, and diabetic/neuropathic lower extremity wounds*. AACN Clin Issues, 2003. **14**(4): p. 442-56; quiz 548-50.
69. Alavi, A., et al., *Diabetic foot ulcers: Part I. Pathophysiology and prevention*. J Am Acad Dermatol, 2014. **70**(1): p. 1 e1-18; quiz 19-20.
70. Fonder, M.A., et al., *Treating the chronic wound: A practical approach to the care of nonhealing wounds and wound care dressings*. J Am Acad Dermatol, 2008. **58**(2): p. 185-206.
71. Maklebust, J. and M.A. Magnan, *Risk factors associated with having a pressure ulcer: a secondary data analysis*. Advances in wound care : the journal for prevention and healing, 1994. **7**(6): p. 25, 27-8, 31-4 passim.
72. Jung, K., et al., *Rapid identification of slow healing wounds*. Wound repair and regeneration : official publication of the Wound Healing Society [and] the European Tissue Repair Society, 2016. **24**(1): p. 181-188.
73. Gottrup, F., et al., *A new concept of a multidisciplinary wound healing center and a national expert function of wound healing*. Arch Surg, 2001. **136**(7): p. 765-72.
74. Sen, C.K., et al., *Human skin wounds: a major and snowballing threat to public health and the economy*. Wound Repair Regen, 2009. **17**(6): p. 763-71.
75. Rice, J.B., et al., *Burden of venous leg ulcers in the United States*. J Med Econ, 2014. **17**(5): p. 347-56.
76. Hinchliffe, R.J., et al., *Effectiveness of revascularization of the ulcerated foot in patients with diabetes and peripheral artery disease: a systematic review*. Diabetes Metab Res Rev, 2016. **32** Suppl 1: p. 136-44.
77. (PHAC), P.H.A.o.C., *Diabetes in Canada: Facts and figures from a public health perspective*. . 2011.

78. Armstrong, D.G., J. Wrobel, and J.M. Robbins, *Guest Editorial: are diabetes-related wounds and amputations worse than cancer?* Int Wound J, 2007. **4**(4): p. 286-7.
79. Aulivola, B., et al., *Major lower extremity amputation: outcome of a modern series.* Arch Surg, 2004. **139**(4): p. 395-9; discussion 399.
80. Sargen, M.R., O. Hoffstad, and D.J. Margolis, *Geographic variation in Medicare spending and mortality for diabetic patients with foot ulcers and amputations.* J Diabetes Complications, 2013. **27**(2): p. 128-33.
81. Moulik, P.K., R. Mtonga, and G.V. Gill, *Amputation and mortality in new-onset diabetic foot ulcers stratified by etiology.* Diabetes Care, 2003. **26**(2): p. 491-4.
82. Canadian Association of Wound Care. *Statistics.* 2017 [cited 2017 February 02, 2017]; Available from: <http://cawc.net/index.php/public/facts-stats-and-tools/statistics/>.
83. Hopkins, R.B., et al., *PDB49 - Burden of illness of diabetic foot ulcers in Canada.* Value in Health, 2014. **17**(3): p. A246.
84. Bekara, F., et al., *New techniques for wound management: A systematic review of their role in the management of chronic wounds.* Arch Plast Surg, 2018. **45**(2): p. 102-110.
85. Cavanagh, P.R. and S.A. Bus, *Off-loading the diabetic foot for ulcer prevention and healing.* J Am Podiatr Med Assoc, 2010. **100**(5): p. 360-8.
86. Werdin, F., et al., *Evidence-based management strategies for treatment of chronic wounds.* Eplasty, 2009. **9**: p. e19.
87. Roth-Albin, I., et al., *Outcomes Following Advanced Wound Care for Diabetic Foot Ulcers: A Canadian Study.* Can J Diabetes, 2017. **41**(1): p. 26-32.
88. Mulder, G., et al., *Fibrin cuff lysis in chronic venous ulcers treated with a hydrocolloid dressing.* Int J Dermatol, 1993. **32**(4): p. 304-6.
89. Powers, J.G., et al., *Wound healing and treating wounds: Chronic wound care and management.* J Am Acad Dermatol, 2016. **74**(4): p. 607-25; quiz 625-8.
90. Demidova-Rice, T.N., A. Geevarghese, and I.M. Herman, *Bioactive peptides derived from vascular endothelial cell extracellular matrices promote microvascular morphogenesis and wound healing in vitro.* Wound Repair Regen, 2011. **19**(1): p. 59-70.
91. Prete, P.E., *Growth effects of Phaenicia sericata larval extracts on fibroblasts: mechanism for wound healing by maggot therapy.* Life Sci, 1997. **60**(8): p. 505-10.
92. Davies, C.E., et al., *Maggots as a wound debridement agent for chronic venous leg ulcers under graduated compression bandages: A randomised controlled trial.* Phlebology, 2014. **30**(10): p. 693-699.
93. Gilead, L., K.Y. Mumcuoglu, and A. Ingber, *The use of maggot debridement therapy in the treatment of chronic wounds in hospitalised and ambulatory patients.* J Wound Care, 2012. **21**(2): p. 78, 80, 82-85.
94. Lipsky, B.A., et al., *Specific guidelines for the treatment of diabetic foot infections 2011.* Diabetes/Metabolism Research and Reviews, 2012. **28**(S1): p. 234-235.
95. Nemeth, A.J., et al., *Faster healing and less pain in skin biopsy sites treated with an occlusive dressing.* Archives of Dermatology, 1991. **127**(11): p. 1679-1683.
96. Cordts, P.R., et al., *A prospective, randomized trial of Unna's boot versus Duoderm CGF hydroactive dressing plus compression in the management of venous leg ulcers.* Journal of Vascular Surgery, 1992. **15**(3): p. 480-486.

97. Ohlsson, P., et al., *A cost-effectiveness study of leg ulcer treatment in primary care: Comparison of saline-gauze and hydrocolloid treatment in a prospective, randomized study*. Scandinavian Journal of Primary Health Care, 1994. **12**(4): p. 295-299.
98. Frykberg, R.G. and J. Banks, *Challenges in the Treatment of Chronic Wounds*. Advances in Wound Care, 2015. **4**(9): p. 560-582.
99. Skorkowska-Telichowska, K., et al., *The local treatment and available dressings designed for chronic wounds*. J Am Acad Dermatol, 2013. **68**(4): p. e117-26.
100. Skorkowska-Telichowska, K., et al., *The local treatment and available dressings designed for chronic wounds*. Journal of the American Academy of Dermatology, 2013. **68**(4): p. e117-e126.
101. Singh, A., et al., *Meta-analysis of randomized controlled trials on hydrocolloid occlusive dressing versus conventional gauze dressing in the healing of chronic wounds*. Asian J Surg, 2004. **27**(4): p. 326-32.
102. Bouza, C., et al., *Efficacy of advanced dressings in the treatment of pressure ulcers: a systematic review*. J Wound Care, 2005. **14**(5): p. 193-9.
103. Greaves, N.S., et al., *The role of skin substitutes in the management of chronic cutaneous wounds*. Wound Repair Regen, 2013. **21**(2): p. 194-210.
104. Compton, C.C., et al., *Organized skin structure is regenerated in vivo from collagen-GAG matrices seeded with autologous keratinocytes*. J Invest Dermatol, 1998. **110**(6): p. 908-16.
105. Pham, C., et al., *Bioengineered skin substitutes for the management of burns: a systematic review*. Burns, 2007. **33**(8): p. 946-57.
106. Bello, Y.M., A.F. Falabella, and W.H. Eaglstein, *Tissue-engineered skin. Current status in wound healing*. Am J Clin Dermatol, 2001. **2**(5): p. 305-13.
107. Tremblay, P.L., et al., *Inosculation of tissue-engineered capillaries with the host's vasculature in a reconstructed skin transplanted on mice*. Am J Transplant, 2005. **5**(5): p. 1002-10.
108. Falanga, V., et al., *Rapid healing of venous ulcers and lack of clinical rejection with an allogeneic cultured human skin equivalent. Human Skin Equivalent Investigators Group*. Arch Dermatol, 1998. **134**(3): p. 293-300.
109. Armstrong, D.G. and L.A. Lavery, *Negative pressure wound therapy after partial diabetic foot amputation: a multicentre, randomised controlled trial*. The Lancet, 2005. **366**(9498): p. 1704-1710.
110. Limengka, Y. and W.S. Jeo, *Spontaneous closure of multiple enterocutaneous fistula due to abdominal tuberculosis using negative pressure wound therapy: a case report*. J Surg Case Rep, 2018. **2018**(1): p. rjy001.
111. Bazalinski, D., et al., *Use of negative pressure wound therapy in a chronic leg wound with coexisting rheumatoid arthritis: a case study*. J Int Med Res, 2018. **46**(6): p. 2495-2499.
112. Almeida, J.E., R. Suarez, and E. Gibson, *A histological analysis of chronic wounds treated with negative pressure wound therapy to aid healing: a case series*. J Wound Care, 2018. **27**(Sup2): p. S28-s34.
113. Glass, G.E., et al., *Systematic review of molecular mechanism of action of negative-pressure wound therapy*. Br J Surg, 2014. **101**(13): p. 1627-36.

114. Stechmiller, J.K., et al., *Effect of Vacuum-Assisted Closure Therapy on the expression of cytokines and proteases in wound fluid of adults with pressure ulcers*. Wound Repair Regen, 2006. **14**(3): p. 371-4.
115. Labler, L., et al., *Vacuum-assisted closure therapy increases local interleukin-8 and vascular endothelial growth factor levels in traumatic wounds*. J Trauma, 2009. **66**(3): p. 749-57.
116. Labler, L., et al., [*Influence of V.A.C.-therapy on cytokines and growth factors in traumatic wounds*]. Zentralbl Chir, 2006. **131 Suppl 1**: p. S62-7.
117. Greene, A.K., et al., *Microdeformational wound therapy: effects on angiogenesis and matrix metalloproteinases in chronic wounds of 3 debilitated patients*. Ann Plast Surg, 2006. **56**(4): p. 418-22.
118. Shi, B., et al., [*Effects of vacuum-assisted closure (VAC) on the expressions of MMP-1, 2, 13 in human granulation wound*]. Zhonghua Zheng Xing Wai Ke Za Zhi, 2003. **19**(4): p. 279-81.
119. Kaur, S., et al., *Evaluation of the efficacy of hyperbaric oxygen therapy in the management of chronic nonhealing ulcer and role of periwound transcutaneous oximetry as a predictor of wound healing response: A randomized prospective controlled trial*. J Anaesthesiol Clin Pharmacol, 2012. **28**(1): p. 70-5.
120. Gill, A.L. and C.N. Bell, *Hyperbaric oxygen: its uses, mechanisms of action and outcomes*. Qjm, 2004. **97**(7): p. 385-95.
121. Hunt, T.K., *The physiology of wound healing*. Annals of Emergency Medicine, 1988. **17**(12): p. 1265-1273.
122. Villanuccis, S.D.M., G. Scholl, M. Pivorine, C. d'Adamo, C. Settimi, F., *CARDIOVASCULAR CHANGES INDUCED BY HYPERBARIC OXYGEN THERAPY*. Undersea and Hyperbaric Medical Society.
123. Sarbjot, K., et al., *Evaluation of the efficacy of hyperbaric oxygen therapy in the management of chronic nonhealing ulcer and role of periwound transcutaneous oximetry as a predictor of wound healing response: A randomized prospective controlled trial*. Journal of Anaesthesiology Clinical Pharmacology, 2012. **28**(1): p. 70-75.
124. O'Reilly, D., et al., *A prospective, double-blind, randomized, controlled clinical trial comparing standard wound care with adjunctive hyperbaric oxygen therapy (HBOT) to standard wound care only for the treatment of chronic, non-healing ulcers of the lower limb in patients with diabetes mellitus: a study protocol*. Trials, 2011. **12**: p. 69.
125. Sanford, N.E., et al., *Efficacy of hyperbaric oxygen therapy in bacterial biofilm eradication*. J Wound Care, 2018. **27**(Sup1): p. S20-s28.
126. Hayes, P.D., et al., *Topical oxygen therapy promotes the healing of chronic diabetic foot ulcers: a pilot study*. J Wound Care, 2017. **26**(11): p. 652-660.
127. Borena, B.M., et al., *Regenerative Skin Wound Healing in Mammals: State-of-the-Art on Growth Factor and Stem Cell Based Treatments*. Cell Physiol Biochem, 2015. **36**(1): p. 1-23.
128. Gilligan, A.M., C.R. Waycaster, and C.T. Milne, *Cost Effectiveness of Becaplermin Gel on Wound Closure for the Treatment of Pressure Injuries*. Wounds, 2018. **30**(6): p. 197-204.

129. Waycaster, C.R., A.M. Gilligan, and T.A. Motley, *Cost-Effectiveness of Becaplermin Gel on Diabetic Foot Ulcer Healing Changes in Wound Surface Area*. J Am Podiatr Med Assoc, 2016. **106**(4): p. 273-82.
130. Tecilazich, F., T.L. Dinh, and A. Veves, *Emerging drugs for the treatment of diabetic ulcers*. Expert Opin Emerg Drugs, 2013. **18**(2): p. 207-17.
131. Hong, J.P., H.D. Jung, and Y.W. Kim, *Recombinant human epidermal growth factor (EGF) to enhance healing for diabetic foot ulcers*. Ann Plast Surg, 2006. **56**(4): p. 394-8; discussion 399-400.
132. Galiano, R.D., et al., *Topical vascular endothelial growth factor accelerates diabetic wound healing through increased angiogenesis and by mobilizing and recruiting bone marrow-derived cells*. Am J Pathol, 2004. **164**(6): p. 1935-47.
133. Tiaka, E.K., et al., *The role of nerve growth factor in the prophylaxis and treatment of diabetic foot ulcers*. Int J Burns Trauma, 2011. **1**(1): p. 68-76.
134. Fu, X., Z. Shen, and Y. Chen, [*Basic fibroblast growth factor (bFGF) and wound healing: a multi-centers and controlled clinical trial in 1024 cases*]. Zhongguo xiu fu chong jian wai ke za zhi = Zhongguo xiufu chongjian waikexue zazhi = Chinese journal of reparative and reconstructive surgery, 1998. **12**(4): p. 209-211.
135. Puppi, D., et al., *Poly(lactic-co-glycolic acid) electrospun fibrous meshes for the controlled release of retinoic acid*. Acta Biomater, 2010. **6**(4): p. 1258-68.
136. Kim, S.W., et al., *Amniotic mesenchymal stem cells enhance wound healing in diabetic NOD/SCID mice through high angiogenic and engraftment capabilities*. PLoS One, 2012. **7**(7): p. e41105.
137. Burgos-Alonso, N., et al., *Adjuvant Biological Therapies in Chronic Leg Ulcers*. Int J Mol Sci, 2017. **18**(12).
138. Kumaran, M.S., *Platelet-rich plasma in dermatology: boon or a bane?* Indian J Dermatol Venereol Leprol, 2014. **80**(1): p. 5-14.
139. Brem, H., et al., *Mechanism of sustained release of vascular endothelial growth factor in accelerating experimental diabetic healing*. J Invest Dermatol, 2009. **129**(9): p. 2275-87.
140. Mulder, G., et al., *Treatment of nonhealing diabetic foot ulcers with a platelet-derived growth factor gene-activated matrix (GAM501): results of a phase 1/2 trial*. Wound Repair Regen, 2009. **17**(6): p. 772-9.
141. Bae, I.-H., J.W. Park, and D.-Y. Kim, *Enhanced regenerative healing efficacy of a highly skin-permeable growth factor nanocomplex in a full-thickness excisional mouse wound model*. International Journal of Nanomedicine, 2014. **9**: p. 4551-4567.
142. Murugan, R. and S. Ramakrishna, *Design strategies of tissue engineering scaffolds with controlled fiber orientation*. Tissue Eng, 2007. **13**(8): p. 1845-66.
143. Rho, K.S., et al., *Electrospinning of collagen nanofibers: effects on the behavior of normal human keratinocytes and early-stage wound healing*. Biomaterials, 2006. **27**(8): p. 1452-61.
144. Dubsky, M., et al., *Nanofibers prepared by needleless electrospinning technology as scaffolds for wound healing*. J Mater Sci Mater Med, 2012. **23**(4): p. 931-41.
145. Karande, T.S., J.L. Ong, and C.M. Agrawal, *Diffusion in musculoskeletal tissue engineering scaffolds: design issues related to porosity, permeability, architecture, and nutrient mixing*. Ann Biomed Eng, 2004. **32**(12): p. 1728-43.

146. Li, W.J., et al., *Electrospun nanofibrous structure: a novel scaffold for tissue engineering*. J Biomed Mater Res, 2002. **60**(4): p. 613-21.
147. Smith, L.A. and P.X. Ma, *Nano-fibrous scaffolds for tissue engineering*. Colloids Surf B Biointerfaces, 2004. **39**(3): p. 125-31.
148. Barnes, C.P., et al., *Nanofiber technology: designing the next generation of tissue engineering scaffolds*. Adv Drug Deliv Rev, 2007. **59**(14): p. 1413-33.
149. Malkar, N.B., et al., *Characterization of Peptide–Amphiphiles Possessing Cellular Activation Sequences*. Biomacromolecules, 2003. **4**(3): p. 518-528.
150. Guillen, G.R., et al., *Preparation and Characterization of Membranes Formed by Nonsolvent Induced Phase Separation: A Review*. Industrial & Engineering Chemistry Research, 2011. **50**(7): p. 3798-3817.
151. Nicholas, M.N., M.G. Jeschke, and S. Amini-Nik, *Methodologies in creating skin substitutes*. Cell Mol Life Sci, 2016. **73**(18): p. 3453-72.
152. Garg, T. and A.K. Goyal, *Biomaterial-based scaffolds--current status and future directions*. Expert Opin Drug Deliv, 2014. **11**(5): p. 767-89.
153. Anchi, P., et al., *Sustained Release Curcumin Microparticles (CuMPs) for Effective Prophylactic Treatment of Exocrine Dysfunction of Pancreas: A Preclinical Study in Cerulein Induced Acute Pancreatitis*. J Pharm Sci, 2018.
154. Quintanar-Guerrero, D., et al., *Impact of the emulsification-diffusion method on the development of pharmaceutical nanoparticles*. Recent Pat Drug Deliv Formul, 2012. **6**(3): p. 184-94.
155. Ranjit, K. and A. Ahmed, *Nanoparticle: An overview of preparation, characterization and application*. Vol. 4. 2013.
156. Lee, S.S., et al., *Evaluation of the sub-acute toxicity of the sclerotium of *Lignosus rhinocerus* (Cooke), the Tiger Milk mushroom*. Journal of Ethnopharmacology, 2011. **138**(1): p. 192-200.
157. Govender, T., et al., *PLGA nanoparticles prepared by nanoprecipitation: drug loading and release studies of a water soluble drug*. Journal of Controlled Release, 1999. **57**(2): p. 171-185.
158. Pawar, A., S. Thakkar, and M. Misra, *A bird's eye view of nanoparticles prepared by electrospaying: advancements in drug delivery field*. J Control Release, 2018. **286**: p. 179-200.
159. Chong, E.J., et al., *Evaluation of electrospun PCL/gelatin nanofibrous scaffold for wound healing and layered dermal reconstitution*. Acta Biomater, 2007. **3**(3): p. 321-30.
160. Yin, H., et al., *A bioengineered drug-Eluting scaffold accelerated cutaneous wound healing In diabetic mice*. Colloids Surf B Biointerfaces, 2016. **145**: p. 226-31.
161. Khorshidi, S., et al., *A review of key challenges of electrospun scaffolds for tissue-engineering applications*. J Tissue Eng Regen Med, 2016. **10**(9): p. 715-38.
162. Plowman, J.E., S. Deb-Choudhury, and J.M. Dyer, *Fibrous protein nanofibers*. Methods Mol Biol, 2013. **996**: p. 61-76.
163. Chou, S.-F., D. Carson, and K.A. Woodrow, *Current strategies for sustaining drug release from electrospun nanofibers*. Journal of Controlled Release, 2015. **220**: p. 584-591.
164. Lim, S.H. and H.Q. Mao, *Electrospun scaffolds for stem cell engineering*. Adv Drug Deliv Rev, 2009. **61**(12): p. 1084-96.

165. Gould, L.J., *Topical Collagen-Based Biomaterials for Chronic Wounds: Rationale and Clinical Application*. Adv Wound Care (New Rochelle), 2016. **5**(1): p. 19-31.
166. Tan, S., et al., *Systematic parameter study for ultra-fine fiber fabrication via electrospinning process*. Polymer, 2005. **46**(16): p. 6128-6134.
167. Katti, D.S., et al., *Bioresorbable nanofiber-based systems for wound healing and drug delivery: optimization of fabrication parameters*. J Biomed Mater Res B Appl Biomater, 2004. **70**(2): p. 286-96.
168. Ji, W., et al., *Bioactive electrospun scaffolds delivering growth factors and genes for tissue engineering applications*. Pharm Res, 2011. **28**(6): p. 1259-72.
169. Yoo, H.S., T.G. Kim, and T.G. Park, *Surface-functionalized electrospun nanofibers for tissue engineering and drug delivery*. Adv Drug Deliv Rev, 2009. **61**(12): p. 1033-42.
170. Falanga, V., *Wound healing and its impairment in the diabetic foot*. Lancet, 2005. **366**(9498): p. 1736-43.
171. Chouhan, D., et al., *Functionalized PVA-silk blended nanofibrous mats promote diabetic wound healing via regulation of extracellular matrix and tissue remodelling*. J Tissue Eng Regen Med, 2018. **12**(3): p. e1559-e1570.
172. Wu, J., et al., *Electrospun nanoyarn scaffold and its application in tissue engineering*. Materials Letters, 2012. **89**: p. 146-149.
173. Nam, J., et al., *Materials selection and residual solvent retention in biodegradable electrospun fibers*. Journal of applied polymer science, 2008. **107**(3): p. 1547-1554.
174. Luo, C.J., et al., *Electrospinning versus fibre production methods: from specifics to technological convergence*. Chem Soc Rev, 2012. **41**(13): p. 4708-35.
175. Persano, L., et al., *Industrial upscaling of electrospinning and applications of polymer nanofibers: a review*. Macromolecular Materials and Engineering, 2013. **298**(5): p. 504-520.
176. Eichhorn, S.J. and W.W. Sampson, *Statistical geometry of pores and statistics of porous nanofibrous assemblies*. J R Soc Interface, 2005. **2**(4): p. 309-18.
177. Yan, G., et al., *Improving Nanofiber Production and Application Performance by Electrospinning at Elevated Temperatures*. Industrial & Engineering Chemistry Research, 2017. **56**(43): p. 12337-12343.
178. Rnjak-Kovacina, J. and A.S. Weiss, *Increasing the pore size of electrospun scaffolds*. Tissue Eng Part B Rev, 2011. **17**(5): p. 365-72.
179. Shabani, I., et al., *Cellular infiltration on nanofibrous scaffolds using a modified electrospinning technique*. Biochemical and biophysical research communications, 2012. **423**(1): p. 50-54.
180. Chen, M., et al., *Role of Fiber Diameter in Adhesion and Proliferation of NIH 3T3 Fibroblast on Electrospun Polycaprolactone Scaffolds*. Vol. 13. 2007. 579-87.
181. Wright, L., T. Andric, and J. Freeman, *Utilizing NaCl to increase the porosity of electrospun materials*. Materials Science and Engineering: C, 2011. **31**(1): p. 30-36.
182. Castro-Mayorga, J.L., et al., *On the Use of the Electrospinning Coating Technique to Produce Antimicrobial Polyhydroxyalkanoate Materials Containing In Situ-Stabilized Silver Nanoparticles*. Nanomaterials, 2017. **7**(1): p. 4.
183. Jouybar, A., et al., *Enhanced Skin Regeneration by Herbal Extract-Coated Poly-L-Lactic Acid Nanofibrous Scaffold*. Artif Organs, 2017. **41**(11): p. E296-e307.

184. Tort, S., F. Acarturk, and A. Besikci, *Evaluation of three-layered doxycycline-collagen loaded nanofiber wound dressing*. Int J Pharm, 2017. **529**(1-2): p. 642-653.
185. Poornima, B. and P.S. Korrapati, *Fabrication of chitosan-polycaprolactone composite nanofibrous scaffold for simultaneous delivery of ferulic acid and resveratrol*. Carbohydr Polym, 2017. **157**: p. 1741-1749.
186. Shoba, E., et al., *Fabrication of core-shell nanofibers for controlled delivery of bromelain and salvianolic acid B for skin regeneration in wound therapeutics*. Biomed Mater, 2017. **12**(3): p. 035005.
187. Pilehvar-Soltanahmadi, Y., et al., *An update on clinical applications of electrospun nanofibers for skin bioengineering*. Artif Cells Nanomed Biotechnol, 2016. **44**(6): p. 1350-64.
188. Zamani, M., M.P. Prabhakaran, and S. Ramakrishna, *Advances in drug delivery via electrospun and electrosprayed nanomaterials*. International journal of nanomedicine, 2013. **8**: p. 2997.
189. Lee, J., et al., *The effect of controlled release of PDGF-BB from heparin-conjugated electrospun PCL/gelatin scaffolds on cellular bioactivity and infiltration*. Biomaterials, 2012. **33**(28): p. 6709-6720.
190. Stephansen, K., I.S. Chronakis, and F. Jessen, *Bioactive electrospun fish sarcoplasmic proteins as a drug delivery system*. Colloids and Surfaces B: Biointerfaces, 2014. **122**: p. 158-165.
191. Volpato, F.Z., et al., *Preservation of FGF-2 bioactivity using heparin-based nanoparticles, and their delivery from electrospun chitosan fibers*. Acta biomaterialia, 2012. **8**(4): p. 1551-1559.
192. Choi, J.S., K.W. Leong, and H.S. Yoo, *In vivo wound healing of diabetic ulcers using electrospun nanofibers immobilized with human epidermal growth factor (EGF)*. Biomaterials, 2008. **29**(5): p. 587-596.
193. Wu, Y., et al., *Electrosprayed core-shell microspheres for protein delivery*. Chem Commun (Camb), 2010. **46**(26): p. 4743-5.
194. Hwang, Y.K., U. Jeong, and E.C. Cho, *Production of uniform-sized polymer core-shell microcapsules by coaxial electrospraying*. Langmuir, 2008. **24**(6): p. 2446-51.
195. Liao, I.-C. and K.W. Leong, *Efficacy of engineered FVIII-producing skeletal muscle enhanced by growth factor-releasing co-axial electrospun fibers*. Biomaterials, 2011. **32**(6): p. 1669-1677.
196. Saraf, A., et al., *Regulated non-viral gene delivery from coaxial electrospun fiber mesh scaffolds*. Journal of Controlled Release, 2010. **143**(1): p. 95-103.
197. Lee, Y.-H., et al., *Release profile characteristics of biodegradable-polymer-coated drug particles fabricated by dual-capillary electrospray*. Journal of controlled Release, 2010. **145**(1): p. 58-65.
198. Wang, H., et al., *Electrospun poly (methyl methacrylate) nanofibers and microparticles*. Journal of materials science, 2010. **45**(4): p. 1032.
199. Xie, J., R.S. Tan, and C.H. Wang, *Biodegradable microparticles and fiber fabrics for sustained delivery of cisplatin to treat C6 glioma in vitro*. Journal of Biomedical Materials Research Part A, 2008. **85**(4): p. 897-908.
200. Loscertales, I.G., et al., *Micro/nano encapsulation via electrified coaxial liquid jets*. Science, 2002. **295**(5560): p. 1695-1698.

201. Farook, U., E. Stride, and M. Edirisinghe, *Stability of microbubbles prepared by co-axial electrohydrodynamic atomisation*. European Biophysics Journal, 2009. **38**(5): p. 713-718.
202. Xie, J., et al., *Encapsulation of protein drugs in biodegradable microparticles by co-axial electrospray*. Journal of Colloid and Interface Science, 2008. **317**(2): p. 469-476.
203. Enayati, M., et al., *One-step electrohydrodynamic production of drug-loaded micro-and nanoparticles*. Journal of the Royal Society Interface, 2010. **7**(45): p. 667-675.
204. Zhang, L., et al., *Coaxial electrospray of microparticles and nanoparticles for biomedical applications*. Expert review of medical devices, 2012. **9**(6): p. 595-612.
205. Lee, Y.-H., M.-Y. Bai, and D.-R. Chen, *Multidrug encapsulation by coaxial tri-capillary electrospray*. Colloids and Surfaces B: Biointerfaces, 2011. **82**(1): p. 104-110.
206. Sohrabi, A., et al., *Sustained drug release and antibacterial activity of ampicillin incorporated poly (methyl methacrylate)–nylon6 core/shell nanofibers*. Polymer, 2013. **54**(11): p. 2699-2705.
207. Wang, C., et al., *Biodegradable core/shell fibers by coaxial electrospinning: processing, fiber characterization, and its application in sustained drug release*. Macromolecules, 2010. **43**(15): p. 6389-6397.
208. Lavielle, N., et al., *Simultaneous Electrospinning and Electro spraying: A Straightforward Approach for Fabricating Hierarchically Structured Composite Membranes*. ACS Applied Materials & Interfaces, 2013. **5**(20): p. 10090-10097.
209. Guo, X., et al., *Creating 3D angiogenic growth factor gradients in fibrous constructs to guide fast angiogenesis*. Biomacromolecules, 2012. **13**(10): p. 3262-71.
210. Zhang, X., M.R. Reagan, and D.L. Kaplan, *Electrospun silk biomaterial scaffolds for regenerative medicine*. Advanced drug delivery reviews, 2009. **61**(12): p. 988-1006.
211. Migneault, I., et al., *Glutaraldehyde: behavior in aqueous solution, reaction with proteins, and application to enzyme crosslinking*. Biotechniques, 2004. **37**(5): p. 790-6, 798-802.
212. Bowes, J.H. and C.W. Cater, *The interaction of aldehydes with collagen*. Biochim Biophys Acta, 1968. **168**(2): p. 341-52.
213. Habeeb, A.J. and R. Hiramoto, *Reaction of proteins with glutaraldehyde*. Arch Biochem Biophys, 1968. **126**(1): p. 16-26.
214. Weetall, H.H., *Immobilized enzymes: analytical applications*. Anal Chem, 1974. **46**(7): p. 602A-4A p.
215. Khor, E., *Methods for the treatment of collagenous tissues for bioprotheses*. Biomaterials, 1997. **18**(2): p. 95-105.
216. Wiebe, D., et al., *Glutaraldehyde release from vascular prostheses of biologic origin*. Surgery, 1988. **104**(1): p. 26-33.
217. Roxana Sava, O., et al., *Trends in Materials Science for Ligament Reconstruction. Current stem cell research & therapy*, 2017. **12**(2): p. 145-154.
218. Kim, T.G. and T.G. Park, *Biomimicking extracellular matrix: cell adhesive RGD peptide modified electrospun poly(D,L-lactic-co-glycolic acid) nanofiber mesh*. Tissue Eng, 2006. **12**(2): p. 221-33.

219. Kim, H.N., et al., *Nanotopography-guided tissue engineering and regenerative medicine*. Adv Drug Deliv Rev, 2013. **65**(4): p. 536-58.
220. Chandrasekaran, A.R., et al., *Fabrication of a nanofibrous scaffold with improved bioactivity for culture of human dermal fibroblasts for skin regeneration*. Biomed Mater, 2011. **6**(1): p. 015001.
221. Gautam, S., A.K. Dinda, and N.C. Mishra, *Fabrication and characterization of PCL/gelatin composite nanofibrous scaffold for tissue engineering applications by electrospinning method*. Mater Sci Eng C Mater Biol Appl, 2013. **33**(3): p. 1228-35.
222. Tracy, L.E., R.A. Minasian, and E.J. Caterson, *Extracellular Matrix and Dermal Fibroblast Function in the Healing Wound*. Advances in Wound Care, 2016. **5**(3): p. 119-136.
223. Liu, Y., L. Ma, and C. Gao, *Facile fabrication of the glutaraldehyde cross-linked collagen/chitosan porous scaffold for skin tissue engineering*. Materials Science and Engineering: C, 2012. **32**(8): p. 2361-2366.
224. Malafaya, P.B., G.A. Silva, and R.L. Reis, *Natural-origin polymers as carriers and scaffolds for biomolecules and cell delivery in tissue engineering applications*. Adv Drug Deliv Rev, 2007. **59**(4-5): p. 207-33.
225. Brett, D., *A Review of Collagen and Collagen-based Wound Dressings*. Wounds-a Compendium of Clinical Research and Practice, 2008. **20**(12): p. 347-356.
226. Hassiba, A.J., et al., *Review of recent research on biomedical applications of electrospun polymer nanofibers for improved wound healing*. Nanomedicine (Lond), 2016. **11**(6): p. 715-37.
227. Pezeshki-Modaress, M., et al., *Gelatin/chondroitin sulfate nanofibrous scaffolds for stimulation of wound healing: In-vitro and in-vivo study*. J Biomed Mater Res A, 2017. **105**(7): p. 2020-2034.
228. Duan, H., et al., *Engineering of epidermis skin grafts using electrospun nanofibrous gelatin/ polycaprolactone membranes*. Int J Nanomedicine, 2013. **8**: p. 2077-84.
229. Kapoor, D.N., et al., *PLGA: a unique polymer for drug delivery*. Ther Deliv, 2015. **6**(1): p. 41-58.
230. Liu, X., et al., *The effect of poly (lactic-co-glycolic) acid composition on the mechanical properties of electrospun fibrous mats*. Int J Pharm, 2017. **529**(1-2): p. 371-380.
231. Kumari, A., S.K. Yadav, and S.C. Yadav, *Biodegradable polymeric nanoparticles based drug delivery systems*. Colloids and Surfaces B: Biointerfaces, 2010. **75**(1): p. 1-18.
232. Vert, M., J. Mauduit, and S. Li, *Biodegradation of PLA/GA polymers: increasing complexity*. Biomaterials, 1994. **15**(15): p. 1209-1213.
233. Astete, C.E. and C.M. Sabliov, *Synthesis and characterization of PLGA nanoparticles*. J Biomater Sci Polym Ed, 2006. **17**(3): p. 247-89.
234. Prabhakaran, M.P., et al., *Electrospraying technique for the fabrication of metronidazole contained PLGA particles and their release profile*. Materials Science and Engineering: C, 2015. **56**: p. 66-73.
235. Watt, F.M. and H. Fujiwara, *Cell-Extracellular Matrix Interactions in Normal and Diseased Skin*. Cold Spring Harbor Perspectives in Biology, 2011. **3**(4): p. a005124.
236. Larsen, M., et al., *The matrix reorganized: extracellular matrix remodeling and integrin signaling*. Curr Opin Cell Biol, 2006. **18**(5): p. 463-71.

237. Schwartz, M.A., *Integrins and extracellular matrix in mechanotransduction*. Cold Spring Harb Perspect Biol, 2010. **2**(12): p. a005066.
238. Bornstein, P., *Thrombospondins as matricellular modulators of cell function*. Journal of Clinical Investigation, 2001. **107**(8): p. 929-934.
239. Midwood, K.S., L.V. Williams, and J.E. Schwarzbauer, *Tissue repair and the dynamics of the extracellular matrix*. Int J Biochem Cell Biol, 2004. **36**(6): p. 1031-7.
240. Litvin, J., et al., *Expression and function of periostin-isoforms in bone*. Journal of Cellular Biochemistry, 2004. **92**(5): p. 1044-1061.
241. Takeshita, S., et al., *Osteoblast-specific factor 2: cloning of a putative bone adhesion protein with homology with the insect protein fasciclin I*. Biochemical Journal, 1993. **294**(Pt 1): p. 271-278.
242. Norris, R.A., et al., *Periostin regulates collagen fibrillogenesis and the biomechanical properties of connective tissues*. J Cell Biochem, 2007. **101**(3): p. 695-711.
243. Horiuchi, K., et al., *Identification and characterization of a novel protein, periostin, with restricted expression to periosteum and periodontal ligament and increased expression by transforming growth factor β* . Journal of bone and mineral research, 1999. **14**(7): p. 1239-1249.
244. Lindner, V., et al., *Vascular Injury Induces Expression of Periostin*. Arteriosclerosis, thrombosis, and vascular biology, 2005. **25**(1): p. 77-83.
245. Kudo, H., et al., *Zebrafish periostin is required for the adhesion of muscle fiber bundles to the myoseptum and for the differentiation of muscle fibers*. Developmental biology, 2004. **267**(2): p. 473-487.
246. Dorn II, G.W., *Periostin and myocardial repair, regeneration, and recovery*. The New England journal of medicine, 2007. **357**(15): p. 1552.
247. Nishiyama, T., et al., *Delayed re-epithelialization in periostin-deficient mice during cutaneous wound healing*. PLoS One, 2011. **6**(4): p. e18410.
248. Ontsuka, K., et al., *Periostin, a matricellular protein, accelerates cutaneous wound repair by activating dermal fibroblasts*. Exp Dermatol, 2012. **21**(5): p. 331-6.
249. Li, G., et al., *Periostin mediates vascular smooth muscle cell migration through the integrins α v β 3 and α v β 5 and focal adhesion kinase (FAK) pathway*. Atherosclerosis, 2010. **208**(2): p. 358-65.
250. Jackson-Boeters, L., W. Wen, and D.W. Hamilton, *Periostin localizes to cells in normal skin, but is associated with the extracellular matrix during wound repair*. J Cell Commun Signal, 2009. **3**(2): p. 125-33.
251. Elliott, C.G., et al., *Periostin modulates myofibroblast differentiation during full-thickness cutaneous wound repair*. J Cell Sci, 2012. **125**(Pt 1): p. 121-32.
252. Jun, J.I. and L.F. Lau, *Taking aim at the extracellular matrix: CCN proteins as emerging therapeutic targets*. Nat Rev Drug Discov, 2011. **10**(12): p. 945-63.
253. Perbal, B., *[The CCN family of cell growth regulators: a new family of normal and pathologic cell growth and differentiation regulators: lessons from the first international workshop on CCN gene family]*. Bull Cancer, 2001. **88**(7): p. 645-9.
254. Chen, C.C. and L.F. Lau, *Functions and mechanisms of action of CCN matricellular proteins*. Int J Biochem Cell Biol, 2009. **41**(4): p. 771-83.
255. Kular, L., et al., *The CCN family: a new class of inflammation modulators?* Biochimie, 2011. **93**(3): p. 377-88.

256. Brigstock, D.R., *Connective tissue growth factor (CCN2, CTGF) and organ fibrosis: lessons from transgenic animals*. J Cell Commun Signal, 2010. **4**(1): p. 1-4.
257. Babic, A.M., et al., *CYR61, a product of a growth factor-inducible immediate early gene, promotes angiogenesis and tumor growth*. Proc Natl Acad Sci U S A, 1998. **95**(11): p. 6355-60.
258. Kubota, S. and M. Takigawa, *CCN family proteins and angiogenesis: from embryo to adulthood*. Angiogenesis, 2007. **10**(1): p. 1-11.
259. Dean, R.A., et al., *Identification of candidate angiogenic inhibitors processed by matrix metalloproteinase 2 (MMP-2) in cell-based proteomic screens: disruption of vascular endothelial growth factor (VEGF)/heparin affinity regulatory peptide (pleiotrophin) and VEGF/Connective tissue growth factor angiogenic inhibitory complexes by MMP-2 proteolysis*. Mol Cell Biol, 2007. **27**(24): p. 8454-65.
260. Inoki, I., et al., *Connective tissue growth factor binds vascular endothelial growth factor (VEGF) and inhibits VEGF-induced angiogenesis*. Faseb j, 2002. **16**(2): p. 219-21.
261. Elliott, C., Wound Repair Regen, Under Review.
262. Elliott, C., *Evaluation of matricellular proteins as potential therapeutics for the treatment of human chronic skin wounds*. 2013.
263. Miyamoto, M., et al., *Molecular cloning of a novel cytokine cDNA encoding the ninth member of the fibroblast growth factor family, which has a unique secretion property*. Molecular and Cellular Biology, 1993. **13**(7): p. 4251-4259.
264. Miyamoto, M., et al., *Molecular cloning of a novel cytokine cDNA encoding the ninth member of the fibroblast growth factor family, which has a unique secretion property*. Mol Cell Biol, 1993. **13**(7): p. 4251-9.
265. Miyakawa, K., et al., *A hydrophobic region locating at the center of fibroblast growth factor-9 is crucial for its secretion*. J Biol Chem, 1999. **274**(41): p. 29352-7.
266. Plotnikov, A.N., et al., *Crystal structure of fibroblast growth factor 9 reveals regions implicated in dimerization and autoinhibition*. J Biol Chem, 2001. **276**(6): p. 4322-9.
267. Kelleher, F.C., et al., *Fibroblast growth factor receptors, developmental corruption and malignant disease*. Carcinogenesis, 2013. **34**(10): p. 2198-205.
268. Brooks, A.N., E. Kilgour, and P.D. Smith, *Molecular Pathways: Fibroblast Growth Factor Signaling: A New Therapeutic Opportunity in Cancer*. Clinical Cancer Research, 2012. **18**(7): p. 1855.
269. Hacker, U., K. Nybakken, and N. Perrimon, *Heparan sulphate proteoglycans: the sweet side of development*. Nat Rev Mol Cell Biol, 2005. **6**(7): p. 530-41.
270. Ornitz, D.M., *FGFs, heparan sulfate and FGFRs: complex interactions essential for development*. Bioessays, 2000. **22**(2): p. 108-12.
271. Colvin, J.S., et al., *Lung hypoplasia and neonatal death in Fgf9-null mice identify this gene as an essential regulator of lung mesenchyme*. Development, 2001. **128**(11): p. 2095-106.
272. Lavine, K.J., et al., *Fibroblast growth factor signals regulate a wave of Hedgehog activation that is essential for coronary vascular development*. Genes Dev, 2006. **20**(12): p. 1651-66.

273. Geske, M.J., et al., *Fgf9 signaling regulates small intestinal elongation and mesenchymal development*. *Development*, 2008. **135**(17): p. 2959-68.
274. Lin, Y., et al., *Neuron-derived FGF9 is essential for scaffold formation of Bergmann radial fibers and migration of granule neurons in the cerebellum*. *Dev Biol*, 2009. **329**(1): p. 44-54.
275. Frontini, M.J., et al., *Fibroblast growth factor 9 delivery during angiogenesis produces durable, vasoresponsive microvessels wrapped by smooth muscle cells*. *Nat Biotechnol*, 2011. **29**(5): p. 421-7.
276. White, A.C., et al., *FGF9 and SHH signaling coordinate lung growth and development through regulation of distinct mesenchymal domains*. *Development*, 2006. **133**(8): p. 1507-17.
277. White, A.C., K.J. Lavine, and D.M. Ornitz, *FGF9 and SHH regulate mesenchymal Vegfa expression and development of the pulmonary capillary network*. *Development*, 2007. **134**(20): p. 3743-52.
278. Yin, H., et al., *Fibroblast Growth Factor 9 Imparts Hierarchy and Vasoreactivity to the Microcirculation of Renal Tumors and Suppresses Metastases*. *J Biol Chem*, 2015. **290**(36): p. 22127-42.
279. Agrotis, A., et al., *Proliferation of neointimal smooth muscle cells after arterial injury. Dependence on interactions between fibroblast growth factor receptor-2 and fibroblast growth factor-9*. *J Biol Chem*, 2004. **279**(40): p. 42221-9.
280. Komi-Kuramochi, A., et al., *Expression of fibroblast growth factors and their receptors during full-thickness skin wound healing in young and aged mice*. *J Endocrinol*, 2005. **186**(2): p. 273-89.
281. Gay, D., et al., *Fgf9 from dermal [gamma][delta] T cells induces hair follicle neogenesis after wounding*. *Nature medicine*, 2013. **19**(7): p. 916-923.
282. Zheng, Z., et al., *Up-regulation of fibroblast growth factor (FGF) 9 expression and FGF-WNT/beta-catenin signaling in laser-induced wound healing*. *Wound Repair Regen*, 2014. **22**(5): p. 660-5.
283. Kan, M., et al., *An essential heparin-binding domain in the fibroblast growth factor receptor kinase*. *Science*, 1993. **259**(5103): p. 1918-21.
284. Said, S.S., et al., *Concurrent and Sustained Delivery of FGF2 and FGF9 from Electrospun Poly(ester amide) Fibrous Mats for Therapeutic Angiogenesis*. *Tissue Eng Part A*, 2016. **22**(7-8): p. 584-96.
285. Said, S.S., J.G. Pickering, and K. Mequanint, *Controlled delivery of fibroblast growth factor-9 from biodegradable poly(ester amide) fibers for building functional neovasculature*. *Pharm Res*, 2014. **31**(12): p. 3335-47.
286. Warburton, D., et al., *Stem/progenitor cells in lung development, injury repair, and regeneration*. *Proceedings of the American Thoracic Society*, 2008. **5**(6): p. 703-706.
287. Pannetier, M., et al., *Molecular aspects of female and male gonadal development in mammals*. *Pediatric endocrinology reviews: PER*, 2004. **1**(3): p. 274-287.

Chapter 2

Influence of Nanofibrous Electrospun Periostin and Connective Tissue Growth Factor 2 Scaffolds on Angiogenesis and Wound Repair in a 28-Day Porcine Model

2.1 – Introduction

The skin is a functional barrier that protects and regulates the bodies internal environment. The two main anatomic layers of the skin, the epidermis and dermis, participate in thermoregulation, sensation, haemostasis, and wound healing [1]. Cutaneous wound healing involves four overlapping phases: hemostasis, inflammation, proliferation, and remodelling to collectively initiate repair, eliminate infection, and restore the barrier upon injury. However, under certain pathological conditions, wound closure does not occur [2]. Chronic wounds are cutaneous tissue defects characterized by a proinflammatory microenvironment, and excessive degradation of connective tissues and signalling molecules that disrupt the normal progression of reparative events, resulting in an open lesion that persists longer than 3 months. Chronic wounds are of significant and growing clinical concern, particularly in relation to diabetes, venous insufficiency and immobility. Chronic wounds are associated with increased rates of amputation, mortality, and pose a significant financial burden on the healthcare system; for instance, the average cost to treat a diabetic foot ulcer in Canada is \$39,000 [3, 4].

Conventional interventions remove necrotic or devitalized tissue, control infection, apply moisture retentive wound dressings, mechanically off-load the affected area, and if necessary, re-establish blood flow with revascularization procedures [5]. However, except for hydrocolloids that promote autolytic debridement, standard dressings are only capable of passive moisturization of the wound environment to facilitate healing and protecting the wound from external mechanical forces. Bioengineered skin substitutes, such as Dermagraft® and Apligraf®, are alternative dressings capable of providing bioactive factors and cell populations to the wound site. However, high costs and short shelf-life are major limitations associated with their use [6].

Granulation tissue-mimetic electrospun nanofibrous scaffolds are ideal for tissue regeneration as they provide tunable pore size, porosity, and fiber diameter, as well as a high surface area to volume ratio, thus closely mimicking the structure of the natural ECM. Furthermore, the electrospinning process is cost-efficient, scalable, compatible with a wide variety of available polymers, and can incorporate bioactive factors [7]. Gelatin is a natural alternative to collagen for the fabrication of electrospun scaffolds, retaining the biocompatibility and biodegradability of collagen, at a fraction of the cost [8].

In addition to tunable architecture, incorporation of bioactive factors such as matricellular proteins enhances biocompatibility and bioactivity of electrospun scaffolds. Matricellular proteins are a class of non-structural ECM components that modulate cell-ECM interaction [9]. The matricellular protein POSTN enhances keratinocyte proliferation and re-epithelialization [10], modulates vascular smooth muscle cell migration [11], facilitates dermal fibroblast activation and wound contraction, and accelerates acute cutaneous wound repair [12]. POSTN is upregulated on day 3 post-wounding and peaks at day 7, correlating with heightened myofibroblast differentiation [13]. The matricellular protein CCN2 is upregulated from day 3 to day 11 in acute wound healing, promoting ECM deposition and fibroplasia, endothelial cell proliferation and chemotaxis, and neovascular tubule formation, as well as regulating other angiogenic factors (e.g., vascular endothelial growth factor-A and -C (VEGF-A/C)) [14-18]. CCN2 modulates the activity and expression of certain inflammatory markers [19]. In previous research, we developed electrospun collagen-based scaffolds for the delivery of POSTN and CCN2. Addition of the scaffolds supported vascular growth and accelerated wound closure in db/db mice (Hamilton lab, In Review, J Tissue Eng).

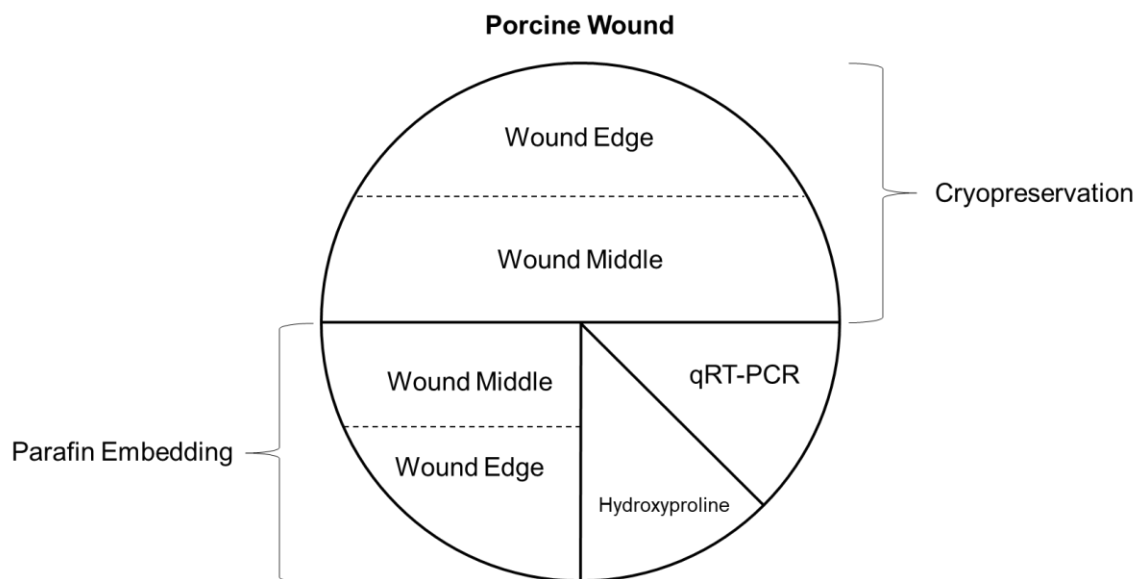
The aim of this study was to investigate the efficacy of POSTN/CCN2 electrospun gelatin scaffolds on tissue repair in a porcine model of cutaneous wound healing. Wound closure kinetics, angiogenic growth, and collagen deposition were evaluated and compared to scaffolds without POSTN/CCN2.

2.2 – Materials and Methods

2.2.1 – 28-Day Porcine Study

All animal procedures followed protocols approved by the University Council on Animal Care at Western University. An *in vivo* porcine model was used to determine the ability of POSTN/CCN2 and galectin 3 (GAL3) loaded gelatin biomaterial scaffolds to facilitate the cutaneous wound-healing process. Four circular, 2 cm diameter, full-thickness, excisional wounds were created on the dorsal surface of six age- and sex-matched healthy Yorkshire pigs, carried out by a veterinarian. In each animal, treatment groups were defined: 1) empty wound, 2) gelatin scaffold containing bovine serum albumin (BSA), 3) gelatin scaffold containing recombinant human (rh) GAL3, and 4) gelatin scaffold containing rhPOSTN (POSTN) and rhCCN2 (CCN2). Healthy pigs were anesthetized, circular full-thickness wounds were excised, and scaffolds (section 2.2.2) were placed (3 per wound) into the wound beds. Wound treatments were rotated clockwise in each pig to minimize positional effects. Euthanasia and tissue isolation occurred at day 28 post-wounding. Immediately after euthanasia, wounded and unwounded tissue samples were removed and prepared for analysis (Figure 2.1). Tissue samples for cryopreservation and paraffin embedding were immediately fixed in 10% neutral buffered formalin (Sigma-Aldrich) for 24 h at 4°C. After formalin fixation, tissues for cryopreservation were rinsed with PBS and transferred to 75 mL 10% sucrose (Sigma-Aldrich) for 24 h at 4°C. Cryopreserved tissues were then transferred to 20% and 30% sucrose for 24 h each at 4°C. Tissue samples were then pre-agitated with 1:1 clear frozen section compound (VWR) and 30% sucrose for 1h before excess hair was removed and the tissues were placed wound-down in a disposable base mold (Fisher Scientific). Tissues were covered with clear frozen-section compound, immediately frozen on dry ice, and stored at -20°C. Serial 8 µm samples were sectioned using a Leica CM1900 UV cryostat (Leica) and stored at -20°C. Tissue samples for paraffin embedding were transferred to 70% ethanol (Commercial Alcohols) after the 24 h formalin fixation, and paraffin embedded using a Leica RM2245 microtome (Leica). Serial 6 µm paraffin sections were cut and stored at room temperature. The final quarter of the wound tissues were divided into eighths and stored at -80°C in 2 mL microtubes for gene expression analysis and quantification of collagen content.

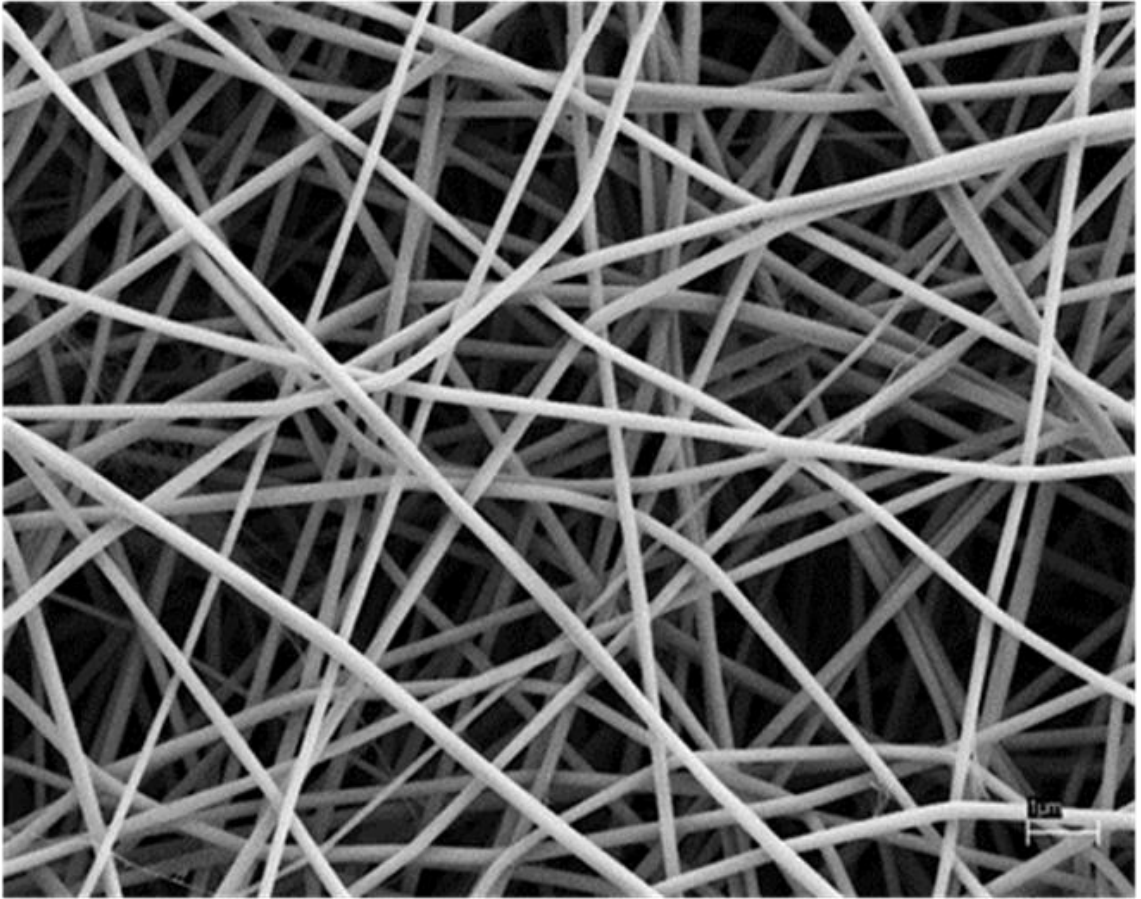
Figure 2. 1 – Division of porcine wounds for post-experimentation. One half and one quarter of each wound was cryopreserved, and paraffin-embedded, respectively, for future immunohistochemical staining. Cryopreserved and paraffin embedded tissues were divided based on proximity to the center of the wound (middle versus edge of the wound bed). One eighth of the wound tissue was taken for qRT-PCR and the final eighth for hydroxyproline quantification.



2.2.2 – Scaffold Preparation

Stock solutions of BSA (Fisher Scientific), GAL3, POSTN, and CCN2 (all matricellular proteins were purchased from R&D) were diluted to 10 $\mu\text{g/mL}$ in 21 wt% Type B gelatin from bovine skin (Sigma-Aldrich) dissolved in 40% v/v acetic acid (Thermo Fisher Scientific) in deionized water. The polymer solution was loaded into a plastic 1 cc syringe and a syringe pump (VWR) delivered the polymer solution through a 20-gauge blunt-tip stainless steel needle connected to a high voltage DC power supply (Gamma High Voltage Research). Rotation of the grounded stainless-steel mandrel was held constant at ~ 100 RPM. A piece of aluminum foil was secured to the rotating mandrel with electrical tape and acted as the collecting surface. Scaffolds were electrospun for two hours using a flow rate of 0.3 mL/h, an applied voltage of 15 kV and a collector distance of 10 cm. After electrospinning, scaffolds were crosslinked for 48 hours by the vapours emitted from a 5 mL solution of 1.5% v/v glutaraldehyde (50 wt% in H_2O) (Sigma-Aldrich) in anhydrous ethyl alcohol (Commercial Alcohols), in a glass desiccator (VWR) containing drierite (W.A. Hammond Drierite Co. Ltd) that was vacuum sealed for 20 minutes [20]. Final processing of the scaffolds involved removal of residual glutaraldehyde with a one hour 0.1 M glycine (Sigma-Aldrich) quench followed by three, 15-minute PBS rinses. Scaffolds were cut with a scalpel in circles, 2 cm in diameter, using the bottom of a 12-well plate as a stencil. The scaffolds, 2 cm in diameter, were separated from the tinfoil and rinsed with PBS followed by sterilization with ultra violet light while submerged in PBS for 30 minutes per side. Sterilized scaffolds were stored in 2 mL serum free Dulbecco's Modified Eagle Medium (DMEM; high glucose; Thermo Fisher) at 4°C until use. Three scaffolds were layered into each wound during the porcine study. A representative image of the scaffolds utilized in the 28-day porcine study is presented in Figure 2.2.

Figure 2. 2 – Representative scanning electron microscopy image of an electrospun nanofibrous scaffold utilized in the 28-day porcine wound-healing study. Representative image of scaffolds fabricated using optimized parameters (section 3.2.2; 0.5 mL/h, 17 kV, 8 cm) and a 21 wt% gelatin solution. Scale bar = 1 μ m.



2.2.3 – Porcine Cutaneous Wound-Healing Outcomes

2.2.3.1 – Wound Closure Kinetics

Digital photography (Nikon Coolpix S3600) was used to image the wounds on the backs of the pigs at various timepoints throughout the 28-day study period. Wound photography occurred during bandage changes, the appropriate timing of which was determined by the veterinary staff. Variability in the timing of bandaging changes resulted in inconsistent imaging timepoints between pigs. Imaging timepoints were as follows:

Pig 1 – days 0, 8, 15, 21, 28

Pig 2 – days 0, 8, 14, 21, 28

Pig 3 – days 0, 12, 21, 28

Pig 4 – days 0, 12, 21, 28

Pig 5 – days 0, 8, 14, 22, 28

Pig 6 – days 8, 14, 22, 28

Pig 6 was not imaged at day 0, and therefore was removed from wound closure kinetic analysis. ImageJ analysis (National Institutes of Health) was used to measure wound area as perimeter of the epithelial border. A ruler included in the digital photographs ensured standardization of scale across images. Data analysis was conducted based on the assumption of minimal differences in wound closure between similar timepoints, allowing binning of data between the following timepoints: 1) day 8, 2) days 12, 14, and 15, 3) days 21 and 22, and 4) day 28. All binned timepoints included data from 5 pigs (N=5), except the day 8 timepoint (N=3). One measurement was made per wound, per pig at each timepoint (n=1).

Wound diameter was measured as the distance between the base of unwounded dermal tissue bordering the wound bed, parallel to the underlying hypodermal tissue using ImageJ software and tissue sections stained with Masson's Trichrome. One Trichrome image (n=1) per condition, per pig (N=6) was analysed. Wound diameter measurement was used as a secondary measure of wound closure to avoid the measurement limitations associated with

digital photography and blocking of the wound border by the wound eschar. GraphPad Prism 6 (GraphPad Software) was used to conduct all statistical analysis in this thesis.

2.2.3.2 – Angiogenesis

Porcine tissue cryosections (section 2.2.1) were rinsed three times in PBS followed by a five-minute incubation in 1% sodium dodecyl sulfate (Bioshop Canada Inc.) in a humidified chamber at room temperature and rinsed a final three times in PBS. Sections were blocked using 10% horse serum (Thermo Fisher) in PBS for 30 minutes at room temperature in a humidified chamber followed by overnight incubation with Endoglin anti-CD105 antibody (1:100, Invitrogen) and anti-CD146 (1:500, Abcam) diluted in 10% horse serum (a full list of antibodies used in this thesis is presented in Appendix T). Negative controls were left in 10% horse serum overnight. The next day, tissues were rinsed three times, consecutively, in PBS, incubated with secondary antibodies [Alexa Fluor (AF) 488 GtαMs 1:100, AF 555 DkαRb 1:100, and Hoechst 33342 1:1000, Thermo Fisher] diluted in 10% horse serum for one hour at room temperature in a humidified chamber and then rinsed again three times in PBS. Coverslips were mounted using Immu-mount (Thermo Fisher) and sealed with CoverGrip Coverslip Sealant (Biotium). Mounted sections were stored at 4°C overnight in a dry container to allow the mounting medium to dry. Vascular structures were imaged using the appropriate filters of an Axio Observer Z.1 inverted microscope (Carl Zeiss). Blood-vessel density (number of blood vessels/mm²), percent wound tissue covered by vascular tissue, and average individual blood-vessel area were quantified with ImageJ color deconvolution and threshold particle analysis. Threshold values for the detection of fluorescence were set using negative control sections stained without primary antibodies (Appendix Q). One CD146+ immunofluorescent image (n=1) per condition, per pig (N=6) was analysed.

2.2.3.3 – Collagen Deposition

Extent of collagen deposition was visualized with Masson's Trichrome staining of cryopreserved tissues (Molecular Pathology, Robarts Research Institute). A hydroxyproline assay kit (Sigma-Aldrich) was used to quantify collagen content. Hydroxyproline is a highly conserved amino acid in collagen and therefore can be used as an indicator of collagen content. A ~10 mg sample was taken from each tissue sample (per condition, per

pig; N=6) and weighed before and after lyophilization with a VirTis Benchtop K freeze dryer (VirTis). Dry tissues were used in the experiment, and dry weight was used to standardize the final calculations of hydroxyproline content. Dry samples were minced with a scalpel and degraded in 400 μ L 6-M HCL at 120°C for three hours. After incubation, wounded and unwounded samples were diluted with 400 μ L and 800 μ L 6-M HCL, respectively. These dilutions were previously optimized in our lab to reduce the concentration of hydroxyproline from the collagen-dense tissues and enhance colorimetric differences in absorbance measurements between samples. Samples were centrifuged at 13,000 g for two minutes and 2- μ L supernatant (from samples and standards) was transferred in duplicate (n=2) to a 96 well transparent flat-bottom microplate. Wells were evaporated to dryness in a 60°C oven for one hour. 100 μ L/well chloramine T/oxidation buffer mixture (6:94 v/v) was added to each well and incubated at room temperature for five minutes. 100 μ L/well diluted DMAB reagent (DMAB concentrate: Perchloric Acid/Isopropanol, 1:1 v/v) was added and samples were incubated at 60°C for 90 minutes. Absorbance was measured using a Tecan² Safire fluorescent/colorimetric microplate reader (Tecan) at a wavelength of 560 nm. The absorbance value was converted to hydroxyproline content using a standard curve (Appendix G), and the different dilutions used for wounded and unwounded tissues after degradation with the 6-M HCL was considered.

2.3 – Results

2.3.1 – Wound Closure Kinetics

Representative images of the wounds from one pig for each treatment are shown at days 0, 8, 14, 21, and 28 post-wounding (Figure 2.3). Wound closure was reduced in the presence of BSA scaffolds when compared to empty control wounds between days 8 and 15 (Figure 2.4A). No differences were observed between any other treatment conditions. All wounds achieved over 94% closure by day 28. Individual 28-day wound closure kinetics for each pig are presented in Figure 2.5 as an indication of the variability in wound closure measurements between pigs. As a secondary measure of wound closure, day 28 wound diameter was measured as the distance between wound borders, parallel to the subcutaneous tissue (Figure 2.4B). No significant differences were observed in wound

diameter between scaffold conditions and empty wounds. Wound closure results including GAL3 data, are presented in Appendix A/B

2.3.2 – Angiogenesis

Our previous work has shown that POSTN/CCN2 electrospun scaffolds can rescue delayed healing in db/db mice and increase neovessel tubule formation. Further investigation of a POSTN/CCN2 scaffold in a 28-day healthy porcine model of cutaneous wound healing revealed no differences in angiogenic growth. CD146 (a cell surface glycoprotein used as a marker for the endothelial cell lineage) positive endothelial tissue was visualized with immunofluorescent staining. Representative cross-sectional images of the wound bed vasculature from one pig at day 28 post-wounding are shown with outlines indicative of blood-vessel measurements by ImageJ software (Figure 2.6). Blood-vessel density, percent wound-tissue area covered by vascular tissue, and the average area of individual blood vessels (blood-vessel area) were calculated with CD146 fluorescent images and ImageJ software (Figure 2.7A-C). No differences were observed in any of these measurements. Day 28 blood-vessel density, percent area, and individual area are analyzed independently per pig in Appendix N. Endoglin/CD105 (a type I membrane glycoprotein which is part of the TGF- β receptor complex, and is upregulated and expressed on the surface of endothelial cells after cutaneous tissue injury) positive endothelial tissue was also visualized with immunofluorescent staining (Figure 2.8) to demonstrate the vascular phenotype of porcine cutaneous wound tissue 28 days post-wounding. Angiogenic results including GAL3 data, are presented in Appendix C-E.

2.3.3 – Collagen Deposition

To determine extent of collagen deposition in porcine cutaneous wound tissue following full-thickness excisional wounding, wounded and unwounded sections were stained with Masson's trichrome (Figure 2.9). At day 28, the wound margin is visible as termination of the pre-existing thick collagen fibers in the connective tissue of unwounded dermis. Masson's Trichrome staining showed no distinction in collagen content between wounded and unwounded tissues. Hydroxyproline content quantified with a Hydroxyproline Assay Kit was used as an indicator of collagen deposition (Figure 2.10). No significant differences

were observed. Collagen deposition results including GAL3 data, are presented in Appendix F.

Figure 2. 3 – Representative images of wound closure from day 0 to day 28 in a porcine full-thickness cutaneous wound-healing model. Age/sex matched Yorkshire pigs (N=5) were subject to four full-thickness excisional wounds per animal (2 cm in diameter). Wounds received either no treatment, gelatin scaffold containing BSA, or gelatin scaffold containing POSTN and CCN2. Representative images of the four treatment conditions from one pig are shown at days 0, 8, 14, 21 and 28. Scale bar = 1 cm.

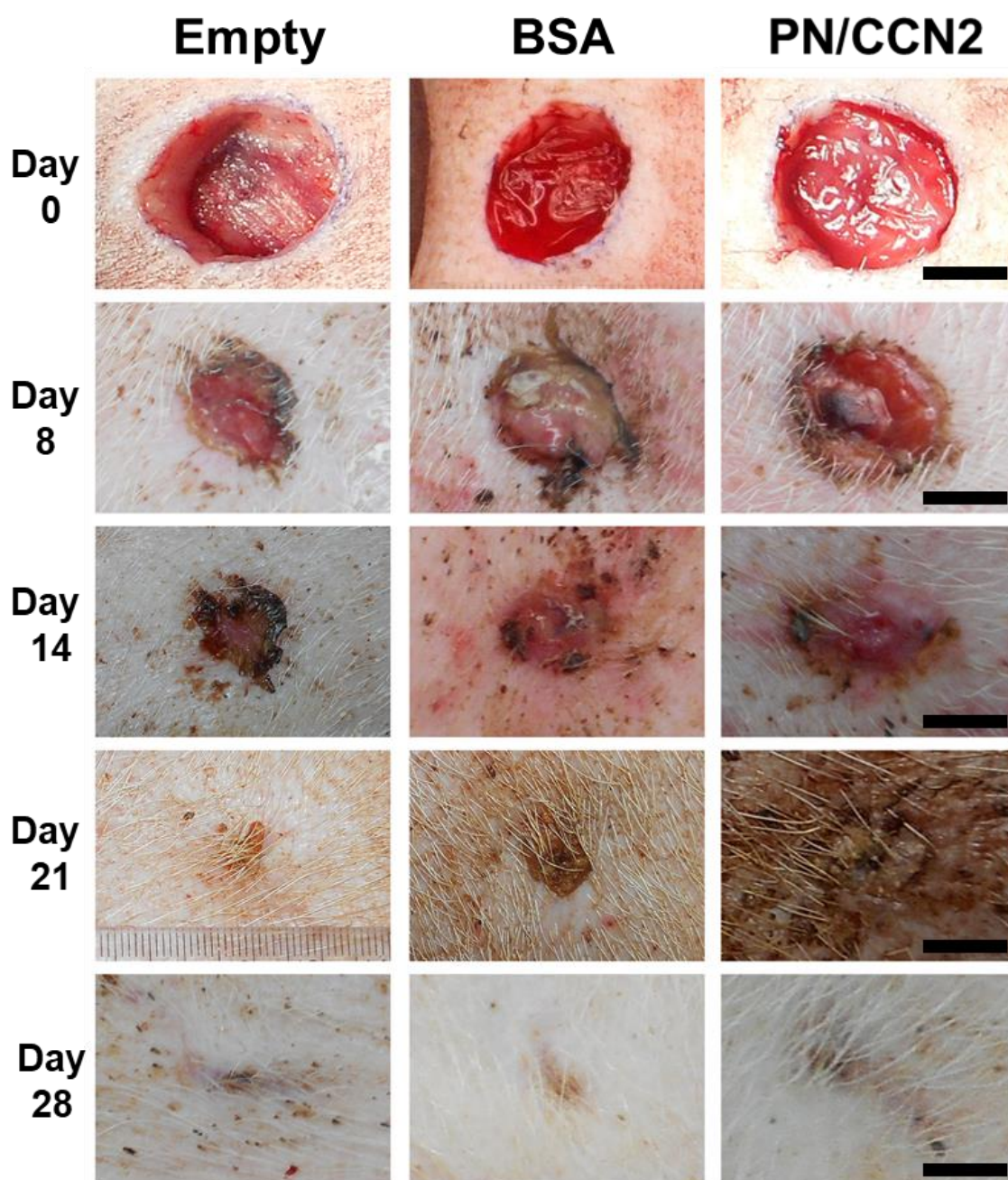


Figure 2. 4 – 28-day wound closure kinetics after full-thickness cutaneous wounding in a porcine model. Wound area was measured at each timepoint using ImageJ software to calculate closure kinetics. **A)** Data are presented as percent of original wound area closed. Wound closure was significantly slowed by BSA scaffolds when compared to empty control wounds from day 8 to day 15. $N=3/5$, $n=1$, two-way ANOVA, Tukey post-test for multiple comparisons, $p<0.05$. **B)** No differences in wound diameter were observed at day 28 post-wounding. One-way ANOVA, Tukey post-test for multiple comparisons, * = $p < 0.05$, ** = $p < 0.01$, *** = $p < 0.001$. Data presented as mean \pm SD.

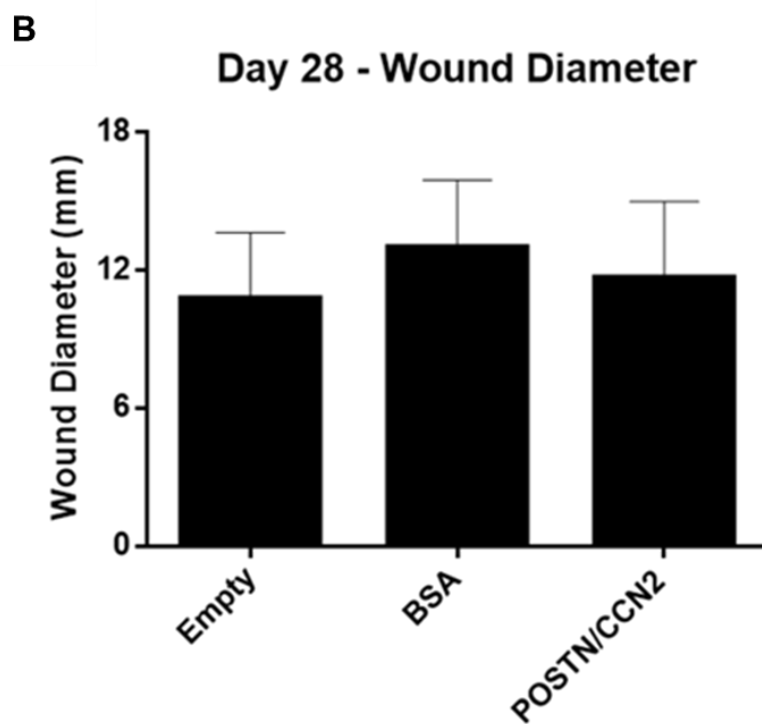
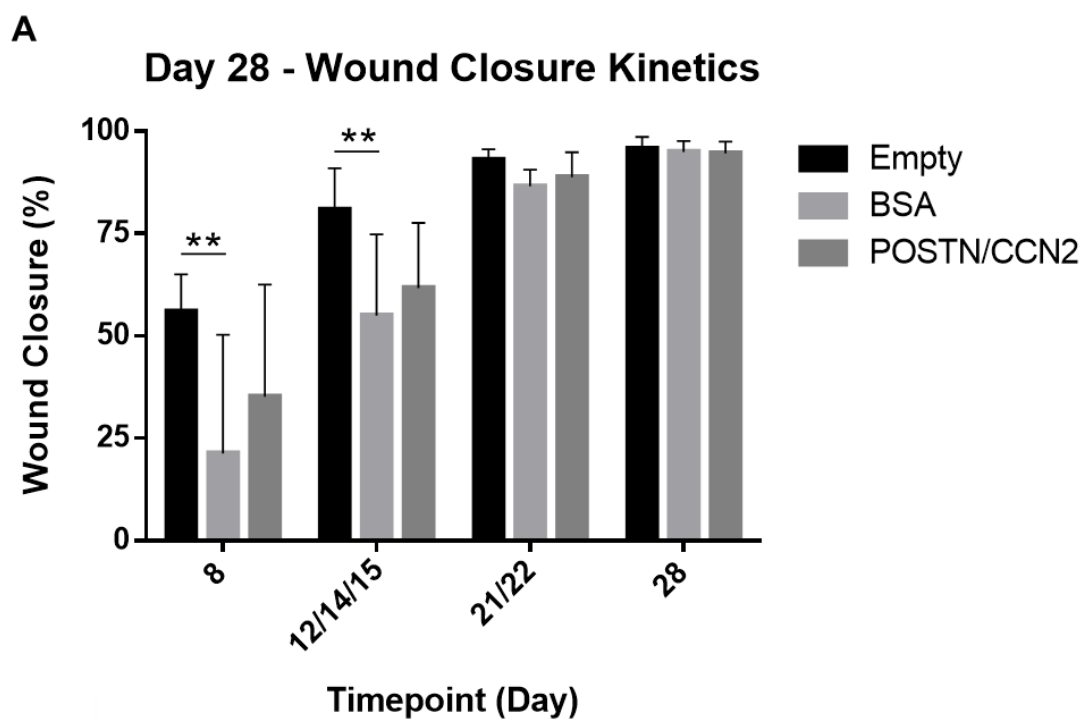


Figure 2. 5 – Individual 28-day wound closure kinetics after full-thickness cutaneous wounding in a porcine model. Wound area was measured at each timepoint using ImageJ software to calculate closure kinetics. **A-E)** Data are presented as percent of original wound area closed. Individual closure kinetics data are presented for each individual pig to show the variability in wound area measurements due to inter-animal variability and limitations of the measurement method associated with wound eschar blocking the wound edge in digital images. Timepoints varied for each pig due to external control of experimental procedures by the UWO Animal Care and Veterinary Services team. Timepoints are outlined in section 2.2.3.1. n=1.

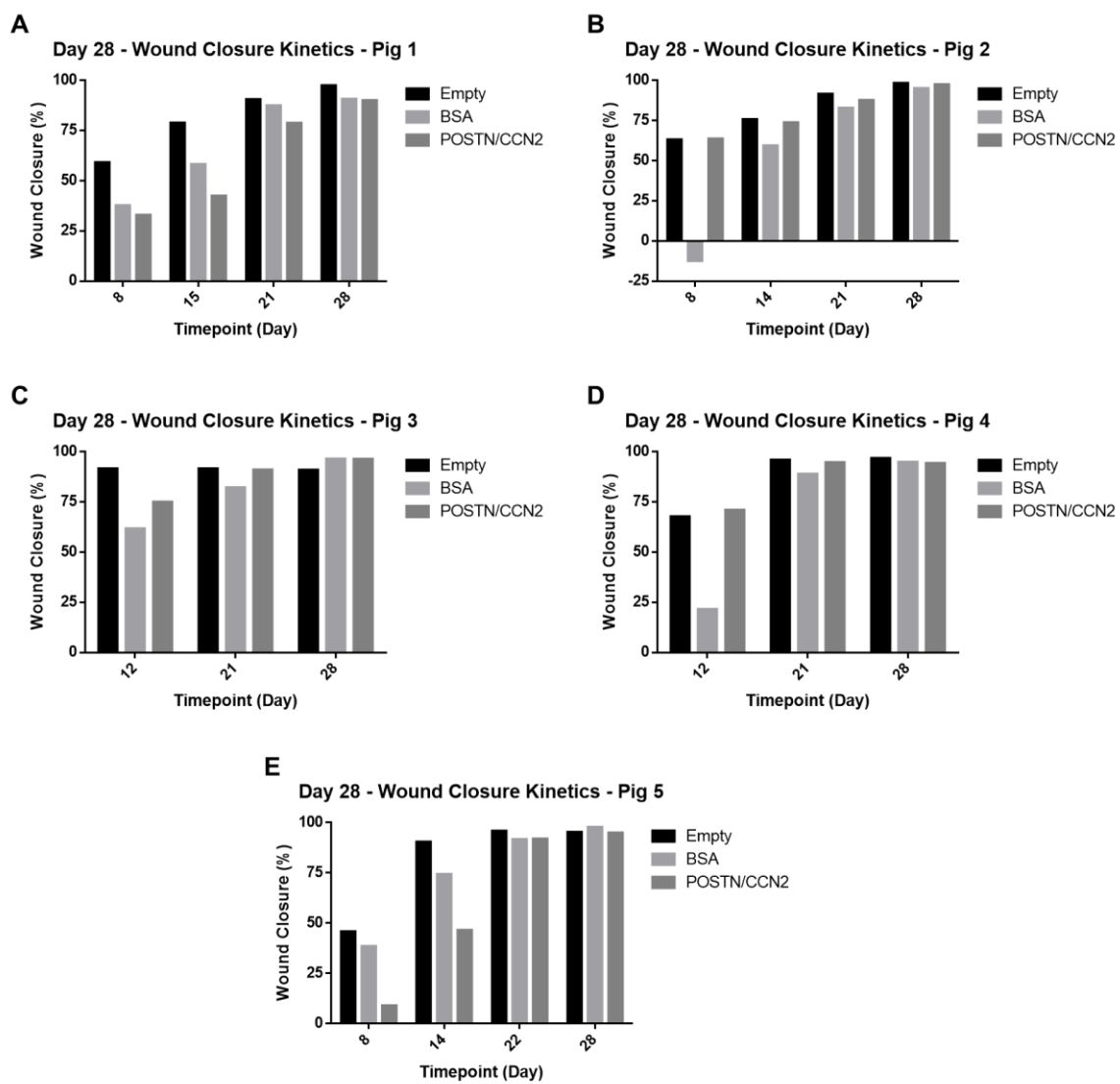


Figure 2. 6 – Representative images of vascular growth 28 days post-wounding in a porcine full-thickness cutaneous wound model. Representative cross-sectional images of the wound bed vasculature from one pig at day 28 post-wounding are shown. Endothelial tissue was visualized with CD146 immunofluorescent staining. Scale bar = 200 μ m.

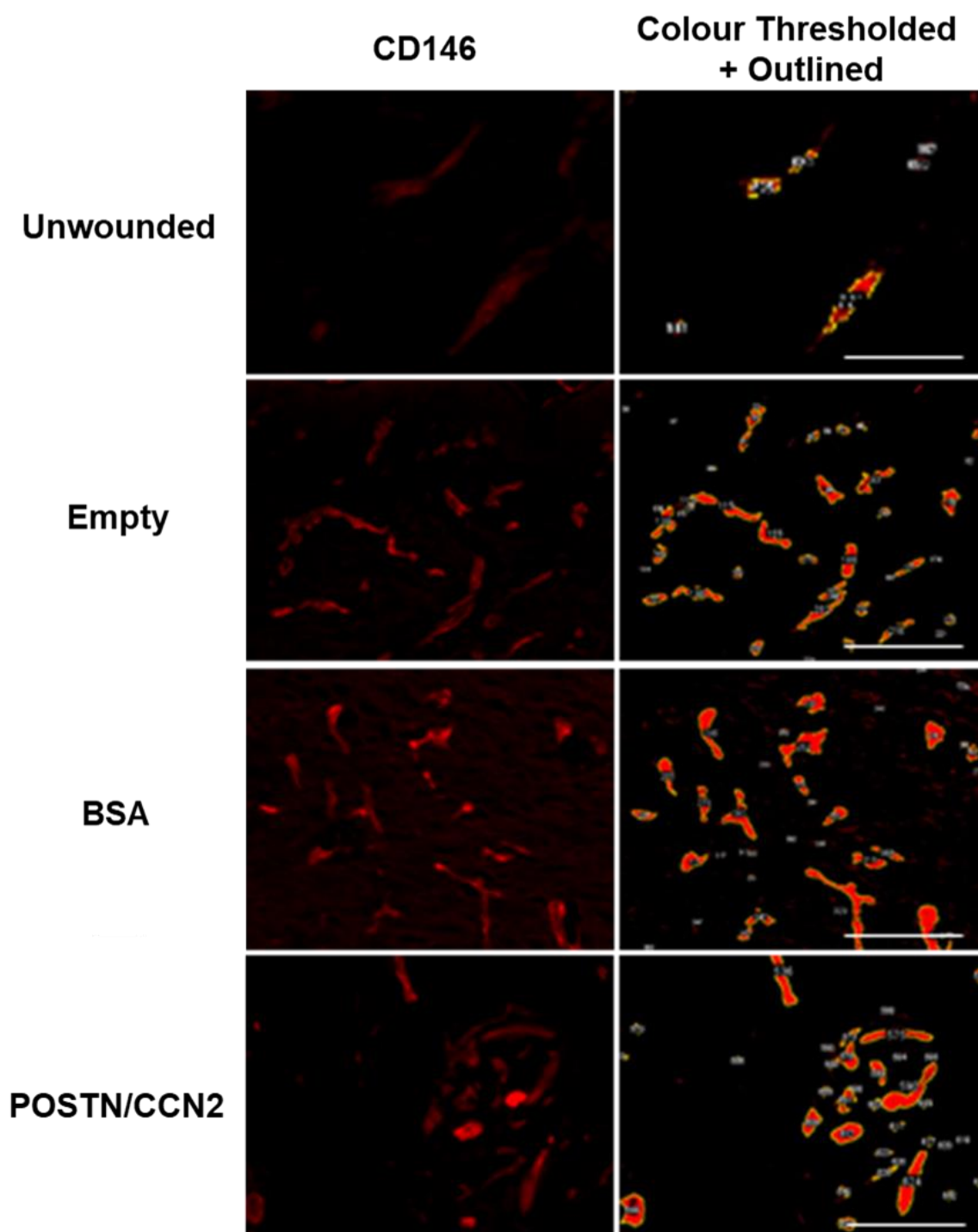


Figure 2. 7 – Effect of biomimetic scaffolds on angiogenesis 28 days post-wounding in a porcine full-thickness cutaneous wound-healing model. Using CD146 as a marker of endothelial tissue in porcine cryosections, blood-vessel density (**A**), percent wound-tissue area covered by vascular tissue (**B**), and individual blood-vessel area (**C**) were quantified with ImageJ's colour deconvolution and threshold particle analysis tools. No differences were observed. N=6, n=1, one-way ANOVA, Tukey post-test for multiple comparisons, $p < 0.05$. Data presented as mean \pm SD. Angiogenic data are presented independently per pig in Appendix N.

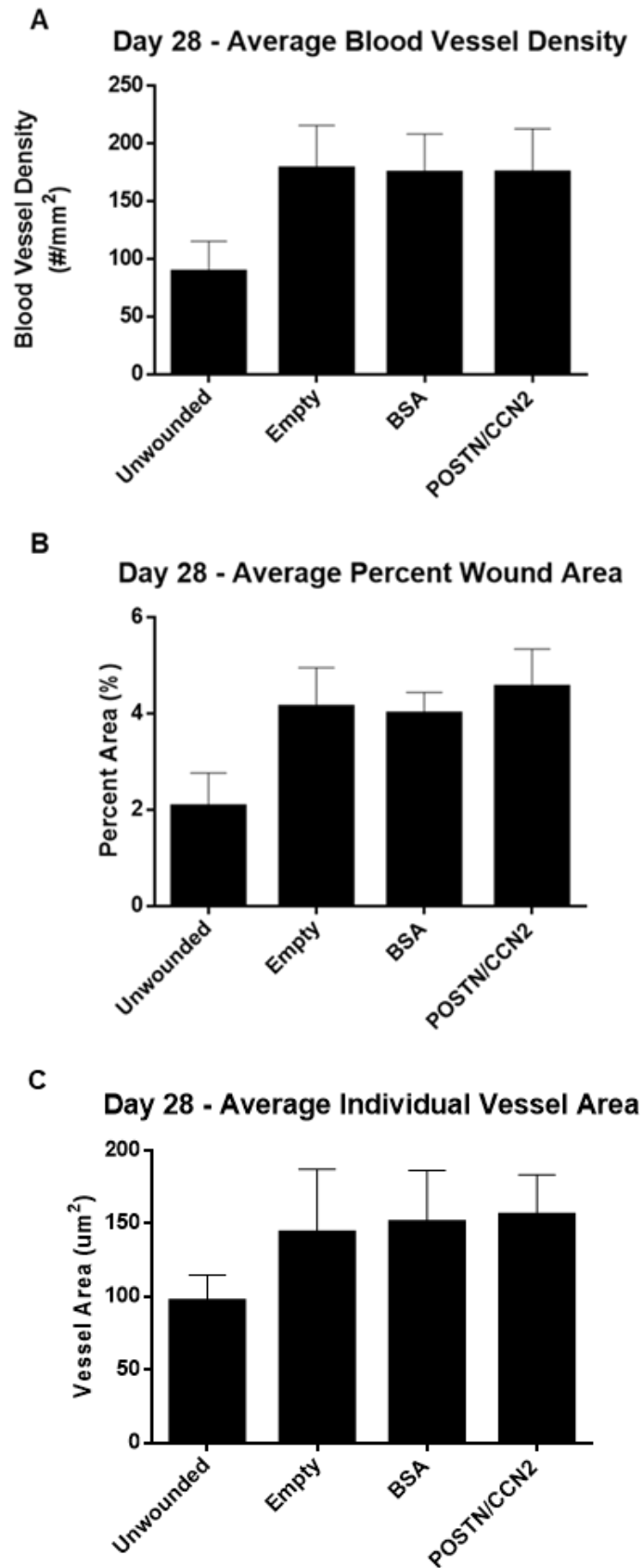


Figure 2. 8 – Angiogenic phenotype in porcine wound tissue 28 days post-wounding. Fluorescent immunohistochemistry of porcine wound tissue 28 days post-wounding revealed angiogenic phenotype after staining for endothelial markers CD146 and CD105/endoglin. Representative images from one pig are shown. Each set of images include a section of epidermal and superficial dermal layers. CD146 (red), CD105/Endoglin (green) and an overlay including CD146, CD105 and Hoechst stained cellular nuclei (blue) are presented. Scale bar = 100 μ m.

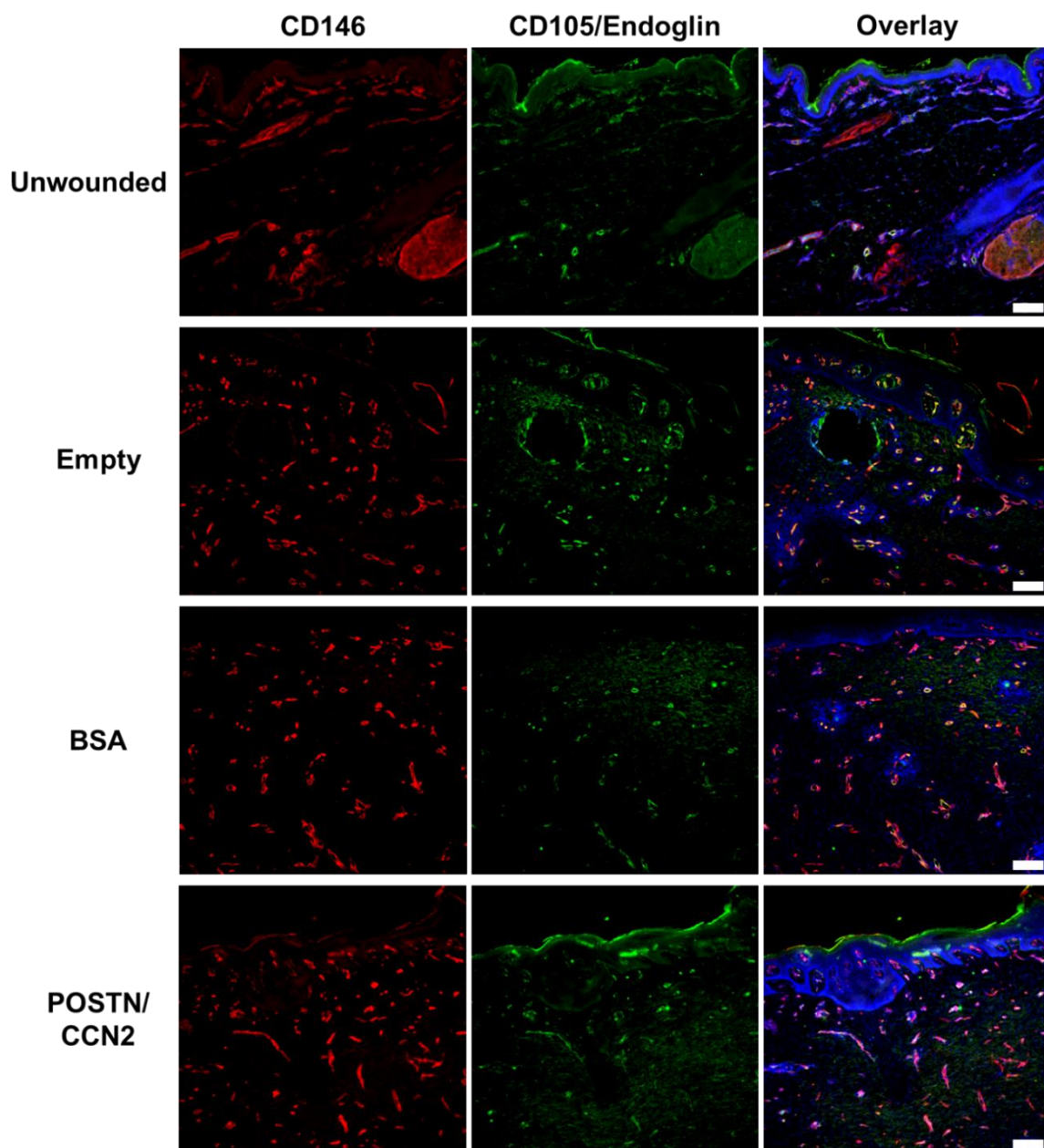
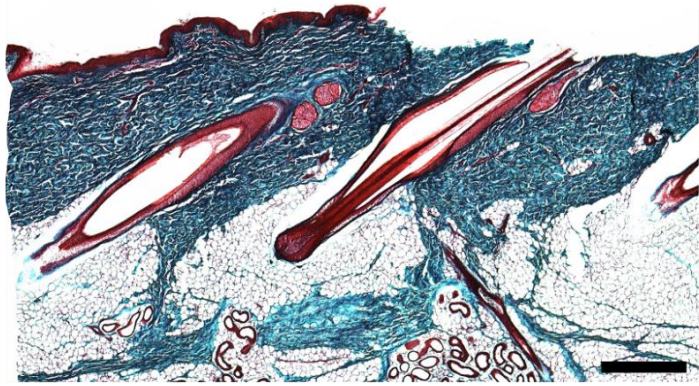
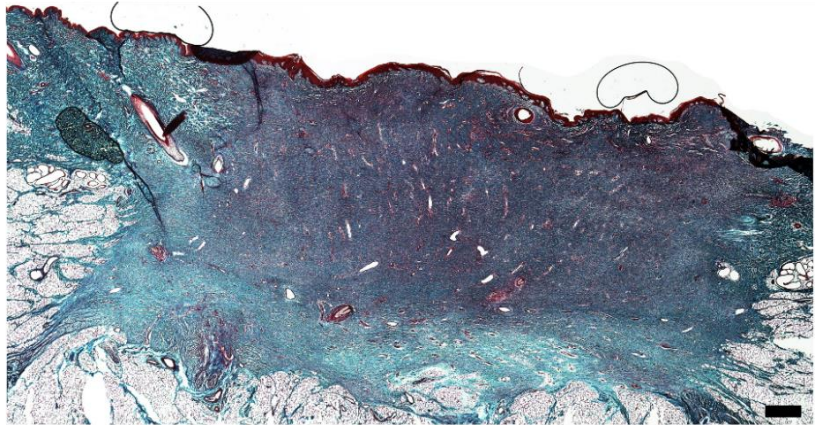


Figure 2. 9 – Effect of biomimetic scaffolds on collagen deposition 28 days post-wounding in a porcine full-thickness cutaneous wound model. Representative cross-sectional images of collagen deposition 28 days post-wounding visualized with Masson's Trichrome staining. Connective tissues (collagen) are stained blue; muscle, erythrocytes and cytoplasm are stained red; and nuclei are stained black. Scale bar = 1 mm.

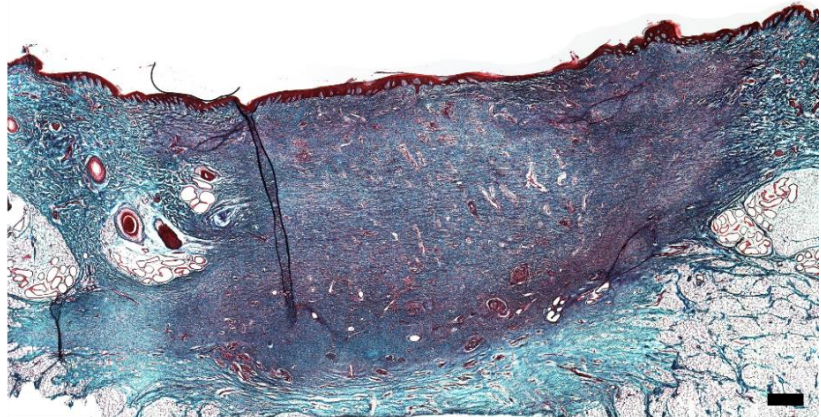
Unwounded



Empty



BSA



POSTN/CCN2

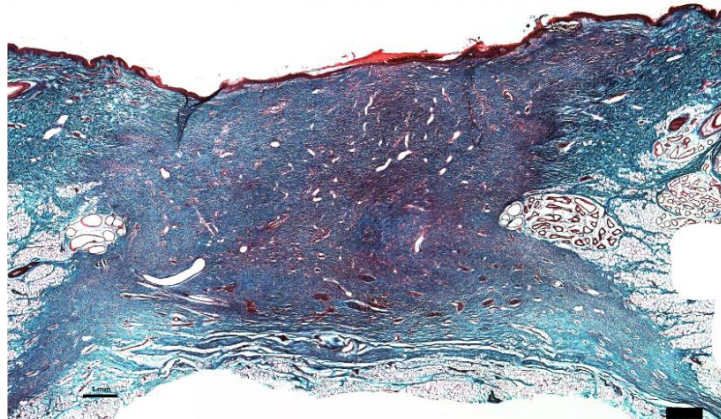
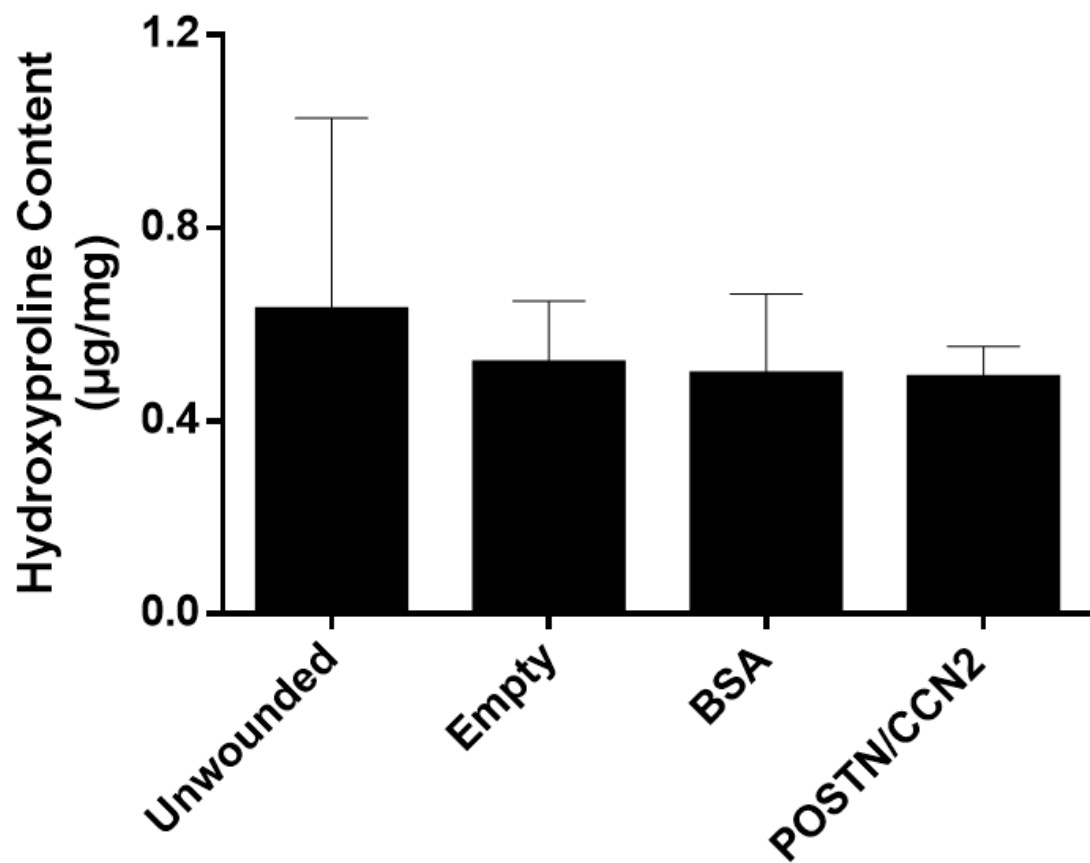


Figure 2. 10 – Hydroxyproline content as an indicator of collagen deposition 28 days post-wounding in a porcine full-thickness cutaneous wound model. Hydroxyproline content was quantified using a Hydroxyproline Assay Kit and normalized based on the dry weight of degraded tissue. No significant differences were observed. N=6, n=2, one-way ANOVA, Tukey post-test for multiple comparisons, $p < 0.05$ Data presented as mean \pm SD.

Day 28 Hydroxyproline Content



2.4 – Discussion

Previous development of an electrospun POSTN/CCN2 collagen scaffold significantly improved angiogenesis and wound closure in db/db mice (Hamilton lab, In Review, J Tissue Eng). The present study aimed to investigate the angiogenic and reparative effects of POSTN/CCN2 scaffolds in a healthy porcine model of cutaneous wound healing.

Wound closure was inhibited from day 8 to day 15 in BSA scaffold treated wounds, but not POSTN/CCN2 scaffold treated wounds compared to empty controls (Figure 2.4A). Gelatin has been shown to elicit a foreign body response against implanted biomaterials [21]. Delayed closure in response to the BSA scaffold treatments may be a result of the foreign body response against gelatin. Both POSTN and CCN2 promote ECM deposition, fibrogenesis, and contraction by proliferating myofibroblasts [10, 12, 14, 22] and POSTN has been shown to enhance keratinocyte proliferation and re-epithelialization [10]. Therefore, POSTN/CCN2 scaffolds may have enhanced the wound repair process following a foreign body response to the scaffold, resulting in no differences between POSTN/CCN2 scaffolds and empty wounds between days 8 to 15. Future work is required to characterize the cellular populations present at day 28 to determine the extent to which POSTN/CCN2 scaffolds may have contributed to wound contraction or re-epithelialization. POSTN has been associated with scar formation. Day 3 upregulation of POSTN following wounding has been shown to peak on day 7 and declines throughout early remodelling to mediate angiogenesis and fibroplasia throughout the wound-healing process in a mouse model [13]. However, overexpression of POSTN in hypertrophic and keloid scarring induces excessive fibroblast proliferation and contractility [23]. Therefore, future work should confirm the effect of POSTN/CCN2 scaffolds on wound closure *in vivo* and characterize the optimal POSTN/CCN2 concentration to balance fibroplasia with fibrosis. Wound closure of all conditions was equivalent by day 28 (all wounds were >94% closed) indicating no lasting negative effects of the scaffolds on the rate of wound closure. This effect demonstrates that in a porcine model, the scaffolds appear biocompatible, with no foreign body response evident in Masson's Trichrome images at 28 days post-implantation. Individual 28-day wound closure kinetics for each pig are presented in Figure 2.5 as an indication of the variability in wound closure measurements, and the high variability in BSA and POSTN/CCN2 scaffold conditions at days 8 and 12/14/15. This variability can

be attributed to limitations associated with the porcine model, including wound eschar blocking the wound border and complicating wound area measurements (as can be seen at day 14 in Figure 2.3), and inter-animal variability.

POSTN and CCN2 have been shown to stimulate vascular smooth muscle cell migration, endothelial cell proliferation and chemotaxis [11, 15, 16], as well as up-regulate pro-angiogenic factors such as VEGF-A/C [17, 18] to promote neovascular tubule formation. Therefore, we anticipated POSTN/CCN2 scaffolds would enhance vascular growth. Vascular size and density in wounded tissues relative to unwounded tissues did not change. Quantification of blood-vessel density, percent wound area covered by vascular tissue, and individual blood-vessel area indicated no significant effects of BSA or POSTN/CCN2 scaffolds. This result however, does not eliminate the possibility that scaffold treatments could have influenced angiogenic growth earlier in the healing process. During inflammation, hypoxia and cellular signalling initiate angiogenesis with robust endothelial cell proliferation, migration and nascent vessel formation [24]. Extensive sprouting and branching results in an immature and poorly perfused vascular network [25]. In the later stages of healing, vascular regression occurs as extraneous vessels are removed and mural cell coverage yields a stable, well-perfused vascular network [26]. Therefore, vascular regression may have reduced the impact of POSTN/CCN2 scaffolds on angiogenic growth observed at day 28.

Elliott et al. demonstrated rescued wound closure and enhanced angiogenic growth in db/db murine wounds treated with POSTN/CCN2 collagen scaffolds (Hamilton lab, In Review, J Tissue Eng). However, our results indicate no effects on closure or angiogenesis by the POSTN/CCN2 scaffolds. This difference could be attributed to the acute state of wound healing in the healthy pigs used in this study. The rapid rate of healing in healthy individuals may reduce treatment effects observed in pathological situations [27]. In addition, normal expression levels of POSTN, CCN2, and other functional molecules in the porcine wounds may have reduced or eliminated the influence of the POSTN/CCN2 scaffold. The porcine model of cutaneous wound healing was chosen for this study because it is considered the gold-standard for cutaneous wound healing research due the physiological and anatomical similarities between human and pig skin [28]. Therefore, the lack of a physiologically

significant response may not eliminate the POSTN/CCN2 scaffold as an appropriate treatment for chronic wound healing. Instead, conflicting evidence presented by Elliot et al. and the 28-day porcine study presented here may highlight how cutaneous wound-healing research conducted in murine models may not be easily translatable to large animal models. However, this does not eliminate the possibility that the scaffolds are effective in pathological situations as seen in the db/db mice, and may still function in human non-healing wounds.

The primary granulation tissue in cutaneous wounds is composed of fibronectin secreted by fibroblasts, which is later remodeled and replaced by fibrillar collagen I and III [29]. Assessment of collagen content in porcine cutaneous wounds at 28-days post-wounding showed similar results irrespective of scaffold treatment. Quantification of hydroxyproline content, as an indicator of collagen deposition, supported the qualitative findings by Masson's trichrome that no differences in content between groups was observed (Figure 2.10). Although the scaffolds contained gelatin, as the empty wounds showed similar hydroxyproline content, it is unlikely that the presence of gelatin influenced the results. Indeed, no scaffolds were evident in Masson's Trichrome images indicating degradation or ejection by 28-days. In previous studies in db/db mice, the scaffolds were observed to be above the granulation tissue and were eventually shed with the eschar (Hamilton lab, In Review, J Tissue Eng).

Finally, the effect of POSTN/CCN2 scaffolds on angiogenesis, collagen deposition, and other measures of wound repair (e.g., extent of re-epithelialization) may not be evident at 28 days. Differences in the healing process could have occurred but were not evident in the wound tissues at 28 days post-wounding. Therefore, a follow-up study at an earlier timepoint was necessary to investigate the effect of POSTN/CCN2 scaffolds during the inflammatory and proliferative stages of wound healing. A separate porcine study involving 6 different pigs, and a 7-day endpoint, was included in the original protocol for this study. However, complications associated with the pig's size and health forced the 7-day timepoint to be removed. The 7-day follow-up study was conducted a year later and is presented in Chapter 3.

2.5 – Conclusions

Wound closure kinetics, angiogenic growth, and collagen deposition in wounds treated with POSTN/CCN2 scaffolds indicate no negative effects of the electrospun scaffolds on the healing process at day 28 in a porcine model. Future research with a larger sample size and at earlier timepoint(s) is necessary to validate the current findings and to investigate the effect of POSTN/CCN2 scaffolds during inflammation and proliferation.

2.6 – References

1. Kanitakis, J., *Anatomy, histology and immunohistochemistry of normal human skin*. European journal of dermatology : EJD, 2002. **12**(4): p. 390-9; quiz 400-1.
2. Eming, S.A., P. Martin, and M. Tomic-Canic, *Wound repair and regeneration: mechanisms, signaling, and translation*. Sci Transl Med, 2014. **6**(265): p. 265sr6.
3. Canadian Diabetes Association. *Diabetes in Canada*. 2016 [cited 2017 February 02, 2017]; Available from: <https://www.diabetes.ca/getmedia/513a0f6c-b1c9-4e56-a77c-6a492bf7350f/diabetes-charter-backgrounder-national-english.pdf.aspx>.
4. Alavi, A., et al., *Diabetic foot ulcers: Part I. Pathophysiology and prevention*. J Am Acad Dermatol, 2014. **70**(1): p. 1 e1-18; quiz 19-20.
5. Bekara, F., et al., *New techniques for wound management: A systematic review of their role in the management of chronic wounds*. Arch Plast Surg, 2018. **45**(2): p. 102-110.
6. Bello, Y.M., A.F. Falabella, and W.H. Eaglstein, *Tissue-engineered skin. Current status in wound healing*. Am J Clin Dermatol, 2001. **2**(5): p. 305-13.
7. Dong, Y., et al., *Degradation Behaviors of Electrospun Resorbable Polyester Nanofibers*. Tissue Engineering Part B: Reviews, 2009. **15**(3): p. 333-351.
8. Hassiba, A.J., et al., *Review of recent research on biomedical applications of electrospun polymer nanofibers for improved wound healing*. Nanomedicine (Lond), 2016. **11**(6): p. 715-37.
9. Bornstein, P. and E.H. Sage, *Matricellular proteins: extracellular modulators of cell function*. Current Opinion in Cell Biology, 2002. **14**(5): p. 608-616.
10. Nishiyama, T., et al., *Delayed re-epithelialization in periostin-deficient mice during cutaneous wound healing*. PLoS One, 2011. **6**(4): p. e18410.
11. Li, G., et al., *Periostin mediates vascular smooth muscle cell migration through the integrins α v β 3 and α v β 5 and focal adhesion kinase (FAK) pathway*. Atherosclerosis, 2010. **208**(2): p. 358-65.
12. Ontsuka, K., et al., *Periostin, a matricellular protein, accelerates cutaneous wound repair by activating dermal fibroblasts*. Exp Dermatol, 2012. **21**(5): p. 331-6.
13. Walker, J.T., et al., *Periostin as a Multifunctional Modulator of the Wound Healing Response*. Cell and tissue research, 2016. **365**(3): p. 453-465.
14. Brigstock, D.R., *Connective tissue growth factor (CCN2, CTGF) and organ fibrosis: lessons from transgenic animals*. J Cell Commun Signal, 2010. **4**(1): p. 1-4.
15. Babic, A.M., et al., *CYR61, a product of a growth factor-inducible immediate early gene, promotes angiogenesis and tumor growth*. Proc Natl Acad Sci U S A, 1998. **95**(11): p. 6355-60.
16. Kubota, S. and M. Takigawa, *CCN family proteins and angiogenesis: from embryo to adulthood*. Angiogenesis, 2007. **10**(1): p. 1-11.
17. Dean, R.A., et al., *Identification of candidate angiogenic inhibitors processed by matrix metalloproteinase 2 (MMP-2) in cell-based proteomic screens: disruption of vascular endothelial growth factor (VEGF)/heparin affinity regulatory peptide (pleiotrophin) and VEGF/Connective tissue growth factor angiogenic inhibitory complexes by MMP-2 proteolysis*. Mol Cell Biol, 2007. **27**(24): p. 8454-65.

18. Inoki, I., et al., *Connective tissue growth factor binds vascular endothelial growth factor (VEGF) and inhibits VEGF-induced angiogenesis*. *Faseb j*, 2002. **16**(2): p. 219-21.
19. Kular, L., et al., *The CCN family: a new class of inflammation modulators?* *Biochimie*, 2011. **93**(3): p. 377-88.
20. Zha, Z., et al., *Fabrication of gelatin nanofibrous scaffolds using ethanol/phosphate buffer saline as a benign solvent*. *Biopolymers*, 2012. **97**(12): p. 1026-36.
21. Yu, T., et al., *Temporal and spatial distribution of macrophage phenotype markers in the foreign body response to glutaraldehyde-crosslinked gelatin hydrogels*. *J Biomater Sci Polym Ed*, 2016. **27**(8): p. 721-42.
22. Elliott, C.G., et al., *Periostin modulates myofibroblast differentiation during full-thickness cutaneous wound repair*. *J Cell Sci*, 2012. **125**(Pt 1): p. 121-32.
23. Crawford, J., et al., *Periostin induces fibroblast proliferation and myofibroblast persistence in hypertrophic scarring*. *Experimental Dermatology*, 2014. **24**(2): p. 120-126.
24. Wietecha, M.S., W.L. Cerny, and L.A. DiPietro, *Mechanisms of vessel regression: toward an understanding of the resolution of angiogenesis*. *Curr Top Microbiol Immunol*, 2013. **367**: p. 3-32.
25. Bluff, J.E., et al., *The microcirculation in acute murine cutaneous incisional wounds shows a spatial and temporal variation in the functionality of vessels*. *Wound Repair Regen*, 2006. **14**(4): p. 434-42.
26. Urao, N., et al., *MicroCT angiography detects vascular formation and regression in skin wound healing*. *Microvascular research*, 2016. **106**: p. 57-66.
27. Wilhelm, K.P., D. Wilhelm, and S. Bielfeldt, *Models of wound healing: an emphasis on clinical studies*. *Skin Res Technol*, 2017. **23**(1): p. 3-12.
28. Sullivan, T.P., et al., *The pig as a model for human wound healing*. *Wound Repair Regen*, 2001. **9**(2): p. 66-76.
29. Kurkinen, M., et al., *Sequential appearance of fibronectin and collagen in experimental granulation tissue*. *Lab Invest*, 1980. **43**(1): p. 47-51.

Chapter 3

Design and Validation of a Matricellular Protein-Loaded Electrospun Scaffold Containing Encapsulated Fibroblast Growth Factor 9 in a Porcine Model of Cutaneous Wound Healing

3.1 – Introduction

In recent years, the use of electrospinning techniques has gained increasing interest for the fabrication of biomaterials. The advantage of electrospun scaffolds is that they exhibit morphological and size similarities to native extracellular matrix, with the potential to increase bioactivity through the incorporation of bioactive factors. The application of electrospinning has great potential to promote wound healing and skin regeneration through development of granulation tissue-mimetic scaffolds, which is the focus of this chapter [1]. However, with respect to growth-factor delivery, suitable release systems must be developed to overcome issues associated with incorporated bioactive factors released into a proteolytic *in vivo* environment where they are rapidly degraded [2-4]. Emulsion electrospaying can be used to fabricate core-shell microspheres with an outer polymer shell and inner colloid core. The polymer shell protects internalized bioactive factors that diffuse through the porous shell to provide sustained release of the factor temporally. Poly(lactic-co glycolic acid) (PLGA) is a biocompatible, biodegradable copolymer that has been used extensively in the development of electrospayed core-shell microspheres for targeted drug delivery. The physicochemical properties of PLGA are tunable based on its chemical composition [2, 5]. In previous work, POSTN/CCN2 scaffolds rescued delayed healing and supported vascular growth in db/db mice. However, a full recovery of wild-type wound-closure rates did not occur, and the vascular growth was composed of incomplete tubule formation and an immature vascular bed (Hamilton lab, In Review, J Tissue Eng). Therefore, although these results are promising, stabilization of developing vasculature could be improved. One candidate factor is fibroblast growth factor 9 (FGF9), which has been shown to promote mural cell layering around neovasculature and stimulate

neointimal smooth muscle cell (SMC) proliferation to improve vascular stability, vasoreactivity, and reduce tissue hypoxia in murine renal tumours [6-8].

The aim of this study was to design and validate a novel electrohydrodynamic scaffold combining electrospun gelatin POSTN/CCN2 nanofibers with electrosprayed PLGA/FGF9 microspheres. It is hypothesized that addition of encapsulated FGF9 core-shell microspheres (FGF9 microspheres) to the POSTN/CCN2 scaffold will protect and sustain the release of FGF9. Released FGF9 will recruit mural cell populations to support the development of neovasculature forming in response to POSTN/CCN2. Enhanced vascular stability in response to released FGF9 will enhance oxygen and nutrient supply to promote regeneration and wound closure. The effect of FGF9 on cell populations involved in wound healing was also investigated.

3.2 – Materials and Methods

3.2.1 - *In Vitro* Effect of FGF9 on Cell Populations Involved in Wound Healing

3.2.1.1 – Isolation and Cell Culture of Primary Dermal Fibroblasts & NIH 3T3 Murine Embryonic Fibroblasts

All procedures involving human tissue were approved by the University of Western Ontario Review Board for Health Sciences Research Involving Human Subjects and the Lawson Health Research Institute. All studies were performed in accordance with the Declaration of Helsinki. Written informed consent was received from participants prior to inclusion in the study. Healthy skin was isolated following lower extremity amputations and was immediately transferred to DMEM supplemented with 10% fetal bovine serum (FBS) and 3% antimycotic-antibiotic (AA; Gibco). Hair was removed, and skin was divided into small sections with a scalpel before plating on cell culture plastic with DMEM (10% FBS; 3% AA). Skin was incubated at 37°C, 5% CO₂ in a CO₂ incubator (Sanyo Scientific) to allow fibroblasts to migrate and adhere to the culture surface. Primary dermal fibroblasts were frozen in liquid nitrogen at 80% confluence. NIH 3T3 murine embryonic fibroblasts and primary human dermal fibroblasts (HDFs) were cultured to American Type Culture Collection standard protocols.

HDFs and murine embryonic NIH 3T3 cells were cultured for two to three passages before use. Frozen cells were thawed and plated onto cell culture plastic with 10 mL DMEM [10% FBS; 1% AA, high serum media (HSM)] and incubated at 37°C with media changes every three days. During passaging and before experimental use, the cells were trypsinized (Trypsin-EDTA 0.5%; Gibco), counted with a Coulter Counter, and re-seeded.

3.2.1.2 - Scratch Assay

The migratory effect of FGF9 on HDFs was investigated using scratch assays. Primary HDFs from three different cell lines (M55H, F64H, M60H; N=3) were seeded in HSM at a concentration of 1.0×10^6 cells per well of a six-well plate and allowed to adhere during overnight incubation at 37°C. The following day, cells were incubated for two hours at 37°C with SFM supplemented with 10 µg/mL mitomycin-c (Sigma-Aldrich) to inhibit proliferation. After two PBS rinses, three parallel scratches were created with the end of a P10 pipet tip and cellular debris was washed away with another two PBS rinses. Media was changed with DMEM [2% FBS; 1% AA, low serum media (LSM)] ± 10 ng/mL FGF9 (Bio-Techne) and the six-well plates were positioned on the stage of an Axio Observer Z.1 inverted microscope. A temperature- and CO₂-controlled incubation chamber maintained appropriate conditions for cell survival (37°C, 5% CO₂). Phase-contrast images of migrating cells were captured in 20-minute intervals for 45 hours. ImageJ software was used to measure scratch area for percent scratch closure calculations at 3-, 6-, 9-, and 12-hour timepoints, at which time the scratches were nearly closed. Each experiment was repeated five times (n=5), with a single replicate per cell line, per condition.

3.2.1.3 - Chemotaxis Assay

The chemotactic effect of FGF9 on HDFs (three primary HDF cell lines - M55H, F64H, M60H; N=3) and NIH3T3 cells was investigated using the Cultrex® Cell Migration Assay kit (Trevigen). Cells were cultured to 80% confluence and serum starved in DMEM [0% FBS; 1% AA, serum free media (SFM)] for 24 hours. After the 24-hour starvation, HDFs were seeded in quadruplicate (n=4) at 2.5×10^4 cells in 50 µL SFM and one NIH3T3 murine embryonic fibroblast cell line (N=1) was seeded in nonuplicate (n=9) at 5.0×10^4 cells in 50 µL SFM per well of the 96 well chemotaxis migration plate. 150 µL of experimental media (SFM, HSM, or SFM + 1, 10, or 100 ng/mL FGF9) was added to the bottom culture

chamber. Cells were incubated and allowed to migrate through the $8 \mu\text{m}^2$ porous surface at 37°C for four hours. Following incubation, media from top and bottom chambers was aspirated and both the insert and culture chambers were washed with PBS. $100\text{-}\mu\text{L}$ calcein-AM dye in cell dissociation solution (1:833.3 v/v) was added to a black assay plate and the cell migration plate was assembled and allowed to incubate at 37°C for one hour. Fluorescence measurement was made by a fluorescence plate reader at a 485 nm excitation wavelength and a 520 nm emission wavelength. RFU was converted to cell number using standard curves (Appendix H/I) to determine migrated cell number.

Standard curve measurement occurred during the four-hour experimental incubation. Cells were recounted, resuspended in cell detachment solution and $50 \mu\text{L}$ of 5×10^5 cells/mL NIH3T3 or 274.5×10^3 cells/mL HDF cell solution was added in duplicate to a Greiner 96 well tissue-culture flat-bottom black plate. Cell solutions were serial diluted (0.5 dilution factor) and $50 \mu\text{L}$ was added in duplicate to an additional 10 wells. Two negative control wells were used with $50 \mu\text{L}$ cell dissociation solution and no cells. $50 \mu\text{L}$ cell dissociation solution and Calcein-AM dye (1:416.7 v/v) was added to each well and incubated at 37°C for 1 hour. Fluorescence measurement was made by a fluorescence plate reader at a 485 nm excitation wavelength and a 520 nm emission wavelength.

3.2.1.4 - Proliferation Assay

The pro-proliferative effect of FGF9 on HDFs (three primary HDF cell lines - M55H, F64H, M60H; N=3) and NIH3T3 murine embryonic fibroblasts was investigated using the CyQUANT® proliferation assay kit (Molecular Probes). Cells were grown to 80% confluence before seeding in quadruplicate (n=4) at a density of 500 cells/well in a 96 well transparent flat bottom microplate. HDFs were incubated for 24 hours in $150 \mu\text{L}$ LSM followed by a 24-hour incubation in SFM at 37°C . After the 24-hour starvation period, the serum-free media was replaced with $150 \mu\text{L}$ treatment media: LSM/HSM $\pm 1 \text{ ng/mL}$; $\pm 10 \text{ ng/mL}$; $\pm 100 \text{ ng/mL}$ FGF9. HDFs were cultured in treatment media for 1, 3, 5, or 7 days at 37°C . Half-media changes ($75 \mu\text{L}$) were performed every two days, between experimental timepoints. On days 1, 3, 5, and 7, the experimental wells were rinsed twice with PBS and the 96 well plates were frozen at -80°C . Fluorescent analysis was completed after the day seven experimental endpoint.

CyQUANT® reagents and experimental plates were warmed to room temperature and were analyzed one at a time for consistency. Working buffer (225 µL cell-lysis buffer diluted 20-fold and CyQUANT® GR dye diluted 400-fold, both in distilled water) was added to each well of the 96 well experimental plate and incubated for five minutes at room temperature, protected from light. 200 µL fluorescent working buffer was transferred to a Greiner 96 well tissue-culture flat black plate after the five-minute incubation and fluorescence was measured by a fluorescence plate reader at a 480 nm excitation wavelength and a 520 nm emission wavelength. RFU was converted to cell number using a standard curve (Appendix J).

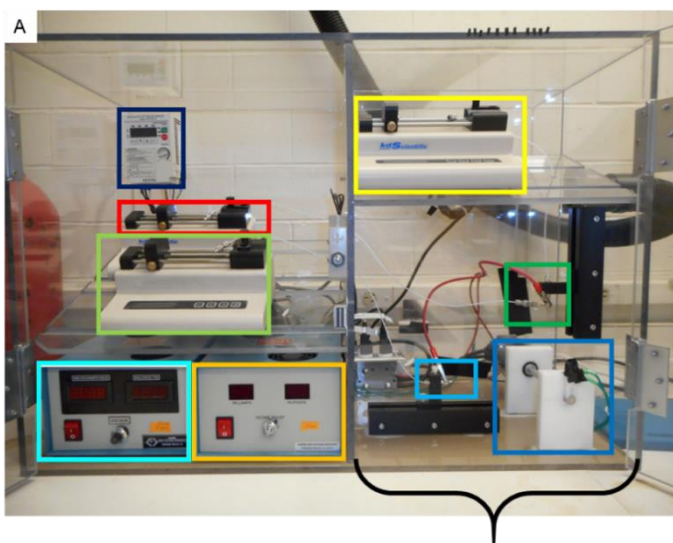
The standard curve was created from a cell pellet (5.0×10^5 cells) frozen on the first day of the experiment. The cell pellet was thawed and serially diluted (x10) in working buffer (dilution factor 0.67). After, 200 µL (2.5×10^5 cells/mL from 2 mL) was added in duplicate to a Greiner 96 well tissue culture flat black plate. Two negative control wells with no cells in the working buffer were included. Cells were incubated in working buffer for five minutes before fluorescence measurement. Fluorescence intensity was measured with a fluorescence plate reader at a 480 nm excitation wavelength and a 520nm emission wavelength.

3.2.2 – Scaffold Fabrication, Design, and Validation

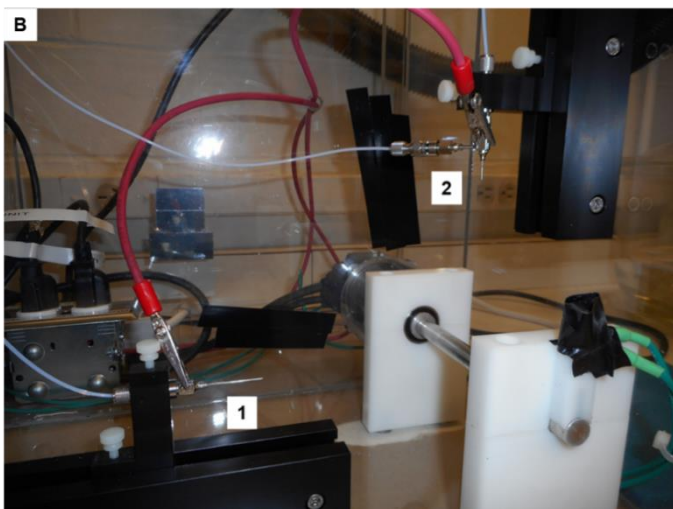
3.2.2.1 Nanofiber Electrospinning

Refer to section 2.2.2 for a description of the electrospinning protocol. For fiber diameter measurements, nanofibers were electrospun for five minutes and one 8 mm² circular piece of scaffold was taken with a biopsy punch (Integra Multex) for each of the three trials per parameter combination (Table 1). Nanofiber morphological characterization was necessary due to the installation of a new electrospinning system (Figure 3.1).

Figure 3. 1 – Electrohydrodynamic Setup. The new electrohydrodynamic system was installed prior to the experimentation presented in Chapter 3. The high-voltage power supplies and syringe pumps were isolated from the main electrohydrodynamic fabrication chamber with plexiglass. **A)** Overview of the electrohydrodynamic system capable of simultaneous electrospinning and electrospraying. Individual components are labelled. **B)** Magnified view of the electrohydrodynamic fabrication chamber showing the electrospinning needle (**B1**) and the coaxial electrospraying needle (**B2**).



Power Supply #1
 Power Supply #2
 PLGA Solution/Syringe Pump A
 FGF9 Solution/Syringe Pump B
 POSTN/CCN2 Solution/Syringe Pump C
 Coaxial Nozzle
 Electrospinning Needle
 Rotating Mandrel
 Mandrel Control Box



3.2.2.2 Scanning Electron Microscopy

An 8 mm² circular sample from each scaffold was taken using a biopsy punch and mounted on a 15 mm aluminum stub with adhesive carbon disc. Samples were osmium coated (OPC-80T, Filgen) and imaged using a LEO 1530 scanning electron microscope (Carl Zeiss) at an accelerating voltage of 3 kV. Five different images were taken at 7500x magnification for fiber diameter measurements and one descriptive image was taken at 1500x magnification to visualize overall scaffold morphology.

3.2.2.3 - Assessment of Fiber Morphology

Three separate trials were conducted per parameter combination outlined in Table 1. 30 fibers were measured from each of 5 SEM images per trial (n=150) using ImageJ software. Final analysis of fiber morphology combined the data collected for the 9 parameter combinations (N=9) with the variable in question held constant (e.g., rows 1-9 in Table 1 for the 0.3 mL/h flow rate – Figure 3.6A). Therefore, 4050 individual fibers were measured per parameter analysed in Figure 3.6 (n=4050).

The effect of polymer solution concentration (19 wt%, 21 wt% and 23 wt% gelatin solution) on scaffold morphology was also investigated, following the procedures described above, with the following exception: data analysis included the three separate trials (N=3) using the refined electrospinning parameters at each gelatin concentration tested. 30 fibers were measured for each of the 5 SEM images acquired per trial (n=150).

Additional information recorded during electrospinning, imaging and fiber diameter measurements included: fiber dispersion on the collection surface (measured distance between dense edges of deposited fibers), fiber density on the collecting surface (relative scale of 1-3, low to high), percentage total structures resembling fibers versus non-fibrous structures (webbing/ribbons), relative fiber diameter variation (minimal, slight, moderate, high), and general notes involving observed trends and unusual scaffold appearance. Inclusion criteria for refining the scaffold parameters included: fiber percentage $\geq 99\%$, fiber distribution on the collecting surface ≥ 5 cm, fiber density on the collecting surface of 3 (on a subjective scale of 1-3 indicating low to high fiber density), and fiber diameter distribution from scanning electron microscopy (SEM) images of minimal to slight. After exclusion of parameter combinations based on these criteria, the resultant parameters were

individually scored (flow rate, voltage and collector distance) and the parameters with the highest score were chosen for fabrication of the refined scaffold.

Table 1 – Electrospinning Parameter Combinations.

Gelatin Concentration (wt%)	Flow Rate (mL/h)	Voltage (kV)	Collector Distance (cm)
21	0.3	13	8
21	0.3	13	10
21	0.3	13	12
21	0.3	15	8
21	0.3	15	10
21	0.3	15	12
21	0.3	17	8
21	0.3	17	10
21	0.3	17	12
21	0.5	13	8
21	0.5	13	10
21	0.5	13	12
21	0.5	15	8
21	0.5	15	10
21	0.5	15	12
21	0.5	17	8
21	0.5	17	10
21	0.5	17	12
21	0.7	13	8
21	0.7	13	10
21	0.7	13	12
21	0.7	15	8
21	0.7	15	10
21	0.7	15	12
21	0.7	17	8
21	0.7	17	10
21	0.7	17	12
19	0.5	17	8
23	0.5	17	8

3.2.2.4 – Microsphere Coaxial Electrospinning

Figure 1.2 outlines the process of dual-stream electrospinning and coaxial electrospinning of nanofibrous scaffolds containing core-shell microspheres as was the original intent for fabrication of the novel electrohydrodynamic scaffold incorporating coaxial microspheres containing FGF9. The shell solution, consisting of 50:50 poly(DL-lactide-co-glycolide) with carboxylate end group (nominal, PLGA) (LACTEL Absorbable Polymers), was dissolved in dichloromethane (methylene chloride/CH₂Cl₂, Sigma-Aldrich) and loaded into a glass 1 cc syringe. Overnight agitation at room temperature was necessary for complete dissolution of PLGA in dichloromethane. For morphological assessment, the core solution consisted of 0.5 wt% heparin sodium salt (Alfa Aesar), 1 μg/mL BSA, and 0.5 wt% Type B Gelatin from bovine skin dissolved in PBS. Heparin was included to stabilize and protect FGF9 from denaturation, BSA to mimic the effects of FGF9 while limiting cost, and gelatin to increase solution viscosity to improve processability [9]. Microspheres electrospayed for morphological assessment will be referred to as PLGA/BSA microspheres. Gelatin dissolution in PBS required 37°C overnight incubation. The core solution was loaded into a plastic 1 cc syringe. Both core and shell solutions were fed into the inner and outer needles of a pre-built type-304 stainless steel coaxial needle (Figure 3.2, 100-10-COAXIAL-2822, ramé-hart instrument co.) by separate syringe pumps, respectively. The coaxial needle was connected to a high-voltage DC power supply producing an electric potential between the tip of the needle and the grounded stainless-steel mandrel, rotating constantly at 100 RPM (Figure 3.1). A piece of aluminum foil was secured to the rotating mandrel with electrical tape to collect the electrospayed microspheres.

Figure 3. 2 – Coaxial Needle dimensions. IID = inside needle inner diameter, IOD = inside needle outer diameter, OID = outside needle inner diameter, OOD = outside needle outer diameter. This figure is reproduced from: http://www.ramehart.com/pdf/coaxial_prebuilt.pdf.

1	Style	-2822
2	Inside Needle Gauge	A
	Inside Needle ID*	28g
	Inside Needle OD*	0.007
3	Outside Needle Gauge	0.014
	Outside Needle ID*	22g
	Outside Needle OD*	0.016
4	DIM C	0.028
5	DIM E	0
6	DIM F	25mm
7	Disassembly Option	10mm
	*ID and OD dimensions In Inch	Std

VIEW A
SCALE 2:1

IID = 0.1778 mm
IOD = 0.3556 mm
OID = 0.4064 mm
OOD = 0.7112 mm

NOTES:
 1. SHAFT MATERIAL: TYPE 304 STAINLESS STEEL.
 2. HUB MATERIAL: CHROME AND ZINC PLATED BRASS.
 3. NEEDLE TIP: PROBE POINT - SQUARE.
 4. PER VIEW A, INSIDE NEEDLE TO BE MADE CONCENTRIC TO OUTSIDE NEEDLE.
 5. PRE-BUILT NEEDLES ARE NOT CONFIGURABLE. IF YOU REQUIRE A DIFFERENT CONFIGURATION, PLEASE ORDER CUSTOM COAXIAL NEEDLE P/N 100-10-COAXIAL.

ramé-hart instrument co.			
19 RT 10 E, ST 11 - SUCCASUNNA - NJ 07857 PH 973-448-0305 ramehart.com			
TOLERANCES UNLESS OTHERWISE NOTED			
0,00±0,010in (0,25mm) 0,000±0,005in (0,127mm) ANGLES ±0°30'			
DRAWN BY	CHECKED	DATE	SCALE
CC	WA	30-JUL-14	NTS
PREBUILT COAXIAL NEEDLES			
TITLE	DWG NO	REV	
PREBUILT	100-10-COAXIAL-XXXX	C	

THIS WORKSHEET CAN BE FOUND AT
http://www.ramehart.com/pdf/coaxial_prebuilt.pdf

3.2.2.5 – Assessment of Microsphere Morphology

Morphological characterization of BSA microspheres followed the parameter combinations outlined in Table 2. SEM imaging was performed as described in section 3.2.2.2. Three trials per parameter combination (N=3) were electrospayed and five images were acquired at 1000x magnification for microsphere diameter measurements and one representational image was acquired at 400x magnification. ImageJ software was used to measure the diameter of 10 microspheres from each SEM image (n=50). Additional information recorded during electrospaying and imaging included: power supply micro-amperes, alternative material ejected onto tinfoil (e.g. droplets), material dispersion on the collecting surface (measured distance between dense edges of deposited material), material density on the collecting surface (relative scale 1-3, low to high), deposited microsphere density (relative scale 1-3, low to high), sphere to fiber ratio (relative scale 1-3, low to high), sphere diameter variability (relative scale 1-3, low to high), collapsed spheres (relative scale 1-3, low to high), large droplets or blotches on the collecting surface (relative scale 1-3, low to high), and general notes.

Table 2 – Electrospaying Parameter Combinations.

PLGA Concentration (wt%)	OUTER Flow Rate (mL/h)	INNER Flow Rate (mL/h)	Voltage (kV)	Collector Distance (cm)
5	1.0	0.1	15	16
5	1.0	0.1	15	18
5	1.0	0.1	15	20
5	1.0	0.1	17.5	20
5	1.0	0.1	20	20
5	1.0	0.1	22.5	20
5	1.0	0.1	15	20
5	1.0	0.2	15	20
5	1.0	0.3	15	20
5	0.3	0.1	15	20
5	0.65	0.1	15	20
5	1.0	0.1	15	20
4	1.0	0.1	15	20
5	1.0	0.1	15	20
6	1.0	0.1	15	20

3.2.2.6 - Microsphere Core-Shell Morphology

Rhodamine B Base (20 $\mu\text{g/mL}$, Sigma-Aldrich) was dissolved in the core solution immediately prior to electrospaying according to section 3.2.2.4. Microspheres were electrospayed with 1.0 mL/h outer solution flow rate, 0.1 mL/h inner solution flow rate, 5 wt% PLGA concentration, 17.5 kV voltage, and 18 cm needle to collector distance, directly onto a stationary glass slide attached to the collecting mandrel with electrical tape. Post-electrospaying sample preparation involved mounting and sealing coverslips with Immount and CoverGrip Coverslip Sealant, respectively. Core and shell structures were imaged with a Zeiss LSM 5 Duo Vario Confocal Microscope (Biotron Integrated Microscopy Facility, Western University). Rhodamine B Base (core structure) was visualized with a helium neon 543 laser and shell structures were visualized with reflectance confocal microscopy (Figure 3.12).

3.2.3 – FGF9 Release Kinetics & Assessment of Biological Activity

3.2.3.1 – Concurrent Release Kinetics Study & HDF Proliferation Assay

To determine core-shell microsphere release kinetics and remaining biological activity of released rhFGF9 (bio-technie), a concurrent release kinetics study and HDF proliferation assay was developed. Initially, microspheres were electrospayed for one hour, using four sets of conditions. PLGA concentration of the shell solution (5 wt%), gelatin concentration of the core solution (0.5 wt%), inner flow rate (0.1 mL/h), outer flow rate (1.0 mL/h), and collector distance (14 cm) were held constant. The protein content of the inner solution was varied between 100 $\mu\text{g/mL}$ BSA, 10 $\mu\text{g/mL}$ FGF9, or 100 $\mu\text{g/mL}$ FGF9. Applied voltage was held constant during the first three conditions but increased to 25 kV for fabrication of the final microsphere treatment (using 100 $\mu\text{g/mL}$ FGF9).

Tinfoil was weighed before and after electrospaying to normalize FGF9 release based on deposited microsphere mass. Tinfoil was attached to the collecting mandrel for microsphere collection and stored at -80°C after weighing. The microspheres were UV sterilized for two hours before starting the release kinetics study. After the sterilization period, the three sections of tinfoil per condition were curled and placed into individual 2 mL microtubes with microspheres facing inwards and 2 mL DMEM (10% heat-shock inactivated FBS; 3% AA) was added as release medium (FGF9 release media). Microspheres were submerged

in release media in triplicate per condition (N=3). Fresh release media supplemented with 100 ng/mL FGF9 was included as a positive control condition. The release study was conducted at 37°C. Fresh release media was added 1, 3, 5, 7, and 14 days after the experimental start-point. At each timepoint, 300 µL release media was collected and combined from each conditional replicate and frozen at -80°C. A human FGF9 enzyme linked immunosorbent assay (ELISA) Kit (Thermo Fisher) was used to quantify cumulative FGF9 release over the 14-day study period using the 900 µL frozen release media. The remaining ~1.7 mL was combined per condition and stored at 4°C (separated by timepoint) for use in the concurrent HDF proliferation study.

3.2.3.1.1 – Human FGF9 ELISA

FGF9 release kinetics from the electrosprayed microspheres were measured using a human FGF9 ELISA Kit. Reagents and samples were prepared according to the assay protocol (EHFGF9, Human FGF-9 ELISA Kit Manual). All reagents and samples were brought to room temperature before use. 100 µL of each of the following solutions was added to the wells of an anti-human FGF9 precoated 96 well strip plate which were washed three times with 1x wash buffer between each of the following incubations. Each solution was incubated with gentle rocking at room temperature in the order and period indicated; standards and samples were run in duplicate (n=2) for 2.5 hours, 1x biotinylated antibody for 1 hour, streptavidin-HRP solution for 45 minutes, and TMB substrate for 30 minutes protected from light. Absorbance was measured using a fluorescent plate reader at a wavelength of 450 nm and 550 nm. Absorbance values measured at 550 nm were subtracted from values measured at 450 nm to correct for optical imperfections in the microplate. The standard curve is shown in Appendix L.

3.2.3.1.2 – HDF Proliferation Assay

Three primary HDF cell lines (M55H, F64H, M60H; N=3) were cultured to 80% confluence and seeded in quadruplicate (n=4) at a density of 500 cells/well in a 96 well transparent flat bottom microplate in 150 µL LSM for 24 hours at 37°C. A 5.0×10^5 cell pellet was frozen at -80°C for use as a standard curve during cell number quantification. After 24 hours, the growth media was changed to 150 µL SFM and the cells were incubated for an additional 24 hours at 37°C. The following day, coinciding with the day one

collection of release medium from the microsphere release kinetics study, HDF growth medium was changed to 150 μ L release medium. Experimental plates were rinsed with PBS and stored at -80°C 1, 4, and 7 days after the addition of treatment media. At days 1, 3, and 5, 150 μ L fresh release media (collected from the release kinetics study on the same day) was added to the HDF proliferation experimental wells. After the study endpoint, HDF proliferation was assessed using the CyQUANT® proliferation assay kit according to the protocol outlined in section 3.2.1.4, with the exceptions mentioned above. The standard curve is shown in Appendix K.

3.2.3.2 – EdU S-Phase DNA Incorporation

To further confirm FGF9 activity, EdU incorporation during S-phase DNA replication in HDFs treated with FGF9 release media was measured using the Click-iT™ EdU Alexa Fluor™ 488 Imaging Kit (Thermo Fisher). Microsphere electrospraying and FGF9 release followed the protocol outlined in section 3.2.3.1, with the following exceptions. Conditions remained the same as in section 3.2.3.1 besides the 10 $\mu\text{g}/\text{mL}$ FGF9 trial, which was removed. Microspheres were incubated for two days at 37°C in DMEM (2% FBS; 3% AA) release medium.

HDF culture also remained the same as in the HDF proliferation assay in section 3.2.3.1.2 (N=3), with the following exceptions: 3×10^3 cells were seeded in quadruplicate (n=4) per well of a 96 well plate, no standard curve was required for the EdU incorporation assay, and 200 μ L release media was added to experimental wells at the beginning of the study (after the 2-day incubation period). HDFs were cultured in treatment media for 24 and 48 hours.

Reagents for the EdU incorporation assay were prepared according to the assay protocol (C10337, Click-iT® EdU Imaging Kit Manual). One-half experimental media (100 μ L) was changed with SFM supplemented with 20 mM EdU to expose the cells to a final concentration of 10 mM EdU, incubated at 37°C for two hours. After the EdU incubation, growth media was removed, and the HDFs were fixed with 100 μ L 4% paraformaldehyde (Sigma-Aldrich) in deionized H_2O for five minutes at room temperature, followed by two 1% BSA rinses. HDFs were incubated with 100 μ L 0.1% Triton X-100 (Caledon) for 15 minutes at room temperature for cell membrane permeabilization. Wells were washed twice

with 1% BSA and 100 μL Click-iT® Reaction Cocktail (C10337, Click-iT® EdU Imaging Kit Manual) containing azide conjugated AlexaFluor 488 fluorescent dye was added and incubated for 30 minutes at room temperature, protected from light. The wells were washed twice with 1% BSA and HDFs were counterstained with Hoechst 33342 in PBS (1:1000) for 30 minutes at room temperature, protected from light. Finally, the wells were washed twice with PBS and the cells were stored at 4°C in 200 μL PBS, wrapped in parafilm. Fluorescent images were captured on an Axio Observer Z.1 inverted microscope. ImageJ software was used to quantify EdU incorporation as the proportion of cells fluorescently labelled with AlexaFluor 488 versus the total number of cells counterstained with Hoechst 33342.

3.2.4 – 7-Day Porcine Study

3.2.4.1 – Porcine Study

Refer to section 2.2.1, with the following exceptions: three pigs were included in the study (Fig 7, 8, and 9 - continuously labelled from the previous 28-day porcine study; N=3), and treatment groups were comprised of: 1) an empty wound, 2) 10 $\mu\text{g}/\text{mL}$ BSA scaffold, 3) 10 $\mu\text{g}/\text{mL}$ POSTN/CCN2 scaffold, 4) 10 $\mu\text{g}/\text{mL}$ BSA + 9 $\mu\text{g}/\text{mL}$ FGF9 microsphere scaffold (BSA/FGF9 scaffold), and 5) 10 $\mu\text{g}/\text{mL}$ POSTN/CCN2 + 9 $\mu\text{g}/\text{mL}$ FGF9 microsphere scaffold (POSTN/CCN2/FGF9 scaffold). Euthanasia and tissue isolation occurred at day 7 post-wounding.

3.2.4.2 – Scaffold Preparation

Scaffold preparation followed the protocol in section 2.2.2, with the following exceptions: no galectin 3 treatment group was included, and a flow rate of 0.5 mL/h was used. Scaffolds were cut into circles, 2 cm in diameter, with a custom biopsy punch.

Following the 0.1 M glycine quench and triple PBS rinses, BSA/FGF9 and POSTN/CCN2/FGF9 scaffolds were reattached to the rotating mandrel and FGF9 microspheres were electrosprayed on the top surface as described in section 3.2.2.4. However, the core solution consisted of 9 $\mu\text{g}/\text{mL}$ FGF9 instead of 1 $\mu\text{g}/\text{mL}$ BSA. Scaffolds were UV sterilized (after being cut into circles 2 cm in diameter) for 30 minutes per side of each scaffold. BSA/FGF9 and POSTN/CCN2/FGF9 scaffolds were stored dry at 4°C. This adapted protocol was necessary to avoid hydrolytic reaction and breakdown of the PLGA

microsphere shell with aqueous 0.1 M glycine and PBS, before cutaneous insertion into the porcine wounds.

3.2.4.3 – Porcine Cutaneous Wound-Healing Outcomes

3.2.4.3.1 – Wound Closure Kinetics

Refer to section 2.2.3.1, with the following exception: wound images were acquired on days 0, 3 and 7, wound closure kinetic measurements included one image (n=1) per condition, per pig (N=3), and wound diameter measurements included two Masson's Trichome images (n=2) per pig.

3.2.4.3.2 – Angiogenesis

Refer to section 2.2.3.2. Two CD146+ immunofluorescent image (n=2) per condition, per pig (N=3) were analysed. No primary antibody negative control CD146/CD105 immunofluorescent images from the day 7 porcine study are shown in Appendix R.

3.2.4.3.3 – Collagen Deposition

Refer to section 2.2.3.3, with the following exceptions: 400 μ L and 1200 μ L 6-M HCL was used for tissue degradation, and 4 μ L and 2 μ L degraded tissue supernatant was transferred to the 96 well plate for drying, for wounded and unwounded samples, respectively. A ~10 mg sample was taken from each tissue sample per condition, per pig (N=3) and measured in duplicate (n=2).

3.3 – Results

3.3.1 – *In Vitro* Effect of FGF9 on Cell Populations involved in Wound Healing

3.3.1.1 – Effect of FGF9 on HDF Migration

A preliminary set of experiments were conducted to assess the effect of FGF9 on HDFs, which has not been previously described. A series of scratch assays were conducted to determine the effect of FGF9 on HDF migration. LSM supplemented with 10 ng/mL FGF9 (LSM + 10 ng/mL FGF9) did not affect the migration rate of HDFs (Figure 3.3B). Representative phase contrast images at 0, 9, and 18 hours post-scratching are shown in Figure 3.3A. Only HSM significantly increased HDF chemotaxis. No differences were observed between FGF9 treatments and SFM.

3.3.1.2 – Effect of FGF9 on HDF Chemotaxis

A set of modified Boyden Chamber assays were conducted to determine the effect of FGF9 on HDF and NIH 3T3 chemotaxis. SFM + 100ng/mL FGF9 significantly increased HDF chemotaxis compared to SFM without FGF9 ($p < 0.05$). Chemotaxis of HDFs treated with HSM significantly increased compared to other conditions except SFM + 100 ng/mL FGF9 (Figure 3.4A). FGF9 had no effect on NIH 3T3 chemotaxis (Figure 3.4B).

3.3.1.3 – Effect of FGF9 on HDF Proliferation

To determine the effect of FGF9 on HDF proliferation, proliferation rate of HDFs exposed to LSM or HSM \pm 1, 10, or 100 ng/mL FGF9 was assessed. At day 7, LSM + 10 ng/mL and +100 ng/mL FGF9 significantly increased HDF proliferation compared to LSM without FGF9 (Figure 3.5A). Between FGF9 treatment conditions, 10 ng/mL FGF9 significantly increased HDF proliferation compared to 1 ng/mL and 100 ng/mL FGF9. HSM enhanced the proliferative effect of FGF9 observed in the proliferation assay conducted with LSM (Figure 3.5B). At day 5, HSM + 10 ng/mL and + 100 ng/mL FGF9 significantly increased HDF proliferation compared to negative controls. All FGF9 conditions significantly increased HDF proliferation at day 7 with a positive linear relationship as FGF9 concentration increased. HSM + 10 ng/mL and HSM + 100ng/mL significantly increased HDF proliferation compared to HSM + 1 ng/mL FGF9 at day 7.

Figure 3. 3 – Effect of FGF9 on HDF migration. Human dermal fibroblasts were seeded 1×10^6 cells per well of a 6 well plate and allowed to adhere overnight. After overnight incubation, three parallel scratches were created with a P10 pipet tip in the confluent cell layer. Growth media was changed to LSM \pm 10 ng/mL FGF9 and time lapse microscopy captured images sequentially every 20 minutes for 48 hours. **A)** Representative images of scratch wound closure for one cell line are shown at three timepoints. Scale bar = 100 μ m. **B)** Migration was measured as average cumulative area closed. No differences at any timepoint were observed. N=3, n=5, t-test, $p < 0.05$. Data presented as mean \pm SD.

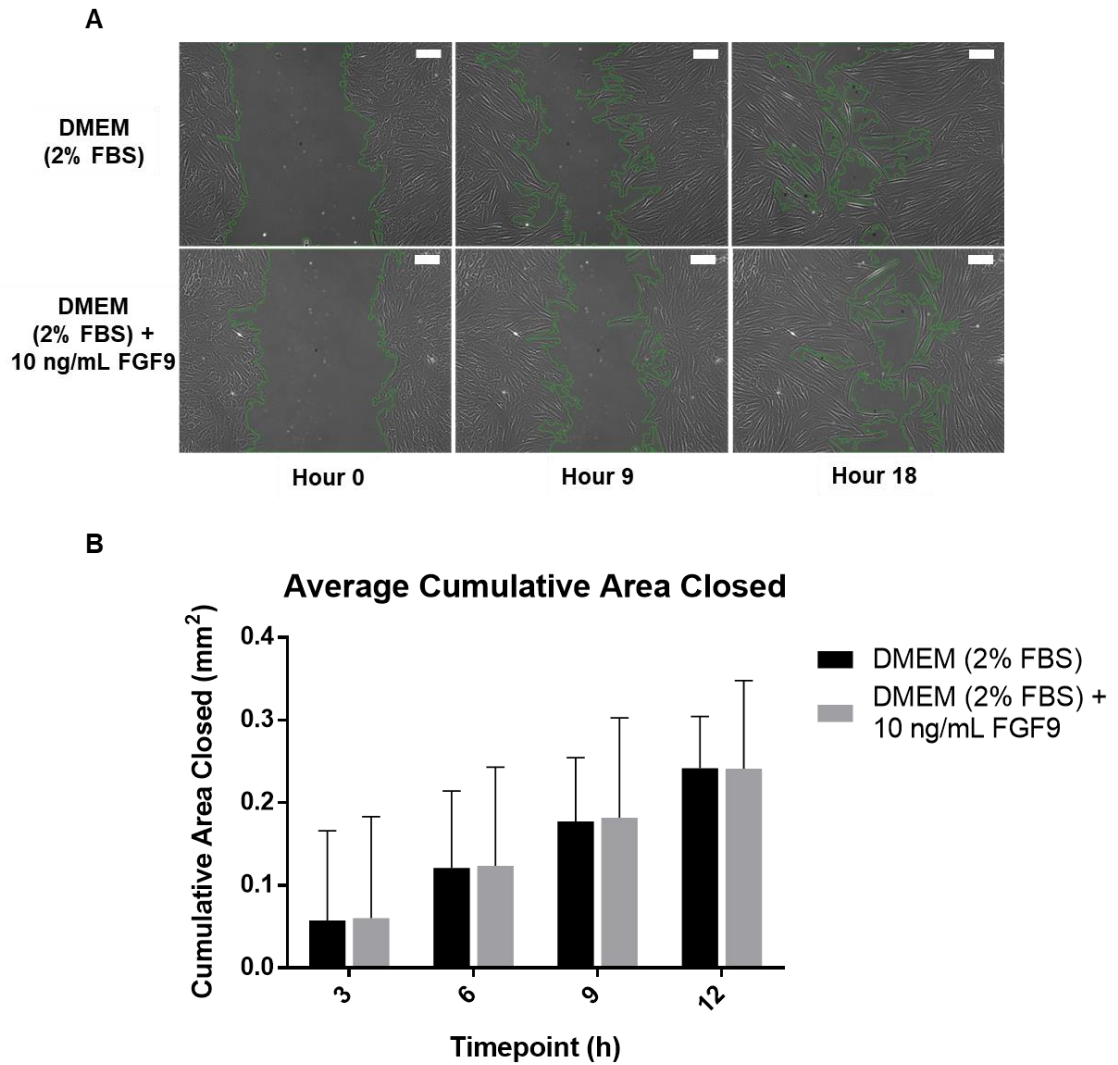


Figure 3. 4 – Effect of FGF9 on HDF chemotaxis. The Cultrex® Cell Migration Assay Kit was used to investigate the chemotactic effect of FGF9 on HDFs (three primary HDF cell lines - M55H, F64H, M60H) and NIH3T3 murine embryonic fibroblasts using modified Boyden Chamber assays. Experimental media included: SFM, HSM, or SFM + 1 ng/mL, + 10 ng/mL or + 100 ng/mL FGF9. Cells migrated at 37°C through an 8 μm^2 porous surface for 4 hours before migrated cell number was quantified with Calcein-AM fluorometric staining. **A)** HDF chemotaxis significantly increased in response to HSM versus SFM, SFM + 1 ng/mL FGF9 and + 10 ng/mL FGF9. HDF chemotaxis significantly increased in response to DMEM (0% FBS) + 100 ng/mL FGF9 compared to SFM. N=3, n=4, two-way ANOVA, Tukey post-test for multiple comparisons, * = $p < 0.05$, ** = $p < 0.01$, **** = $p < 0.0001$. **B)** Chemotactic migration of NIH3T3 cells significantly increased in response to HSM versus all other treatments. No differences were observed between SFM and any FGF9 treatment. N=1, n=9, one-way ANOVA, Tukey post-test for multiple comparisons, **** = $p < 0.0001$. Data presented as mean \pm SD.

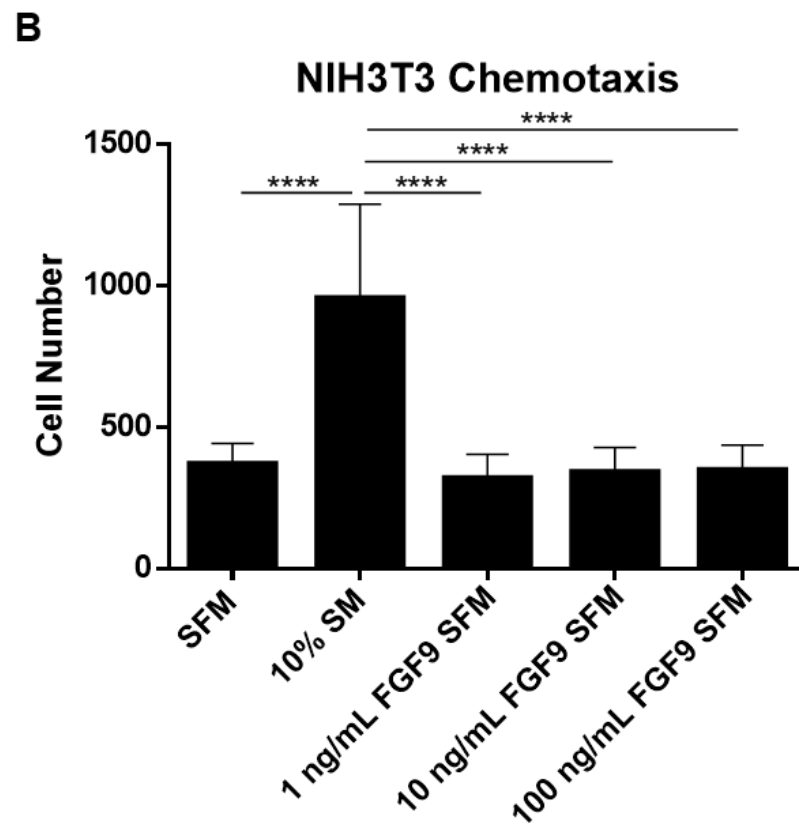
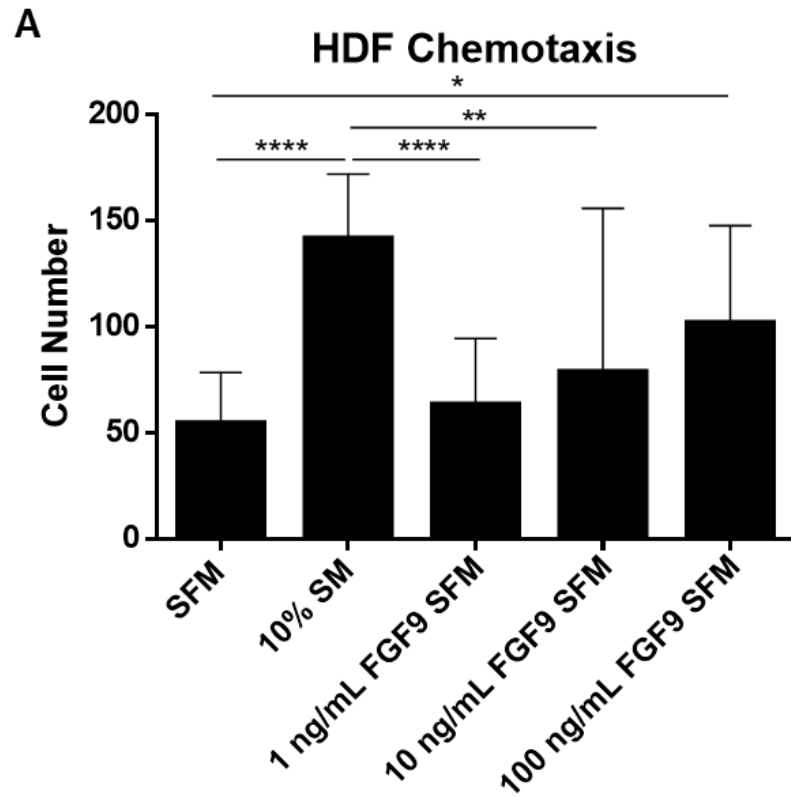
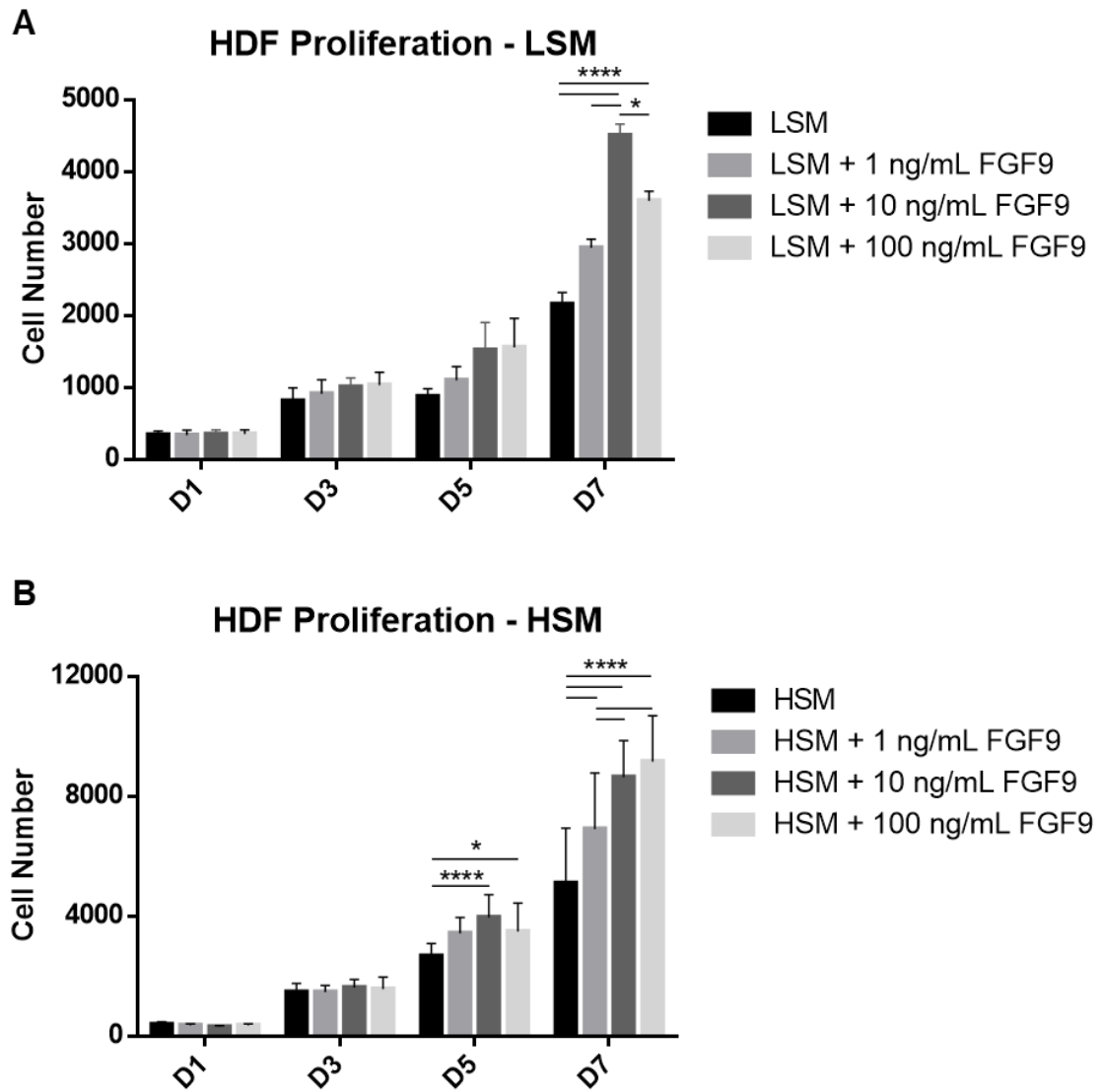


Figure 3. 5 – Effect of FGF9 on HDF proliferation. Human dermal fibroblasts (three primary HDF cell lines - M55H, F64H, M60H) were cultured on tissue culture plastic for 7 days with LSM or HSM \pm 1 ng/mL, \pm 10 ng/mL or \pm 100 ng/mL FGF9. At study endpoint, cells from each timepoint were stained with CyQUANT® GR dye and fluorescent intensity was converted to cell number at days 1, 4, and 7 using a standard curve. **A)** Cell number significantly increased at day 7 in response to LSM + 10 ng/mL and + 100 ng/mL compared to LSM. Media supplemented with 10 ng/mL FGF9 increased HDF proliferation significantly more than all other treatment groups. No differences were observed on days 1, 3, or 5. N=3, n=4, two-way ANOVA, Tukey post-test for multiple comparisons, * = $p < 0.05$, **** = $p < 0.0001$. **B)** HSM + 10 ng/mL FGF9 and + 100 ng/mL FGF9 significantly increased HDF proliferation compared to controls at day 5. Proliferation increased in response to FGF9 at all three concentrations at day 7. Proliferation was significantly greater for cells in media supplemented with 10 ng/mL FGF9 and 100 ng/mL FGF9 versus those in media supplemented with 1 ng/mL FGF9 at day 7. No differences were observed on days 1 or 3. N=3, n=4, two-way ANOVA, Tukey post-test for multiple comparisons, * = $p < 0.05$, **** = $p < 0.0001$. Data presented as mean \pm SD.



3.3.2 – Scaffold Fabrication, Design, and Validation

3.3.2.1 – Assessment of Fiber Diameter

To determine the effect of varying electrospinning parameters on gelatin fibre morphology, diameter of nanofibers electrospun using 27 parameter combinations (Table 1) were quantified. Increasing solution flow rate and applied voltage significantly decreased fiber diameter (Figure 3.6A/B, respectively). Increasing distance above 8 cm significantly increased fiber diameter however, no difference in fiber diameter was observed between 10 cm and 12 cm (Figure 3.6C).

To determine the effect of gelatin concentration on scaffold morphology, diameter of nanofibers electrospun using 19 wt%, 21 wt%, and 23 wt% gelatin solutions were quantified. Gelatin concentration had no substantial visible effect on scaffold morphology (Figure 3.7A-F). However, quantification of fiber diameter showed that increasing gelatin concentration significantly increased fiber diameter (Figure 3.7J). Frequency and Gaussian distribution plots, mean, and standard deviation of fiber diameters are presented in Figures 3.7G-I.

A set of refined electrospinning parameters were chosen based on data recorded during the fiber diameter quantification process. The final optimized parameters produced a nanofibrous scaffold with the lowest average fiber diameter and second lowest standard deviation to produce ECM biomimetic scaffolds with highly homogeneous fiber morphology (Figure 3.8).

3.3.2.2 – Assessment of Microsphere Diameter

To determine the effect of varied electrospaying parameters on PLGA/BSA microsphere morphology, diameter of spheres electrospayed using 15 parameter combinations (Table 2) were quantified. Significant or observable trends did not exist for applied voltages, PLGA concentrations, inner flow rates, or collector distances however, there were differences between individual parameters. An applied voltage of 20 kV produced spheres with significantly lower diameter than at 17.5 kV and 22.5 kV, and an applied voltage of 22.5 kV produced spheres with significantly higher diameter than at 17.5 kV and 20 kV (Figure 3.9B). Sphere diameter significantly increased when electrospayed with 6 wt % PLGA solution and 0.3 mL/h inner flow rate compared to 5 wt% and 0.2 mL/h, respectively

(Figure 3.9C/D). Despite these differences, no significant trends were observed except with variation of outer flow rate. Sphere diameter significantly increased when outer flow rate was raised above 0.3 mL/h (Figure 3.9A). No other differences were observed. Representative images of PLGA/BSA microspheres electrosprayed at the various parameter combinations are presented in Figure 3.10.

To determine the effect of potential extraneous variable(s) on the outcome of electrosprayed BSA/PLGA microsphere morphology, a separate analysis was conducted based on trials with the highest and lowest sphere diameter variability. Representative images (Figure 3.11B/C) indicate the significant decrease in sphere diameter with increased diameter variability (Figure 3.11A). BSA/PLGA sphere diameter measurements follow a normal distribution in trials with monodisperse spheres compared to a right skewed distribution of trials with high diameter variability. The spread of diameter measurements is wider when variability is higher (0.55-19.42 μm versus 0.84-13.64 μm) (Figure 3.11D/E).

3.3.2.3 – Microsphere Core-Shell Morphology

PLGA/BSA microsphere core and shell structures were visualized with immunofluorescent staining and confocal microscopy. Representative images of PLGA shell and protein core structures are independently presented in Figure 3.12A/B. Magnification of one representative sphere shows the distinction between core and shell structures and the localization of the fluorescently labelled protein solution within the core of the microsphere (Figure 3.12D).

Figure 3. 6 – Effect of flow rate, distance and voltage on electrospun fiber diameter.

Fiber diameter was measured using ImageJ software and SEM images of scaffolds electrospun using the 27 parameter combinations outlined in Table 1. Concentration of gelatin solution was held constant at 21 wt%. A-C represent combined data of the nine parameter combinations at each flow rate, voltage and collector distance. **A)** Fiber diameter significantly decreased with increasing flow rate. **B)** Fiber diameter significantly decreased from 13 kV to 17 kV and significantly increased between 15 kV and 17 kV. **C)** Increasing collector distance significantly increased fiber diameter at each distance. The Y-axes have been adjusted to enhance visualization of the observed relationships. N=9, n=4050, one-way ANOVA, Tukey post-test for multiple comparisons, * = $p < 0.05$, ** = $p < 0.01$, **** = $p < 0.0001$. Data presented as mean \pm SD.

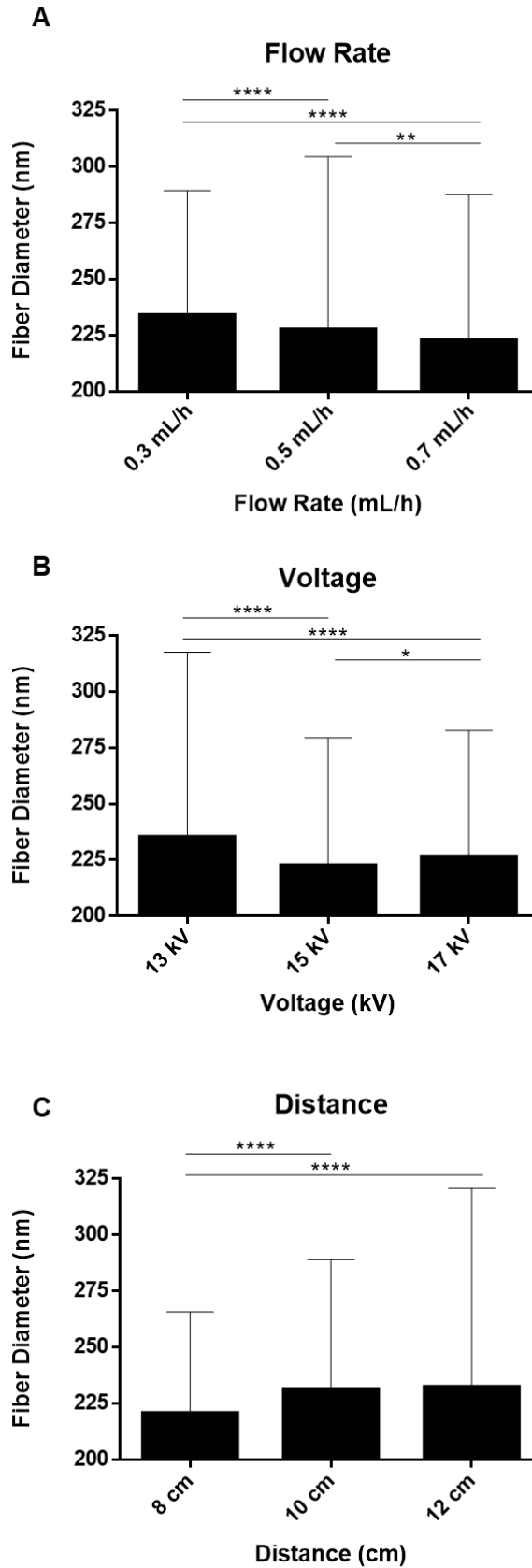


Figure 3. 7 – Effect of varied gelatin solution concentration on fiber diameter. Fiber diameter measurements were calculated using ImageJ software and SEM images of scaffolds electrospun using three different gelatin concentrations (19 wt%, 21 wt% and 23 wt%). Optimized parameters were held constant: 0.5 mL/h flow rate, 17 kV voltage, 8 cm collector distance. **A-F)** Representative images of scaffolds 7500x magnification (A-C scale bar = 1 μ m) and 1500x magnification (D-F scale bar = 10 μ m). **G-I)** Frequency and Gaussian distributions at each gelatin concentration showing percentage of fiber diameters within each bin range relative to the total number of measurements. N=3, n=150, bin size: G-I=20 nm. **J)** Fiber diameter significantly increased with increasing gelatin concentration. N=3, n=150, one-way ANOVA, Tukey post-test for multiple comparisons, **** = $p < 0.0001$. Data presented as mean \pm SD.

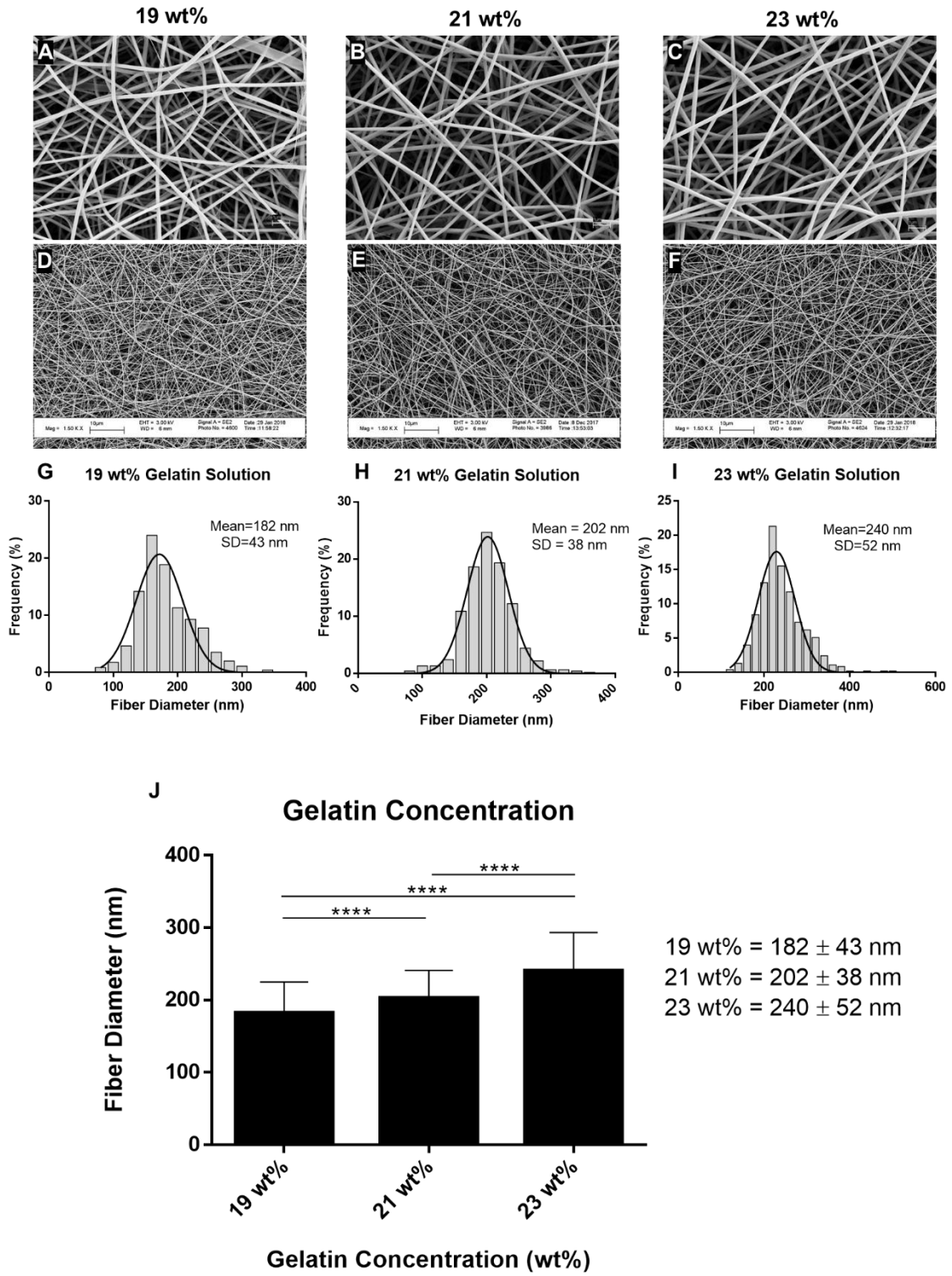
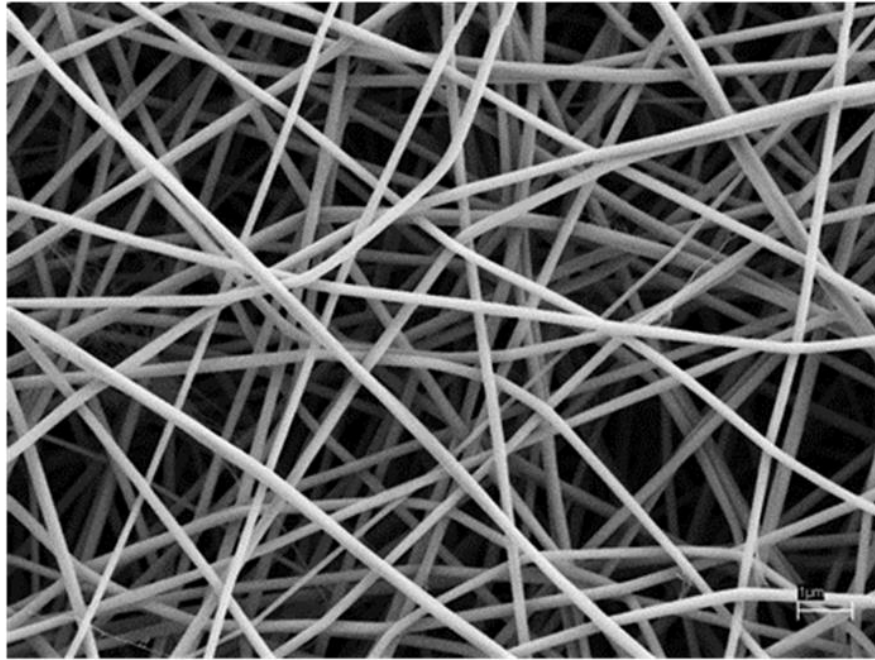


Figure 3. 8 – Refined scaffold morphology. Quantitative and qualitative information recorded during the electrospinning, imaging, and quantification of fiber diameter was used to make the final decision of an optimized scaffold parameter combination. The final optimized scaffold parameters were: 0.5 mL/h flow rate, 17 kV applied voltage and 8cm collector distance. This combination produced attractive results (regarding the quantitative and qualitative observations measured) in all categories of all three experimental trials, had the lowest average fiber diameter and second lowest standard deviation among all parameter combinations. **A)** Representative image of scaffolds fabricated using the optimized parameters (0.5 mL/h, 17 kV, 8 cm) and a 21 wt% gelatin solution. Scale bar = 1 μ m. **B)** Frequency and Gaussian distribution of fiber diameters electrospun with the optimized parameters. Percentage fibers within each bin range are shown relative to the total number of measurements. N=3, n=150, bin size=20 nm.

A**B**

21 wt% Gelatin Solution

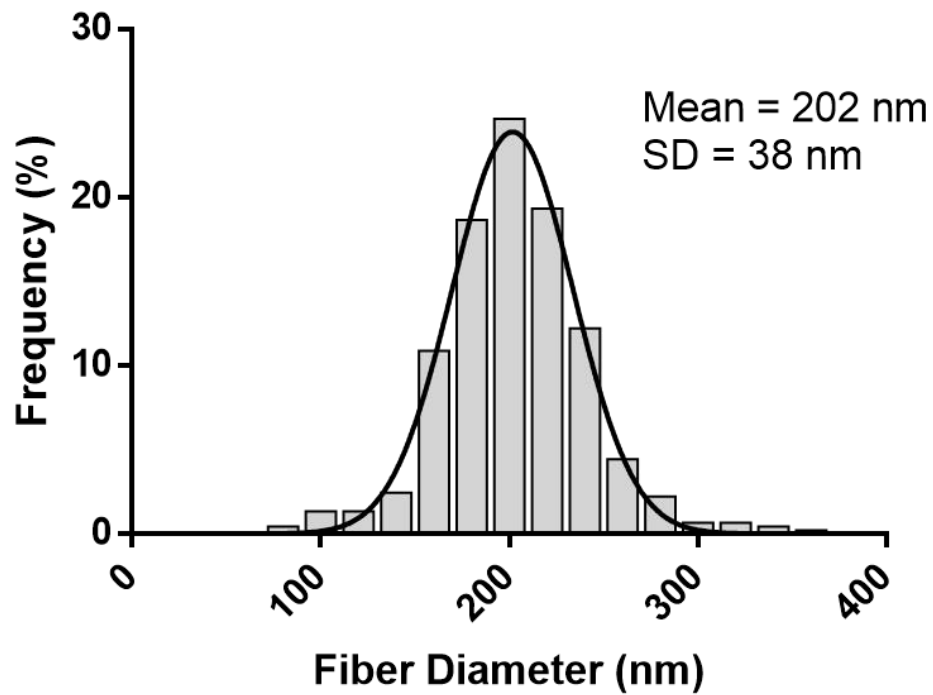


Figure 3. 9 – Effect of electro spraying parameter variation on microsphere diameter.

Microspheres were electrosprayed using the conditions outlined in Table 2, with varied outer solution flow rate (0.3 mL/h, 0.65 mL/h, 1.0 mL/h), applied voltage (17.5 kV, 20 kV, 22.5 kV), PLGA concentration of the outer solution (4 wt%, 5 wt%, 6 wt%), inner solution flow rate (0.1 mL/h, 0.2 mL/h, 0.3 mL/h), and distance from tip of the coaxial needle to collecting surface (16 cm, 18 cm, 20 cm). Concentration of gelatin in the inner solution was held constant at 0.5 wt%. 8 mm² circular sections were osmium coated (OPC-80T, Filgen) for SEM imaging and ImageJ software was used to measure microsphere diameter in response to the varied experimental parameters. **A)** Microsphere diameter significantly increased with increasing outer flow rate. **B-E)** Differences existed between certain conditions for the remaining parameters however, no consistent trends were observed. N=3, n=50, one-way ANOVA, Tukey post-test for multiple comparisons, * = p < 0.05, ** = p < 0.01, *** = p < 0.001, **** = p < 0.0001. Data presented as mean ± SD.

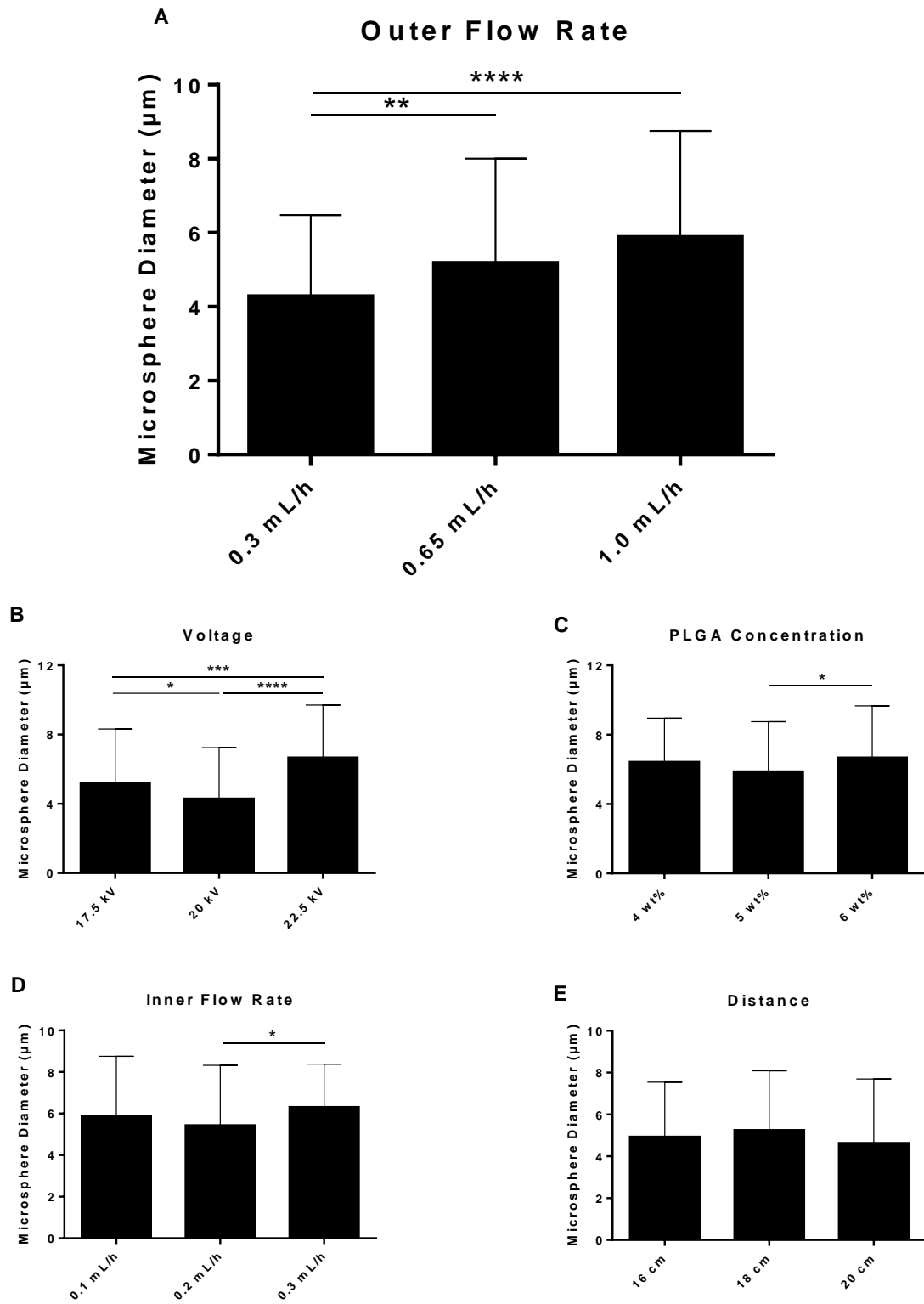


Figure 3. 10 – Representative images of microspheres electrospayed at each parameter combination. Parameters not under investigation were held constant at: 1.0 mL/h outer flow rate, 0.1 mL/h inner flow rate, 5 wt% PLGA concentration, 15 kV voltage, and 20 cm collector distance. Scale bar = 20 μ m.

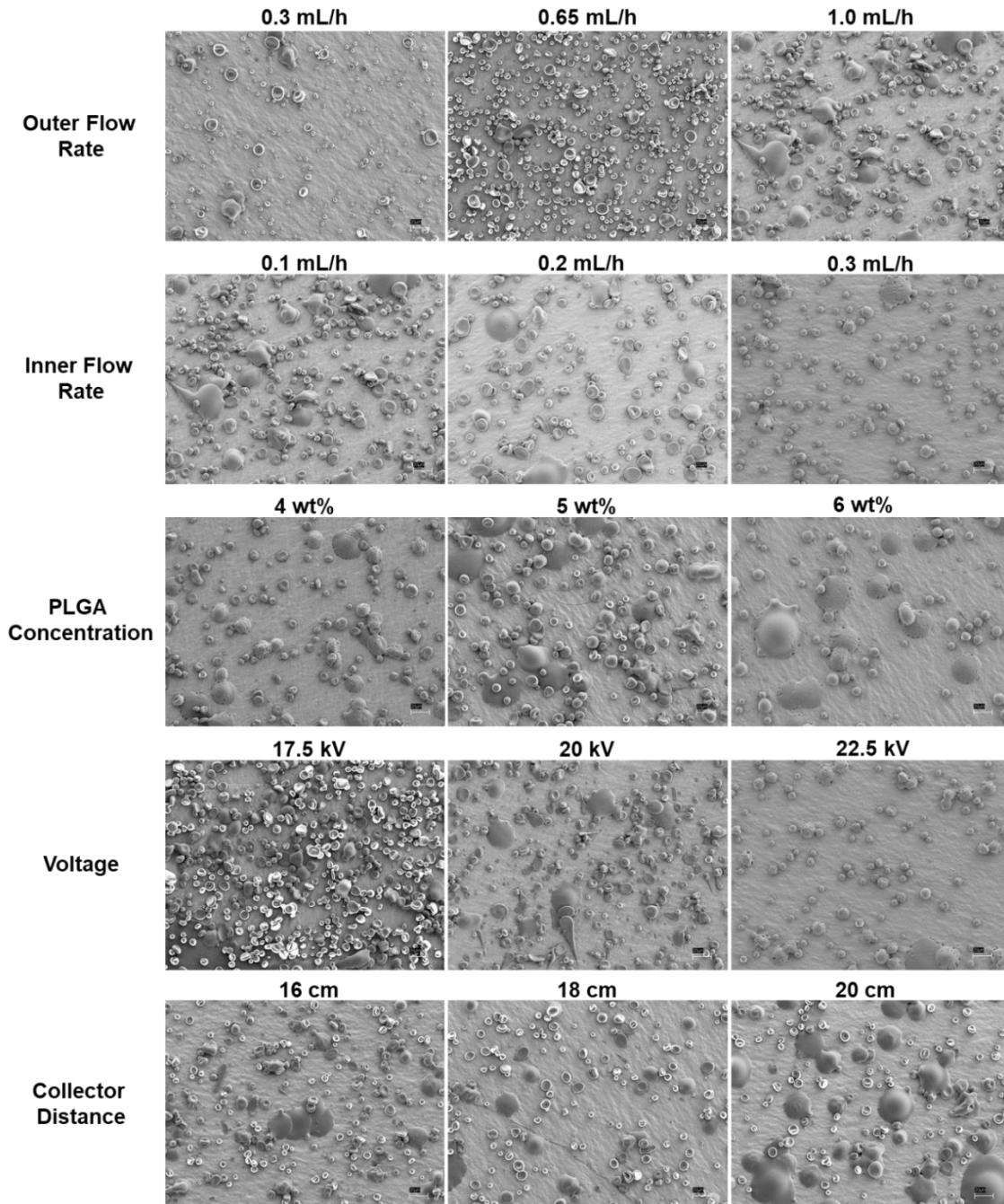


Figure 3. 11 – Potential confounding effect of extraneous variables on microsphere diameter measurements. A separate analysis was conducted to determine the effect of potential extraneous variables on the results presented in Figure 3.9. Within the three samples measured for each condition, trials with the highest and lowest microsphere diameter standard deviation were chosen for analysis, corresponding to “high” and “low” variability, respectively. **A)** Microsphere diameter significantly decreased when variability in microsphere diameter was high. 50 microspheres (n=50) were measured for each of the 15 individual parameter combination trials included (N=15), Mann-Whitney test, **** = $p < 0.0001$. Data presented as mean \pm SD. **B-C)** Representative SEM images of low and high variability trials. Scale bar = 5 μm . **D-E)** Frequency distributions of low and high variability microsphere diameter, and the Gaussian distribution of the low variability condition, showing percentage of microsphere diameters within each bin range relative to the total number of measurements. N=15, n=50, bin size = 1 μm .

A Variability of Microsphere Size Distribution

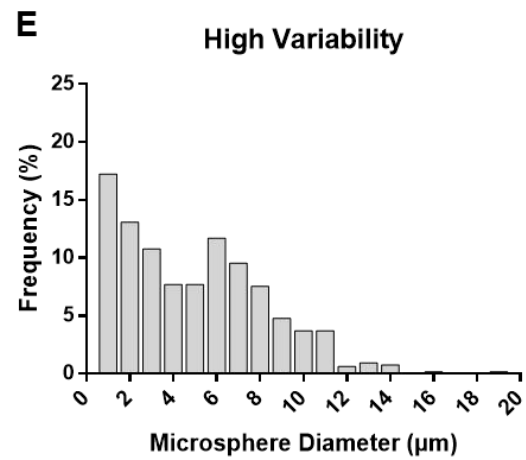
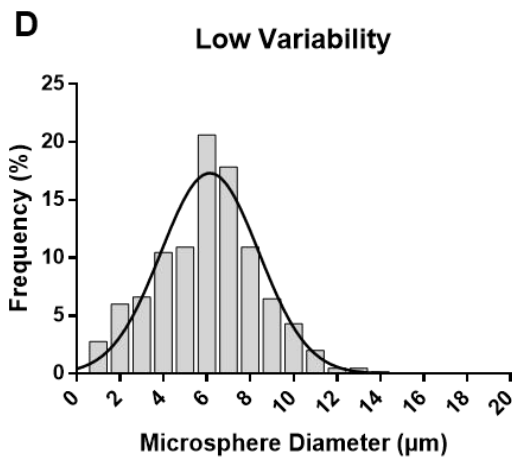
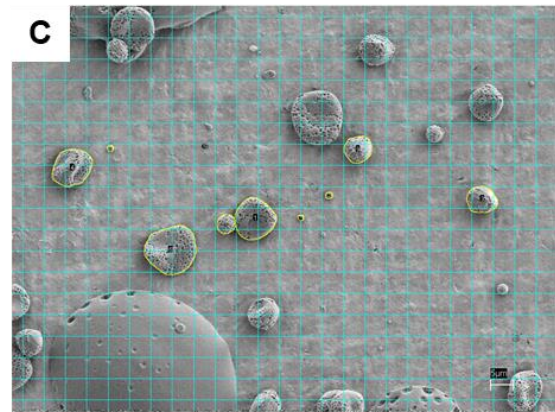
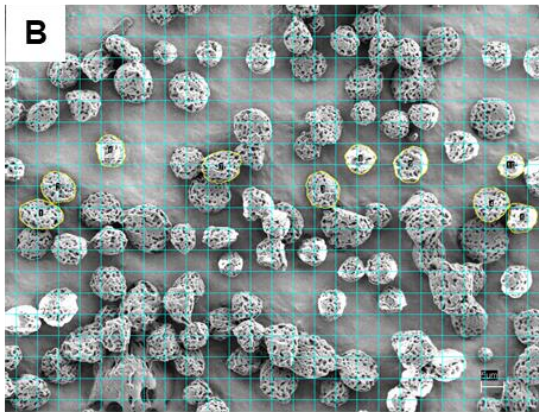
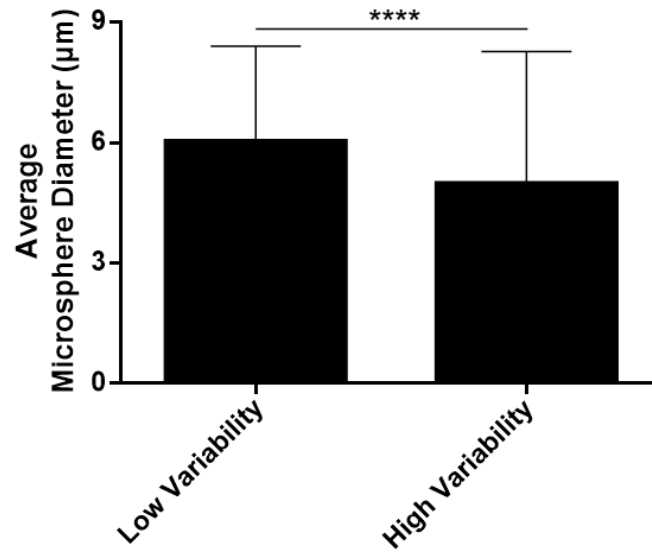
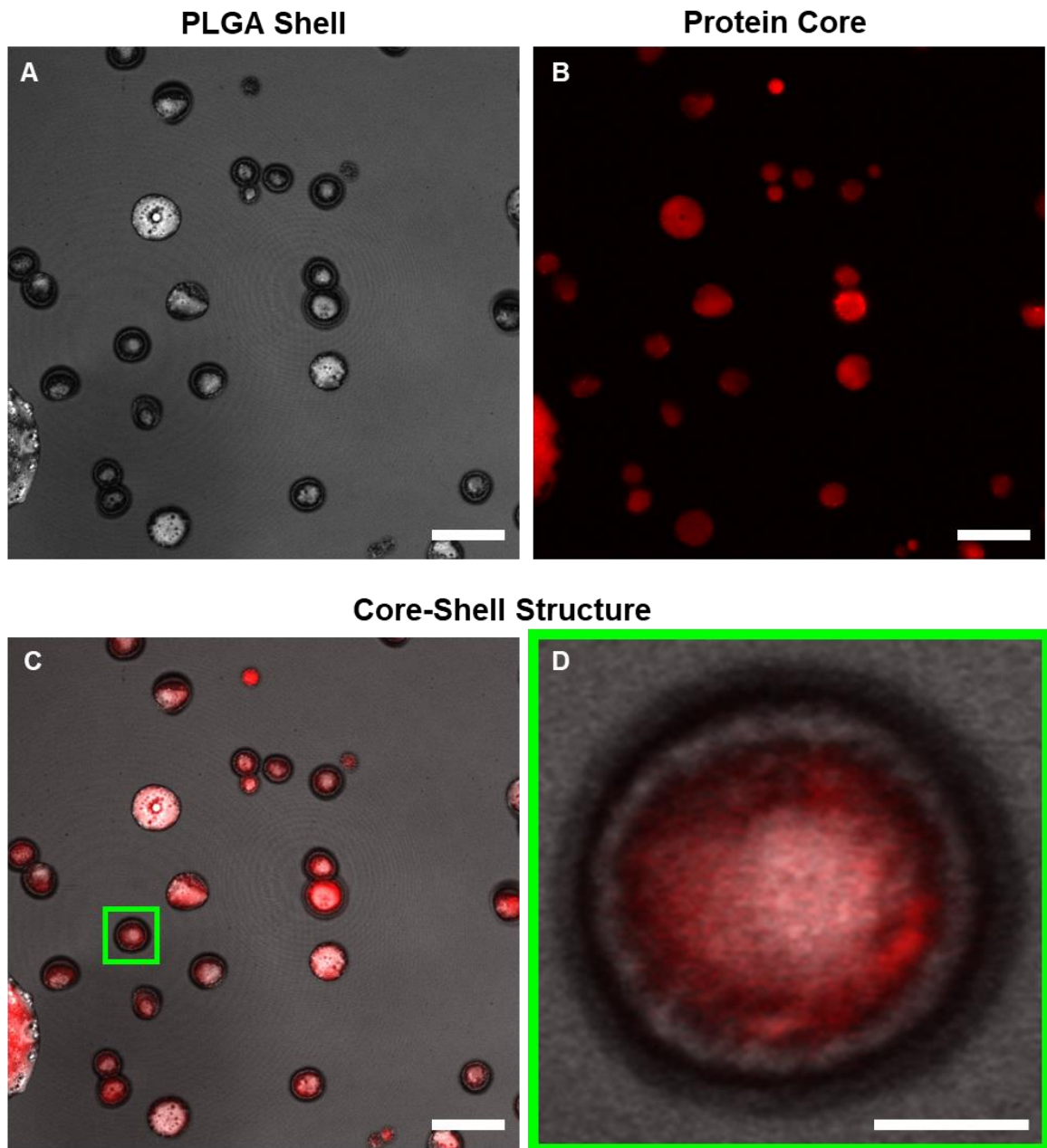


Figure 3. 12 – Confocal imaging shows core-shell structure of electrospayed microspheres. The core and shell structures of electrospayed microspheres were visualized with a Zeiss LSM 5 Duo Vario Confocal Microscope. Microspheres were electrospayed at 1.0 mL/h outer solution flow rate, 0.1 mL/h inner solution flow rate, 5 wt% PLGA concentration, 17.5 kV voltage, and 18 cm needle to collector distance. **A)** Confocal reflectance microscopy was used to visualize microsphere shell structure. **B)** Rhodamine B Base (20 $\mu\text{g}/\text{mL}$) was dissolved in the inner solution and a helium neon 543 laser was used to fluorescently visualize the microsphere core. **C)** Combined core-shell microspheres (A-C Scale bar = 20 μm). **D)** Magnified core-shell structure of an electrospayed microsphere. Scale bar = 5 μm .



3.3.3 – FGF9 Release Kinetics & Assessment of Biological Activity

3.3.3.1 – FGF9 Release Kinetics & Effect on HDF Proliferation

To determine the release profile and bioactivity of FGF9 released from the microspheres, a solid-phase sandwich ELISA and concurrent HDF proliferation assay were conducted to assess release kinetics and biological activity of FGF9, respectively. Significantly more FGF9 was detected in the release media of microspheres electrosprayed at 17.5 kV and 25 kV with an inner solution concentration of 100 $\mu\text{g/mL}$ FGF9 than an inner solution concentration of 10 $\mu\text{g/mL}$ FGF9, or negative control BSA microspheres. Microspheres electrosprayed with an applied voltage of 25 kV released significantly more FGF9 than microspheres electrosprayed at 17.5 kV (Figure 3.13A). However, media containing FGF9 had no effect on HDF proliferation (Figure 3.13B).

3.3.3.2 – Effect of Released FGF9 on HDF EdU S-Phase DNA Incorporation

Due to the initial complete burst release of FGF9 from the microspheres, it was determined that cellular exposure to FGF9 would have been limited to the first day of the experiment before the first complete media change on day 2. Therefore, a 48-hour 5-ethynyl-2'-deoxyuridine (EdU) S-phase incorporation assay was designed as a follow-up measure of HDF proliferation in response to FGF9 released for 2 days from PLGA microspheres. Proportion of HDF S-phase transition was determined by immunofluorescent staining of cellular nuclei labelled with Alexa Fluor 488 azide dye or counter-stained with Hoechst 33342. No differences were observed between treatment groups at the 24-hour timepoint (Figure 3.14A). At 48 hours, FGF9 microspheres electrosprayed with 100 $\mu\text{g/mL}$ FGF9 at 17.5 kV and 25 kV released bioactive FGF9 which induced a significant proliferative response from the HDFs (Figure 3.14B). At 24 and 48 hours, positive control media supplemented with 100 ng/mL FGF9 significantly increased HDF EdU incorporation compared to all other conditions (Figure 3.14A/B). Immunofluorescent images revealed the positive relationship of FGF9 release media on HDF proliferation at 48 hours (Figure 3.14C/D). EdU incorporation data are presented independently per cell line in Appendix O.

Figure 3. 13 – Release kinetics and biological activity of encapsulated rhFGF9. **A)** FGF9 released from the microspheres was measured with a solid-phase sandwich ELISA. A majority of the encapsulated FGF9 was released in an initial burst during the first day of the study. There was significantly more FGF9 released from microspheres electrosprayed with 100 $\mu\text{g/mL}$ FGF9 (at 17.5 kV and 25 kV) than with 10 $\mu\text{g/mL}$ FGF9. Released FGF9 was prolonged until day three in the 100 $\mu\text{g/mL}$ FGF9 trial (17.5 kV). N=3, n=2, two-way ANOVA, Tukey post-test for multiple comparisons, *** = $p < 0.001$, **** = $p < 0.0001$. Data presented as mean \pm SD. **B)** Human dermal fibroblasts were cultured on tissue culture plastic for 7 days with DMEM (10% heat-inactivated FBS; 3% AA) BSA/FGF9 release medium or DMEM (10% heat-inactivated FBS; 3% AA) + 100 ng/mL FGF9. After the study endpoint, cells were stained with CyQUANT® GR dye and fluorescent intensity was converted to cell number at days 1, 4, and 7 using a standard curve. No differences were observed on days 1 or 4. Cell number significantly increased at day 7 in response to DMEM (10% heat-inactivated FBS) + 100 ng/mL FGF9 compared to all other conditions. No differences existed between the negative control, or FGF9 microsphere treatments at day 7. N=3, n=4, two-way ANOVA, Tukey post-test for multiple comparisons, **** = $p < 0.0001$. Data presented as mean \pm SD.

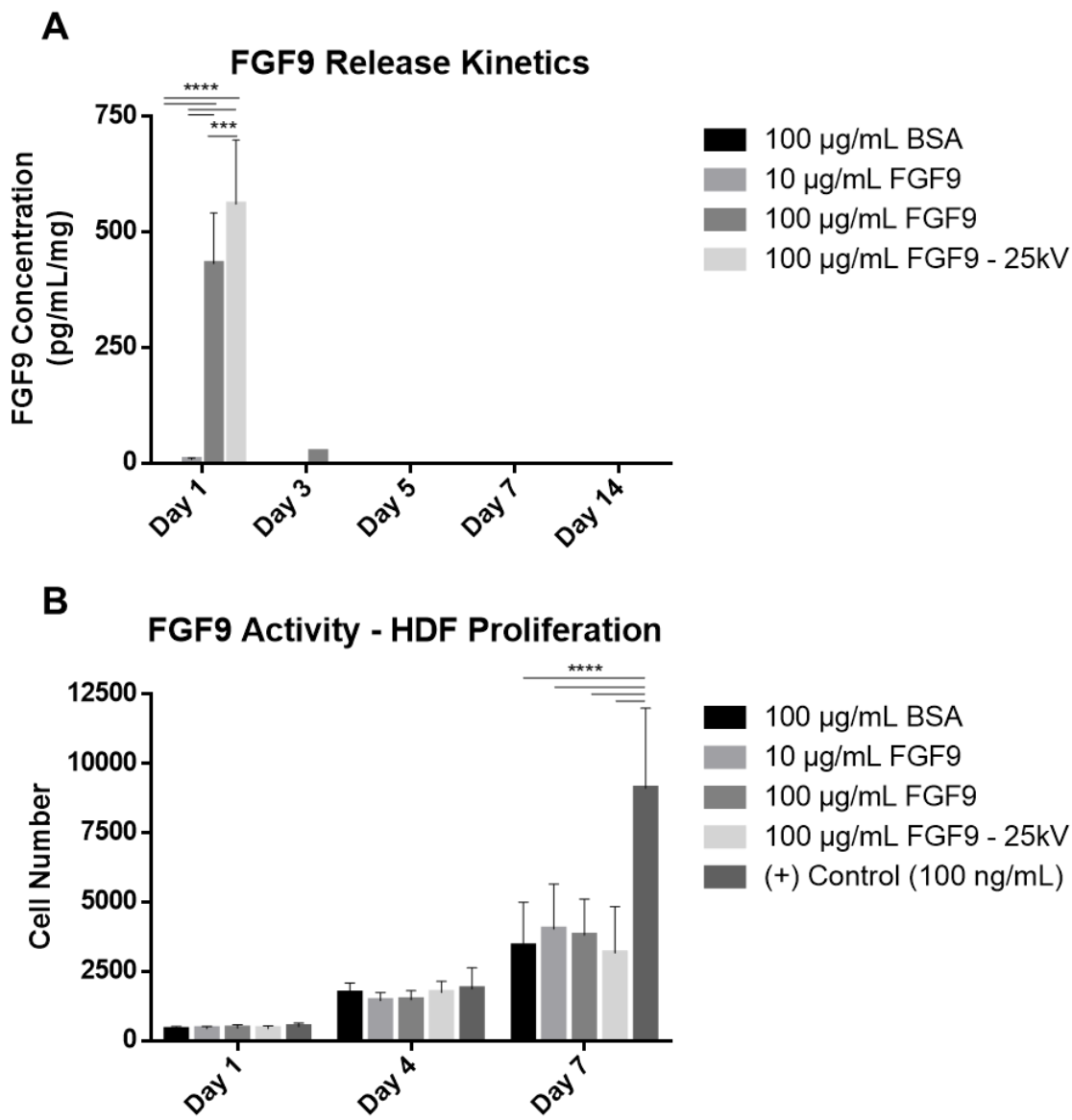
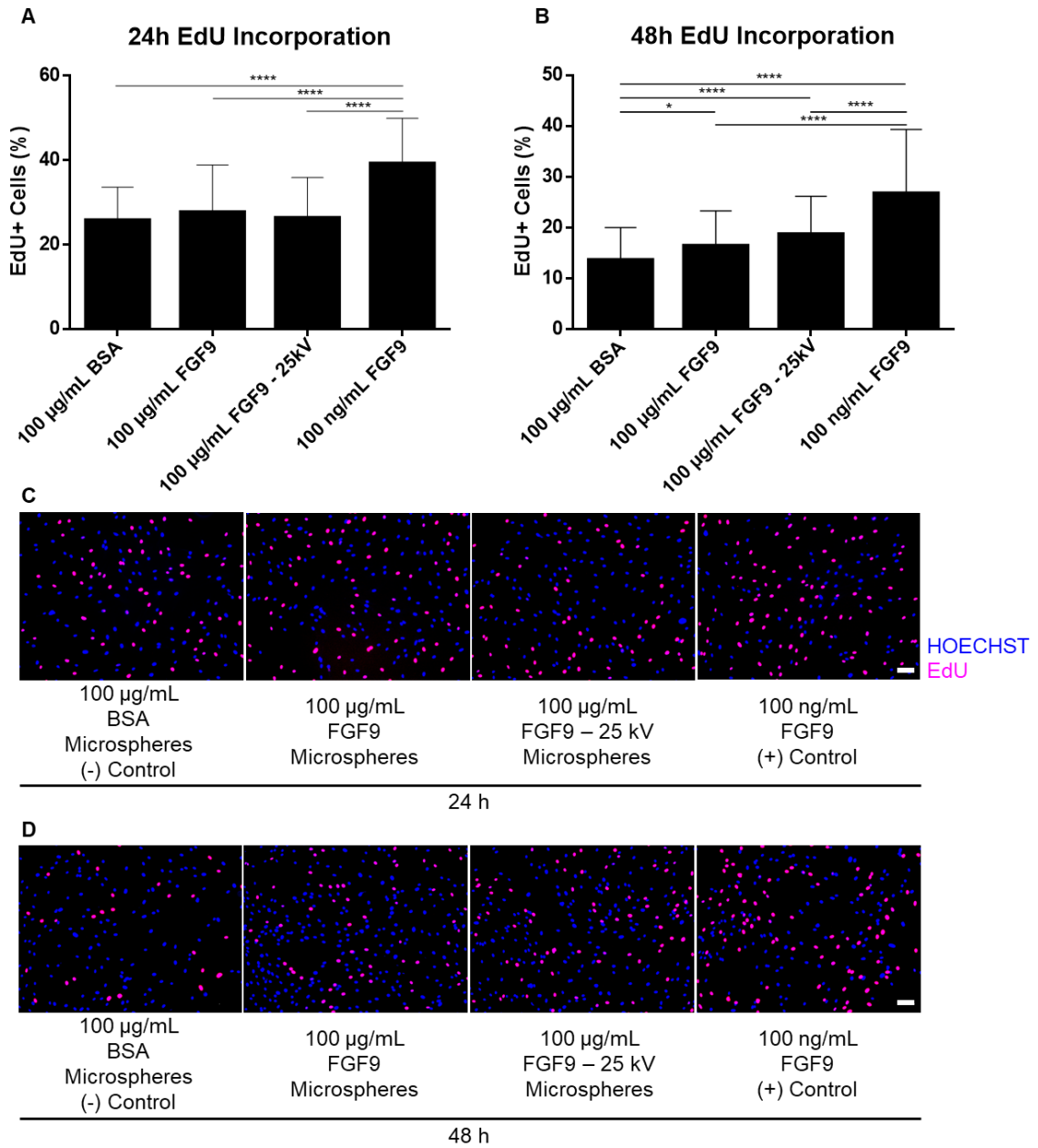


Figure 3. 14 – Edu incorporation during S-phase DNA replication as an indicator of HDF proliferation and biological activity of released FGF9. Microspheres electro sprayed with core solutions containing 100 µg/mL BSA or FGF9 were submerged in DMEM (2% FBS; 3% AA) release medium. Three primary HDF cell line were seeded 3000 cells/well in quadruplicate into a 96 well plate. Cells were treated with 200 µL release media from each condition or DMEM (2% FBS; 3% AA) supplemented with fresh 100 ng/mL FGF9. HDFs were incubated with treatment media for 24 or 48 hours before fibroblast nuclei were fluorescently labelled for incorporated EdU (pink) and counterstained with Hoechst 33342 (blue). EdU incorporation into DNA during S-phase replication indicated the proportion of proliferating cells relative to HDFs presenting only Hoechst staining. **A)** FGF9 released from electro sprayed coaxial microspheres had no effect on HDF proliferation after 24 hours. HDFs cultured with DMEM (2% FBS; 3% AA) supplemented with 100 ng/mL fresh FGF9 significantly increased proliferation at 24 hours. N=3, n=4, two-way ANOVA, Tukey post-test for multiple comparisons, **** = $p < 0.0001$. Data presented as mean \pm SD. **B)** Released FGF9 significantly increased HDF proliferation after 48 hours compared to negative controls. Media supplemented with 100 ng/mL FGF9 significantly increased fibroblast proliferation compared to all other treatments. N=3, n=4, two-way ANOVA, Tukey post-test for multiple comparisons, * = $p < 0.05$, **** = $p < 0.0001$. Data presented as mean \pm SD. **C-D)** Representative images of EdU and Hoechst nuclear staining 24 and 48 hours after treatment with DMEM release medium containing microspheres with 100 µg/mL encapsulated BSA or FGF9 and a positive control containing 100 ng/mL fresh FGF9. Scale bar = 100 µm. EdU incorporation data are presented independently per cell line in Appendix O.



3.3.4 – 7-Day Porcine Study

3.3.4.1 – Wound Closure Kinetics

To determine the effect of POSTN/CCN2 scaffolds and gelatin/PLGA scaffolds with and without FGF9 microspheres on the proliferative stage of healing, a 7-day porcine wound-healing study was conducted. Full-thickness, excisional wounds, 2 cm in diameter, were created bilaterally on the dorsal surface of three healthy pigs. Representative images of the wounds from one pig for each treatment are shown at days 0, 3, and 7 post-wounding (Figure 3.15). Figure 3.16A/B show a representative image and magnified view of BSA/FGF9 and POSTN/CCN2/FGF9 scaffolds. Wound closure was quantified, and no significant differences were observed between treatments at 3 or 7 days post-wounding (Figure 3.17A). Individual 7-day wound closure kinetics for each pig are presented in Figure 3.18 as an indication of the variability in wound closure measurements between pigs. Wound diameter was measured as the distance between wound borders, parallel to the subcutaneous tissue from Masson's Trichrome stained sections (Figure 3.17C). Wound diameter measurement at day 7 was used as a secondary measure of wound closure to avoid the measurement limitations associated with digital photography and blocking of the wound border by the wound eschar. BSA/FGF9 and POSTN/CCN2/FGF9 scaffolds significantly reduced wound diameter at day 7 compared to empty wounds (16.85 mm and 16.16 mm versus 18.42 mm, respectively).

3.3.4.2 – Angiogenesis

To determine the effect of POSTN/CCN2 and POSTN/CCN2/FGF9 scaffolds on angiogenesis during the proliferative stage of healing, CD146 positive endothelial tissue was visualized with immunofluorescent staining. Representative cross-sectional images of the wound bed vasculature from one pig at day 7 post-wounding are shown with outlines indicative of blood-vessel measurements by ImageJ software (Figure 3.19). Blood-vessel density and percent wound area covered by vascular tissue significantly increased in wounded tissues compared to unwounded tissues (Figure 3.20A/B). Individual blood vessel area significantly increased in empty and POSTN/CCN2/FGF9 scaffold conditions compared to unwounded tissues (Figure 3.20C). Day 7 blood-vessel density, percent area, and individual area are analyzed independently per pig in Appendix P. Endoglin/CD105 positive endothelial tissue was also visualized with immunofluorescent staining (Figure

3.21) to demonstrate the vascular phenotype of porcine cutaneous wound tissue 7 days post-wounding.

3.3.4.3 – Collagen Deposition

Collagen deposition in sections of cutaneous wound tissue following full-thickness excisional wounding, and in unwounded tissues, was visualized with Masson's Trichrome staining (Figure 3.22). 7-day wound margins are visible as termination of the pre-existing thick collagen fibers in the connective tissue of unwounded dermis. Hydroxyproline content was quantified as a measure of collagen deposition (Figure 3.23). Wounded tissues contained significantly less hydroxyproline than unwounded tissue. BSA scaffolds significantly increased wound bed hydroxyproline content compared to empty control wounds (0.2570 and 0.1632 $\mu\text{g}/\mu\text{L}/\text{mg}$, respectively).

Figure 3. 15 – Representative images of wound closure from day 0 to day 7 in a porcine full-thickness cutaneous wound model. Age/sex matched Yorkshire pigs (N=3) were subject to five full-thickness excisional wounds per animal (2 cm in diameter). Experimental conditions included: 1) empty wound, 2) BSA gelatin scaffold, 3) POSTN/CCN2 gelatin scaffold, 4) BSA gelatin scaffold + FGF9/PLGA microspheres, and 5) POSTN/CCN2 gelatin scaffold + FGF9/PLGA microspheres. Representative images of the wounds from one pig are shown at days 0, 3, and 7. Scale bar = 1 cm.

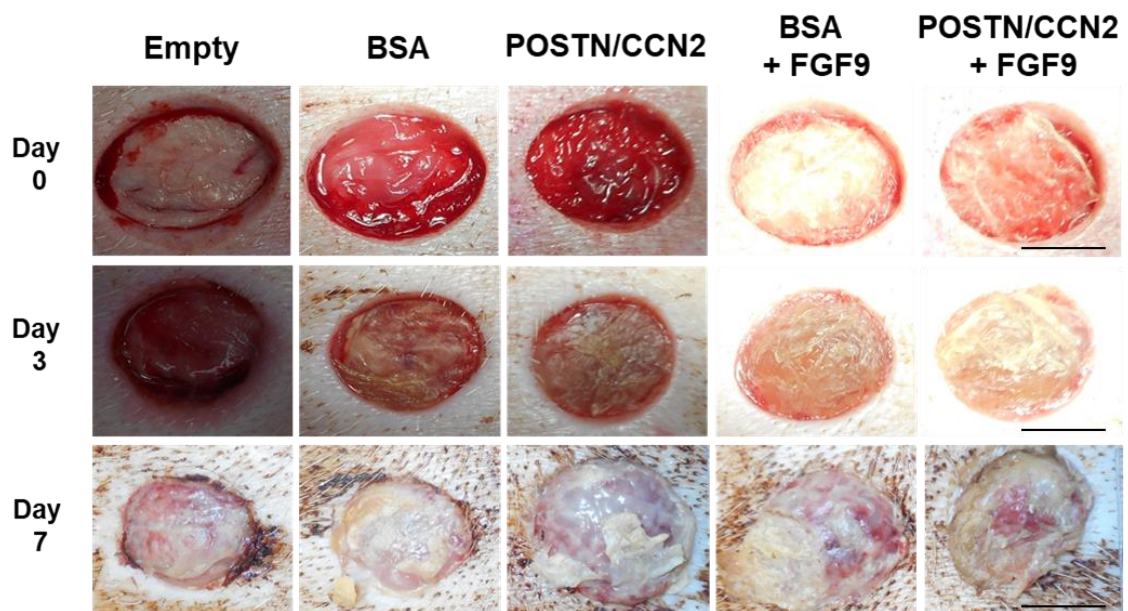


Figure 3. 16 – Representative image of POSTN/CCN2/FGF9 scaffolds used in the 7-day porcine full-thickness cutaneous wound study. None of the electrospun fibers are visible beneath the layer of aggregated microspheres. **A)** 400x magnification of overall scaffold morphology. Scale bar = 10 μm . **B)** 1500x magnification of porous microspheres. Scale bar = 10 μm .

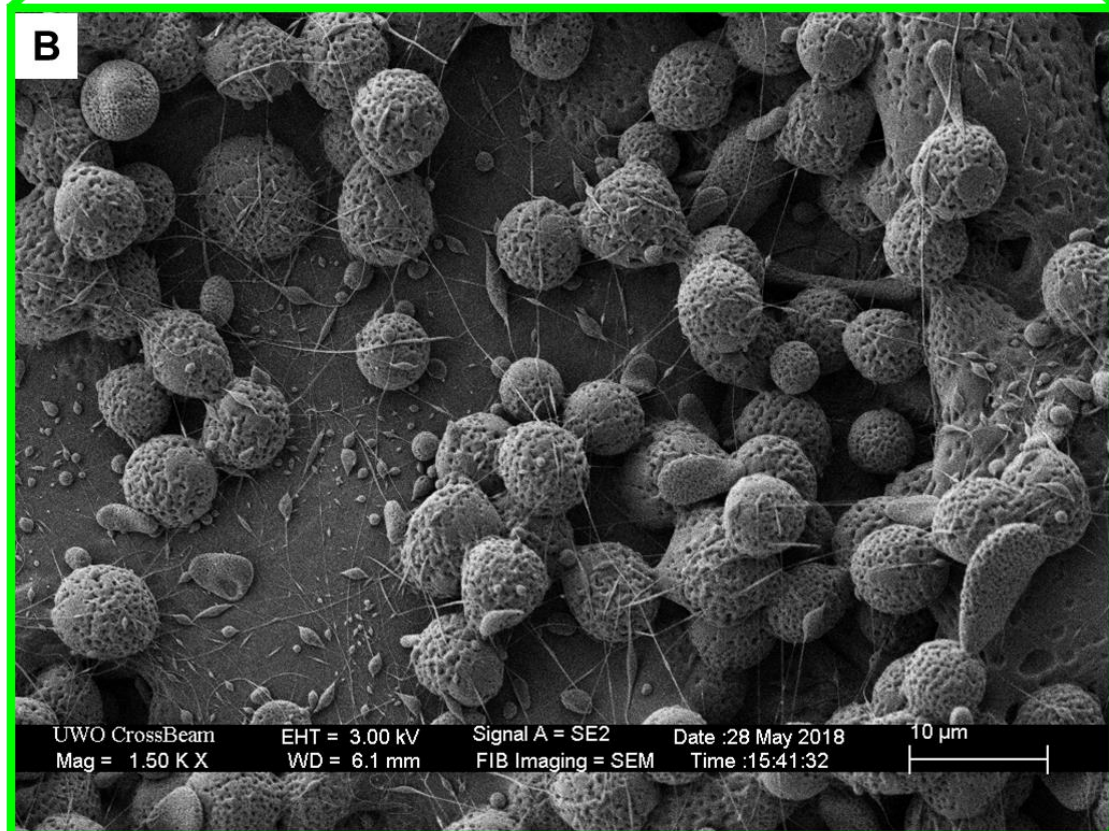
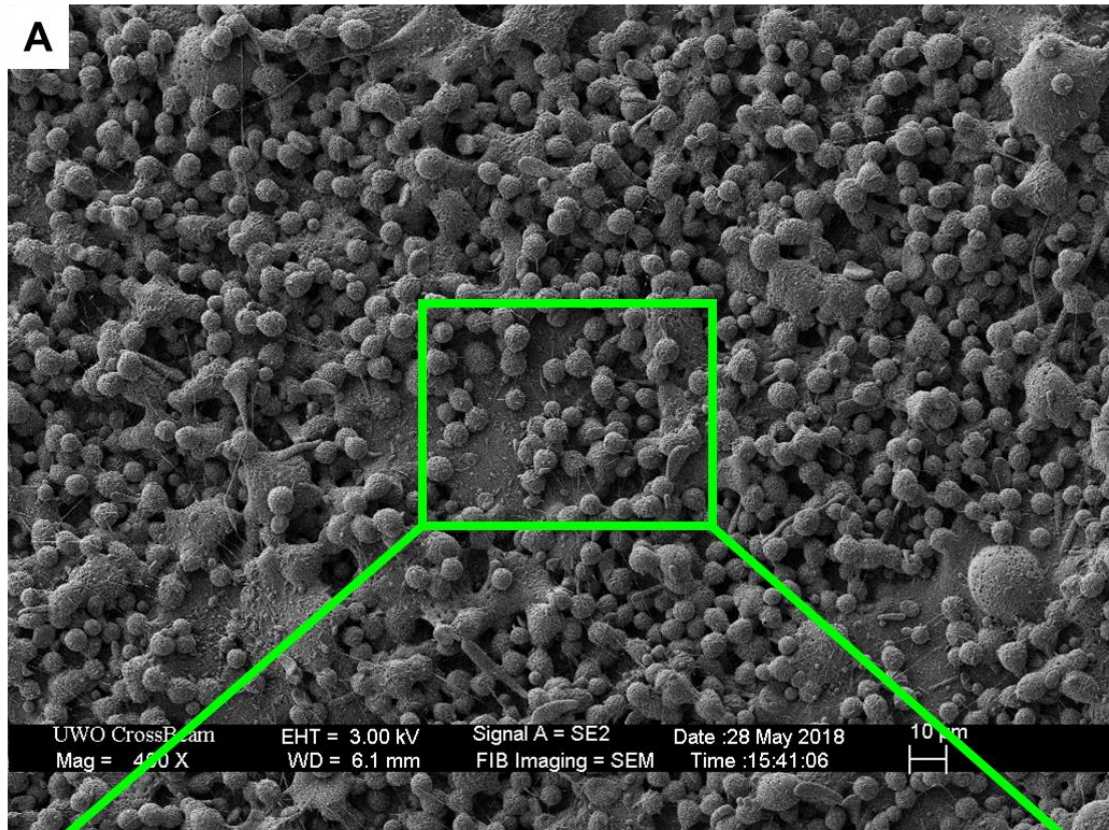


Figure 3. 17 – 7-day wound closure kinetics after full-thickness porcine cutaneous wounding. Wound closure kinetics were calculated from wound areas measured at each timepoint using digital photography and ImageJ software. **A-B)** Data are presented as percent of original wound area closed. Average wound closure is separated based on timepoint (A) and condition (B), each bar corresponding to day 3 or 7, respectively. No differences in wound closure existed. N=3, n=1, two-way ANOVA, Tukey post-test for multiple comparisons, $p < 0.05$. **C)** Using ImageJ software, day 7 wound diameter was measured as the distance between the base of unwounded dermis bordering the wound bed, parallel to the underlying hypodermal tissue, in Masson's Trichrome stained sections. BSA and POSTN/CCN2 gelatin scaffolds with FGF9/PLGA microspheres significantly reduced wound diameter at day 7 compared to controls. N=3, n=2, one-way ANOVA, Tukey post-test for multiple comparisons, * = $p < 0.05$. Data presented as mean \pm SD.

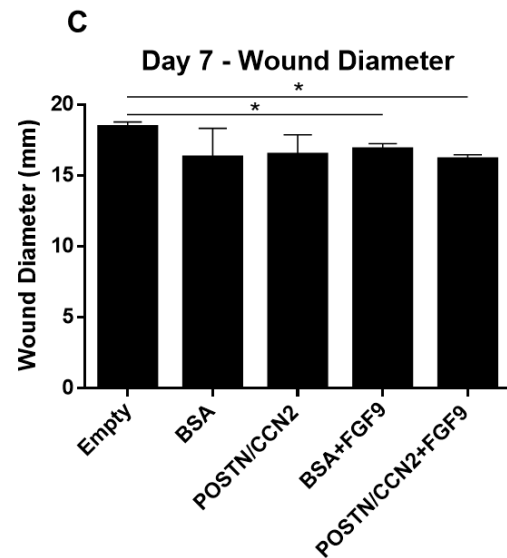
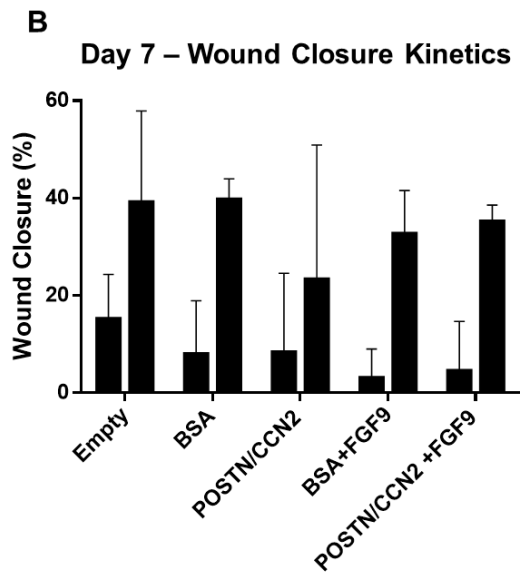
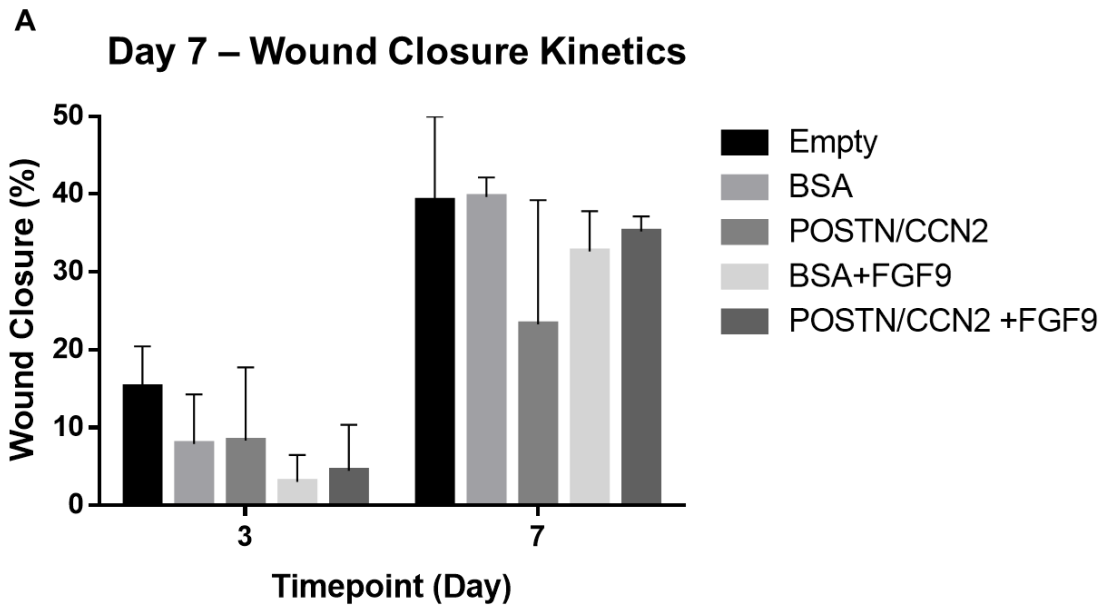


Figure 3. 18 – Individual 7-day wound closure kinetics after full-thickness cutaneous wounding in a porcine model. Wound area was measured at each timepoint using ImageJ software to calculate closure kinetics. **A-C)** Data are presented as percent of original wound area closed. Individual closure kinetics data are presented for each individual pig to show the variability in wound area measurements due to inter-animal variability and limitations of the measurement method associated with wound eschar blocking the wound edge in digital images. One image (n=1) was measured per condition, per pig (N=1).

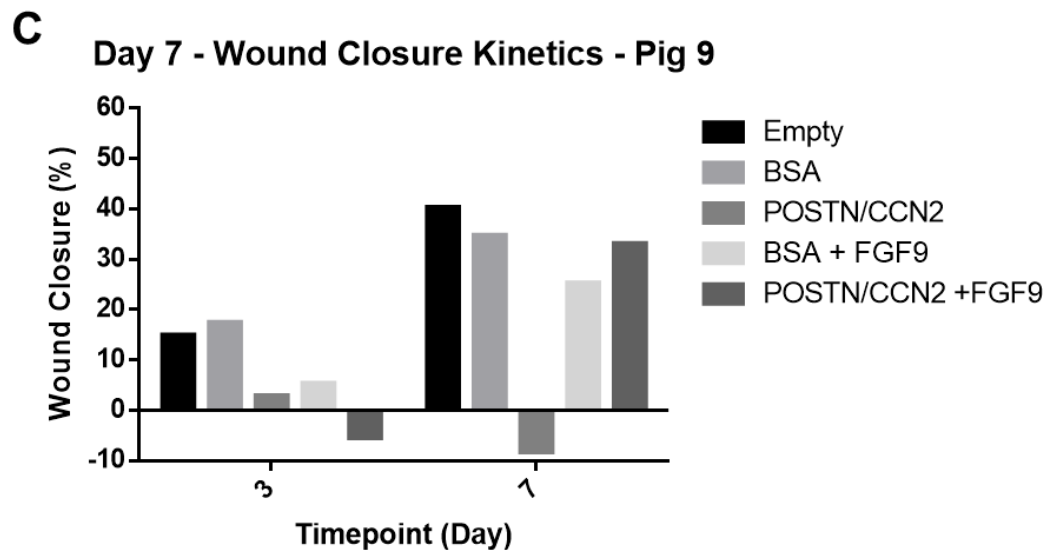
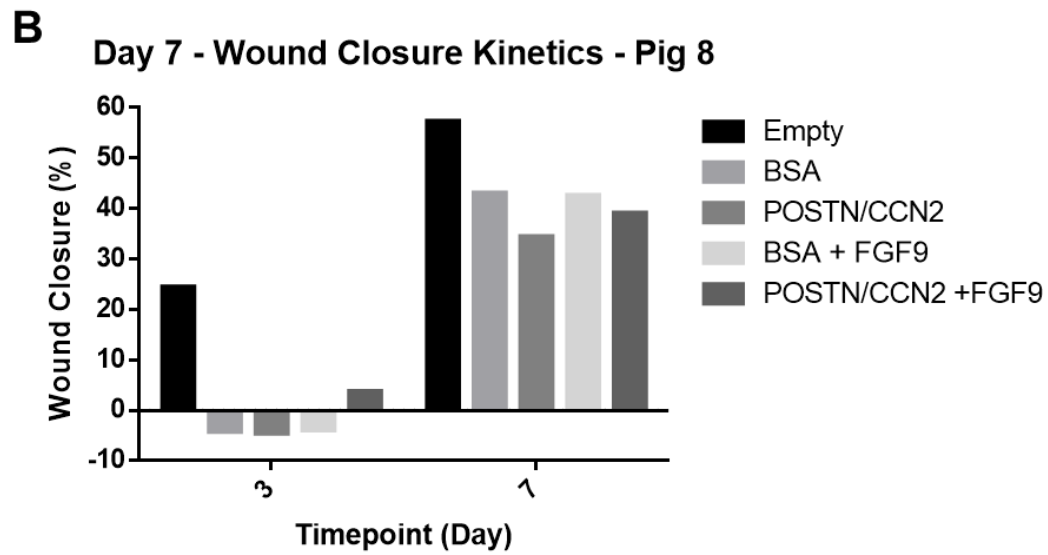
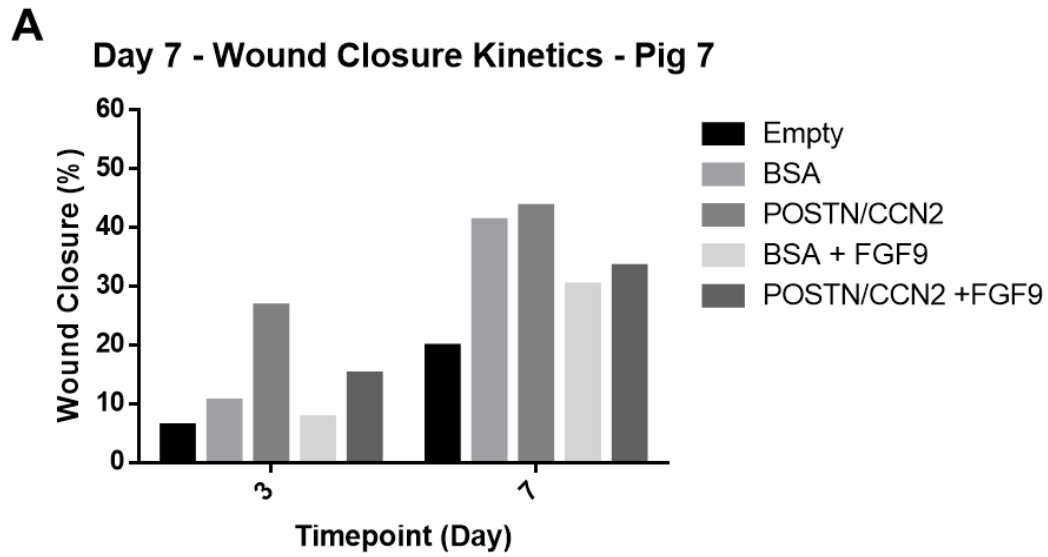


Figure 3. 19 – Representative images of vascular growth 7 days post-wounding in a porcine full-thickness cutaneous wound model. Endothelial tissue was visualized with CD146 immunofluorescent staining. Representative cross-sectional images of the wound bed vasculature from one pig at day 7 post-wounding are shown. Original CD146 fluorescent images and corresponding images after colour thresholding and vessel measurement are shown. Scale bar = 250 μm .

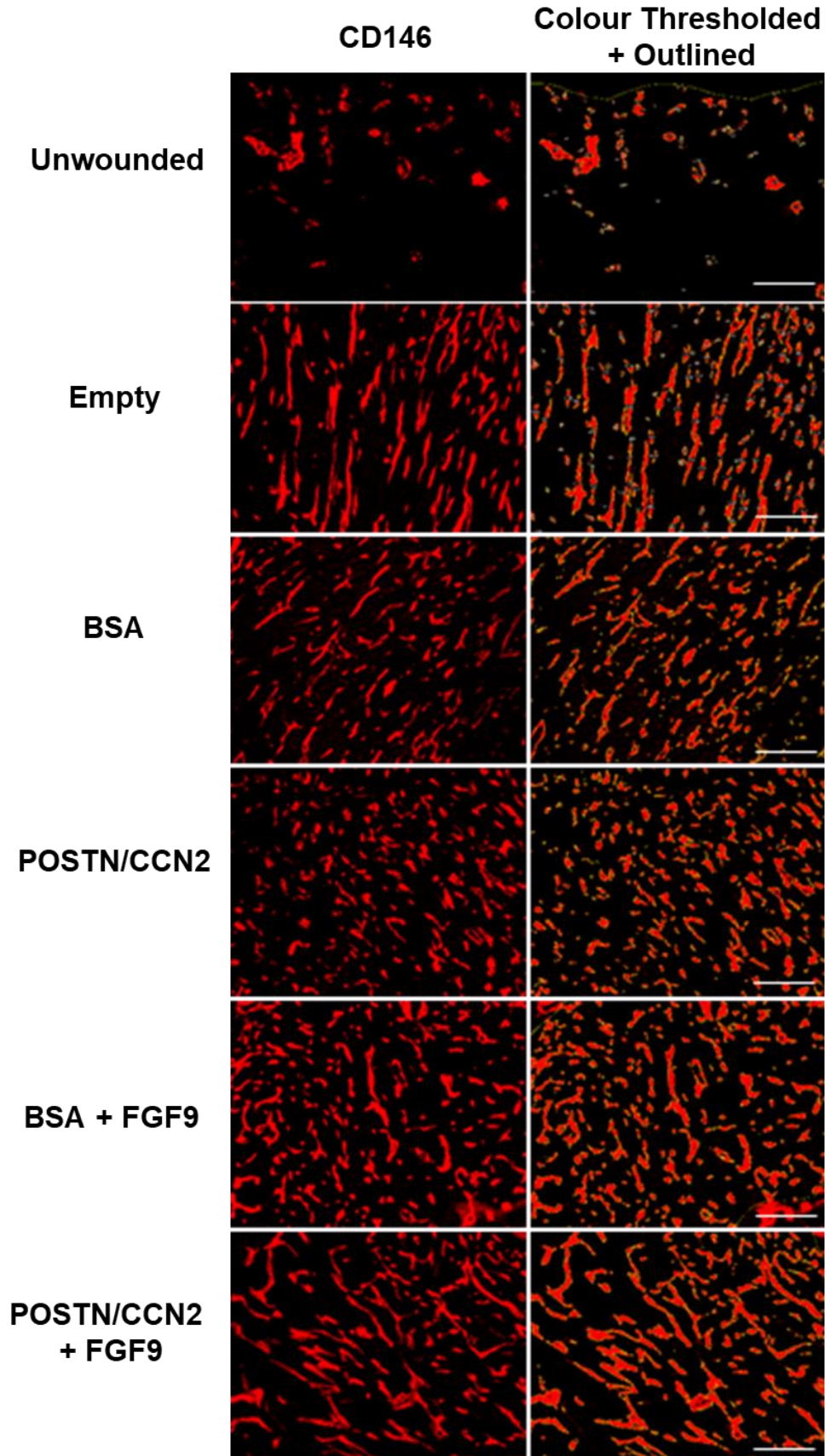


Figure 3. 20 – Effect of biomimetic scaffolds on angiogenesis 7 days post-wounding in a porcine full-thickness cutaneous wound model. Using CD146 as a marker of endothelial tissue in porcine cryosections, blood-vessel density (A), percent wound-tissue area covered by vascular tissue (B), and individual blood-vessel area (C) were quantified with ImageJ’s color deconvolution and threshold particle analysis tools. No differences, in any angiogenic outcome, existed between treatment conditions. **A)** Blood-vessel density significantly increased in wounded tissue. No differences in blood-vessel density existed between treatment conditions. **B)** The proportion of wound area covered by vascular tissue was significantly greater for all treatment conditions compared to controls, except the BSA + FGF9 treatment. **C)** Average individual vessel area was significantly greater in empty and POSTN/CCN2 + FGF9 scaffold treated conditions compared to controls. No other differences were observed. N=3, n=2, one-way ANOVA, Tukey post-test for multiple comparisons, * = $p < 0.05$, ** = $p < 0.01$, *** = $p < 0.001$, **** = $p < 0.0001$. Data presented as mean \pm SD. Angiogenic data are presented independently per pig in Appendix P.

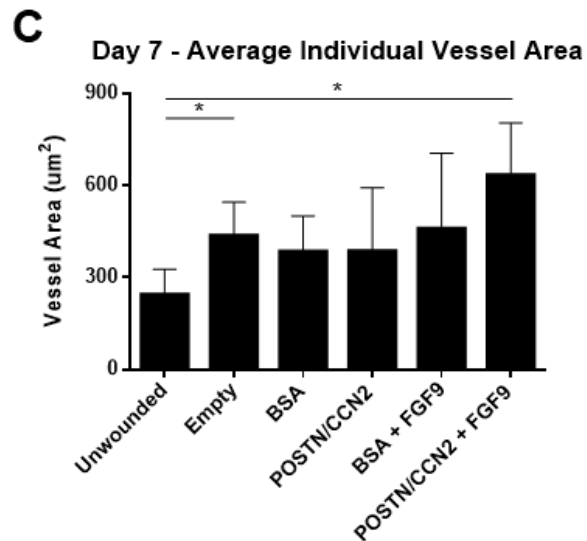
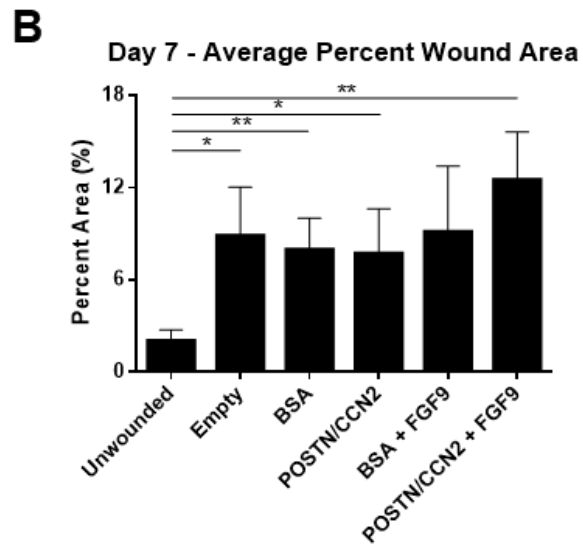
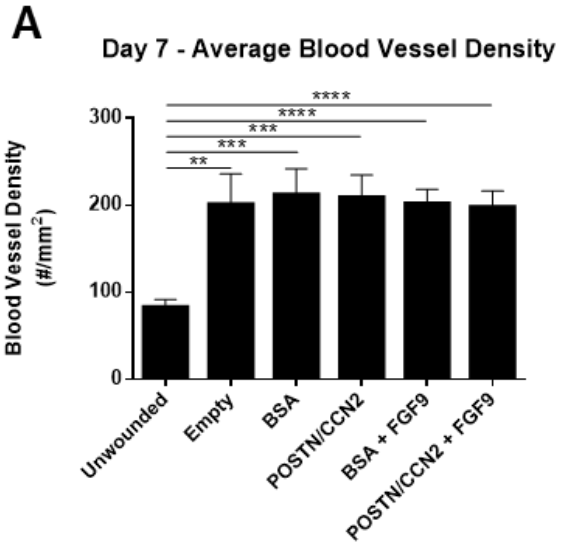


Figure 3. 21 – Angiogenic phenotype in porcine wound tissue 7 days post-wounding.

Fluorescent immunohistochemistry of porcine wound tissue 28 days post-wounding revealed angiogenic phenotype after staining for endothelial markers CD146 and CD105/endoglin. Representative images from one pig are shown. Each set of images include a section of epidermal and superficial dermal wound tissue. CD146 (red), CD105/Endoglin (green), and an overlay including CD146, CD105 and Hoechst stained cellular nuclei (blue) are presented. Scale bar = 50 μ m.

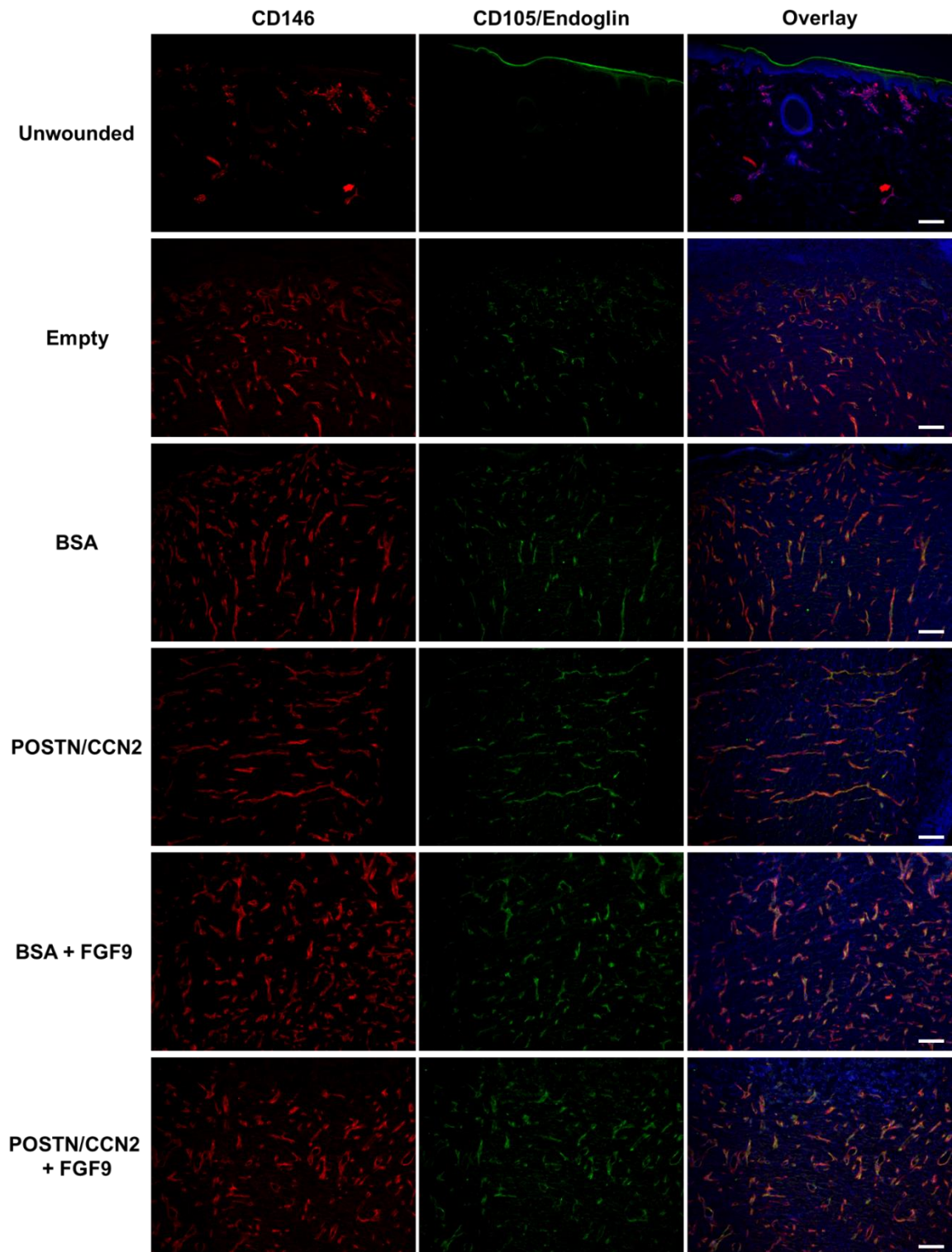
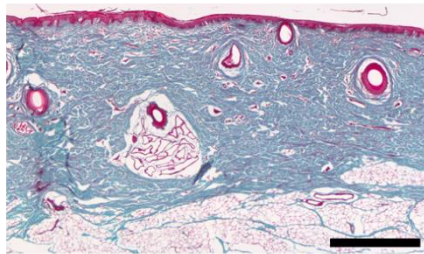
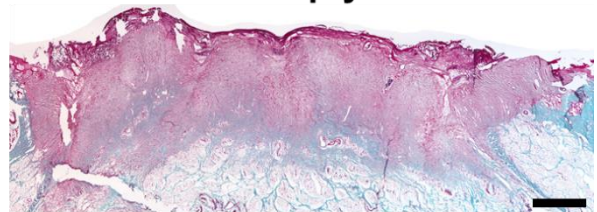


Figure 3. 22 – Effect of biomimetic scaffolds on collagen deposition 7 days post-wounding in a porcine full-thickness cutaneous wound model. Representative cross-sectional images of wound bed collagen deposition 7 days post-wounding, visualized with Masson’s Trichrome staining. Connective tissues (collagen) are stained blue; muscle, erythrocytes and cytoplasm are stained red; and nuclei are stained black. Scale bar = 2 mm.

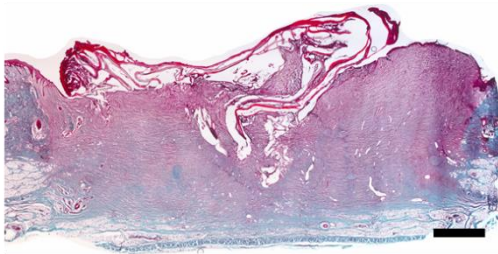
Unwounded



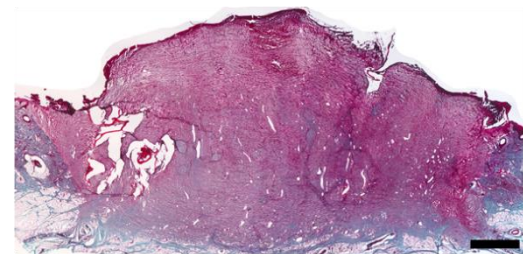
Empty



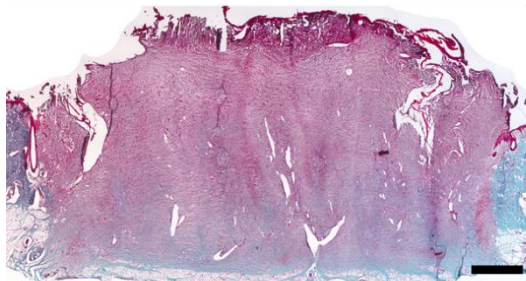
BSA



POSTN/CCN2



BSA + FGF9



POSTN/CCN2 + FGF9

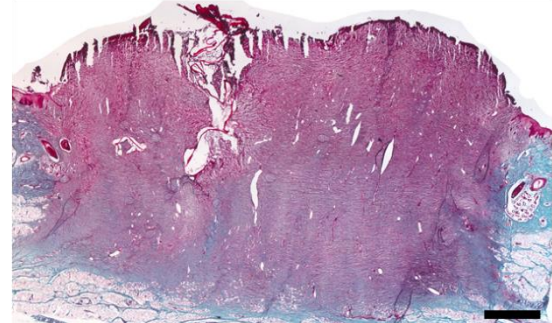
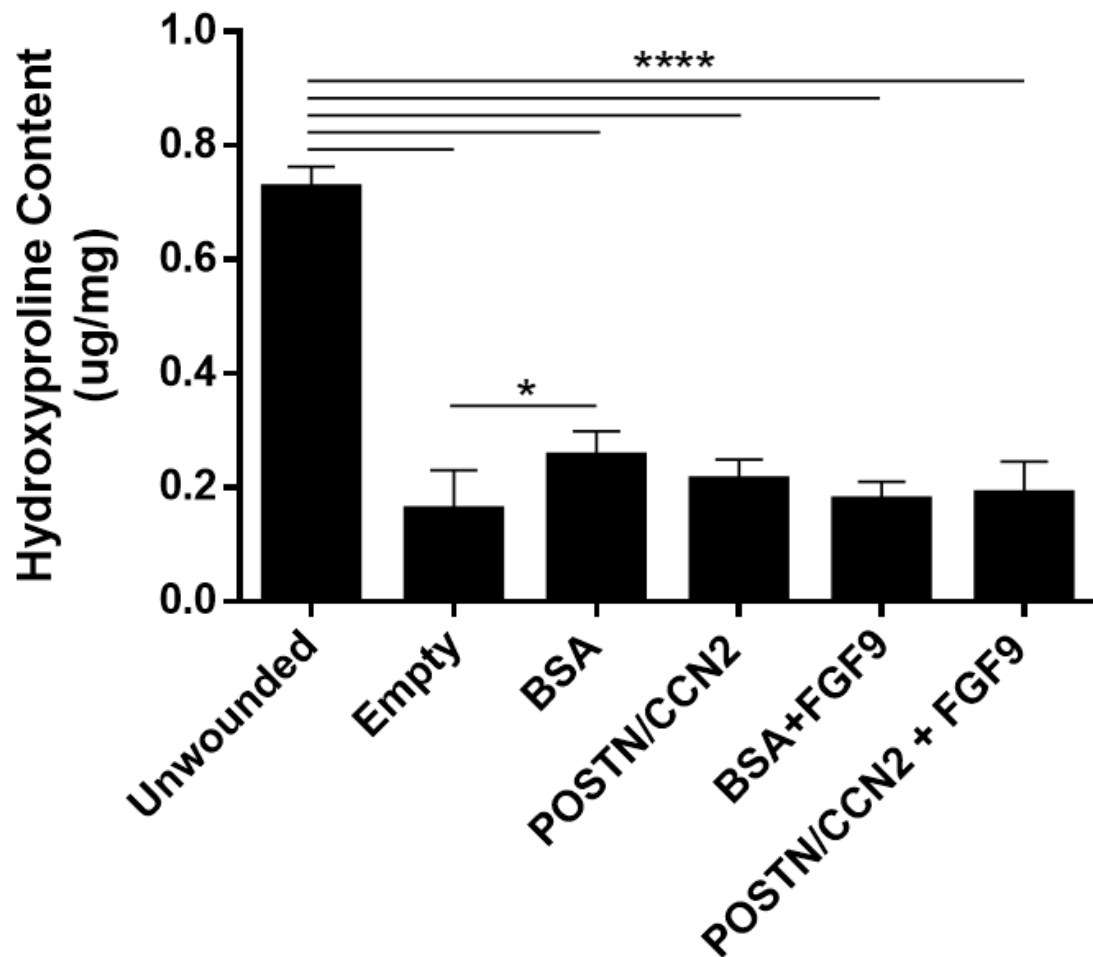


Figure 3. 23 – Hydroxyproline content as an indicator of collagen deposition 7 days post-wounding in a porcine full-thickness cutaneous wound model. Hydroxyproline content was quantified using a Hydroxyproline Assay Kit and normalized based on the dry weight of degraded tissue. Hydroxyproline content was significantly reduced in wounded tissues compared to unwounded tissues. Hydroxyproline content was significantly increased in the BSA scaffold condition compared to empty control wounds. N=3, n=2, one-way ANOVA, Tukey post-test for multiple comparisons, * = $p < 0.05$, **** = $p < 0.0001$. Data presented as mean \pm SD.

D7 - Hydroxyproline Content



3.4 – Discussion

It has been previously shown that POSTN/CCN2 collagen scaffolds enhance angiogenesis in full-thickness, excisional, cutaneous wound in db/db mice (Hamilton lab, In Review, J Tissue Eng). However, incomplete tubule formation and an immature vascular bed likely contributed to the inability of the murine wounds to recover to wild-type rates of wound closure. The series of experiments described in this chapter aimed to design and validate a novel electrohydrodynamic scaffold composed of POSTN/CCN2 electrospun nanofibers and FGF9 electrosprayed core-shell microspheres. Preliminary investigations aimed to reveal the effect of FGF9 on migratory and proliferative actions of HDFs and NIH3T3 murine embryonic fibroblasts to elucidate potential mechanisms of action of FGF9 during wound healing, and as potential indicators of FGF9 activity after release from electrosprayed microspheres. Morphological characterization of electrospun nanofibers and electrosprayed core-shell microspheres was investigated during manipulation of electrohydrodynamic parameters, and *in vitro* release kinetics and biological activity of FGF9 microspheres were assessed to determine microsphere impact. Finally, the efficacy of POSTN/CCN2 scaffolds and FGF9 microspheres in wound repair was investigated in a 7-day porcine model of cutaneous wound healing. Wound closure kinetics, angiogenic growth, and collagen deposition were evaluated and compared to scaffolds without POSTN/CCN2 and FGF9 microspheres.

3.4.1 – *In Vitro* Effects of FGF9 on Cell Populations Involved in Wound Healing

The delivery of FGF9 as a therapeutic wound-healing agent has not been investigated yet. Preliminary experiments aimed to reveal potential cellular effects of FGF9 to elucidate potential mechanisms of action and to serve as indicators of bioactivity after FGF9 release from the microspheres. Dermal fibroblasts are an important cellular component in wound healing. Fibroblasts degrade the fibrin clot, secrete collagen III, fibronectin and hyaluronic acid to compose the granulation tissue's structural matrix, and participate in wound contraction after differentiation into α -smooth muscle actin expressing, contractile myofibroblasts [10]. The effects of FGF9 on migration, chemotaxis, and proliferation of HDFs and of NIH 3T3 mouse embryonic fibroblast chemotaxis were assessed. FGF9 had no effect on HDF migration or NIH 3T3 chemotaxis but significantly increased HDF

chemotaxis and proliferation. Information regarding FGF9's role during wound healing and its effect on dermal fibroblasts is limited however, certain evidence such as induction of hair neogenesis by FGF-Wnt/ β -catenin activation of dermal fibroblasts in mice, illustrates the multifaceted role of FGF9 during wound healing [11]. Future work is necessary to elucidate the molecular mechanisms responsible for the chemotactic and proliferative effects of FGF9 on HDFs.

3.4.2 – Scaffold Fabrication, Design, and Validation

The materials and methods utilized to fabricate the novel electrohydrodynamic scaffold presented here were chosen based on cost-efficiency, scalability, and stability of the incorporated bioactive factors. Gelatin is a cost-efficient natural alternative to collagen [12], capable of dissolution in acetic acid to reduce protein denaturation compared to harsher organic solvents [13]. Organic solvents disrupt secondary and tertiary protein structure, reducing bioactivity of the incorporated factors [13]. Benign solvents such as low concentration acetic acid have been used to produce electrospun collagen fibers of 100-200nm thickness [14, 15]. Furthermore, gelatin was observed to increase average pore size relative to electrospun collagen scaffolds (2000 to 6000 nm² and 1500-4000 nm², respectively) [16]. Gelatin was chosen as the electrospinning polymer because it maintains the biocompatibility and biodegradability of collagen, at a fraction of the cost, without potential antigenicity, and has been shown to stimulate cellular adhesion, migration and proliferation, and accelerate wound healing *in vivo* [17-20].

The release profile of bioactive factors from uniaxial fibers is similar to core-shell microspheres (an initial burst followed by sustained release) however, 30 day cumulative release of bioactive factors from electrospun fibers is substantially lower than from core-shell microspheres (<70% and >80%, respectively) [21-24]. Electrospun fibers were chosen for the delivery of POSTN/CCN2 because the release profile of bioactive factors from uniaxial electrospun fibers correlates with POSTN/CCN2 upregulation on day 3 during wound healing [25]. Both electrospun fibers and electrosprayed microspheres sustain release of bioactive factors and improve bioactivity compared to topical application of bioactive factors [26, 27]. Concurrent release of FGF9 and FGF2 from electrospun fibers directed SMC migration to stabilize endothelial cell/SMC tube formation [21]. FGF9

released alone from electrospun PEA fibers recruited mural cells and enhanced vascular maturation via upregulation of platelet derived growth factor receptor- β [22]. Release of FGF9 from the PEA scaffolds retained bioactivity with limited burst release however, 30-day cumulative FGF9 release only reached 18% and 10% for blend and emulsion electrospinning, respectively. Sustained release of vascular endothelial growth factor-A and -C from core-shell polyurethane nanofibers was achieved by Liao and Leong [28]. Core-shell microspheres have not been used for the delivery of FGF9. To maximize release, improve control over release, and enhance protection of encapsulated bioactive factors, electrospayed core-shell microspheres were chosen for the delivery of FGF9. Physical separation of immiscible core and shell solutions ensure FGF9 stability during processing, and control of shell thickness and porosity by parameter variation and polymer composition enhance FGF9 stability and release *in vivo* [29]. PLGA was chosen as the shell polymer because it is a European Medicines Agency and Federal Drug Association approved, biocompatible, and biodegradable copolymer extensively used in electrohydrodynamic fabrication of wound-healing constructs due to its tunable physicochemical properties [30]. Heparin sodium salt was added to the core solution to increase the stability of FGF9 and FGF9-FGFR binding [31].

Our initial intent was to produce a co-structural scaffold containing evenly dispersed microspheres throughout the nanofiber mesh by simultaneously electrospinning nanofibers and electrospaying microspheres (Figure 1.2). Fabrication of a 3D angiogenic growth factor gradient using this method successfully guided angiogenesis in a murine model [9]. However, an alternative protocol was adopted due to risk of premature hydrolytic degradation during glycine quenching and storage. Therefore, scaffolds and microspheres were fabricated separately with an intermediate glycine quench to block unreacted aldehyde groups after lysin/hydroxylysine crosslinking by glutaraldehyde [32, 33].

For scaffold design, we first characterized electrospun fiber diameter to determine the basis for future manipulation of scaffold morphology. Increasing flow rate and applied voltage decreased fiber diameter whereas increasing collector distance and gelatin concentration increased fiber diameter (Figure 3.6A-C, Figure 3.7J). Parameter variation had no observable effects on fiber orientation.

Several studies support the effect of polymer solution concentration on fiber diameter [34-37]. The interplay between viscosity, surface tension and coulombic repulsion of the polymer solution as it travels towards the collecting surface determines the final fiber diameter with varied solution concentration [38]. At low solution concentrations, the repulsive electrical forces will overcome the surface tension of the polymer solution as solvent evaporates and charge density on the surface of the polymer increases, forming droplets [39]. As solution concentration increases, viscosity increases until the electrical force is no longer strong enough to dissipate the polymer ejection into droplets due to surface tension acting to reduce surface area to mass, instead forming a chain of disjointed beads [35]. Increasing solution concentration enhances the effect of viscoelastic forces, which eventually overcome the influence of surface tension and form smooth fibers. As the solution concentration and viscosity increase further, strengthening viscoelastic forces allow thicker fibers to form [34].

Decreased fiber diameter in response to increased applied voltage is also supported in the literature [34, 40]. At higher applied voltage, the surface charge and field strength of the ejected polymer solution are elevated, increasing coulombic repulsion of the polymer solution to elongate and thin the polymer fiber [34]. Conflicting evidence suggests applied voltage either increases or decreases fiber diameter due to altered mass of polymer ejected, and variation in jet morphology (i.e., the number of ejections) [37].

Flow rate has not been shown to influence fiber diameter [37, 41]. However, increased accumulation of solution at needle tip with increasing flow rate reduces the charge ratio of the solution and decreases the amount of ejected solution due to interference by uncharged particles. Lowering the volume of solution ejected decreases viscoelastic forces as solvent evaporation occurs, which may account for the decreased fiber diameter in response to increasing flow rate [40, 41].

Lengthening the collector distance alters deposition time, evaporation rate, and whipping interval [42]. If the collector distance is too short, inadequate evaporation produces wet fibers, increasing diameter. Limited evidence exists to explain the phenomenon witnessed in this study. Dissipation of electrical forces during transit may reduce the strength of

coulombic repulsion, allowing aggregation of the polymer fiber before deposition, increasing fiber diameter.

The refined scaffold parameters produced a scaffold with the lowest average fiber diameter, low diameter variation, high fiber dispersion on the collection surface, high deposition density, and minimal alternative structures (such as webbing, ribbons, and beads). The lowest fiber diameter was chosen because it most accurately mimicked the fiber diameter of the natural ECM, reportedly between 50-500 nm or 30-130 nm [43, 44], and decreased cell adhesion has been observed as fiber diameter increases [45]. The collector distance was changed to 10 cm in subsequent studies to improve fiber dispersion which was very narrow at 8 cm.

We next assessed the effect of electrospaying parameter variation on microsphere diameter. Maintaining homogeneity in the size, shape and porosity of fabricated microspheres can dictate their performance *in vivo* [37]. Any factor thickening the initial jet diameter will produce spheres of greater diameter after atomization. Increased outer and inner liquid flow rate provide more material to the tip of the needle, increasing the diameter of the coaxial jet which increases sphere diameter [29, 46]. As applied voltage increases, electrical stress elongates the ejected fiber promoting the break-up of the coaxial jet into particles of reduced size [29]. Obvious trends were not observed in response to varied voltage, PLGA concentration, inner flow rate, or collector distance. This result may be due to extraneous confounding variable(s). Solution properties (viscosity, polymer concentration, molecular weight of polymer, electrical conductivity, elasticity, surface tension), processing conditions (applied voltage, collector distance, solution flow rate, needle diameter), and ambient conditions (temperature, humidity, and atmospheric pressure) contribute to the final morphology of electrospayed microspheres [37]. Electrospaying occurred in a laboratory without tight environmental regulation. Therefore, variation in the ambient conditions between trials may account for the variability in sphere morphology (Figure 3.11), compounded by the complexity of coaxial electrospaying with the interaction of multiple proteins and solvents. Impurities in the outer solution may have become lodged in the thin space (diameter = 0.0508 mm) between inner and outer needles, disturbing the flow of the outer solution. The high variability between trials may be

attributable to the inability to achieve a stable Taylor cone. Between the inner and outer solutions, the driving liquid is the solution effecting the electrostatic force of the applied voltage, transferring the electrical stress and fluid motion to the other solution via viscosity [47]. The driving solution is defined as the solution with the lower electrical relaxation time:

$$t_e = \epsilon_r \epsilon_0 / K$$

Where ϵ_r is the relative electrical permittivity (capacitance of an electric field in a particular medium), K is the electrical conductivity of the liquid, and ϵ_0 is the vacuum permittivity constant (8.85×10^{-12} F/m) [47]. BSA was described as the driving liquid in an electro spraying system with outer solution PLGA dissolved in dichloromethane and inner solution BSA dissolved in water, due to the high electrical conductivity of BSA [5, 48]. Microspheres electro sprayed with BSA and PLGA in these studies corroborated our findings of the proportional effect of PLGA concentration on particle size [5, 48]. However, electro spraying with an inner solution as the driving liquid decreases stability of the Taylor cone [49]. The inner BSA solution during electro spraying in the diameter measurement study may account for the inability to achieve a stable Taylor cone and the variability between the trials. Future work is required to electro spray using a needle with a larger inner to outer needle diameter, enhanced environmental control, and a solution combination that produces an outer driving solution to enhance formation and stability of the Taylor cone

The core and shell structures of electro sprayed microspheres were visualized with confocal microscopy. Almost all electro sprayed microspheres contained fluorescent dye, indicating a high encapsulation rate. Future work is necessary to quantify microsphere core-shell morphology, including porosity, core to shell ratio, and thickness in response to varied processing parameters. Quantification of average shell and core diameter in response to varied process parameters such as PLGA concentration, PLGA LA:GA ratio, alternative polymers and solvents, and manipulation of electro spraying parameters should be conducted in the future with release kinetics studies and SEM imaging to determine the effect on microsphere porosity and release. Release of encapsulated bioactive factors is highly dependent on diffusion through the polymer shell relative to porosity and thickness [50]. Increasing shell thickness from 120 nm to 230 nm increased time to 70% drug release

from 11 to 30 days [51]. Increasing outer flow rate, outer solution concentration, and the molecular weight of the outer solution polymer are three methods of thickening the shell structure [37, 52, 53]. Alternatively, introduction of porogens into the shell solution increase porosity to accelerate diffusion of encapsulated factors [54]. The final optimized microsphere will sustain FGF9 release throughout POSTN/CCN2 induced angiogenesis, stabilizing tubule formation and improving the maturity of the vasculature to enhance oxygen and nutrient delivery and promote regeneration.

3.4.3 – FGF9 Release Kinetics & Assessment of Biological Activity

The chosen set of refined electrospaying parameters from the sphere diameter study consistently produced monodisperse microspheres. To determine FGF9 release and bioactivity from the refined microspheres, a concurrent release kinetics study and HDF proliferation assay were conducted. Over 94% of the final concentration of FGF9 in the release media was released on the first day of the study. This burst release may be attributable to high porosity resulting from solvent evaporation during the electrospaying process or shell thickness which may have been thin enough for bulk hydrolytic degradation to fully degrade the shell structure of the microspheres within 24 hours [55]. Decreasing porosity and increasing shell thickness would extend the burst release and promote sustained release from the microspheres. Outer flow rate and shell polymer concentration proportionally control shell thickness, attributable to elevated material density and chain entanglements, and to higher viscosity and surface tension, respectively [52]. Alternatively, increasing voltage has been shown to decrease shell thickness from 119 nm at 3.4 kV to 53 nm at 4.6 kV, accounting for enhanced FGF9 release from microspheres electrospayed at 25 kV [52].

Differential solvent evaporation between the shell and core solutions solidifies the polymer shell before the core solvent has completely evaporated. Vapour pressure eventually overcomes the structural integrity of the solidified shell, producing pores in the shell structure as the evaporated gas escapes [56]. Time to solidification of the shell structure has been delayed by raising polymer concentration to increase viscosity and surface tension which directly counteract the escape of pore forming gas, and by utilizing solvents with elevated boiling points/vapour pressure to reduce evaporation of the shell solution,

prolonging the ability of evaporating gas to escape from the core [52, 57]. Alternatively, blocking pores with dimethyl sulfoxide successfully improved protein entrapment and produced linear release without significant denaturation of the encapsulated protein [58]. Future characterization of FGF9 release at earlier timepoints (e.g., 6, 12, and 18 hours) may enhance our understanding of the mechanisms of release resulting in the 24-hour burst release.

Microspheres electrosprayed with an applied voltage of 25 kV released significantly more FGF9 on the first day. Observations presented here and evidence in the literature suggest that surface charge and field strength increase with elevated voltage, increasing coulombic repulsion and elongating the ejected fiber [29, 34]. Elongation of the coaxial polymer fiber produces core-shell microspheres with reduced diameter [29, 46]. Reducing the diameter of the coaxial polymer ejection subsequently reduces the amount of encapsulated protein after atomization of the jet into core-shell microspheres [59]. Concentration of electrical charge may elongate the outer solution liquid relative to the inner solution, thinning the shell structure and increasing core to shell volume ratio [29]. A thinner shell and larger core may have increased the amount of FGF9 released. Alternatively, increased voltage may improve the stability of the core-shell ejection to increase encapsulation efficiency and the amount of FGF9 available for release without changing the core to shell volume [59].

The HDF proliferation assay began 24 hours after the start of the release kinetics study. Quantification of FGF9 release kinetics indicated that over 94% of the encapsulated FGF9 was released on the first day of the study. HDFs were exposed to 9.01 ng/mL or 8.07 ng/mL FGF9 in the 100 µg/mL FGF9 and 100µg/mL FGF9 – 25 kV trials, respectively. The HDF proliferation assay involved a complete media change on the second day of the study. Therefore, exposure of HDFs to FGF9 was effectively terminated on the second day of the experiment and released FGF9 was observed to have no effect on HDF proliferation. A follow-up study was designed to test the bioactivity of FGF9 released in 48 hours. HDFs were exposed to release media or media supplemented with 100 ng/mL fresh FGF9. The proportion of cells entering S-phase at 24 and 48 hours was quantified by fluorescent EdU incorporation. A significant increase in HDF proliferation in response to FGF9 release media was observed at 48-hours, indicating that the biological activity of released FGF9

was maintained. Future work is required to optimize the release kinetics of FGF9 microspheres to prolong its release.

3.4.4 – 7-Day Porcine Study

Based on the evidence suggesting that FGF9 released from the microspheres was bioactive, the influence of the novel POSTN/CCN2/FGF9 scaffold on angiogenesis and wound repair was investigated in a 7-day porcine model. Representative images of the FGF9 scaffolds are presented in Figure 3.16. The underlying nanofibrous scaffold is not visible due to aggregation of microspheres, PLGA fibers, and larger collapsed droplets.

No differences were observed in percent wound closure at day 3 or 7. Individual 7-day wound closure kinetics for each pig are presented in Figure 3.18 as an indication of the variability in wound closure measurements between pigs. This variability can be attributed to limitations associated with the porcine model, including wound eschar blocking the wound border (as can be seen at day 7 in Figure 3.15), and inter-animal variability. Wound diameter significantly decreased in response to BSA/FGF9 and POSTN/CCN2/FGF9 scaffolds compared to empty wounds at day 7. Hydroxyproline content significantly decreased in wounded tissues compared to unwounded tissue. POSTN and CCN2 have been shown to facilitate myofibroblast differentiation and promote ECM deposition and fibrogenesis by proliferating fibroblasts during cutaneous wound healing [60-62]. In addition, application of rhCCN2 to a rhesus-monkey burn wound model increased wound closure, fibroblast migration into the wound bed and collagen deposition, and accelerated re-epithelialization [63]. However, BSA/FGF9 scaffolds also significantly decreased wound diameter compared to empty wounds, indicating that FGF9, and not POSTN/CCN2, may have contributed to reduced wound diameter at day 7. Based on our findings that FGF9 increases HDF chemotaxis and proliferation, FGF9 released from the scaffolds may have recruited dermal fibroblasts to the site of injury, enhancing granulation tissue formation and subsequent myofibroblast presence, increasing contraction of the wound bed and reducing wound diameter. Additional work is required to quantify cellular populations in the wound bed tissue to determine potential mechanisms of action of FGF9 that would account for the reduction in wound diameter in the treatment conditions with FGF9 microspheres.

We have observed for the first-time chemotactic and pro-proliferative effects of FGF9 on HDFs *in vitro*. FGF9 action on HDFs *in vivo* has not been investigated however, based on these results, we suggest that reduced wound diameter at day 7, in response to BSA/FGF9 and POSTN/CCN2/FGF9 scaffold treatments, may be a result of FGF9 action on HDF proliferation and chemotaxis. Future work is required to determine the role of FGF9 during wound healing *in vivo*. In Masson's Trichrome stained sections, collagen bundle formation appears to be occurring at the level of the subcutaneous tissue, deep within the wound bed. Scaffolds are still visible in the wound eschar or within the granulation tissue.

3.5 – Conclusions

Preliminary experimentation revealed proliferative and chemotactic effects of FGF9 on HDFs. A novel electrohydrodynamic scaffold was designed and validated *in vitro* and *in vivo*. Processing control over fiber diameter was presented however, extraneous variables inhibited a clear observation of the effect of process parameters on microsphere diameter. Refined microspheres exhibited complete 24-72 hour burst release of encapsulated FGF9 that retained its bioactivity. Scaffolds containing FGF9 microspheres significantly decreased wound diameter compared to empty wounds in a 7-day porcine cutaneous wound-healing model. No other differences between treatment conditions were observed, which may be due to the acute state of the wound healing model. Future work is required to characterize the proportion of cell populations (fibroblasts, myofibroblasts, M1 and M2 macrophages) in the wound bed to evaluate scaffold influence on wound closure.

3.6 – References

1. Pilehvar-Soltanahmadi, Y., et al., *An update on clinical applications of electrospun nanofibers for skin bioengineering*. *Artif Cells Nanomed Biotechnol*, 2016. **44**(6): p. 1350-64.
2. Prabhakaran, M.P., et al., *Electrospraying technique for the fabrication of metronidazole contained PLGA particles and their release profile*. *Materials Science and Engineering: C*, 2015. **56**: p. 66-73.
3. Lee, J., et al., *The effect of controlled release of PDGF-BB from heparin-conjugated electrospun PCL/gelatin scaffolds on cellular bioactivity and infiltration*. *Biomaterials*, 2012. **33**(28): p. 6709-20.
4. Stephansen, K., I.S. Chronakis, and F. Jessen, *Bioactive electrospun fish sarcoplasmic proteins as a drug delivery system*. *Colloids Surf B Biointerfaces*, 2014. **122**: p. 158-165.
5. Xie, J., et al., *Encapsulation of protein drugs in biodegradable microparticles by co-axial electrospray*. *Journal of Colloid and Interface Science*, 2008. **317**(2): p. 469-476.
6. Frontini, M.J., et al., *Fibroblast growth factor 9 delivery during angiogenesis produces durable, vasoresponsive microvessels wrapped by smooth muscle cells*. *Nat Biotechnol*, 2011. **29**(5): p. 421-7.
7. Yin, H., et al., *Fibroblast Growth Factor 9 Imparts Hierarchy and Vasoreactivity to the Microcirculation of Renal Tumors and Suppresses Metastases*. *J Biol Chem*, 2015. **290**(36): p. 22127-42.
8. Agrotis, A., et al., *Proliferation of neointimal smooth muscle cells after arterial injury. Dependence on interactions between fibroblast growth factor receptor-2 and fibroblast growth factor-9*. *J Biol Chem*, 2004. **279**(40): p. 42221-9.
9. Guo, X., et al., *Creating 3D angiogenic growth factor gradients in fibrous constructs to guide fast angiogenesis*. *Biomacromolecules*, 2012. **13**(10): p. 3262-71.
10. P, B., *Wound healing and the role of fibroblasts*. *Journal of Wound Care*, 2013. **22**(8): p. 407-412.
11. Gay, D., et al., *Fgf9 from dermal gammadelta T cells induces hair follicle neogenesis after wounding*. *Nat Med*, 2013. **19**(7): p. 916-23.
12. Malafaya, P.B., G.A. Silva, and R.L. Reis, *Natural-origin polymers as carriers and scaffolds for biomolecules and cell delivery in tissue engineering applications*. *Adv Drug Deliv Rev*, 2007. **59**(4-5): p. 207-33.
13. Gast, K., et al., *Fluoroalcohol-induced structural changes of proteins: some aspects of cosolvent-protein interactions*. *Eur Biophys J*, 2001. **30**(4): p. 273-83.
14. Liu, T., et al., *Photochemical crosslinked electrospun collagen nanofibers: synthesis, characterization and neural stem cell interactions*. *J Biomed Mater Res A*, 2010. **95**(1): p. 276-82.
15. Erencia, M., et al., *Resolving the electrospinnability zones and diameter prediction for the electrospinning of the gelatin/water/acetic acid system*. *Langmuir*, 2014. **30**(24): p. 7198-205.
16. Plowman, J.E., S. Deb-Choudhury, and J.M. Dyer, *Fibrous protein nanofibers*. *Methods Mol Biol*, 2013. **996**: p. 61-76.

17. Hassiba, A.J., et al., *Review of recent research on biomedical applications of electrospun polymer nanofibers for improved wound healing*. Nanomedicine (Lond), 2016. **11**(6): p. 715-37.
18. Pezeshki-Modaress, M., et al., *Gelatin/chondroitin sulfate nanofibrous scaffolds for stimulation of wound healing: In-vitro and in-vivo study*. J Biomed Mater Res A, 2017. **105**(7): p. 2020-2034.
19. Duan, H., et al., *Engineering of epidermis skin grafts using electrospun nanofibrous gelatin/ polycaprolactone membranes*. Int J Nanomedicine, 2013. **8**: p. 2077-84.
20. Dubsky, M., et al., *Nanofibers prepared by needleless electrospinning technology as scaffolds for wound healing*. J Mater Sci Mater Med, 2012. **23**(4): p. 931-41.
21. Said, S.S., et al., *Concurrent and Sustained Delivery of FGF2 and FGF9 from Electrospun Poly(ester amide) Fibrous Mats for Therapeutic Angiogenesis*. Tissue Eng Part A, 2016. **22**(7-8): p. 584-96.
22. Said, S.S., J.G. Pickering, and K. Mequanint, *Controlled delivery of fibroblast growth factor-9 from biodegradable poly(ester amide) fibers for building functional neovasculature*. Pharm Res, 2014. **31**(12): p. 3335-47.
23. Ji, W., et al., *Fibrous scaffolds loaded with protein prepared by blend or coaxial electrospinning*. Acta Biomater, 2010. **6**(11): p. 4199-207.
24. Pek, Y.S., P. Pitukmanorom, and J. Y Ying, *Sustained Release of Bupivacaine for Post-Surgical Pain Relief Using Core-Shell Microspheres*. Vol. 2. 2014.
25. Hamilton, D., et al., *Cell-matrix interactions governing skin repair: matricellular proteins as diverse modulators of cell function*. Research and Reports in Biochemistry, 2015: p. 73.
26. Saraf, A., et al., *Regulated non-viral gene delivery from coaxial electrospun fiber mesh scaffolds*. J Control Release, 2010. **143**(1): p. 95-103.
27. Lee, Y.H., et al., *Release profile characteristics of biodegradable-polymer-coated drug particles fabricated by dual-capillary electrospray*. J Control Release, 2010. **145**(1): p. 58-65.
28. Liao, I.-C. and K.W. Leong, *Efficacy of engineered FVIII-producing skeletal muscle enhanced by growth factor-releasing co-axial electrospun fibers*. Biomaterials, 2011. **32**(6): p. 1669-1677.
29. Yuan, S., et al., *Coaxial Electrospray of Curcumin-Loaded Microparticles for Sustained Drug Release*. PLoS One, 2015. **10**(7): p. e0132609.
30. Evrova, O., et al., *Hybrid Randomly Electrospun Poly(lactic-co-glycolic acid):Poly(ethylene oxide) (PLGA:PEO) Fibrous Scaffolds Enhancing Myoblast Differentiation and Alignment*. ACS Appl Mater Interfaces, 2016. **8**(46): p. 31574-31586.
31. Geske, M.J., et al., *Fgf9 signaling regulates small intestinal elongation and mesenchymal development*. Development, 2008. **135**(17): p. 2959-68.
32. Damink, L.O., et al., *Glutaraldehyde as a crosslinking agent for collagen-based biomaterials*. Journal of materials science: materials in medicine, 1995. **6**(8): p. 460-472.
33. Akin, H. and N. Hasirci, *Preparation and characterization of crosslinked gelatin microspheres*. Journal of Applied Polymer Science, 1995. **58**(1): p. 95-100.
34. Katti, D.S., et al., *Bioresorbable nanofiber-based systems for wound healing and drug delivery: optimization of fabrication parameters*. J Biomed Mater Res B Appl Biomater, 2004. **70**(2): p. 286-96.

35. Fong, H., I. Chun, and D.H. Reneker, *Beaded nanofibers formed during electrospinning*. Polymer, 1999. **40**(16): p. 4585-4592.
36. Reneker, D.H., et al., *Bending instability of electrically charged liquid jets of polymer solutions in electrospinning*. Journal of Applied Physics, 2000. **87**(9): p. 4531-4547.
37. Tan, S.H., et al., *Systematic parameter study for ultra-fine fiber fabrication via electrospinning process*. Polymer, 2005. **46**(16): p. 6128-6134.
38. Rayleigh, L., XX. *On the equilibrium of liquid conducting masses charged with electricity*. The London, Edinburgh, and Dublin Philosophical Magazine and Journal of Science, 1882. **14**(87): p. 184-186.
39. Zeleny, J., *The Electrical Discharge from Liquid Points, and a Hydrostatic Method of Measuring the Electric Intensity at Their Surfaces*. Physical Review, 1914. **3**(2): p. 69-91.
40. Pezeshki-Modaress, M., H. Mirzadeh, and M. Zandi, *Gelatin-GAG electrospun nanofibrous scaffold for skin tissue engineering: Fabrication and modeling of process parameters*. Mater Sci Eng C Mater Biol Appl, 2015. **48**: p. 704-12.
41. Bakar, S.S.S., et al., *Effect of Voltage and Flow Rate Electrospinning Parameters on Polyacrylonitrile Electrospun Fibers*. IOP Conference Series: Materials Science and Engineering, 2018. **318**(1): p. 012076.
42. Subbiah, T., et al., *Electrospinning of nanofibers*. Journal of Applied Polymer Science, 2005. **96**(2): p. 557-569.
43. Rho, K.S., et al., *Electrospinning of collagen nanofibers: effects on the behavior of normal human keratinocytes and early-stage wound healing*. Biomaterials, 2006. **27**(8): p. 1452-61.
44. Murugan, R. and S. Ramakrishna, *Design strategies of tissue engineering scaffolds with controlled fiber orientation*. Tissue Eng, 2007. **13**(8): p. 1845-66.
45. Chen, M., et al., *Role of Fiber Diameter in Adhesion and Proliferation of NIH 3T3 Fibroblast on Electrospun Polycaprolactone Scaffolds*. Vol. 13. 2007. 579-87.
46. Si, T., et al., *Experimental design and instability analysis of coaxial electrospay process for microencapsulation of drugs and imaging agents*. J Biomed Opt, 2013. **18**(7): p. 075003.
47. Olvera-Trejo, D. and L.F. Velasquez-Garcia, *Additively manufactured MEMS multiplexed coaxial electrospay sources for high-throughput, uniform generation of core-shell microparticles*. Lab Chip, 2016. **16**(21): p. 4121-4132.
48. Xu, Y. and M.A. Hanna, *Morphological and structural properties of two-phase coaxial jet electrospayed BSA-PLA capsules*. Journal of Microencapsulation, 2008. **25**(7): p. 469-477.
49. Fan, M. and C. Da-Ren, *Operational Modes of Dual-capillary Electrospaying and the Formation of the Stable Compound Cone-jet Mod.* Aerosol and Air Quality Research, 2008. **8**(2): p. 218-232.
50. Lee, Y.H., M.Y. Bai, and D.R. Chen, *Multidrug encapsulation by coaxial tri-capillary electrospay*. Colloids Surf B Biointerfaces, 2011. **82**(1): p. 104-10.
51. Wang, C., et al., *Biodegradable Core/Shell Fibers by Coaxial Electrospinning: Processing, Fiber Characterization, and Its Application in Sustained Drug Release*. Macromolecules, 2010. **43**(15): p. 6389-6397.

52. Chang, M.-W., E. Stride, and M. Edirisinghe, *Controlling the thickness of hollow polymeric microspheres prepared by electrohydrodynamic atomization*. Journal of the Royal Society Interface, 2010. **7**(Suppl 4): p. S451-S460.
53. Shang, Y., et al., *Dual-drug release from chitin-based core-shell microspheres fabricated by coaxial electrospray*. Advances in Polymer Technology, 2017. **0**(0).
54. Cai, Y., et al., *Porous microsphere and its applications*. International Journal of Nanomedicine, 2013. **8**: p. 1111-1120.
55. Kumari, A., S.K. Yadav, and S.C. Yadav, *Biodegradable polymeric nanoparticles based drug delivery systems*. Colloids and Surfaces B: Biointerfaces, 2010. **75**(1): p. 1-18.
56. Yao, J., et al., *Characterization of electrospraying process for polymeric particle fabrication*. Journal of Aerosol Science, 2008. **39**(11): p. 987-1002.
57. Bohr, A., et al., *Release profile and characteristics of electrosprayed particles for oral delivery of a practically insoluble drug*. Journal of the Royal Society Interface, 2012. **9**(75): p. 2437-2449.
58. Paik, D.-H. and S.-W. Choi, *Entrapment of Protein Using Electrosprayed Poly(D,L-lactide-co-glycolide) Microspheres with a Porous Structure for Sustained Release*. Macromolecular Rapid Communications, 2014. **35**(11): p. 1033-1038.
59. Nguyen, D.N., C. Clasen, and G. Van den Mooter, *Pharmaceutical Applications of Electrospraying*. Journal of Pharmaceutical Sciences, 2016. **105**(9): p. 2601-2620.
60. Elliott, C.G., et al., *Periostin modulates myofibroblast differentiation during full-thickness cutaneous wound repair*. Journal of Cell Science, 2011.
61. Elliott, C.G., et al., *Periostin modulates myofibroblast differentiation during full-thickness cutaneous wound repair*. J Cell Sci, 2012. **125**(Pt 1): p. 121-32.
62. Brigstock, D.R., *Connective tissue growth factor (CCN2, CTGF) and organ fibrosis: lessons from transgenic animals*. J Cell Commun Signal, 2010. **4**(1): p. 1-4.
63. Liu, L.D., et al., *The repairing effect of a recombinant human connective-tissue growth factor in a burn-wounded rhesus-monkey (Macaca mulatta) model*. Biotechnol Appl Biochem, 2007. **47**(Pt 2): p. 105-12.

Chapter 4

General Discussion

4.1 – Summary & Final Conclusions

4.1.1 – Objective 1. To determine the influence of nanofibrous electrospun POSTN/CCN2 scaffolds on angiogenesis and wound repair 28 days post-wounding in a porcine model of cutaneous wound healing.

BSA scaffolds significantly delayed wound closure between days 8 and 15. No differences were observed in wound diameter between scaffold treated wounds and empty control wounds at day 28. No significant differences were observed in angiogenesis or collagen deposition.

4.1.2 – Objective 2. To design and validate an electrospun POSTN/CCN2 scaffold with coaxially electrosprayed core-shell microspheres encapsulating FGF9.

a. Assess *in vitro* effect of FGF9 on cellular populations involved in wound healing.

FGF9 significantly increased HDF proliferation and chemotaxis in a dose-dependent manner. No differences of FGF9 treatment on HDF 2-D migration or NIH 3T3 chemotaxis were observed.

b. Design and validate a POSTN/CCN2 scaffold with FGF9/PLGA microspheres using a new electrohydrodynamic system.

For scaffold optimization, we first characterized the effect of varying processing parameters on electrospun fiber diameter. Increasing flow rate and the applied voltage resulted in decreasing fiber diameter whereas increasing collector distance and gelatin concentration increased fiber diameter, consistent with previous findings [1-3]. Refined electrospinning parameters produced a scaffold with the lowest fiber diameter, within the range of dermal ECM collagen fibers [4, 5]. Processing parameters of the refined scaffold included: 0.5 mL/h flow rate, 17 kV applied voltage, and 8 cm collector distance. Increasing outer flow rate increased the diameter of microspheres. Lack of control over ambient conditions, clogging of the coaxial needle, or an inner driving liquid may have contributed

to high variability between electro spraying trials, resulting in no clear effects of applied voltage, PLGA concentration, inner flow rate, or collector distance on microsphere diameter. Confocal microscopy indicated a high encapsulation rate and a clear core-shell structure of electro sprayed microspheres.

c. Determine biological activity and release kinetics of encapsulated FGF9/PLGA microspheres.

Initial experimentation indicated a 24-hour burst release of FGF9 from the microspheres with no effect on HDF proliferation, indicating loss of bioactivity. However, a follow-up study with a revised protocol tailored to the burst release kinetics showed that FGF9 released from the microspheres significantly increased HDF proliferation at 48 hours.

4.1.3 – Objective 3. To determine the influence of nanofibrous electro spun POSTN/CCN2 scaffolds with FGF9/PLGA microspheres on angiogenesis and wound repair 7 days post-wounding in a porcine model of cutaneous wound healing.

Wound closure rates were similar between all conditions 7 days post-wounding. However, wound diameter was significantly reduced in BSA/FGF9 and POSTN/CCN2/FGF9 scaffold treated wounds compared to empty control wounds. Angiogenesis significantly increased in all wounds irrespective of treatment. Visualization of the vascular bed indicates a branching vascular network in POSTN/CCN2/FGF9 sections relative to the linear parallel vessels observed in empty wound sections. Hydroxyproline content was significantly reduced in all wounded tissues relative to unwounded tissues at day 7 post-wounding. BSA scaffolds significantly increased hydroxyproline content compared to empty wounds. No evidence was found of any of the scaffold treatments resulting in a foreign body response 7 days post-wounding.

4.2 – Contributions to the Current State of Knowledge

4.2.1 – General Significance

Chronic wounds are characterized by a pro-inflammatory microenvironment, enhanced proteolytic activity, and excessive degradation of matrix components and signalling molecules [6]. Cellular senescence, reduced mitogenic activity, and heightened bacterial

load disrupt fibrogenesis, angiogenesis, re-epithelialization, matrix deposition, and wound contraction producing the pathophysiology indicative of chronic wounds [7]. Pathological angiogenesis has been indicated as a key contributor to the development of chronic wounds, but no wound care based strategy to influence this has been developed [8]. Standard chronic wound therapies manage infection, establish moisture balance with moisture retentive wound dressings, remove necrotic tissue, and support the healing process with pressure offloading and revascularization procedures [9]. However, these methods are suboptimal, leading to ulcer recurrence in up to 70% of patients due to the inability of conventional dressings to properly address the underlying pathological mechanisms acting within the chronic wound environment resulting in fibrotic repair [10]. Conventional dressings reduce bacterial burden and provide moisture control but do very little to actively re-establish the native wound microenvironment to promote tissue regeneration. Furthermore, current bioactive alternatives such as bioengineered skin substitutes (e.g., Dermagraft®) and growth factor therapies have low clinical efficacy and are limited by high costs, short shelf life (under 5 days), fragility, and rapid degradation of bioactive factors upon release *in vivo* [11, 12].

Angiogenesis is impaired in all chronic wounds, contributing to further tissue damage through chronic hypoxia, impaired nutrient delivery, and defective granulation tissue formation [13]. Previous work in our laboratory showed that POSTN was significantly suppressed at the edge of human chronic wounds and that blood vessels do not grow into the wound bed [14]. However, POSTN/CCN2 scaffolds rescued delayed healing and supported vascular growth in db/db mice (Hamilton lab, In Review, J Tissue Eng), although micro-CT angiography showed the blood vessels formed were leaky and mural cell recruitment and stabilization was required. Electrohydrodynamic atomization is a cost-efficient, simple, scalable alternative to conventional methods of biomaterial scaffold fabrication. We have designed and validated a novel electrohydrodynamic granulation tissue-mimetic biomaterial scaffold as a delivery vehicle of POSTN, CCN2, and FGF9 to re-establish the presence of these bioactive factors within the proteolytic chronic wound microenvironment and to promote and stabilize new vascular growth. FGF9 has been shown to enhance mural cell wrapping during endothelial tubule formation to stabilize vasculature and improve vasoreactivity of the vessels [15]. Therefore, the aim of the novel

POSTN/CCN2/FGF9 scaffold was to re-establish POSTN and CCN2 to promote angiogenesis within the inflammatory chronic wound microenvironment, and to support that vascular growth via FGF9 mediated mural cell layering to facilitate oxygen and nutrient delivery, and to promote inflammatory to proliferative transition in chronic wounds [13].

4.2.2 – POSTN/CCN2/FGF9 Scaffolds for Tissue Repair

POSTN and CCN2 are matricellular proteins upregulated during the proliferative phase of wound healing. POSTN facilitates dermal fibroblast activation, differentiation and contraction, contributing to dermal regeneration and wound closure [16-18]. CCN2 promotes myofibroblast ECM deposition and fibrogenesis, stimulates endothelial cell proliferation and chemotaxis for neovascular tubule formation, and regulates expression of angiogenic factors such as vascular endothelial growth factor-A and -C [19-23]. FGF9 promotes mural cell wrapping of nascent vasculature to improve stability and vasoreactivity of the vessels [15]. With clinical translation in mind, the overall aim of this thesis was to develop cost-efficient methods for the delivery of POSTN, CCN2, and FGF9 for wound-healing purposes.

We utilized electrospinning, which is an excellent method for reproducibly fabricating biomimetic nanofibrous scaffolds from a wide variety of natural and synthetic polymers with biologically relevant features [24]. Various studies have electrospun nanofibrous scaffolds with structural mimicry to the dermal ECM (fiber diameters of 30 to 500nm) [4, 5, 25-28] indicating a decrease in cell adhesion and growth kinetics as fiber diameter increases [29]. Therefore, we chose the electrospinning combination that produced the lowest average fiber diameter while maintaining uniform fibers. However, the bioactive potential of uniaxial electrospun nanofibers is limited by increased protein denaturation due to direct solvent exposure during blending of the polymer electrospinning solution, and rapid degradation of bioactive factors on the surface of the fibers exposed to the proteolytic *in vivo* microenvironment [6]. Electrospayed core-shell microspheres reduce protein-solvent interaction and physically protect encapsulated bioactive factors from proteolytic degradation. POSTN/CCN2 collagen scaffolds previously enhanced angiogenic growth and wound closure in db/db mice (Hamilton lab, In Review, J Tissue Eng). In this study,

the collagen scaffold was redesigned using gelatin as the electrospinning polymer to reduce costs while maintaining the functional and mechanical properties of the original scaffold. FGF9 electrosprayed microspheres were designed as an additional component of the POSTN/CCN2 scaffold, to protect and sustain release of FGF9 throughout POSTN/CCN2 action during wound healing, with the goal of promoting the stabilization of POSTN/CCN2 induced vascular formation via mural cell wrapping [15].

The influence of POSTN/CCN2 and the novel POSTN/CCN2/FGF9 scaffolds on angiogenesis and wound repair was investigated during the proliferative and remodelling stages of wound healing in two porcine studies. To our knowledge, this was the first investigation of FGF9 in a porcine model of cutaneous wound healing.

Gelatin biomaterials have been shown to elicit a foreign body response in mice [30], which may account for delayed wound closure in BSA scaffolds treated wounds compared to empty control wounds between days 8 and 15 in the 28-day porcine study. Based on their defined roles in healing [19-21, 31], the POSTN/CCN2 scaffold may have stimulated fibroblast migration, proliferation, deposition of fibronectin and collagen, and differentiation into myofibroblasts to begin contraction, accounting for the lack of a significant difference in wound closure between POSTN/CCN2 scaffolds and empty wound conditions. Day 7 wound diameter was significantly reduced in BSA/FGF9 and POSTN/CCN2/FGF9 scaffold treated wounds compared to empty wounds, indicating a potential role of encapsulated FGF9, and not POSTN and CCN2, on wound closure. Further work is necessary to characterize the cellular populations within the wound bed at day 28 to determine potential cellular effects of FGF9 on wound closure *in vivo*.

Day-7 angiogenic measures indicated significant increases in blood-vessel density, percent wound area covered by vascular tissue, and individual vessel size in wounded tissues compared to unwounded tissue. Furthermore, vessel phenotype changes between wounded conditions. Linear, elongated vasculature forming in empty wounds branches into a more randomized vascular bed in response to scaffold treated wounds, especially BSA/FGF9 and POSTN/CCN2/FGF9 scaffolds. FGF9 is known to enhance vascular stability and vasoreactivity via mural cell wrapping of developing vasculature [15]. Therefore, enhanced branching observed in the fluorescent images of the vascular bed may be indicative of

improved vessel stability by released FGF9. However, proteolytic, acidic and temperature-related mechanisms present within the healthy wound microenvironment quickly degrade bioactive factors *in vivo* [32]. In the acute porcine wounds, burst released FGF9 during the first 24 hours of the study was likely degraded. Therefore, FGF9 is most likely not the cause of enhanced vascular growth. Future work is required to increase shell thickness and reduce porosity to improve sustained release and protect FGF9 from the enhanced proteolytic mechanisms in the chronic wound microenvironment [6].

POSTN promotes migration and tube formation of human umbilical vein endothelial cells via extracellular signal-regulated kinase (ERK) -1/2 and focal adhesion kinase signalling [33], and CCN2 stimulates endothelial cell proliferation and chemotaxis to promote neovascular tubule formation [21]. No differences were observed between angiogenic measures of POSTN/CCN2 and BSA scaffolds in the 28-day porcine study, suggesting the POSTN/CCN2 scaffold did not influence angiogenic processes despite previous evidence indicating an influence of POSTN and CCN2 on endothelial cell migration, proliferation, and tube formation [33, 34]. This may be due to the acute nature of the wound healing model masking the effects of POSTN and CCN2 released into the wound bed. Healthy wound healing mechanisms and a normal balance of wound healing mediators may have reduced the observable effect of exogenous POSTN and CCN2 [35].

Between days 7 and 28, blood-vessel density (204.91 vessels/mm² versus 180.96 vessels/mm², respectively), percent wound area covered by vascular tissue (4.27% versus 9.14%, respectively), and individual blood-vessel area (462.22 μm^2 versus 155.11 μm^2 , respectively) significantly decreased (Appendix S). Decreased vessel density and size at day 28 are indicative of vascular regression as the preliminary vascular network is remodelled and stabilized in the later stages of healing [36-38]. The natural reduction of vascular tissue may explain the lack of differences in blood-vessel density between wounded and unwounded tissues during the 28-day porcine study.

POSTN and CCN2 have been indicated in fibroblast activation, differentiation, and ECM deposition [16, 17, 19, 39]. POSTN/CCN2 scaffolds did not elicit increased collagen deposition in the porcine wounds at day 7 or day 28, contradictory to previous descriptions of the action of these matricellular proteins during wound healing. The rapid rate of healing

and normal expression of POSTN, CCN2, and FGF9 in the healthy pigs may have reduced the influence of the POSTN/CCN2 and POSTN/CCN2/FGF9 scaffolds at days 7 and 28, respectively [35].

In this thesis, we have presented for the first time the influence of a novel POSTN/CCN2/FGF9 electrohydrodynamic granulation tissue biomimetic scaffold on wound healing in the gold standard pre-clinical model of cutaneous wound-healing research. No adverse or negative effects of the POSTN/CCN2/FGF9 scaffold were observed. The absence of significant effects, relative to reduced wound closure and enhanced angiogenic growth in db/db mice observed by Elliot et al., may be due to the healthy state of the porcine model (Hamilton lab, In Review, J Tissue Eng), indicating the need for future work to investigate the effects of the POSTN/CCN2/FGF9 scaffold on angiogenesis and wound repair in pathological wound healing.

Preclinical trials assess nonhuman efficacy and toxicity. Once a substantial body of evidence exists supporting the efficacy and absence of toxicity in applicable animal models, a phase I clinical trial can begin. The phase I clinical trial evaluates safety and adverse effects related to administration of the biomaterial [40]. Human chronic wounds are characterized by a lack of vascular ingrowth, ECM deposition, and cellular infiltration [14]. Scaffolds containing FGF9 microspheres decreased wound diameter at day 7 compared to empty wounds in the 7-day porcine model, without causing any adverse events, indicating the potential efficacy of the novel scaffold in human chronic wound healing. Therefore, this work may support the use of the novel POSTN/CCN2/FGF9 scaffold in a phase I human clinical trial to determine efficacy and toxicity of the scaffold in human wound healing [40].

4.2.3 – Therapeutic Efficacy of Fibroblast Growth Factor 9

FGF9 promotes mural cell layering around newly forming vasculature to improve the stability and vasoreactivity of neovessels [15]. In addition, FGF9 stimulates neointimal smooth muscle cell proliferation via the ERK1/2 pathway *in vitro* [15, 34]. For the first time, we have shown that FGF9 stimulates primary HDF proliferation and chemotaxis, although whether this effect is ERK1/2 mediated has yet to be investigated. Future work is required to determine the FGF9 concentration which optimizes HDF proliferation and

chemotaxis. This information would be valuable as a target for FGF9 release kinetics from the FGF9 microspheres. Furthermore, the effect of FGF9 on HDFs *in vivo* and during wound healing is largely unknown. FGF9 was upregulated 2- to 33-fold between days 2 and 21 (peaking on days 7 through 10) during full-thickness cutaneous murine wound healing [41], suggesting FGF9 may actively participate in the late stages of inflammation and throughout the proliferative stage of wound healing. In addition, FGF9 stimulates Wnt/ β -catenin signalling when cultured with human epidermal keratinocytes [42] and FGF9 expression has been linked to autocrine dermal fibroblast Wnt signalling and hair neogenesis in mice cutaneous wounds [43]. These results suggest a multifaceted, regenerative role of FGF9 during wound healing, which has yet to be fully elucidated.

Future work should investigate effects of the POSTN/CCN2/FGF9 scaffold with and without incorporated POSTN/CCN2, and with topical application of FGF9 to elucidate the role of this growth factor during wound healing. Our findings of the proliferative and chemotactic effects of FGF9 on primary HDFs suggest that sustained release of FGF9 from optimized microspheres may serve a secondary role besides stabilization of the developing vasculature in a human chronic wound. However, burst release of FGF9 in the initial 24 hours post-implantation during the 7-day porcine study may have reduced the potential effects of FGF9 due to rapid proteolytic degradation. To accurately measure the therapeutic efficacy of FGF9 for chronic wound healing, future animal models are required with application of the POSTN/CCN2/FGF9 scaffold after microsphere optimization to improve sustained FGF9 release.

4.2.4 – The Porcine Model for Chronic Wound-Healing Research

The porcine model is considered the gold-standard for wound-healing research due to the structural and functional similarities between pig and human skin [44]. However, significant limitations are associated with the porcine model. Pigs are difficult to work with due to their large size, species-specific reagents are not readily available, they are extremely expensive to house and maintain, and transgenic disease models are less prevalent and more difficult to produce than other species [45]. Alternatively, the feasibility of murine models is much higher: costs are low, they are easy to work with due their small size, they are much more cost-efficient, and many species-specific reagents and applicable transgenic models

exist [45]. However, the structure and function of the skin in murine models differs substantially from the human skin, limiting the translatability of murine outcomes to the human condition [45, 46].

Porcine diabetic and chronic non-healing wound models have yet to recapitulate human chronic wounds as healing returns to normal within 3 weeks, inconsistent with the human condition [47-50]. Therefore, delayed wounding in the pig can not be considered chronic wounding. However, this problem persists among small animal models. The rabbit-ear ulcer model generates an ischemic wound after suturing of blood flow to the ear however, this model does not accurately replicate hypoxia in human chronic wounds [51, 52]. Magnetic ischemia-reperfusion wounds in rats reproduce the cellular and molecular mechanisms underlying human pressure ulcers however, they are limited in applicability to chronic non-healing wounds [53]. Genetically induced diabetes in db/db mice is a popular model in chronic wound-healing research however, the diabetic condition and healing deficiencies observed in db/db mice are not equivalent to the human condition [54]. Animal models mirror pathological conditions observed in human chronic wounds however, discrepancies in molecular mechanisms distinguish chronic wounding in animals from humans [55].

We have learned many lessons during the two porcine studies conducted in this thesis, which may benefit other groups who utilize the porcine model. We can attest to the impracticality of the porcine model, as well as the high cost. During the 28-day porcine study, the adolescent pigs were housed from 4 to 5 months of age, at which time they had grown from 40 kg to 83 kg. Multiple members of the veterinary and research teams were required to move the pigs before and after surgery. Imaging of the wounds was completed while the pigs were awake, making clear photography with an accurately placed ruler very difficult and time consuming to accomplish. Furthermore, large variability between animals was a limiting factor to the results of this research. Our experience suggests health related complications involved in porcine models that have not been described elsewhere. One pig died under anaesthetic during the surgical procedure in the 28-day study, and the original 7-day study was cancelled due to the death of one pig with myocardial encephalopathy. These outcomes demonstrate some of the potential health risks involved with the porcine

model, even with animals that are considered healthy at the onset of the study. Development of porcine models of impaired healing may exacerbate the health-related risks that we observed, further decreasing the feasibility of the porcine model.

The porcine model is considered the gold standard for pre-clinical wound-healing research due to the structural and functional similarities between human and pig skin [44]. However, our results did not correlate with the enhanced angiogenesis and wound closure kinetics observed by Elliot et al. in db/db mice (Hamilton lab, In Review, J Tissue Eng), indicating a disconnect between wound-healing research in pathological and acute wounding. Comparison of chronic wound treatments in the porcine model, alternative animal models of impaired healing, and in the human condition is necessary to determine the validity of the porcine model as the gold standard for human wound-healing research.

4.3 – Limitations

4.3.1 – Microsphere Fabrication

A set of electrospaying conditions capable of consistently producing a stable Taylor cone was not discovered during the morphological characterization of microsphere diameter. The accumulation of solution on the tip of the coaxial needle occasionally produced microspheres with high size variability, confounding measurement of microsphere diameter in response to varying electrospaying parameters. Ambient conditions, an inner driving liquid, or clogging of the needle due to impurities in the outer solution may be responsible for this outcome. The lack of control over microsphere morphology and core-shell structure contributed to the complete release of FGF9 within 3 days, which may have limited effects of the POSTN/CCN2/FGF9 scaffold on angiogenesis and wound repair in the 7-day porcine study.

4.3.2 – Acute Porcine Wound-Healing Model

Animal models have yet to recapitulate the complex, multifactorial nature of human chronic wounds [52]. Healthy Yorkshire pigs were selected as the wound-healing model for this research. The rapid rate of healing and normal expression of bioactive factors in the acute wounds created on the dorsal surface of the healthy pigs may have reduced the influence of POSTN/CCN/FGF9 scaffolds [35]. Wound area measurement was limited by the wound

eschar. The eschar was not removed to avoid disrupting the underlying granulation tissue. Wounds with occlusive eschar were measured based on visible area of the wound border, increasing variability in wound measurements. Furthermore, the porcine studies were limited by small samples sizes due to the logistical considerations and high costs associated with the porcine model (day 28 N = 6, day 7 N = 3).

4.4 – Future Directions

4.4.1 – Animal Wound Models

Despite the similarities between pig and human skin, the cellular and molecular mechanisms involved in acute and chronic wounding greatly differ [50]. Accelerated healing and normal expression of signalling molecules relative to the pathological condition may have reduced or eliminated the influence of scaffold treatments in these studies. Follow-up studies are required in impaired pig models to investigate the effect of the scaffolds in a model that better simulates chronic wounding. Follow-up studies in the acute porcine wound-healing model are required to increase sample size and statistical power to elucidate effects that were not observed here. To evaluate the efficacy of FGF9 in chronic wound-healing, the effect of POSTN/CCN2/FGF9 scaffolds on vascular stability in db/db mice should be conducted and compared with previous work by Elliot et al. (Hamilton lab, In Review, J Tissue Eng).

4.4.2 – Co-Structural Scaffold Development

Originally, the POSTN/CCN2/FGF9 scaffold was meant to be fabricated by simultaneous electrospaying of FGF9 microspheres for even dispersion within electrospun POSTN/CCN2 nanofibers (Figure 1.2). However, hydrolytic degradation of the PLGA shell was a concern during glycine quenching and storage. Therefore, POSTN/CCN2 scaffolds were electrospun, crosslinked, and neutralized before a secondary electrospaying step deposited the FGF9 microspheres in a layer on top of the nanofibrous scaffold (Figure 3.16). Future scaffold development may utilize PLGA with a higher concentration of lactic acid to reduce the hydrolytic degradation rate of the core-shell microspheres, and increase the feasibility of the original protocol for the fabrication of the co-structural POSTN/CCN2/FGF9 scaffold [56]. Microspheres evenly dispersed throughout the scaffold

will improve control over the sustained release of FGF9 [57]. In addition, biological effects of FGF9 may have been inhibited due to initial burst release and rapid proteolytic degradation. Future microsphere optimization is required to thicken the PLGA shell and reduce porosity to improve sustained release *in vivo*. Quantification of shell thickness in response to varying process parameters will contribute to control over release kinetics. Finally, optimization of coaxial electrospaying requires a consistent, stable Taylor cone. Future work should control ambient conditions (stable environmental control, drierite under the collecting mandrel to absorb excess moisture in the air), electrospay with an outer driving liquid [58], and utilize needles of different dimensions, to increase the consistency and stability of the Taylor cone.

4.5 – Final Summary

The results presented in this thesis demonstrate successful encapsulation of FGF9 within core-shell PLGA microspheres fabricated by coaxial electrospaying. Sustained release of FGF9 was not achieved however, bioactivity was retained. For the first time, FGF9 was observed to increase HDF proliferation and chemotaxis, indicating a potential cellular mechanism of action during wound healing. Scaffold conditions containing encapsulated FGF9 decreased wound diameter at day 7 in a porcine model of wound healing. Normative collagen deposition and blood-vessel density in scaffold treated wounds without a foreign body response, adverse events, or negative results support further investigation of the novel POSTN/CCN2/FGF9 scaffold in animal models of impaired wound healing. Future work is required to optimize microsphere morphology to sustain release of encapsulated bioactive factors and investigate the role of the POSTN/CCN2/FGF9 scaffold in a more applicable model of chronic wound healing.

4.6 – References

1. Katti, D.S., et al., *Bioresorbable nanofiber-based systems for wound healing and drug delivery: optimization of fabrication parameters*. J Biomed Mater Res B Appl Biomater, 2004. **70**(2): p. 286-96.
2. Pezeshki-Modaress, M., H. Mirzadeh, and M. Zandi, *Gelatin-GAG electrospun nanofibrous scaffold for skin tissue engineering: fabrication and modeling of process parameters*. Mater Sci Eng C Mater Biol Appl, 2015. **48**: p. 704-12.
3. Subbiah, T., et al., *Electrospinning of nanofibers*. Journal of Applied Polymer Science, 2005. **96**(2): p. 557-569.
4. Rho, K.S., et al., *Electrospinning of collagen nanofibers: effects on the behavior of normal human keratinocytes and early-stage wound healing*. Biomaterials, 2006. **27**(8): p. 1452-61.
5. Murugan, R. and S. Ramakrishna, *Design strategies of tissue engineering scaffolds with controlled fiber orientation*. Tissue Eng, 2007. **13**(8): p. 1845-66.
6. Morton, L.M. and T.J. Phillips, *Wound healing and treating wounds: Differential diagnosis and evaluation of chronic wounds*. J Am Acad Dermatol, 2016. **74**(4): p. 589-605; quiz 605-6.
7. Panasci, K., *Chapter 12 - Burns and Wounds*, in *Acute Care Handbook for Physical Therapists (Fourth Edition)*, J.C. Paz and M.P. West, Editors. 2014, W.B. Saunders: St. Louis. p. 283-311.
8. Edsberg, L.E., et al., *Analysis of the proteomic profile of chronic pressure ulcers*. Wound Repair Regen, 2012. **20**(3): p. 378-401.
9. Baltzis, D., I. Eleftheriadou, and A. Veves, *Pathogenesis and treatment of impaired wound healing in diabetes mellitus: new insights*. Adv Ther, 2014. **31**(8): p. 817-36.
10. Frykberg, R.G. and J. Banks, *Challenges in the Treatment of Chronic Wounds*. Advances in Wound Care, 2015. **4**(9): p. 560-582.
11. Bello, Y.M., A.F. Falabella, and W.H. Eaglstein, *Tissue-engineered skin. Current status in wound healing*. Am J Clin Dermatol, 2001. **2**(5): p. 305-13.
12. Debels, H., et al., *Dermal Matrices and Bioengineered Skin Substitutes: A Critical Review of Current Options*. Plastic and Reconstructive Surgery Global Open, 2015. **3**(1): p. e284.
13. Cui, T., R.S. Kirsner, and J. Li, *Angiogenesis in Chronic Wounds*, in *Advances in Wound Care: Volume 1*. 2010, Mary Ann Liebert, Inc., publishers: New Rochelle. p. 347-352.
14. Elliott, C.G., et al., *Inflammatory microenvironment and tumor necrosis factor alpha as modulators of periostin and CCN2 expression in human non-healing skin wounds and dermal fibroblasts*. Matrix Biol, 2015. **43**: p. 71-84.
15. Frontini, M.J., et al., *Fibroblast growth factor 9 delivery during angiogenesis produces durable, vasoresponsive microvessels wrapped by smooth muscle cells*. Nat Biotechnol, 2011. **29**(5): p. 421-7.
16. Nishiyama, T., et al., *Delayed re-epithelialization in periostin-deficient mice during cutaneous wound healing*. PLoS One, 2011. **6**(4): p. e18410.
17. Ontsuka, K., et al., *Periostin, a matricellular protein, accelerates cutaneous wound repair by activating dermal fibroblasts*. Exp Dermatol, 2012. **21**(5): p. 331-6.

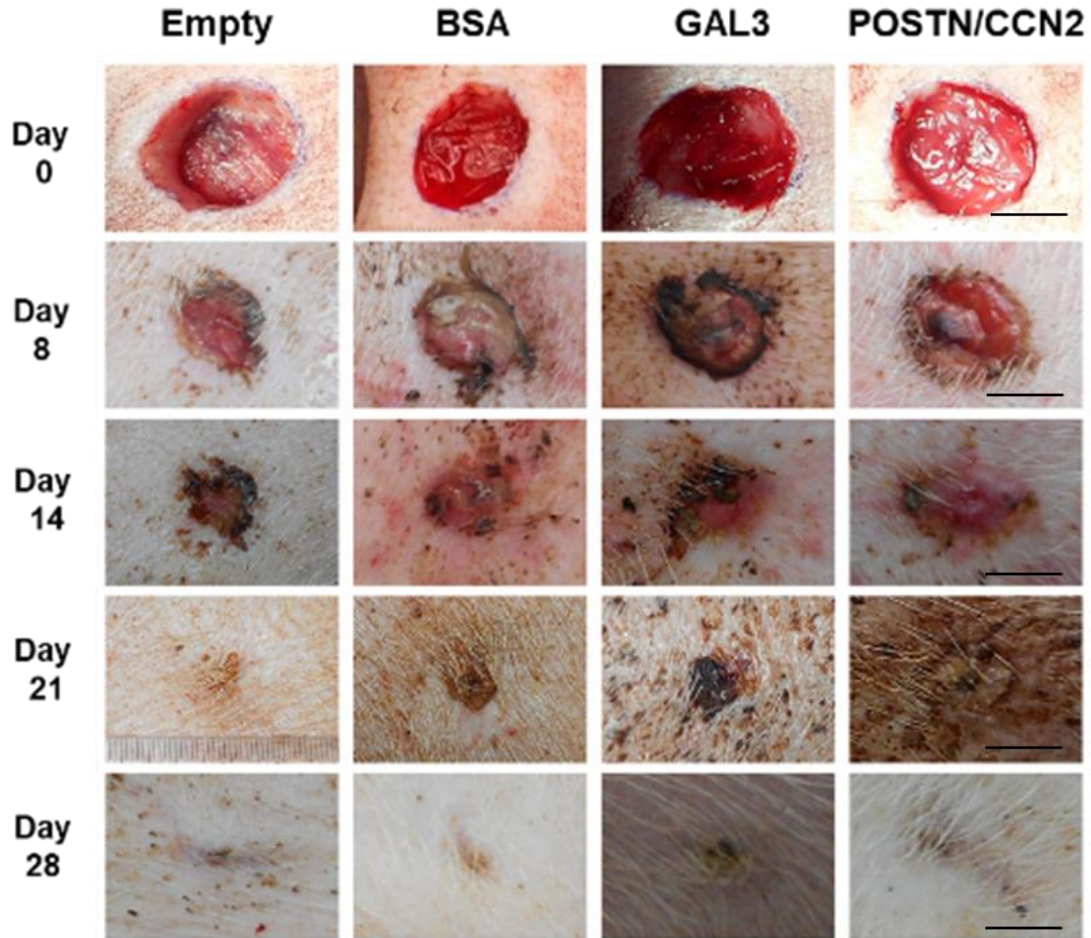
18. Elliott, C.G., et al., *Periostin modulates myofibroblast differentiation during full-thickness cutaneous wound repair*. J Cell Sci, 2012. **125**(Pt 1): p. 121-32.
19. Brigstock, D.R., *Connective tissue growth factor (CCN2, CTGF) and organ fibrosis: lessons from transgenic animals*. J Cell Commun Signal, 2010. **4**(1): p. 1-4.
20. Babic, A.M., et al., *CYR61, a product of a growth factor-inducible immediate early gene, promotes angiogenesis and tumor growth*. Proc Natl Acad Sci U S A, 1998. **95**(11): p. 6355-60.
21. Kubota, S. and M. Takigawa, *CCN family proteins and angiogenesis: from embryo to adulthood*. Angiogenesis, 2007. **10**(1): p. 1-11.
22. Dean, R.A., et al., *Identification of candidate angiogenic inhibitors processed by matrix metalloproteinase 2 (MMP-2) in cell-based proteomic screens: disruption of vascular endothelial growth factor (VEGF)/heparin affin regulatory peptide (pleiotrophin) and VEGF/Connective tissue growth factor angiogenic inhibitory complexes by MMP-2 proteolysis*. Mol Cell Biol, 2007. **27**(24): p. 8454-65.
23. Inoki, I., et al., *Connective tissue growth factor binds vascular endothelial growth factor (VEGF) and inhibits VEGF-induced angiogenesis*. Faseb j, 2002. **16**(2): p. 219-21.
24. Greiner, A. and J.H. Wendorff, *Electrospinning: a fascinating method for the preparation of ultrathin fibers*. Angew Chem Int Ed Engl, 2007. **46**(30): p. 5670-703.
25. van Zuijlen, P.P., et al., *Collagen morphology in human skin and scar tissue: no adaptations in response to mechanical loading at joints*. Burns, 2003. **29**(5): p. 423-31.
26. Matthews, J.A., et al., *Electrospinning of Collagen Nanofibers*. Biomacromolecules, 2002. **3**(2): p. 232-238.
27. Powell, H.M. and S.T. Boyce, *Fiber density of electrospun gelatin scaffolds regulates morphogenesis of dermal-epidermal skin substitutes*. J Biomed Mater Res A, 2008. **84**(4): p. 1078-86.
28. Kumbhar, S.G., et al., *Electrospun poly(lactic acid-co-glycolic acid) scaffolds for skin tissue engineering*. Biomaterials, 2008. **29**(30): p. 4100-7.
29. Chen, M., et al., *Role of Fiber Diameter in Adhesion and Proliferation of NIH 3T3 Fibroblast on Electrospun Polycaprolactone Scaffolds*. Vol. 13. 2007. 579-87.
30. Yu, T., et al., *Temporal and spatial distribution of macrophage phenotype markers in the foreign body response to glutaraldehyde-crosslinked gelatin hydrogels*. J Biomater Sci Polym Ed, 2016. **27**(8): p. 721-42.
31. Walker, J.T., et al., *Periostin as a Multifunctional Modulator of the Wound Healing Response*. Cell and tissue research, 2016. **365**(3): p. 453-465.
32. Puppi, D., et al., *Poly(lactic-co-glycolic acid) electrospun fibrous meshes for the controlled release of retinoic acid*. Acta Biomater, 2010. **6**(4): p. 1258-68.
33. Zhang, Z.H.E., et al., *Upregulated periostin promotes angiogenesis in keloids through activation of the ERK 1/2 and focal adhesion kinase pathways, as well as the upregulated expression of VEGF and angiopoietin-1*. Molecular Medicine Reports, 2015. **11**(2): p. 857-864.
34. Agrotis, A., et al., *Proliferation of neointimal smooth muscle cells after arterial injury. Dependence on interactions between fibroblast growth factor receptor-2 and fibroblast growth factor-9*. J Biol Chem, 2004. **279**(40): p. 42221-9.

35. Wilhelm, K.P., D. Wilhelm, and S. Bielfeldt, *Models of wound healing: an emphasis on clinical studies*. Skin Res Technol, 2017. **23**(1): p. 3-12.
36. Wietecha, M.S., W.L. Cerny, and L.A. DiPietro, *Mechanisms of vessel regression: toward an understanding of the resolution of angiogenesis*. Curr Top Microbiol Immunol, 2013. **367**: p. 3-32.
37. Bluff, J.E., et al., *The microcirculation in acute murine cutaneous incisional wounds shows a spatial and temporal variation in the functionality of vessels*. Wound Repair Regen, 2006. **14**(4): p. 434-42.
38. Urao, N., et al., *MicroCT angiography detects vascular formation and regression in skin wound healing*. Microvascular research, 2016. **106**: p. 57-66.
39. Elliott, C.G., et al., *Periostin modulates myofibroblast differentiation during full-thickness cutaneous wound repair*. Journal of Cell Science, 2011.
40. Mahipal, A. and D. Nguyen, *Risks and benefits of phase 1 clinical trial participation*. Cancer Control, 2014. **21**(3): p. 193-9.
41. Komi-Kuramochi, A., et al., *Expression of fibroblast growth factors and their receptors during full-thickness skin wound healing in young and aged mice*. J Endocrinol, 2005. **186**(2): p. 273-89.
42. Zheng, Z., et al., *Up-regulation of fibroblast growth factor (FGF) 9 expression and FGF-WNT/beta-catenin signaling in laser-induced wound healing*. Wound Repair Regen, 2014. **22**(5): p. 660-5.
43. Gay, D., et al., *Fgf9 from dermal gammadelta T cells induces hair follicle neogenesis after wounding*. Nat Med, 2013. **19**(7): p. 916-23.
44. Sullivan, T.P., et al., *The pig as a model for human wound healing*. Wound Repair Regen, 2001. **9**(2): p. 66-76.
45. Seaton, M., A. Hocking, and N.S. Gibran, *Porcine models of cutaneous wound healing*. Ilar j, 2015. **56**(1): p. 127-38.
46. Wong, V.W., et al., *Surgical approaches to create murine models of human wound healing*. J Biomed Biotechnol, 2011. **2011**: p. 969618.
47. Roy, S., et al., *Characterization of a preclinical model of chronic ischemic wound*. Physiol Genomics, 2009. **37**(3): p. 211-24.
48. Bernatchez, S.F., et al., *Histological characterization of a delayed wound healing model in pig*. Wound Repair Regen, 1998. **6**(3): p. 223-33.
49. Hyodo, A., et al., *Evaluation of a pressure sore model using monoplegic pigs*. Plast Reconstr Surg, 1995. **96**(2): p. 421-8.
50. Velander, P., et al., *Impaired wound healing in an acute diabetic pig model and the effects of local hyperglycemia*. Wound Repair Regen, 2008. **16**(2): p. 288-93.
51. Liechty, K.W., et al., *Elevated platelet-derived growth factor-B in congenital cystic adenomatoid malformations requiring fetal resection*. J Pediatr Surg, 1999. **34**(5): p. 805-9; discussion 809-10.
52. Nunan, R., K.G. Harding, and P. Martin, *Clinical challenges of chronic wounds: searching for an optimal animal model to recapitulate their complexity*. Dis Model Mech, 2014. **7**(11): p. 1205-13.
53. Peirce, S.M., T.C. Skalak, and G.T. Rodeheaver, *Ischemia-reperfusion injury in chronic pressure ulcer formation: a skin model in the rat*. Wound Repair Regen, 2000. **8**(1): p. 68-76.

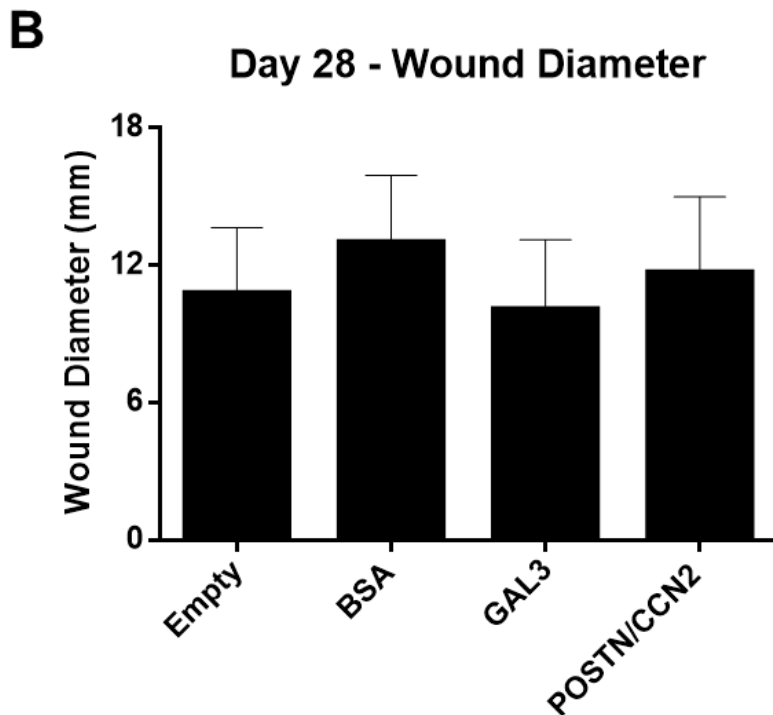
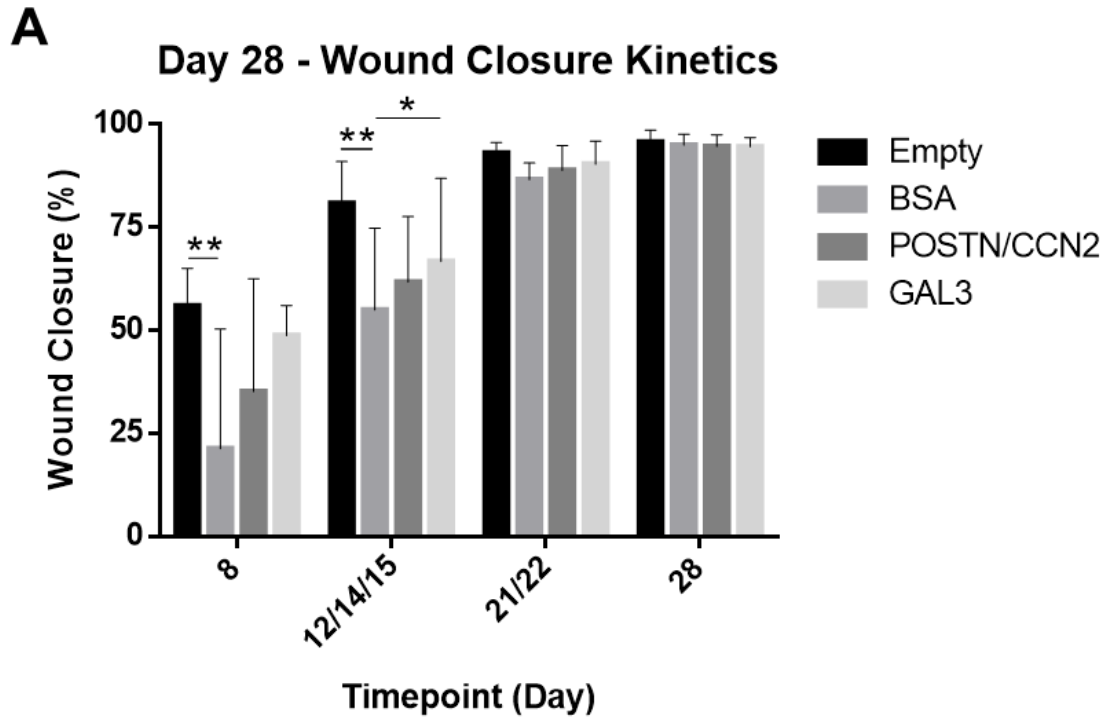
54. Fang, R.C., et al., *Limitations of the db/db mouse in translational wound healing research: Is the NONcNZO10 polygenic mouse model superior?* Wound Repair Regen, 2010. **18**(6): p. 605-13.
55. Trøstrup, H., et al., *Animal models of chronic wound care&58; the application of biofilms in clinical research.* Chronic Wound Care Management and Research, 2017. **55**: p. 123-132.
56. Kapoor, D.N., et al., *PLGA: a unique polymer for drug delivery.* Ther Deliv, 2015. **6**(1): p. 41-58.
57. Guo, X., et al., *Creating 3D angiogenic growth factor gradients in fibrous constructs to guide fast angiogenesis.* Biomacromolecules, 2012. **13**(10): p. 3262-71.
58. Olvera-Trejo, D. and L.F. Velasquez-Garcia, *Additively manufactured MEMS multiplexed coaxial electrospray sources for high-throughput, uniform generation of core-shell microparticles.* Lab Chip, 2016. **16**(21): p. 4121-4132.

Appendices

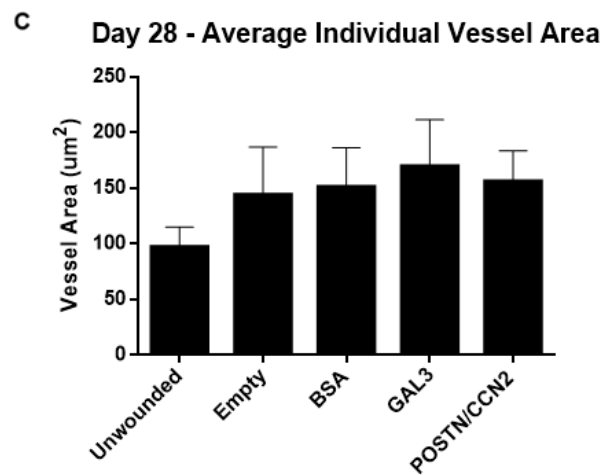
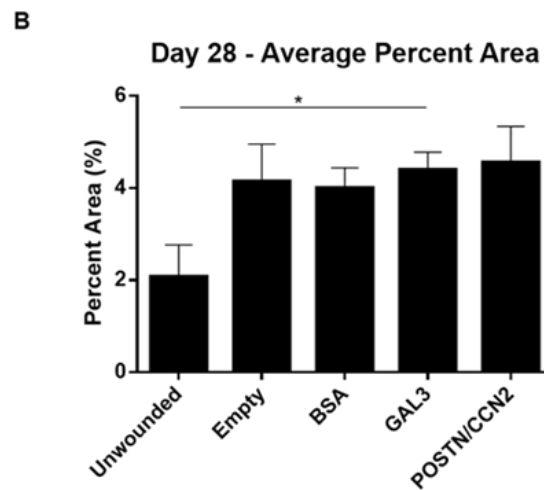
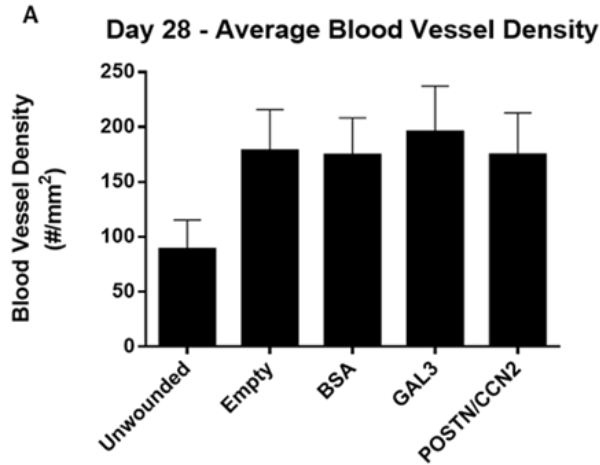
Appendix A: GAL3 results included in representative wound images from the day 28 porcine cutaneous wound-healing study.



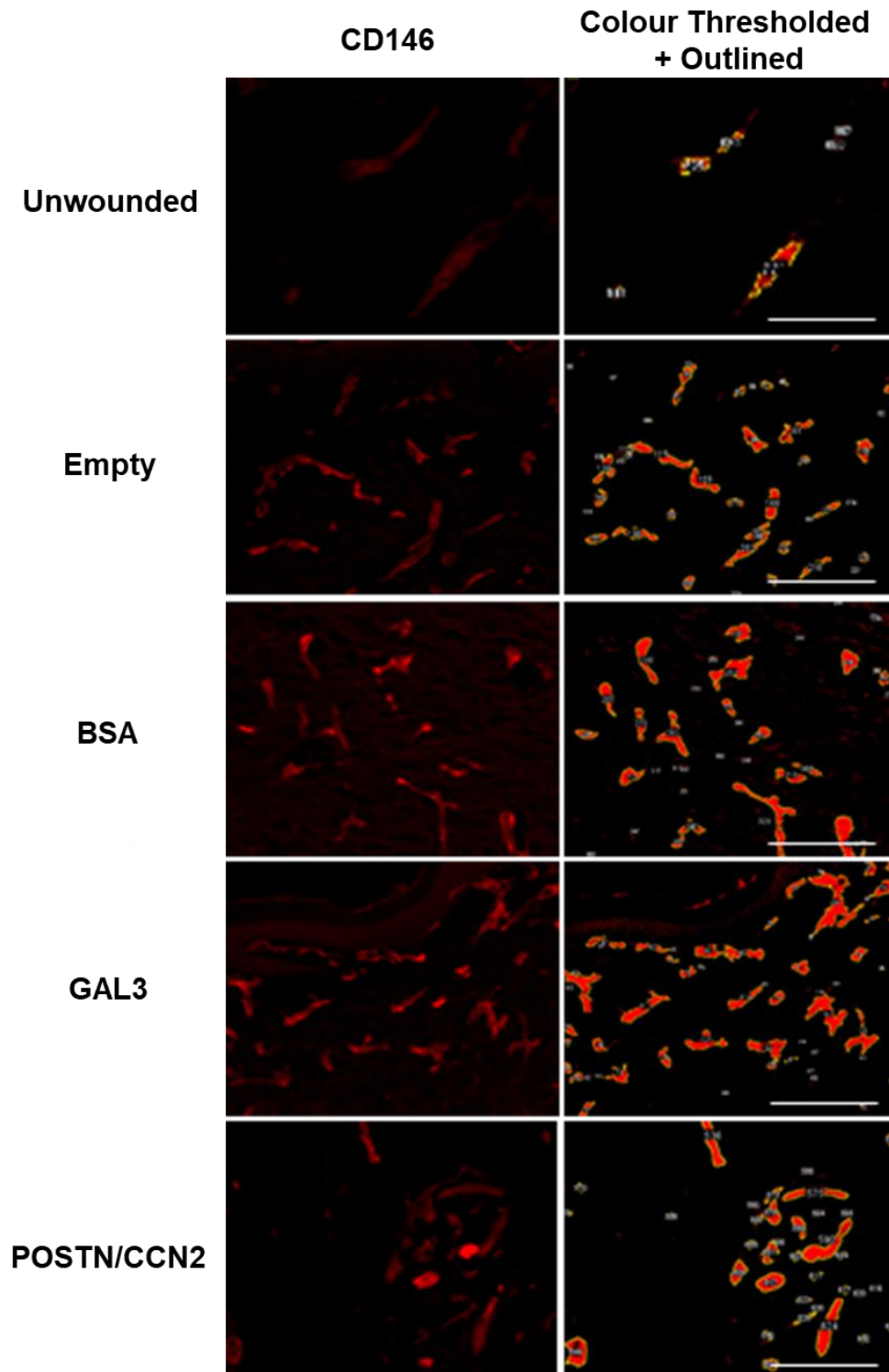
Appendix B: GAL3 results included in wound closure kinetics data from the day 28 porcine cutaneous wound-healing study.



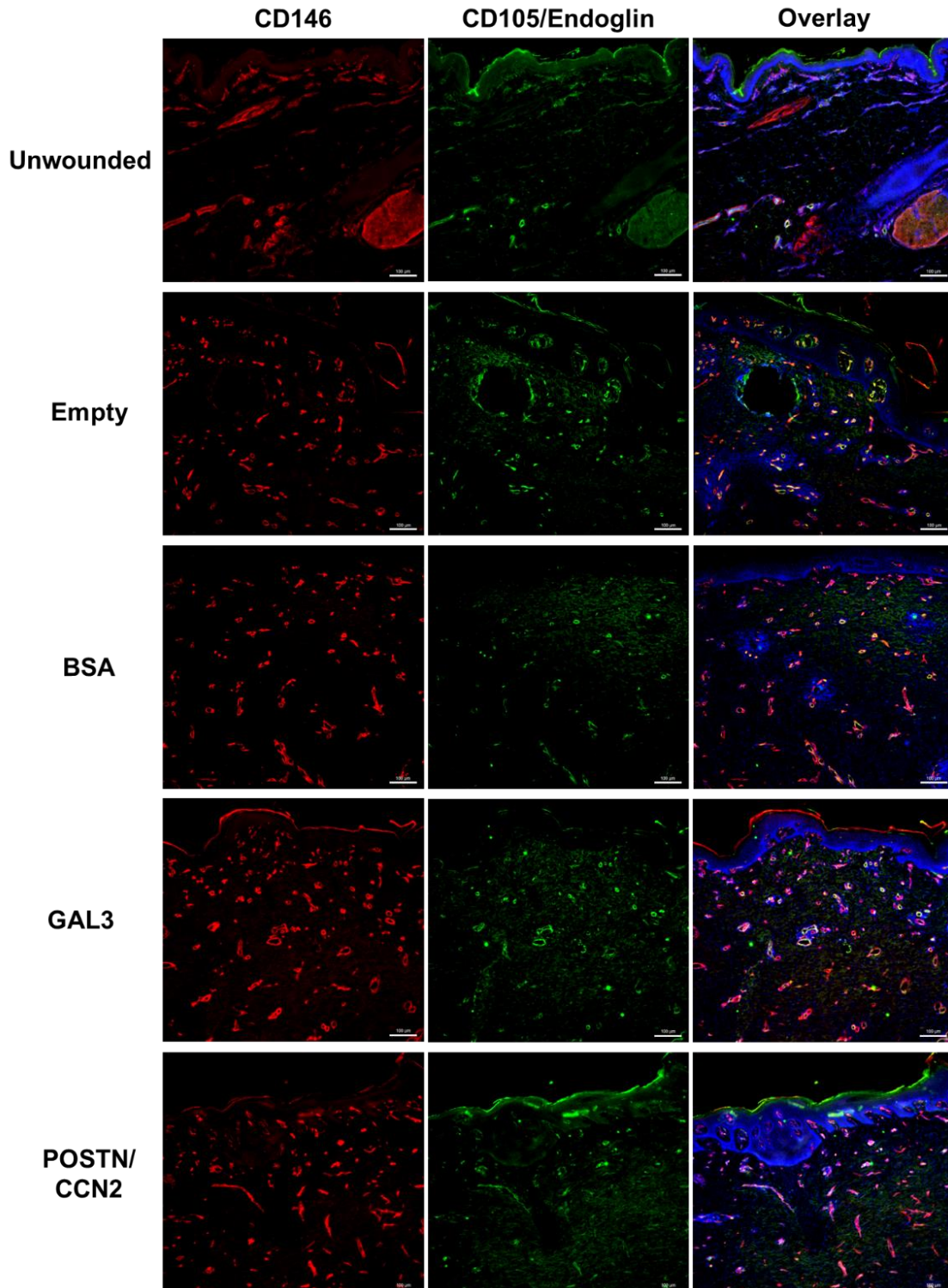
Appendix C: GAL3 results included in angiogenic outcomes from the day 28 porcine cutaneous wound-healing study.



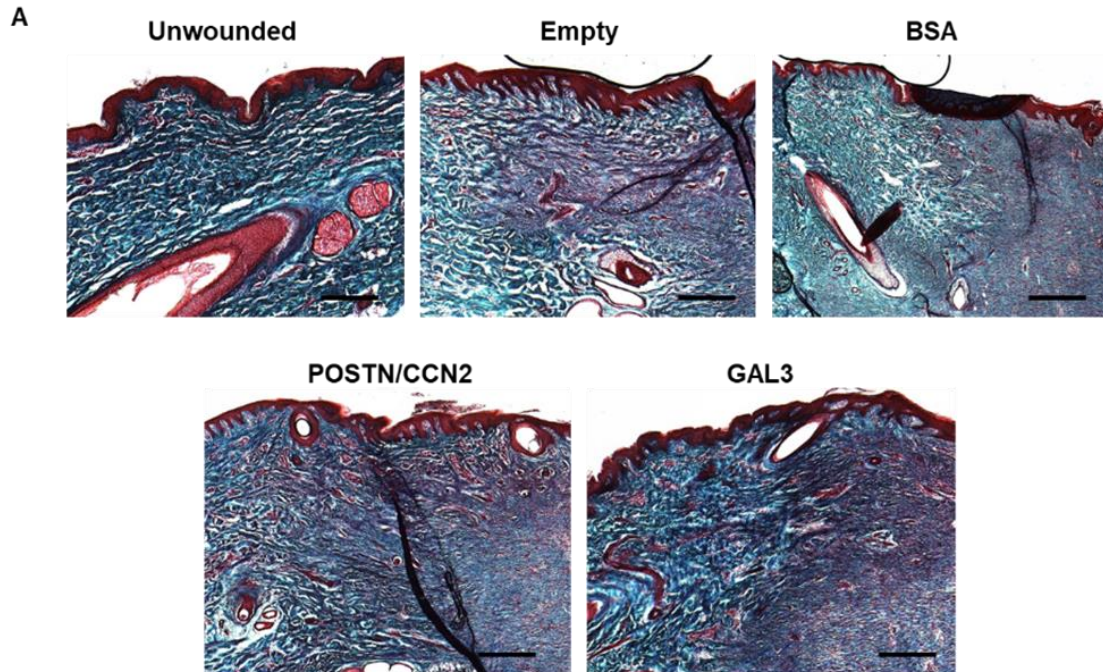
Appendix D: GAL3 results included in representative CD146 immunofluorescent images of the wound bed vasculature from the day 28 porcine cutaneous wound-healing study.



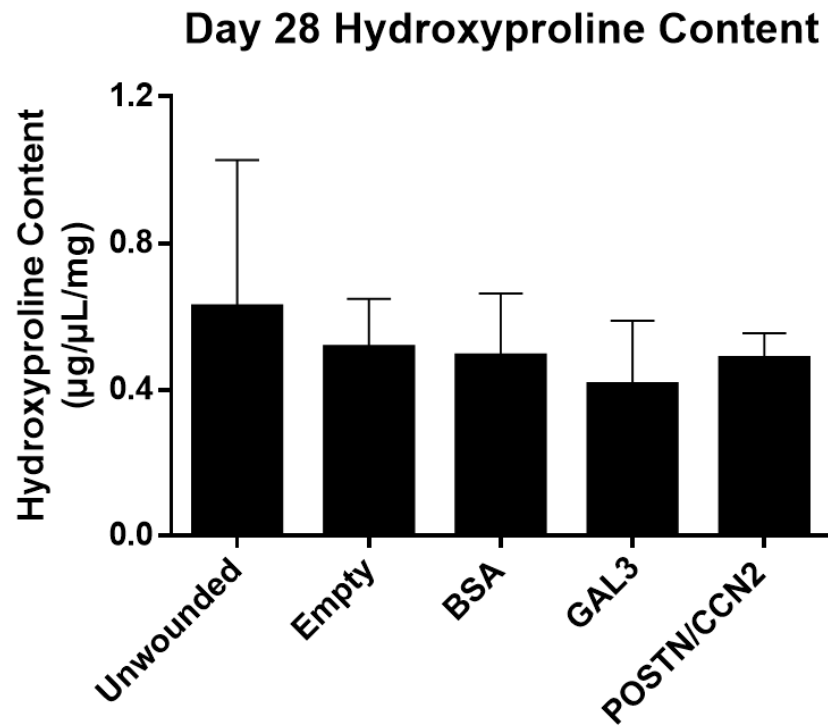
Appendix E: GAL3 results included in representative CD146/CD105 immunofluorescent images of the wound bed vasculature from the day 28 porcine cutaneous wound-healing study.



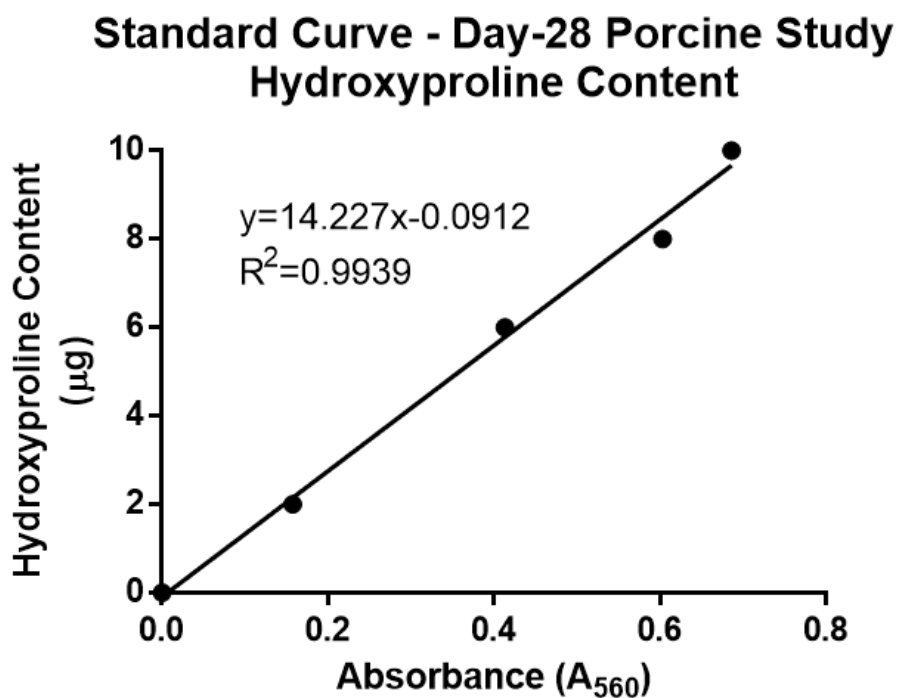
Appendix F: GAL3 results included in Masson's Trichrome images and hydroxyproline content from the day 28 porcine cutaneous wound-healing study.



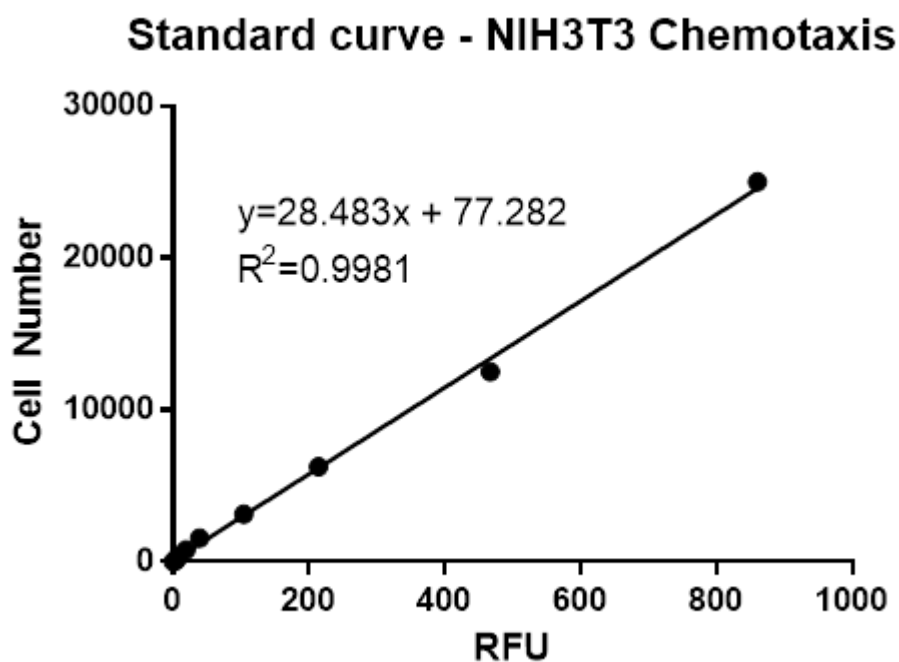
B



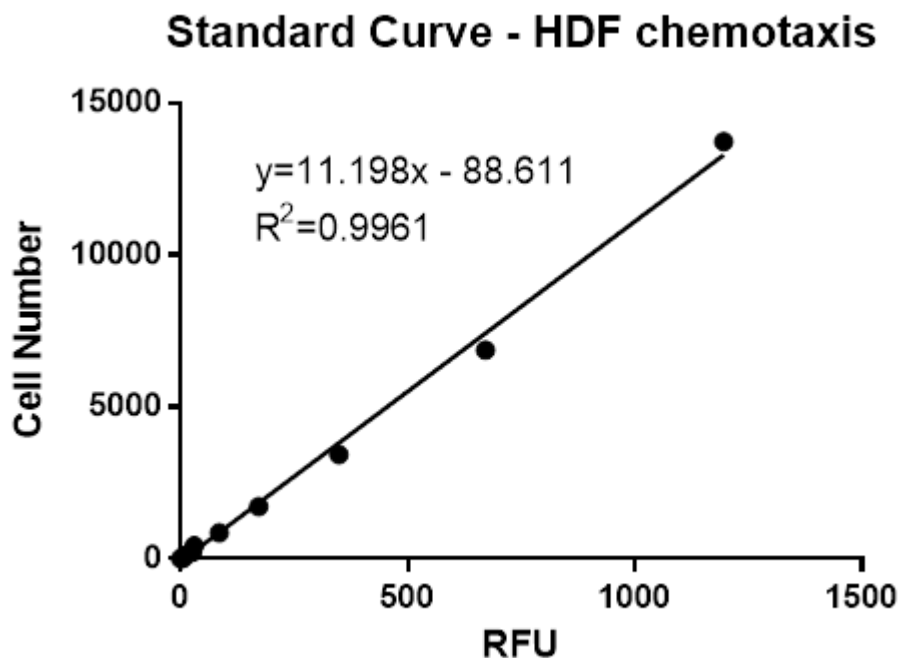
Appendix G: Standard curve for the quantification of hydroxyproline content in 28-day porcine tissues using a Hydroxyproline Assay Kit.



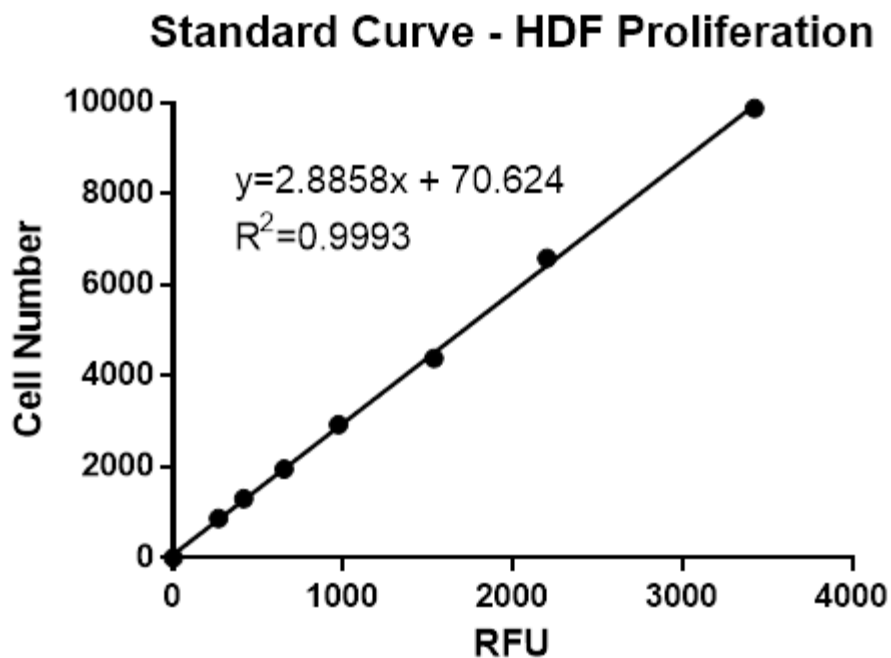
Appendix H: Standard curve for the quantification of NIH3T3 cell number using the Cultrex® Cell Migration Assay Kit.



Appendix I: Standard curve for the quantification of HDF cell number using the Cultrex® Cell Migration Assay Kit.

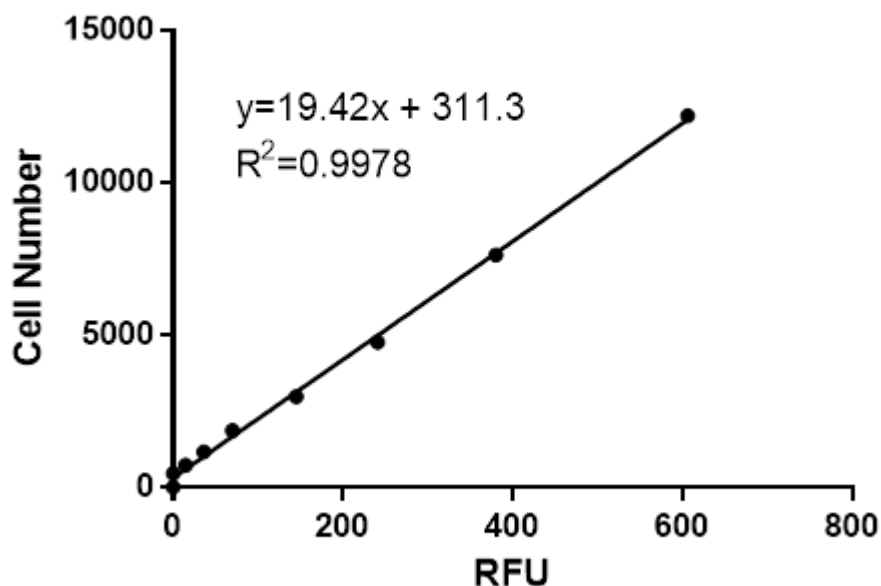


Appendix J: Standard curve for the quantification of HDF cell number using the CyQUANT® Proliferation Assay Kit.



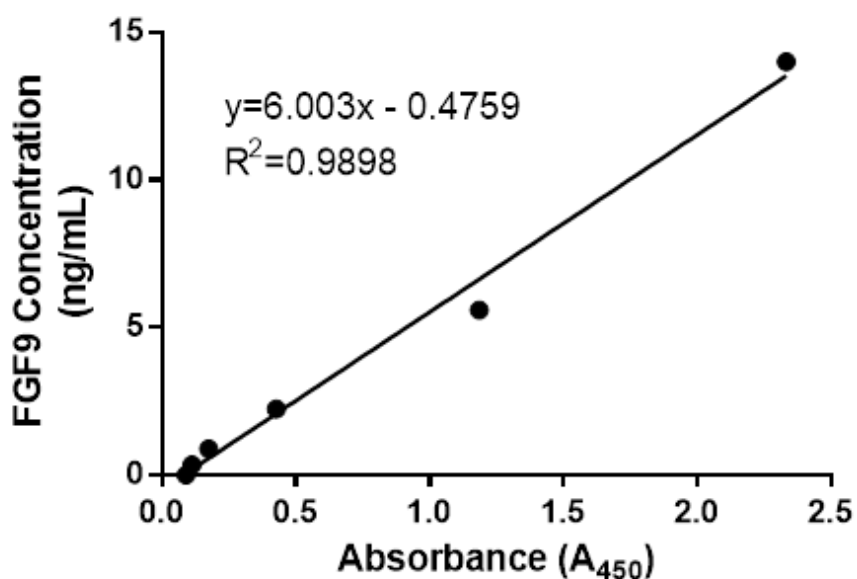
Appendix K: Standard curve for the quantification of HDF cell number using the CyQUANT® Proliferation Assay Kit.

Standard Curve - Effect of Released FGF9 on HDF Proliferation

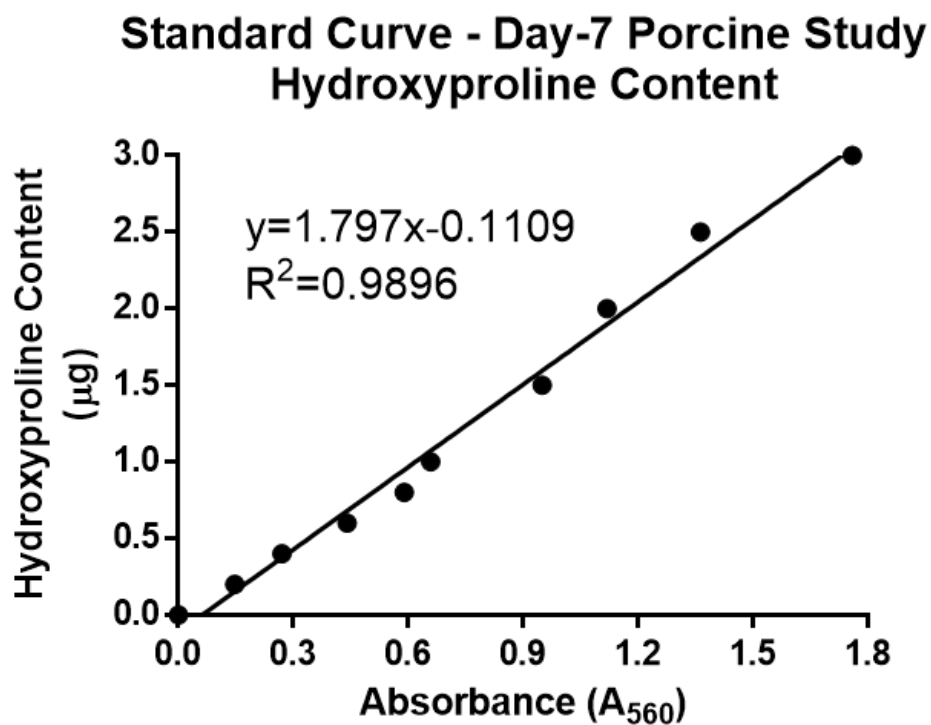


Appendix L: Standard curve for the quantification of released FGF9 from electrosprayed PLGA microspheres using the Human FGF9 ELISA Kit.

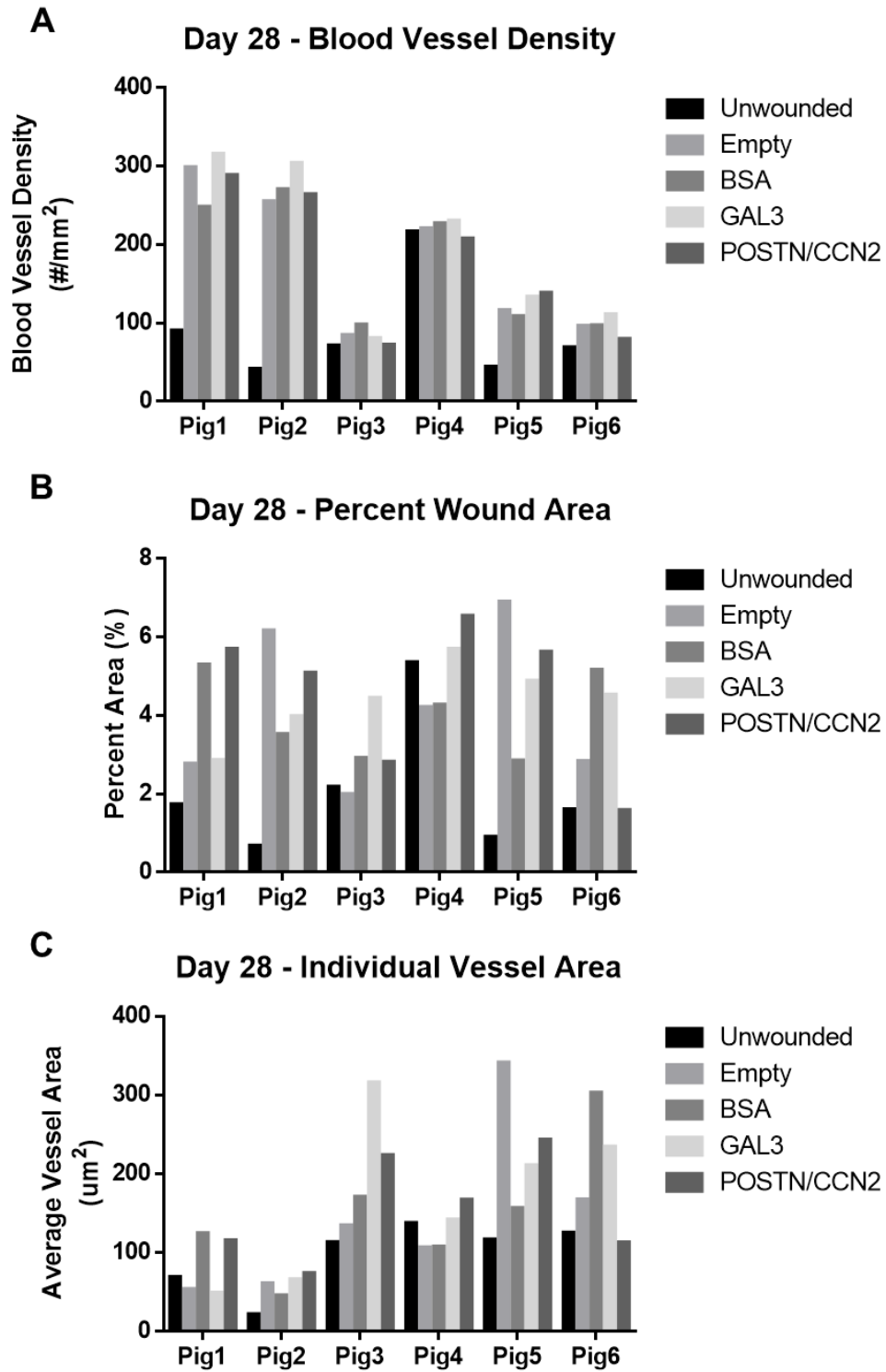
Standard Curve - Human FGF9 ELISA



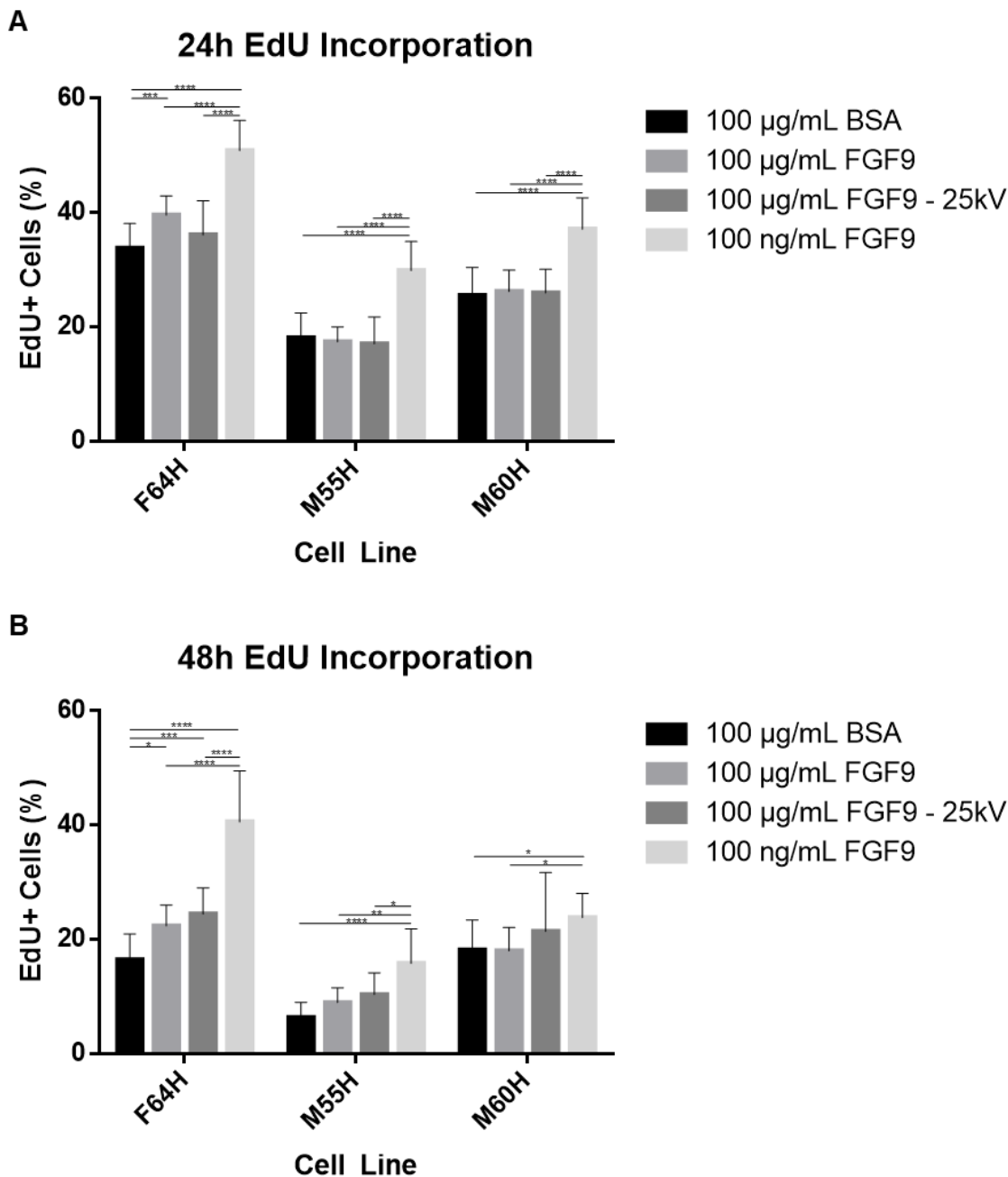
Appendix M: Standard curve for the quantification of hydroxyproline content in 7-day porcine tissues using a Hydroxyproline Assay Kit.



Appendix N: Angiogenic outcomes of the 28-day porcine wound-healing study presented per pig.

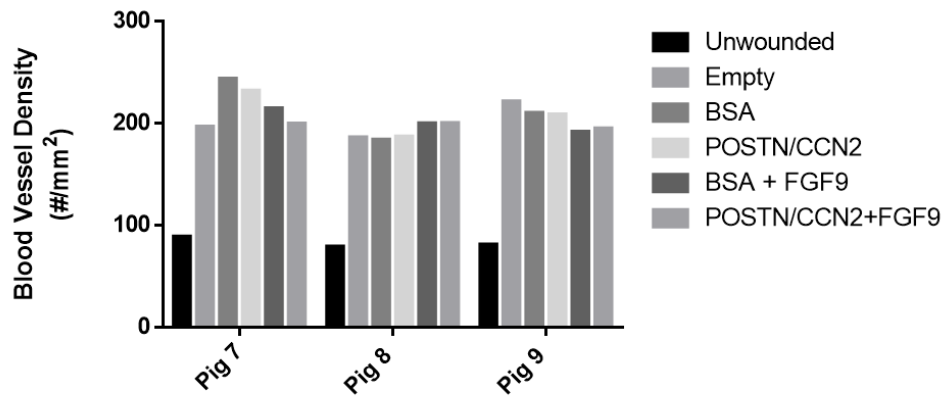


Appendix O: S-phase EdU incorporation at 48 hours in response to elevated levels of FGF9 released from core-shell microspheres presented per cell line.

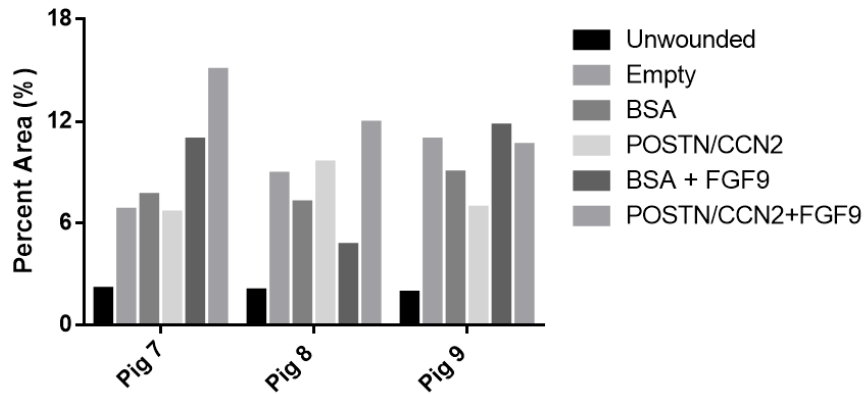


Appendix P: Angiogenic outcomes of the 7-day porcine wound-healing study presented per pig.

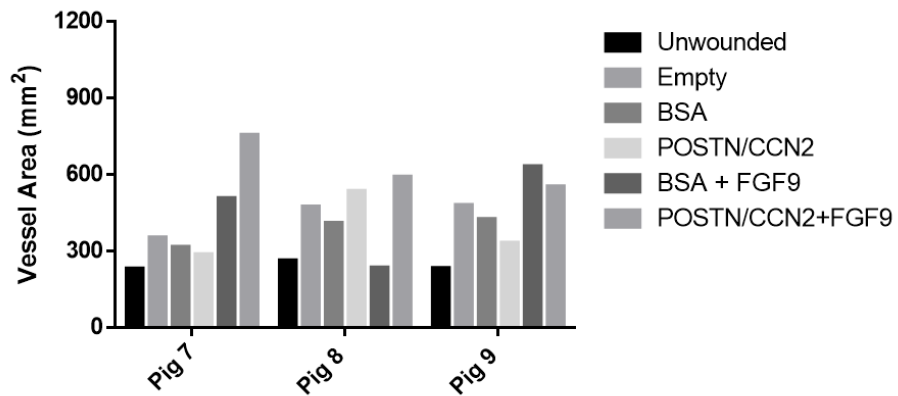
A Day 7 - Blood Vessel Density



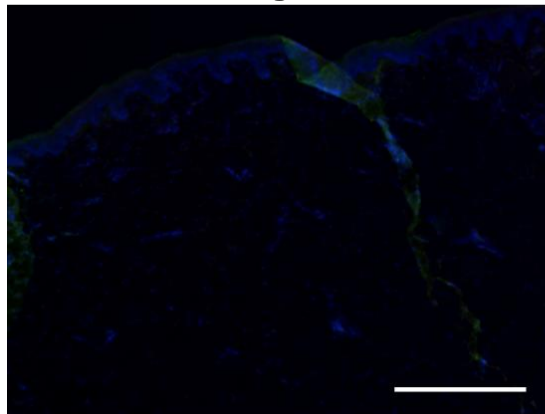
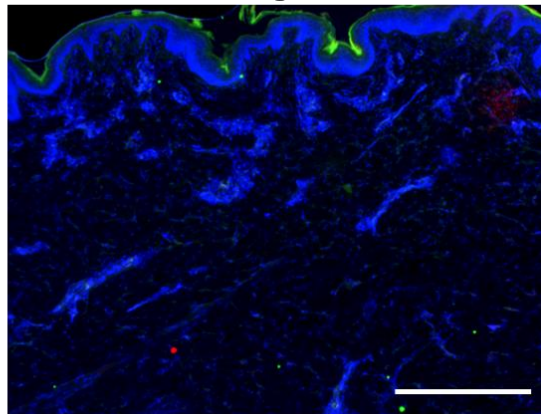
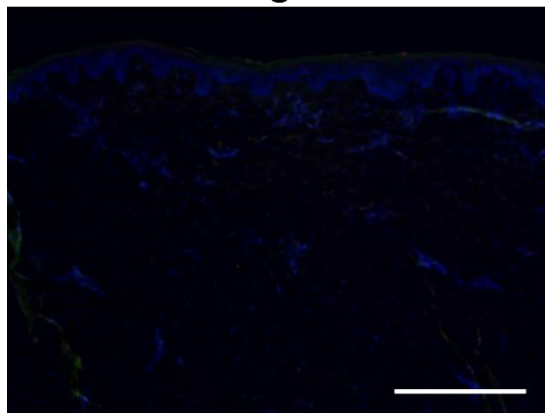
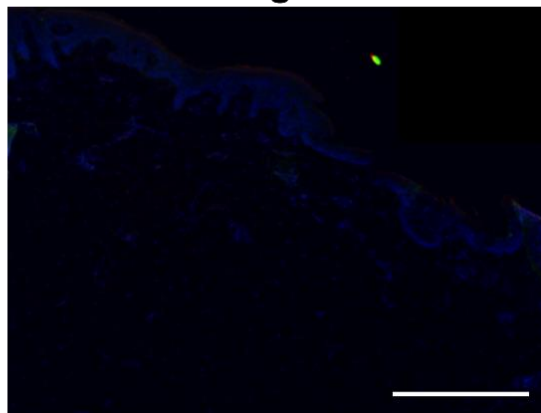
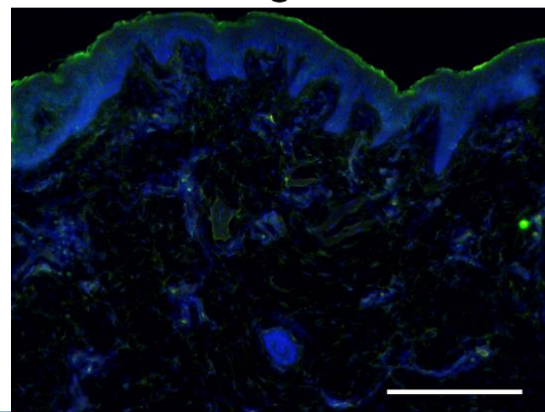
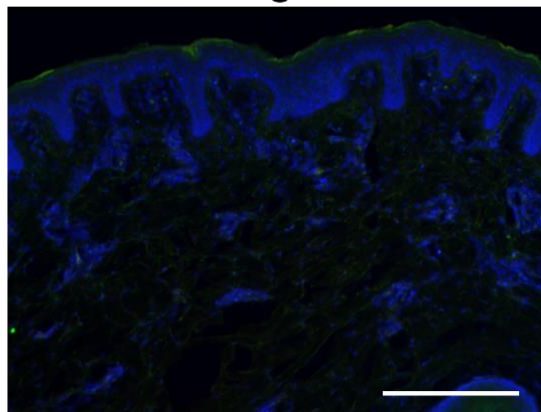
B Day 7 - Percent Wound Area



C Day 7 - Individual Vessel Area

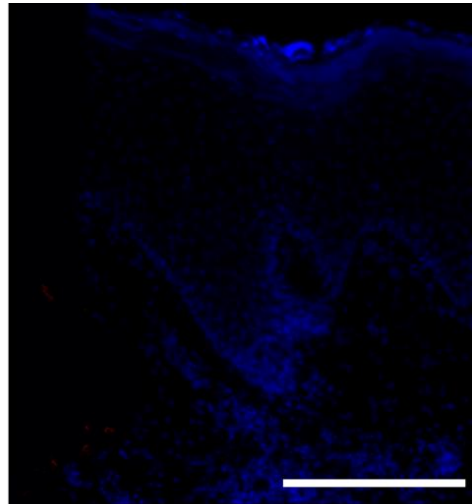


Appendix Q: No primary antibody negative control images of CD146/CD105 (Endoglin) immunofluorescent staining in the 28-day porcine study (scale bar = 200 μ m).

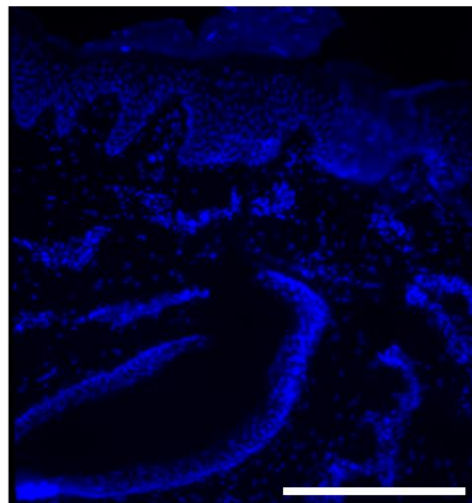
Pig 1**Pig 4****Pig 2****Pig 5****Pig 3****Pig 6**

Appendix R: No primary antibody negative control images of CD146/CD105 (Endoglin) immunofluorescent staining in the day 7 porcine study (scale bar = 250 μm).

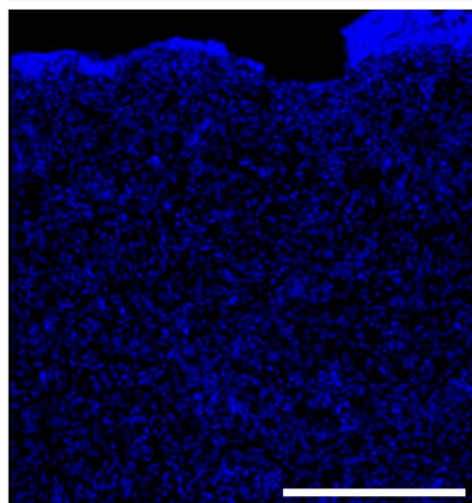
Pig 1



Pig 2

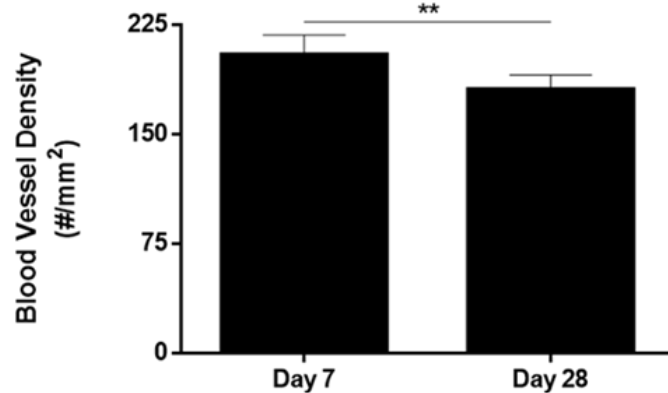


Pig 3

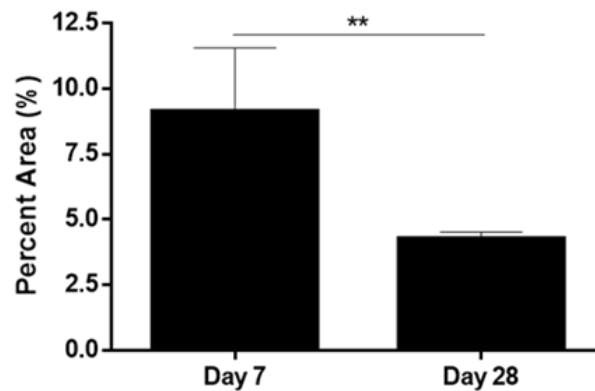


Appendix S: Porcine cutaneous wound-healing angiogenic outcomes on day 7 compared to day 28 (= $p < 0.01$, *** = $p < 0.001$).**

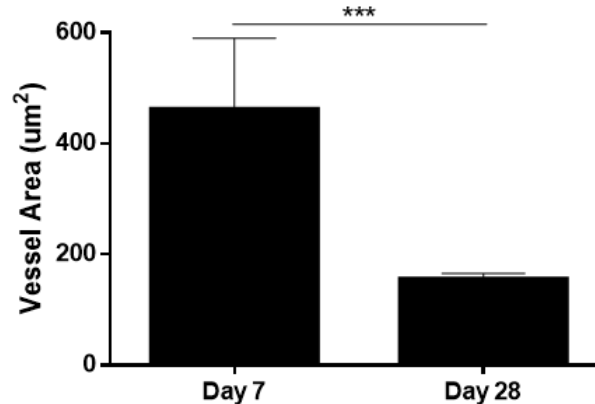
A Day 7 vs. Day 28 - Average Blood Vessel Density



B Day 7 vs. Day 28 - Average Percent Wound Area



C Day 7 vs. 28 - Average Individual Vessel Area



Appendix T: List of Antibodies

1^o Mouse monoclonal anti-CD105 endoglin antibody (Invitrogen)

Rabbit monoclonal anti-CD146 (Abcam)

2^o AF 488 goat anti-mouse IgG (Thermo Fisher)

AF 555 donkey anti-rabbit IgG (Thermo Fisher)

Hoechst 33342 (Thermo Fisher)

Rhodamine B Base (Sigma)

Curriculum Vitae

Name	Adam Hopfgartner
Post-secondary Education and Degrees	The University of Western Ontario London, Ontario, Canada 2011-2015 BMSc
	The University of Western Ontario London, Ontario, Canada 2016-2018 MEd
Related Work Experience	Research Assistant Lawson Health Research Institute January 2016 – August 2016
Other Contributions	Poster Presentation <i>Assessment of Matricellular Protein Biomimetic Scaffolds in a Porcine Model of Cutaneous Wound Healing</i> Annual Meeting of the Wound Healing Society April 2018